

**MATERIALS FOR ADAPTIVE STRUCTURAL
ACOUSTIC CONTROL**

Period February 1, 1995 to January 31, 1996

Annual Report

VOLUME V

OFFICE OF NAVAL RESEARCH
Contract No.: N00014-92-J-1510

APPROVED FOR PUBLIC RELEASE — DISTRIBUTION UNLIMITED

Reproduction in whole or in part is permitted
for any purpose of the United States Government

19960703 065

L. Eric Cross

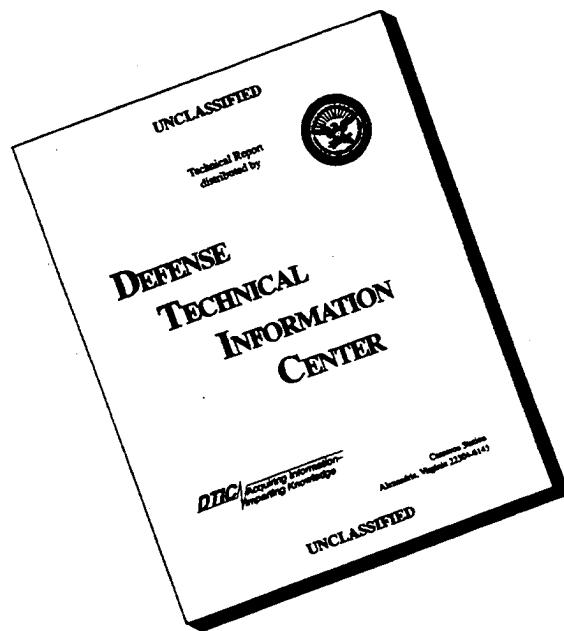
PENNSTATE



THE MATERIALS RESEARCH LABORATORY
UNIVERSITY PARK, PA

DTIC QUALITY INSPECTED 1

DISCLAIMER NOTICE



THIS DOCUMENT IS BEST QUALITY AVAILABLE. THE COPY FURNISHED TO DTIC CONTAINED A SIGNIFICANT NUMBER OF PAGES WHICH DO NOT REPRODUCE LEGIBLY.

REPORT DOCUMENTATION PAGE			Form Approved OMB No. 0704-0188	
Public reporting burden for this collection of information is estimated to average 1 hour per response, including the time for reviewing instructions, searching existing data sources, gathering and maintaining the data needed, and completing and reviewing the collection of information. Send comments regarding this burden estimate or any other aspect of this collection of information, including suggestions for reducing this burden, to Washington Headquarters Services, Directorate for Information Operations and Reports, 1215 Jefferson Davis Highway, Suite 1204, Arlington, VA 22202-4302, and to the Office of Management and Budget, Paperwork Reduction Project (0704-0188), Washington, DC 20503.				
1. AGENCY USE ONLY (Leave blank)	2. REPORT DATE 3/13/96	3. REPORT TYPE AND DATES COVERED ANNUAL REPORT 02/01/95 TO 01/31/96		
4. TITLE AND SUBTITLE MATERIALS FOR ADAPTIVE STRUCTURAL ACOUSTIC CONTROL			5. FUNDING NUMBERS	
6. AUTHOR(S) L. ERIC CROSS				
7. PERFORMING ORGANIZATION NAME(S) AND ADDRESS(ES) MATERIALS RESEARCH LABORATORY THE PENNSYLVANIA STATE UNIVERSITY UNIVERSITY PARK, PA 16802			8. PERFORMING ORGANIZATION REPORT NUMBER	
9. SPONSORING / MONITORING AGENCY NAME(S) AND ADDRESS(ES) OFFICE OF NAVAL RESEARCH GERALD T. SMITH CODE 1513:NRJ OFFICE OF NAVAL RESEARCH RES. REP. 800 NORTH QUINCY STREET 536 SOUTH CLARK STREET, RM 286 ARLINGTON, VA 22217-5660 CHICAGO, ILLINOIS 60606-1588			10. SPONSORING / MONITORING AGENCY REPORT NUMBER	
11. SUPPLEMENTARY NOTES				
12a. DISTRIBUTION / AVAILABILITY STATEMENT <div style="border: 1px solid black; padding: 5px; text-align: center;"> DISTRIBUTION STATEMENT A Approved for public release Distribution Unlimited </div>			12b. DISTRIBUTION CODE	
13. ABSTRACT (Maximum 200 words) <p style="text-align: center;">SEE FOLLOWING THREE PAGES</p>				
14. SUBJECT TERMS			15. NUMBER OF PAGES	
			16. PRICE CODE	
17. SECURITY CLASSIFICATION OF REPORT	18. SECURITY CLASSIFICATION OF THIS PAGE	19. SECURITY CLASSIFICATION OF ABSTRACT	20. LIMITATION OF ABSTRACT	

GENERAL INSTRUCTIONS FOR COMPLETING SF 298

The Report Documentation Page (RDP) is used in announcing and cataloging reports. It is important that this information be consistent with the rest of the report, particularly the cover and title page. Instructions for filling in each block of the form follow. It is important to *stay within the lines* to meet *optical scanning requirements*.

Block 1. Agency Use Only (Leave blank).

Block 2. Report Date. Full publication date including day, month, and year, if available (e.g. 1 Jan 88). Must cite at least the year.

Block 3. Type of Report and Dates Covered. State whether report is interim, final, etc. If applicable, enter inclusive report dates (e.g. 10 Jun 87 - 30 Jun 88).

Block 4. Title and Subtitle. A title is taken from the part of the report that provides the most meaningful and complete information. When a report is prepared in more than one volume, repeat the primary title, add volume number, and include subtitle for the specific volume. On classified documents enter the title classification in parentheses.

Block 5. Funding Numbers. To include contract and grant numbers; may include program element number(s), project number(s), task number(s), and work unit number(s). Use the following labels:

C - Contract	PR - Project
G - Grant	TA - Task
PE - Program Element	WU - Work Unit Accession No.

Block 6. Author(s). Name(s) of person(s) responsible for writing the report, performing the research, or credited with the content of the report. If editor or compiler, this should follow the name(s).

Block 7. Performing Organization Name(s) and Address(es). Self-explanatory.

Block 8. Performing Organization Report Number. Enter the unique alphanumeric report number(s) assigned by the organization performing the report.

Block 9. Sponsoring/Monitoring Agency Name(s) and Address(es). Self-explanatory.

Block 10. Sponsoring/Monitoring Agency Report Number. (If known)

Block 11. Supplementary Notes. Enter information not included elsewhere such as: Prepared in cooperation with...; Trans. of...; To be published in.... When a report is revised, include a statement whether the new report supercedes or supplements the older report.

Block 12a. Distribution/Availability Statement. Denotes public availability or limitations. Cite any availability to the public. Enter additional limitations or special markings in all capitals (e.g. NOFORN, REL, ITAR).

DOD - See DoDD 5230.24, "Distribution Statements on Technical Documents."

DOE - See authorities.

NASA - See Handbook NHB 2200.2.

NTIS - Leave blank.

Block 12b. Distribution Code.

DOD - Leave blank.

DOE - Enter DOE distribution categories from the Standard Distribution for Unclassified Scientific and Technical Reports.

NASA - Leave blank.

NTIS - Leave blank.

Block 13. Abstract. Include a brief (*Maximum 200 words*) factual summary of the most significant information contained in the report.

Block 14. Subject Terms. Keywords or phrases identifying major subjects in the report.

Block 15. Number of Pages. Enter the total number of pages.

Block 16. Price Code. Enter appropriate price code (*NTIS only*).

Blocks 17. - 19. Security Classifications. Self-explanatory. Enter U.S. Security Classification in accordance with U.S. Security Regulations (i.e., UNCLASSIFIED). If form contains classified information, stamp classification on the top and bottom of the page.

Block 20. Limitation of Abstract. This block must be completed to assign a limitation to the abstract. Enter either UL (unlimited) or SAR (same as report). An entry in this block is necessary if the abstract is to be limited. If blank, the abstract is assumed to be unlimited.

ABSTRACT

This report documents work carried forward over the fourth year of a five year ONR sponsored University Research Initiative (URI) entitled "Materials for Adaptive Structural Acoustic Control." The program has continued to underpin the development of new electro-ceramic, single crystal and composite materials combinations for both the sensing and actuation functions in adaptive structures.

For the lead based perovskite structure relaxor ferroelectric electrostrictors, new experimental and theoretical studies have underscored the critical role of nano-scale heterogeneity on either A or B sites of the ABO_3 in promoting dispersive dielectric response and the very strong opposing role of elastic stress and electrostrictive coupling in suppressing polarization fluctuations. Most important for practical application is the regimen where, under high electric field nano-polar regions begin to amalgamate into ferroelectric macro-domains with very mobile walls lead to unusually large extrinsic piezoelectric coefficients.

The program has explored a range of new relaxor:ferroelectric solid solutions which exhibit morphotropic phase boundaries between rhombohedral and tetragonal ferroelectric phases. Some of these compositions are much more tractable than PZT to grow in single crystal form. A major surprise is the very strong enhancement of the piezoelectric d_{33} and d_{31} in the crystal over that in the corresponding ceramic, and the massive anisotropy for different orientations and directions of poling. Optical studies suggest that the unusual effects reside largely in the extrinsic (domain controlled) response and we speculate about the mobility of walls in metastable phases, however further studies are required.

Antiferroelectric:ferroelectric phase switching studies in a wide range of compositions in the lead lanthanum zirconate stannate titanate system show that the first abrupt switchover to the rhombohedral ferroelectric phase only produces volume strain $\sim 0.2\%$ as checked both by dilatometry and by X-ray. There is a large enhancement under higher field to $\sim 0.6\%$ volume strain although the polarization does not change markedly. From thin film and single crystals studies there is mounting evidence of higher field ferroelectric:ferroelectric phase change, but again additional work is needed.

Size effect studies in perovskite ferroelectrics are continuing on this program and on the NSF/MRG in MRL. Scaling of the 90° stripe domains in thinned TEM samples of tetragonal composition begin to show departure from the accepted $1/2$ power law at sub micron sizes. The structure of domains under the three dimensional constraints of grains inside the ceramic is still however almost completely unknown. Computer modeling appear to show promise and codes are being explored which permit the mutual interactions to be varied and the corresponding two dimensional structures visualized.

In composite sensors, the focus has continued upon the flextensional configurations with the new inexpensive cymbal shaped amplifier proving superior in every respect to the original "moonie." The flat section on the cymbal end cap permits very easy stacking of elements and work is now in progress to develop large area panels for low frequency testing at the Penn State ARL.

Work has continued on the thin sheet 2:2 piezoceramic polymer composites, where the transverse poling and low density lead to a desirable combination of low electrical and low acoustic impedance. An alternative fabrication procedure using extruded PZT honeycomb appears most attractive.

Two problems of major importance in actuation have been topics for study. First what are the "intrinsic" material limitations for high strain electrically driven actuation in polarization controlled systems, and secondly what are the practical limitations in multilayer actuators as they are currently fabricated and how may they be alleviated. Work on the first topic is now largely completed, showing that strains $\sim 0.4\%$ could be switched more than 10^9 cycles in suitable PLZT compositions. Such reliability however requires near theoretical density, homogeneity, grain size control, critical attention to electrodes and electric field uniformity, none of which are adequately controlled in current actuator systems.

For practical actuators fabricated by inexpensive tape casting and co-firing techniques electrode termination is a major problem. In the simple MLC like designs, cracks initiate at field concentrations associated with the tip of the buried conductor layer. A new floating electrode design has been found to reduce this problem. For cracking near the end surfaces, poling of the termination layers reduces their stiffness and markedly improves performance. In the conventional structures it is also found that the floating electrode may be used directly as an acoustic emission pickup, giving early warning of cracking problems.

Under resonant driving conditions, the problems in actuators are markedly different. Heat build up and temperature run-away are significant problems traceable to dielectric loss, and new hard compositions and anti-resonant driving methods have been explored to reduce these problems.

In integration work on the high activity 0-3 composites in nearing completion. A new type of zig-zag actuator is being explored for the capability to combine both longitudinal and transverse actuation. Under a new ONR sponsored program with Virginia Polytechnic Institute and University new double amplifiers combining bimorph and flextensional concepts are being examined.

Processing studies permit the fabrication of the wide range of compositions and forms required in these material researches. Rate controlled sintering is proving to be highly advantageous, particularly for reducing delamination in integrated structures. Electrophoretic and

dielectrophoretic forming are showing promise in green assembly of thick film components where high green density is critical.

Thin film papers have been selected from the very broad range of work in MRL because of their relevance to transduction in piezoelectric and in phase switching systems.

**MATERIALS FOR ADAPTIVE STRUCTURAL
ACOUSTIC CONTROL**

Period February 1, 1995 to January 31, 1996

Annual Report

VOLUME V

OFFICE OF NAVAL RESEARCH
Contract No.: N00014-92-J-1510

APPROVED FOR PUBLIC RELEASE — DISTRIBUTION UNLIMITED

Reproduction in whole or in part is permitted
for any purpose of the United States Government

L. Eric Cross

PENNSSTATE



THE MATERIALS RESEARCH LABORATORY
UNIVERSITY PARK, PA

TABLE OF CONTENTS

ABSTRACT	8
INTRODUCTION	10
1.0 GENERAL SUMMARY PAPERS	11
2.0 MATERIALS STUDIES	12
3.0 COMPOSITE SENSORS	12
4.0 ACTUATORS STUDIES	13
5.0 INTEGRATION ISSUES	14
6.0 PROCESSING STUDIES	14
7.0 THIN FILM FERROELECTRICS	15
8.0 GRADUATE STUDENTS IN THE PROGRAM	16
9.0 HONORS AND AWARDS	16
10.0 APPRENTICE PROGRAM	16
11.0 PAPERS PUBLISHED IN REFEREED JOURNALS	17
12.0 INVITED PAPERS PRESENTATIONS AT NATIONAL AND INTERNATIONAL MEETINGS	21
13.0 INVITED PAPERS PRESENTED AT UNIVERSITY, INDUSTRY AND GOVERNMENT LABORATORIES	23
14.0 CONTRIBUTED PAPERS AT NATIONAL AND INTERNATIONAL MEETINGS	24
15.0 BOOKS (AND SECTIONS THEREOF)	27

APPENDICES

VOLUME I

General Summary Papers

1. Cross, L.E., "Ferroelectric Materials for Electromechanical Transducer Applications," *Jpn. J. Appl. Phys.* **34**, 2525-2532 (1995).
2. Fernandez, J.F., A. Dogan, Q.M. Zhang, J.F. Tressler, and R.E. Newnham, "Hollow Piezoelectric Composites," submitted to *Sensors and Actuators: A. Physical* (1995).
3. Uchino, K., "Recent Developments in Ceramic Actuators—Comparison among USA, Japan and Europe," Workshop on Microsystem Technologies in the USA and Canada, Dusseldorf (1995).
4. Trolier-McKinstry, S., J. Chen, K. Vedam, and R.E. Newnham, "In Situ Annealing Studies of Sol-Gel Ferroelectric Thin Films by Spectroscopic Ellipsometry," *J. Am. Ceram. Soc.* **78** [7], 1907-1913 (1995).
5. Nair, N., A. Bhalla, and R. Roy, "Inorganic Lead Compounds in Electroceramics and Glasses," *Am. Cer. Soc. Bull.* **75** [1], 77-82 (1996).
6. Gentile, A. and F.W. Ainger, "Single Crystals," Chapter 9, Materials Science and Technology, A Comprehensive Treatment, **17A** Processing of Ceramics, Part 1 (R.J. Brook, editor), VCH Verlagsgesellschaft mbH, Weinheim, Fed. Repl. of Germany (1996).

Materials Studies

7. Choi, S.W., J.M. Jung, and A.S. Bhalla, "Dielectric, Pyroelectric and Piezoelectric Properties of Calcium-Modified Lead Magnesium Tantalate-Lead Titanate Ceramics."
8. Kim, Y.J., S.W. Choi, and A.S. Bhalla, "Dielectric, Pyroelectric Properties, and Morphotropic Phase Boundary in La-Doped $(1-x)\text{Pb}(\text{Mg}_{1/3}\text{Ta}_{2/3})_2\text{-xPbTiO}_3$ Solid Solution Ceramics", *Ferroelectrics* **173**, 87-96 (1995).
9. Alberta, E. and A.S. Bhalla, "A Processing and Electrical Property Investigation of the Solid Solution: $(x)\text{Pb}(\text{In}_{1/2}\text{Nb}_{1/2})\text{O}_3\text{-(1-x)Pb}(\text{Sc}_{1/2}\text{Ta}_{1/2})\text{O}_3$," submitted to *Ferroelectrics* (1995).
10. Zhang, Q.M., H. You, M.L. Mulvihill, and S.J. Jang, "An X-ray Diffraction Study of Superlattice Ordering in Lead Magnesium Niobate," *Solid State Comm.* **97** [8], 693-698 (1996).
11. Zhang, Q.M., J. Zhao, and L.E. Cross, "Aging of the Dielectric and Piezoelectric Properties of Relaxor Ferroelectric Lead Magnesium Niobate-Lead Titanate in the Electric Field Biased State," *J. Appl. Phys.* **79** (6), 1-7 (1996).

VOLUME II

Materials Studies (continued)

12. Zhang, Q.M., J. Zhao, T.R. Shrout, and L.E. Cross, "The Effect of Ferroelastic Coupling in Controlling the Abnormal Aging Behavior in Lead Magnesium Niobate-Lead Titanate Relaxor Ferroelectrics," submitted *J. Mat. Res.*
13. Mulvihill, M.L., L.E. Cross, and K. Uchino, "Low-Temperature Observation of Relaxor Ferroelectric Domains in Lead Zinc Niobate," *J. Am. Ceram Soc.* **78** (12) 3345-3351 (1995).
14. Mulvihill, M.L., L.E. Cross, and K. Uchino, "Dynamic Motion of the Domain Configuration in Relaxor Ferroelectric Single Crystals as a Function of Temperature and Electric Field," 8th Euro. Mtg. Ferroelectricity, Nijmegen (1995).
15. Mulvihill, M.L., K. Uchino, Z. Li, and Wenwu Cao, "In-Situ Observation of the Domain Configurations During the Phase Transitions in Barium Titanate," accepted *Phil. Mag. B* (1995).
16. Oh, K.Y., K. Uchino, and L.E. Cross, "Electric Properties and Domain Structures in Ba(Ti,Sn)O₃ Ceramics."
17. Cao, W., "Elastic and Electric Constraints in the Formation of Ferroelectric Domains," *Ferroelectrics*, **172**, 31-37 (1995).
18. Cao, W. and C.A. Randall, "The Grain Size and Domain Size Relations in Bulk Ceramic Ferroelectric Materials," accepted *J. Phys. Chem. Solids* (1995).
19. Cao, W., "Defect Stabilized Periodic Amplitude Modulations in Ferroelectrics," accepted *Phase Transitions* (1995).
20. Sopko, J., A. Bhalla, and L.E. Cross, "An Improved Quantitative Method for Determining Dynamic Current Response of Ppyroelectric Materials," *Ferroelectrics*, **173**, 139-152 (1995)

VOLUME III

Composite Sensors

21. Tressler, J.F., A. Dogan, J.F. Fernandez, J.T. Fielding, Jr., K. Uchino, and R.E. Newnham, "Capped Ceramic Hydrophones," submitted to Proc. IEEE Int'l Ultrasonics Symp., Seattle (1995).
22. Koc, B., A. Dogan, J.F. Fernandez, R.E. Newnham, and K. Uchino, "Accelerometer Application of the Modified Moonie (Cymbal) Transducer," submitted *Jpn. J. Appl. Phys.* (1995).
23. Zhao, J., Q.M. Zhang, and W. Cao, "Effects of Face Plates and Edge Strips on Hydrostatic Piezoelectric Response of 1-3 Composites," *Ferroelectrics* **173**, 243-256 (1995).
24. Wu, S.J., W. Qi, and W. Cao, "Numerical Study of Ultrasonic Beam Pattern of a 1-3 Piezocomposite Transducer," accepted *Proc. IEEE Trans. Ultrasonics, Ferroelectridcs and Frequency Control*. (1995).

Composite Sensors (continued)—Volume III

25. Wang, H., Q.M. Zhang, and L.E. Cross, "Tailoring Material Properties by Structure Design--Radially Poled Piezoelectric Cylindrical Tube," *Ferroelectrics Lett.* (in press).
26. Zhang, Q.M. and X. Geng, "Electric Field Forced Vibration of a Periodic Piezocomposite Plate with Laminated Structure and Reflection and Transmission of a Plane Wave at the Fluid-Composite Interface," submitted to *IEEE Transactions on Ultrasonics, Ferroelectrics, and Frequency Control* (1995).
27. Geng, X., and Q.M. Zhang, "Dynamic Behavior of Periodic Piezoceramic-Polymer Composite Plates," *Appl. Phys. Lett.* **67** (21) (1995).
28. Zhang, Q.M., "Transverse Piezoelectric Mode Piezoceramic Polymer Composites with High Hydrostatic Piezoelectric Responses," *Proc. Int. Conf. on Electronic Components and Materials Sensors and Actuators*, Xi'an, China, 159-162 (1995)
29. Zhang, Q.M., H. Wang, J. Zhao, J.T. Fielding, Jr., R.E. Newnham, and L.E. Cross, "A High Sensitivity Hydrostatic Piezoelectric Transducer Based on Transverse Piezoelectric Mode Honeycomb Ceramic Composites," *IEEE Transactions on Ultrasonics, Ferroelectrics and Frequency Control* **43** (1), 26-42 (1996).
30. Zhang, Q.M., J. Chen, H. Wang, J. Zhao, L.E. Cross, and M.C. Trottier, "A New Transverse Piezoelectric Mode 2-2 Piezocomposite for Underwater Transducer Applications," *IEEE Transactions on Ultrasonics, Ferroelectrics, and Frequency Control* **42** (4), 774-780 (1995).
31. Cao, W., Q.M. Zhang, J.Z. Zhao, and L.E. Cross, "Effects of Face Plates on Surface Displacement Profile in 2-2 Piezoelectric Composites," *IEEE Transactions on Ultrasonics, Ferroelectrics, and Frequency Control* **42** (1), 37-41 (1995).
32. Cao, W. and W. Qi, "Plane Wave Propagation in Finite 2-2 Composites," *J. Appl. Phys.* **78** (7), 4627-4632 (1995).
33. Qi, W. and W. Cao, "Finite Element Analysis and Experimental Studies on the Thickness Resonance of Piezocomposite Transducers," accepted *Ultrasonic Imaging* (1995).
34. Cao, W. and W. Qi, "Multisource Excitations in a Stratified Biphase Structure," *J. Appl. Phys.* **78** (7), 4640-4646 (1995).

VOLUME IV

Actuator Studies

35. Uchino, K., "Materials Update: Advances in ceramic actuator materials," *Materials Lett.* **22**, 1-4 (1995).
36. Uchino, K., "Novel Ceramic Actuator Materials."
37. Aburatani, H., K. Uchino, and A.F. Yoshiaki, "Destruction Mechanism and Destruction Detection Technique for Multilayer Ceramic Actuators," *Proc. of the 9th Annual International Symposium on the Applications of Ferroelectrics*, 750-752 (1995).

Actuator Studies (continued)—Volume IV

38. Uchino, K. "Manufacturing Technology of Multilayered Transducers," *Proc. Amer. Ceram. Soc.*, Manufacture of Ceramic Components, 81-93 (1995).
39. Uchino, K. "Piezoelectric Actuators/Ultrasonic Motors--Their Development and Markets," *Proc. 9th ISAF*, 319-324 (1995).
40. Dogan, A., J.F. Fernandez, K. Uchino, and R.E. Newnham, "New Piezoelectric Composite Actuator Designs for Displacement Amplification," in press *Proc. Euroceram 95* (1995).
41. Onitsuka, O., A. Dogan, J.F. Tressler, Q.Su, S. Yoshikawa, and R.E. Newnham, "Metal-Ceramic Composite Transducer, The 'Moonie' ," *J. Intelligent Materials Systems and Structures* **6**, 447-455 (1995).
42. Fernandez, J.F., A. Dogan, J.T. Fielding, K. Uchino, and R.E. Newnham, "Tailoring High Displacement Performance of Ceramic-Metal Piezocomposite Actuators 'Cymbals'," submitted to *IEEE Transactions on Ultrasonics, Ferroelectrics, and Frequency Control* (1995).
43. Hirose, S., S. Takahashi, K. Uchino, M. Aoyagi, and Y. Tomikawa, "Measuring Methods for High-Power Characteristics of Piezoelectric Materials," *Mat. Res. Soc. Symp. Proc.* **360**, 15-20 (1995).
44. Takahashi, S., S. Hirose, K. Uchino, and K.Y. Oh, "Electro-Mechanical Characteristics of Lead-Zirconate-Titanate Ceramics Under Vibration-Level Change," *Proc. 9th ISAF*, 377-382 (1995).
45. Takahashi, Sadayuki, Yasuhiro Sasaki, Seiji Hirose, and Kenji Uchino, "Electro-Mechanical Properties of PbZrO_3 - PbTiO_3 - $\text{Pb}(\text{Mn}_{1/3}\text{Sb}_{2/3})\text{O}_3$ Ceramics Under Vibration-Level Change," *Mat. Res. Soc. Symp. Proc.* **360**, 305-310 (1995).

VOLUME V

46. Zheng, Jiehui, Sadayuki Takahashi, Shoko Yoshikawa, Kenji Uchino, and J.W.C. de Vries, "Heat Generation in Multilayer Piezoelectric Actuators," submitted to *J. Am. Ceram. Soc.* (1995).
47. Uchino, Kenji, "Review: Photostriction and its Applications," in press *J. Innovations in Mater. Res.* (1995).
48. Chu, Sheng-Yuan, and Kenji Uchino, "Photo-Acoustic Devices Using $(\text{Pb},\text{La})(\text{Zr},\text{Ti})\text{O}_3$ Ceramics," *Proc. 9th ISAF*, 743-745 (1995).

Integration Issues

49. Matsko, M.G., Q.C. Xu, and R.E. Newnham, "Zig-Zag Piezoelectric Actuators: Geometrical Control of Displacement and Resonance," *J. Intell. Mat. Syst. and Struct.* **6** (6), 783-786 (1995).
50. Xu, Baomin, Qiming Zhang, V.D. Kugel, and L.E. Cross, "Piezoelectric Air Transducer for Active Noise Control," submitted *Proc. SPIE* (1996).

Integration Issues (continued)–Volume V

51. Kumar, S., A.S. Bhalla, and L.E. Cross, "Underwater Acoustic Absorption by Collocated Smart Materials," accepted *Ferroelectric Letters* (1995).
52. Elissalde, Catherine and Leslie Eric Cross, "Dynamic Characteristics of Rainbow Ceramics," *J. Am. Ceram. Soc.* **78** [8], 2233-2236 (1995).

Processing Studies

53. Bowen, Christopher P., Thomas R. Shrout, Robert E. Newnham, and Clive A. Randall, "Tunable Electric Field Processing of Composite Materials," *J. of Intelligent Material Systems and Structures* **6** (2), 159-168 (1995).
54. Zhang, Q.M., J. Zhao, T. Shrout, N. Kim, and L.E. Cross, "Characteristics of the Electromechanical Response and Polarization of Electric Field Biased Ferroelectrics," *J. Appl. Phys.* **77** (5), 2549-2555 (1995).
55. Zhao, J., Q.M. Zhang, N. Kim, and T. Shrout, "Electromechanical Properties of Relaxor Ferroelectric Lead Magnesium Niobate-Lead Titanate Ceramics," *Jpn. J. Appl. Phys.* **34**, 5658-5663 (1995).
56. Zipparo, M.J., K.K. Shung, and T.R. Shrout, "Piezoelectric Properties of Fine Grain PZT Materials," *Proc. IEEE Int'l Ultrasonics Symposium* (1995).
57. Yoshikawa, Shoko, Ulagaraj Selvaraj, Paul Moses, John Witham, Richard Meyer, and Thomas Shrout, "Pb(Zr,Ti)O₃[PZT] Fibers–Fabrication and Measurement Methods," *J. Intell. Mat. Syst. and Struct.* **6** (2), 152-158 (1995).
58. Hackenberger, W.S., T.R. Shrout, A. Nakano, and R.F. Speyer, "Rate Controlled Sintering of Low Temperature Cofired Ceramic Multilayers Used for Electronic Packaging."
59. Randall, C.A., N. Kim, W. Cao, and T.R. Shrout, "Domain-Grain Size Relation in Morphotropic Phase Boundary, Pb(Zr_{0.52}Ti_{0.48})O₃," 7th US:Japan Mtg. on Dielectric and Piezoelectric Ceramics, Tsukuba, 145-149 (1995).
60. Cann, David P., Clive A. Randall, and Thomas R. Shrout, "Investigation of the Dielectric Properties of Bismuth Pyrochlores," accepted *Solid State Communication* (1995).

VOLUME VI

61. Mulvihill, Maureen L., Seung Eek Park, George Risch, Zhuang Li, Kenji Uchino, and Thomas R. Shrout, "The Role of Processing Variables in the Flux Growth of PZN-PT Relaxor Ferroelectric Single Crystals."

Thin Films Ferroelectrics

62. Chen, H.D., K.R. Udayakumar, L.E. Cross, J.J. Bernstein, and L.C. Niles, "Dielectric, Ferroelectric, and Piezoelectric Properties of Lead Zirconate Titanate Thick Films on Silicon Substrates," *J. Appl. Phys.* **77** (7), 3349-3353 (1995).

Thin Films Ferroelectrics (continued)—Volume VI

63. Udayakumar, K.R., P.J. Schuele, J. Chen, S.B. Krupanidhi, and L.E. Cross, "Thickness-Dependent Electrical Characteristics of Lead Zirconate Titanate Thin Films," *J. Appl. Phys.* **77** (8), 3981-3986 (1995).
64. Chen, H.D., K.R. Udayakumar, C.J. Gaskey, and L.E. Cross, "Electrical Properties' Maxima in Thin Films of the Lead Zirconate-Lead Titanate Solid Solution System," *Appl. Phys. Lett.* **67** (23), 3411-3413 (1995).
65. Gaskey, C.J., K.R. Udayakumar, H.D. Chen, and L.E. Cross, "'Square' Hysteresis Loops in Phase-Switching Nb-Doped Lead Zirconate Stannate Titanate Thin Films," *J. Mater. Res.* **10** (11), 2764-2769 (1995).
66. Yamakawa, K., S. Trolier-McKinstry, J.P. Dougherty, and S. Krupanidhi, "Reactive Magnetron Co-Sputtered Antiferroelectric Lead Zirconate Thin Films," *Appl. Phys. Lett.* **67** (14), 2014-2016 (1995).
67. Ravichandran, D., K. Yamakawa, A.S. Bhalla, and R. Roy, "Alkoxide Derived $\text{SrBi}_2\text{Ta}_2\text{O}_9$ Phase Pure Powder and Thin Films."
68. Thakoor, Sarita, A.P. Thakoor, and L. Eric Cross, "Optical Non-Invasive Evaluation of Ferroelectric Films/Memory Capacitors," *Mat. Res. Soc. Symp. Proc.* **360**, 157-167 (1995).

ACTUATOR STUDIES

(continued)

APPENDIX 46

Heat Generation in Multilayer Piezoelectric Actuators

Jiehui Zheng,^{*} Sadayuki Takahashi,[†] Shoko Yoshikawa^{*} and Kenji Uchino^{*}

**International Center for Actuators and Transducers, Materials Research Laboratory,
The Pennsylvania State University, University Park, PA 16802**

J.W.C. de Vries

Philips Components B.V., Roermond, The Netherlands

Multilayer piezoelectric actuators when driven under high frequency, generate significant heat, which influences the reliability and other piezoelectric properties. In this paper, heat generation in various types of multilayer PZT-based actuators was studied. Experimental results showed that heat generation is mainly caused by electrical loss. A simplified analytic method was established to evaluate the temperature rise, which is useful for the design of multilayer and other high power actuators.

**Presented at the 97th Annual Meeting of the American Ceramic Society, Cincinnati, Ohio, May 1, 1995
(Electronics Division, Paper No. E-14-95).**

Supported by Philips Components.

^{*}Member, American Ceramic Society.

[†]Permanent address: R & D Group, NEC Corporation, Miyazaki, Miyamae-ku, Kawasaki 216, Japan.

I. Introduction

Multilayer piezoelectric actuators were under intensive development during the past decade¹⁻⁶ and have obtained some applications such as impact printer heads⁷⁻⁸, ultrasonic linear motors⁹ and x-y stages¹⁰. Today, low voltages are the trend for electronic systems, cars and medical devices.¹¹ This trend has made the multilayer structure with thin layers necessary. Efforts have been made and thin layers down to 20 μm have been achieved.⁵

In order to obtain maximum displacement of the actuator, an electric field of 1-3 kV/mm is usually necessary. For some applications, like the commercialized high speed impact printer head with a printing speed of 3 kHz,⁷ a high frequency voltage is applied to the actuator. Under such continuous high frequency, and driving with a high electric field, a fairly large heat generation was observed.¹² Heat generation influences the reliability and other properties and may also limit the application of the actuators. Therefore, a comprehensive investigation of heat generation becomes very important.

This paper studied heat generation in various types of multilayer PZT-based actuators. A simplified analytic method was established to evaluate the temperature rise, which is very useful for the design of multilayer and other high power actuators.

II. Experimental Procedure

Multilayer PZT-based ceramic actuators of various types (see Table I) were prepared by a tape casting technique. The thickness of the active layers was 20 or 40 μm . After cutting and the application of the end termination, the samples were poled by applying a high voltage at an elevated temperature.

The experiments were carried out by applying continuous triangular unipolar voltages to the samples. The voltages were generated by an NF 1940 Function Synthesizer, amplified through an NF 4010 High Speed Power Amplifier (the voltage being in the range of 300 V, current range 1.2 A), and then applied to the actuators.

Temperature rise of the actuators was measured by attaching a very fine ($\varnothing = 0.001$ in.) chromel-alumel thermocouple (CHAL-001, OMEGA Engineering Inc.) to the center of the sample surface. Silicone grease was used as a connective material.

III. Results

(1) *Temperature Rise Phenomena*

Heat generation for various size actuators, while driving under 3 kV/mm at 300 Hz, is shown in Fig. 1. It is seen from the figure that the actuator temperature initially increases exponentially with an increase in the driving time (t), and then it saturates. Temperature rise ΔT is defined as

$$\Delta T = T - T_0 \quad (1)$$

where T and T_0 indicate the maximum and initial actuator temperatures. The relationship between ΔT and v_e/A , where v_e is the effective volume where electric field is applied, and A is the total surface area of the sample, is shown in Fig. 2. Temperature rise ΔT is approximately proportional to the value v_e/A , because the heat generation is assumed to be proportional to the " v_e " defined above, and the heat dissipation is proportional to the surface area A .

Heat generation depends on driving frequency (f). The frequency dependence of the temperature rise ΔT is given in Fig. 3 for various applied electric fields. At the low electric field level, the ΔT increases almost linearly with increasing driving frequency. As the electric field level becomes higher (> 1 kV/mm), the $\Delta T \sim f$ curves gradually deviate from the linear trend.

Heat generation is also electric field (E) dependent. The temperature as a function of time for the actuator with dimension of $7 \times 7 \times 2$ mm is shown in Fig. 4. Figure 5 gives

the temperature rise ΔT as a function of applied electric field at various frequencies. The ΔT is initially proportional to E^2 . But the curves then deviate from this square relationship under higher electric field levels.

(2) *P-E hysteresis loss*

Heat generation in piezoelectric actuators is considered to be caused by losses,¹²⁻¹⁴ such as mechanical loss and electrical loss. The electrical loss was studied by measuring the polarization (P) - electric field (E) hysteresis loops. The P-E hysteresis loops of different size actuators are almost the same, because all of the actuators are made of the same composition. However, the hysteresis loops depend on temperature, frequency and the electric field. At different sample temperatures, hysteresis loops are slightly different. Figure 6 shows the P-E hysteresis loops at 25 and 98 °C, while driving under 3 kV/mm, 300 Hz. The hysteresis areas represent the ferroelectric loss per driving cycle, u . The ferroelectric loss u as a function of sample temperature is shown in Fig. 7. It is seen that the electrical loss decreases slightly with an increase of the sample temperature. The P-E hysteresis loss also decreases slightly with increasing frequency (Fig. 8). However, it increases remarkably when the applied electric field is increased (Fig. 9). The hysteresis loss is approximately proportional to E^2 (Fig. 10).

IV. Theoretical Analysis and Discussion

Since the conduction heat transfer rate through the lead wire in this experiment is negligibly small (i.e. roughly 1/25 of the convection), if we assume uniform temperature distribution in the sample, the relation for the rate of heat storage resulting from the heat generation and dissipation effects can be expressed as

$$ufv_e - A[\sigma\epsilon(T^4 - T_0^4) + \bar{h}_c(T - T_0)] = v\rho c(dT/dt) \quad (1)$$

where u is the hysteresis loss of the sample per driving cycle per unit volume, σ is the Stefan-Boltzman constant ($5.67 \times 10^{-8} \text{ W/m}^2\text{K}^4$), ϵ is the emissivity of the sample, \bar{h}_c is the average convective heat transfer coefficient, and v , ρ , c are total volume (Notice that $v > v_e$), density and specific heat, respectively, of the sample. Equation (1) can be written in the form

$$u f v_e - A k(T) (T - T_0) = v \rho c (dT/dt) \quad (2)$$

where

$$k(T) = \sigma \epsilon (T^2 + T_0^2)(T + T_0) + \bar{h}_c \quad (3)$$

is defined as the overall heat transfer coefficient. The first term of $k(T)$, $\sigma \epsilon (T^2 + T_0^2)(T + T_0)$, is $5.58 \text{ W/m}^2\text{K}$ at 25°C and $9.08 \text{ W/m}^2\text{K}$ at 125°C , if we take ϵ of the sample as 0.93

(similar to rough fused quartz). While \bar{h}_c has the magnitude of $6 \sim 30 \text{ W/m}^2\text{K}$ for free convection in air (Our results in Figs. 12 and 13 suggest that \bar{h}_c is close to $20 \text{ W/m}^2\text{K}$).¹⁵

Therefore, we can take $k(T)$ as a constant relatively insensitive to temperature change.

Then, the solution to equation (2) for the actuator temperature as a function of time is

$$T - T_0 = \frac{u f v_e}{k(T) A} (1 - e^{-\frac{k(T) A}{v \rho c} t}) \quad (4)$$

The time constant in equation (4) is

$$\tau = \frac{v \rho c}{k(T) A} \quad (5)$$

As $t \rightarrow \infty$, the maximum temperature rise in the actuator becomes

$$\Delta T = \frac{u f v_e}{k(T) A} \quad (6)$$

At $t \rightarrow 0$, where there is no heat dissipation effect, the initial rate of temperature rise is

$$\left(\frac{dT}{dt}\right)_{t \rightarrow 0} = \frac{ufv_e}{\rho cv} = \frac{\Delta T}{\tau} \quad (7)$$

Curve fit to the experimental data with the solution form

$$T = T_0 + \Delta T(1 - e^{-t/\tau}) \quad (8)$$

is provided in Fig. 11 as an example. Fitting curves well match the experimental data, which indicates that the analytic result adequately describes the heat generation phenomena. Consequently, we can calculate the total loss u of the actuator through equation (7). The calculated results are shown in Table II. The experimental data of P-E hysteresis losses are also listed for comparison. It is seen that the P-E hysteresis losses are nearly equal to the total losses. Since the experiments were carried out without external stress applying to the samples, it can be concluded that under the stress free condition, heat generation in piezoelectric actuators is mainly due to electrical loss, and mechanical loss is negligibly small.

Regarding the heat generation from piezoelectric vibrators, Hirose et al. reported intriguing results.¹⁶ When a piezoelectric vibrator is driven at the resonance point, the main contribution to the total loss is from the mechanical loss under a small vibration velocity level, while the contribution from the electrical loss increases drastically above a certain critical vibration velocity such as 0.2 - 0.3 m/s, where the actual heat generation starts to be observed.

By determining the time constant τ , the overall heat transfer coefficient $k(T)$ can be calculated through equation (5). The values of $k(T)$ for various actuators while driving under 3 kV/mm, 300 Hz are provided in Table II. The $k(T)$ as functions of frequency and electric field are shown in Fig. 12 and 13. It is seen from Fig. 12 that $k(T)$ is relatively insensitive to frequency under the low electric field level, while increases gradually with increasing frequency when the applied electric field level is higher (> 1 kV/mm). From Fig. 13, it is seen that $k(T)$ increases with increasing the applied electric field. The increase

in $k(T)$ may be caused by the convection increase due to the vibration level (i.e. vibration velocity) change with E and f . If we summarize the frequency dependence of u and $k(T)$, we can see that u is insensitive to frequency, $k(T)$ is also relatively insensitive to f at the low electric field level, but gradually increases with increasing frequency at higher electric field levels (> 1 kV/mm). Thus, according to equation (6), temperature rise is almost linearly proportional to f under the low electric field level, while at higher electric field levels (> 1 kV/mm), the $\Delta T \sim f$ relationship deviates from the linear trend due to the increase of $k(T)$ at higher f . This analysis coincides with the experimental results shown in Fig. 4. For the electric field dependence, u is proportional to E^2 , while $k(T)$ increases significantly with increasing E . That is why ΔT is nearly proportional to E^2 under low electric field as shown in Fig. 6, while deviates from this square relationship at a higher electric field level.

V. Conclusion

Heat generation in multilayer piezoelectric actuators was studied. Under the stress free condition, heat generation is mainly due to electrical loss, not to mechanical loss. Temperature rise of the actuator can be estimated by the expression $\Delta T = \frac{ufv_e}{k(T)A}$. The proposed analytic method is useful for the design of multilayer and other high power actuators from a viewpoint of heat generation.

References

- ¹Sadayuki Takahashi, Takeshi Yano, Izumu Fukui and Eiichi Sato, "Multilayer Piezoelectric Ceramic Actuator with Varying Thickness Layers," *Jpn. J. Appl. Phys.*, **24**, Suppl. 24-3, 206-8 (1985).
- ²Sadayuki Takahashi, "Longitudinal Mode Multilayer Piezoelectric Actuators," *Ceram. Bull.*, **65** [8] 1156-7 (1986).
- ³W. Wersing, H. Wahl and M. Schnoller, "PZT-Based Multilayer Piezoelectric Ceramics with AgPd-Internal Electrodes," *Ferroelectrics*, **87**, 271-94 (1988).
- ⁴S. Takahashi, "Recent Developments in Multilayer Piezoelectric Ceramic Actuators and Their Applications," *Ferroelectrics*, **91**, 293-302 (1989).
- ⁵B. C. H. Fransen, G. J. Janssen, S. J. J. Oostra and J. W. C. de Vries, "Integration of Mechanics and Electronics: Low Voltage Ceramic Multilayer Actuators," Presented at *CARTS-Europe'92*, October 5-8, 1992, Brugge, Belgium.
- ⁶Kenji Uchino, "Manufacturing Technology of Multilayered Transducers," *Proc. Amer. Ceram. Soc.* (1994) (in Press).
- ⁷Takeshi Yano, Eiichi Sato, Izumu Fukui and Shinichi Hori, "Piezoelectric Impact Printhead Utilizing Longitudinal Piezoelectric Effect," *SID 89 Digest*, **XX**, 180 (1989).
- ⁸Shuo Hung Chang and Han-Chung Wang, "A High Speed Impact Actuator Using Multilayer Piezoelectric Ceramics," *Sens. and Actuators A*, **24**, 239-44 (1990).
- ⁹Kenji Uchino, "Ceramic Actuators: Principles and Applications," *MRS Bull.*, **18** [4] 42-8 (1993).
- ¹⁰Shigeo Moriyama, Tatsuo Harada and Akihiro Takanashi, "Precision X-Y Stage with a Piezo-driven Fine-table," *Bull. Jpn. Soc. Prec. Eng.*, **22** [1] 13-7 (1988).
- ¹¹K. Lubitz, H. Hellebrand, "Properties of PZT Multilayer Actuators," *Proc. IEEE Int. Symp. Appl. Ferroelectrics*, 7th, 1990, 509-12 (1990).
- ¹²Atushi Ochi, Sadayuki Takahashi, and Satoru Tagami, "Temperature Characteristics for Multilayer Piezoelectric Ceramic Actuator," *Jpn. J. Appl. Phys.*, **24**, Suppl. 24-3, 209-12 (1985).

¹³J. H. Belding and M. G. McLaren, "Behavior of Modified Lead Zirconate - Lead Titanate Piezoelectric Ceramics under High Electric Fields," *Ceram. Bull.*, **49** [12] 1025-9 (1970).

¹⁴R. A. Gdula, "High-Field Losses of Adulterated Lead Zirconate-Titanate Piezoelectric Ceramics," *J. Am. Ceram. Soc.*, **51** [12] 683-7 (1968).

¹⁵Frank Kreith and Mark S. Bohn, *Principles of Heat Transfer*, pp. 17. Published by Harper & Row, Publishers, New York, 1986.

¹⁶S. Hirose, S. Takahashi, K. Uchino, M Aoyagi and Y. Tomikawa, "Measuring Methods for High-Power Characteristics of Piezoelectric Materials", *Mat. Res. Symp. Proc.* **360**, 15-20, (1995).

Figure Captions

Fig. 1. Heat generation for various actuators (driven at 3 kV/mm, 300 Hz).

Fig. 2. Temperature rise vs v/A (3 kV/mm, 300 Hz).

Fig. 3. Temperature rise vs frequency under various applied electric fields (data from the actuator with dimension of 7x7x7 mm).

Fig. 4. Heat generation while driving under various electric fields at 400 Hz (data from the actuator with dimension of 7x7x2 mm).

Fig. 5. Temperature rise as a function of applied electric fields (data from the actuator with dimension of 7x7x2 mm).

Fig. 6. P-E hysteresis loops at different sample temperatures: (a) 25 °C, (b) 98 °C. (3 kV/mm, 300 Hz)

Fig. 7. P-E hysteresis loss as a function of sample temperatures. (3 kV/mm, 300 Hz)

Fig. 8. P-E hysteresis loss as a function of frequency. ($T = 25$ °C, $E = 2$ kV/mm)

Fig. 9. P-E hysteresis loops of various applied electric fields: (a) 1 kV/mm, (b) 2 kV/mm, (c) 3 kV/mm. ($T = 25$ °C, $f = 300$ Hz)

Fig. 10. P-E hysteresis loss as a function of electric fields. ($T = 25$ °C, $f = 300$ Hz)

Fig. 11. Curve fit with the equation $T = T_0 + \Delta T(1 - e^{-\alpha t})$. (Data from the actuator with dimension of 7x7x2 mm, driven under 3 kV/mm, 300 Hz)

Fig. 12. Overall heat transfer coefficient $k(T)$ as a function of frequency (data from the actuator with dimension of 7x7x2 mm).

Fig. 13. $k(T)$ as a function of applied electric fields (400 Hz, data from the actuator with dimension of 7x7x2 mm).

Table I. Various Sizes of Multilayer Actuators

Actuator type	Dimensions (mm)	Layer thickness (μm)	Surface area A (mm^2)	Effective volume* v_e (mm^3)	v_e/A (mm)
d_{33}	4.5x3.5x2	20	63.5	18.8	0.293
	7x7x2	40	154	72.3	0.470
	5x5x20	40	450	308	0.882
d_{31}	17x3.5x1	20	160	40.2	0.251
Multimorph	31x9x0.3	20	582	34.7	0.078

*Effective volume is a volume that actually generates heat.

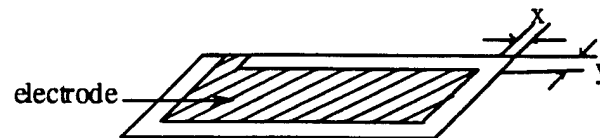


Table II. Loss and Overall Heat Transfer Coefficient
($E = 3 \text{ kV/mm}$, $f = 300 \text{ Hz}$)

Actuator	4.5x3.5x2 mm	7x7x2 mm	17x3.5x1 mm
Total loss ($\times 10^3 \text{ J/m}^3$)			
$u = \frac{\rho c v}{f v_e} \left(\frac{dT}{dt} \right)_{t \rightarrow 0}$	19.2	19.9	19.7
P-E hysteresis loss ($\times 10^3 \text{ J/m}^3$)	18.5	17.8	17.4
$k(T)$ ($\text{W/m}^2\text{K}$)	38.4	39.2	34.1

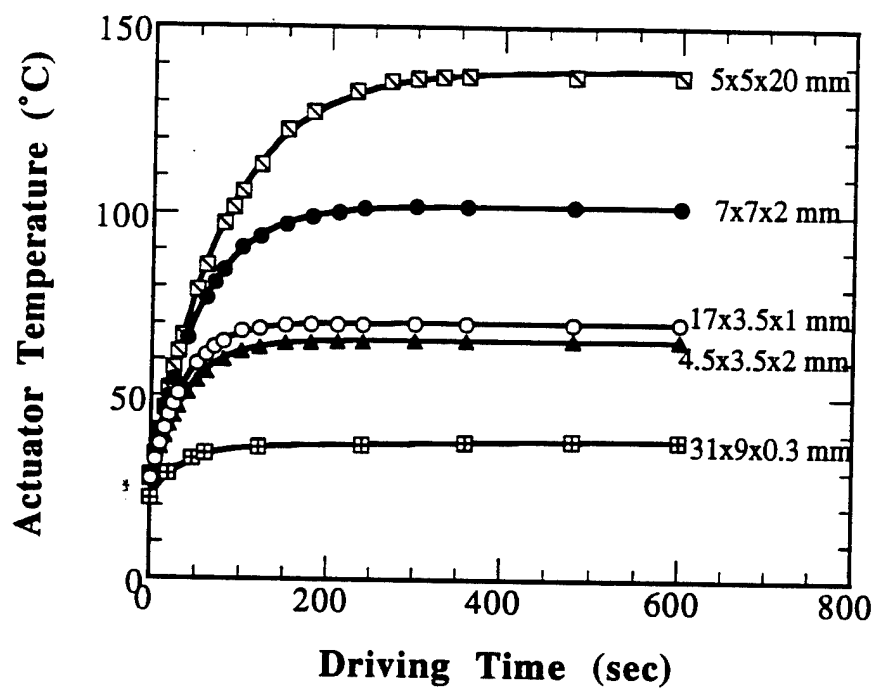


Fig. 1. Heat generation for various actuators
(driven at 3 kV/mm, 300 Hz)

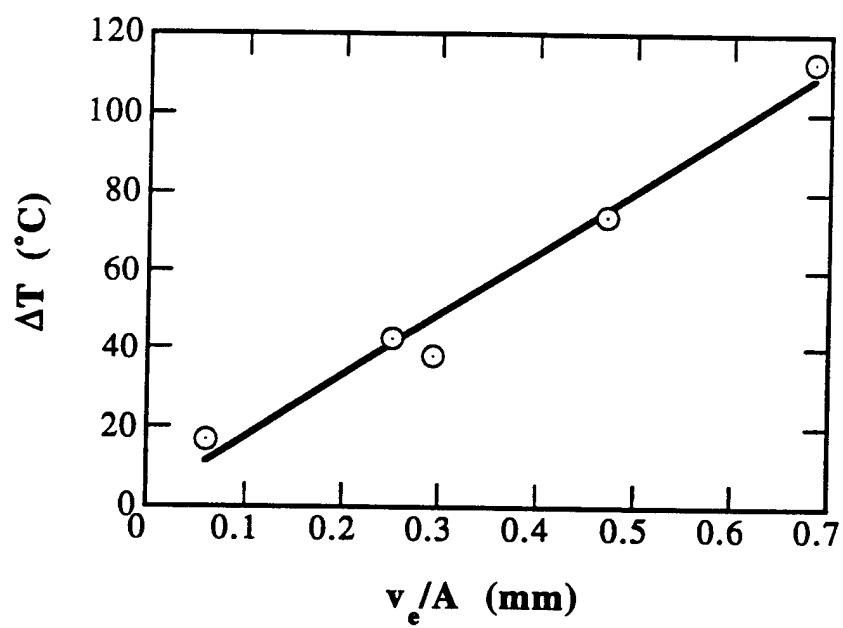


Fig. 2. Temperature rise vs v_e/A (3 kV/mm, 300 Hz).

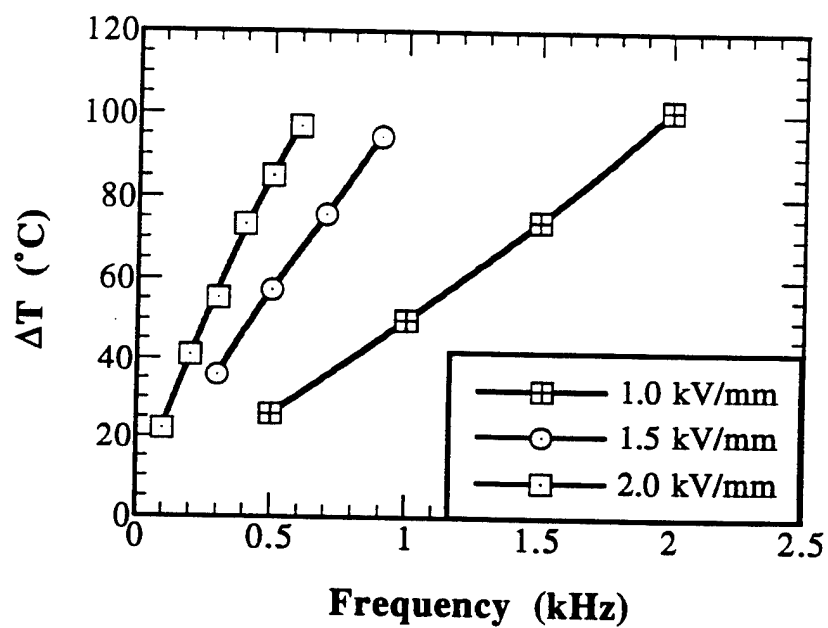


Fig. 3. Temperature rise vs frequency under various applied electric fields (data from the actuator with dimension of 7x7x2 mm).

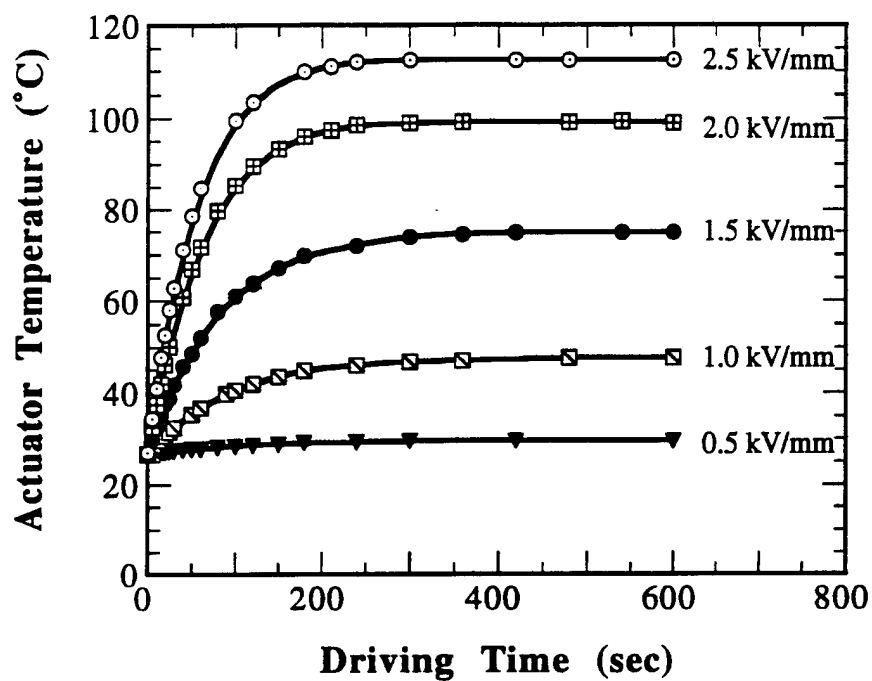


Fig. 4. Heat generation while driving under various electric fields at 400 Hz (data from the actuator with dimension of 7x7x2 mm).

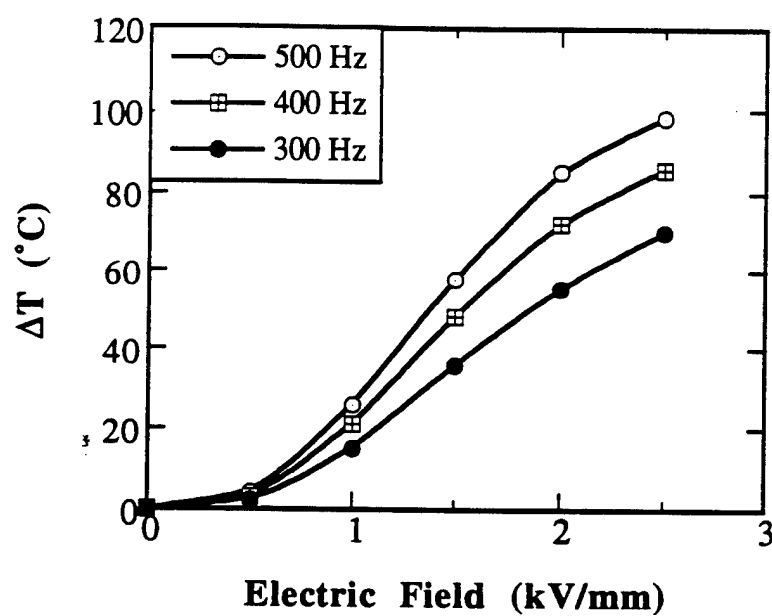


Fig. 5. Temperature rise for the actuator as a function of applied electric fields (data from the actuator with dimension of $7 \times 7 \times 2$ mm).

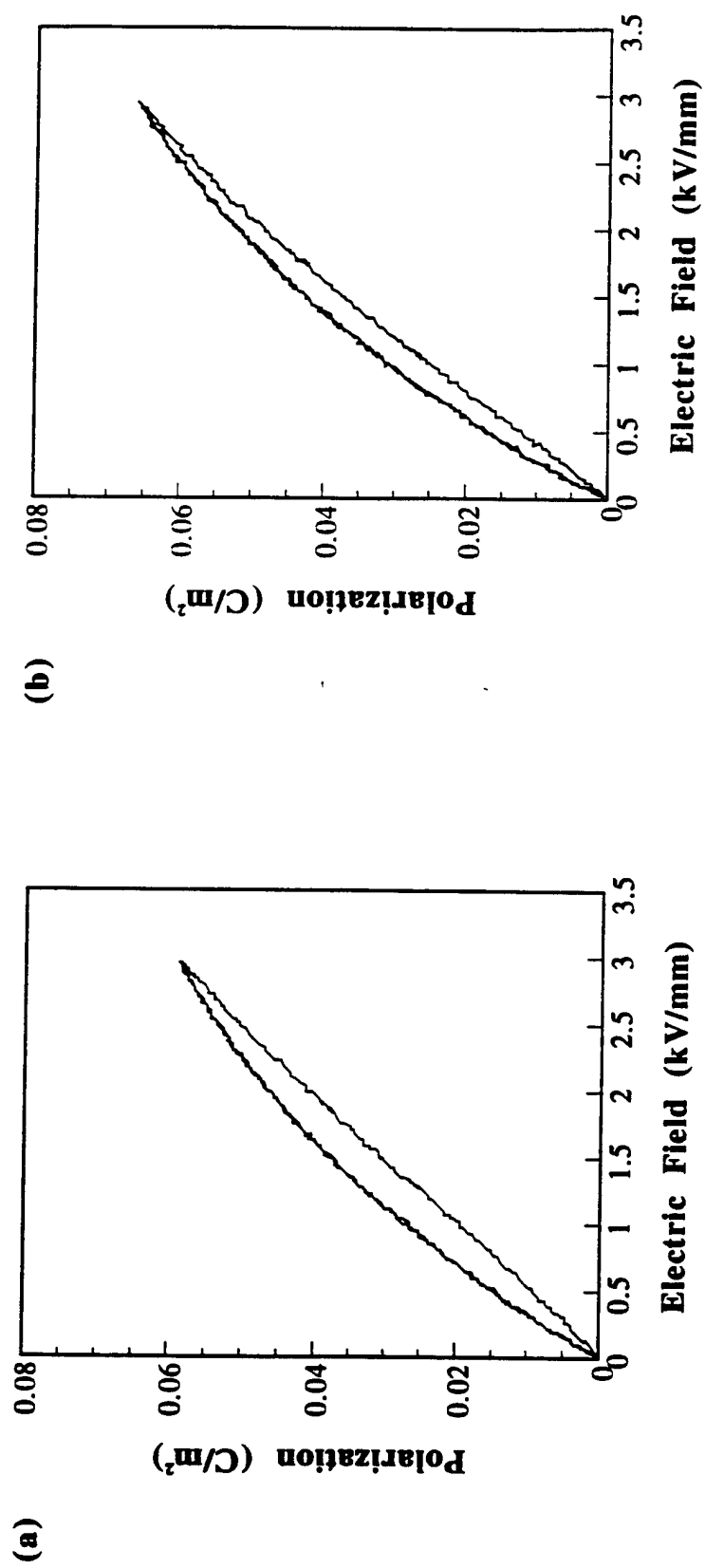


Fig. 6. P-E hysteresis loops at different sample temperature: (a) 25°C, (b) 98°C. (3kV/mm, 300Hz)

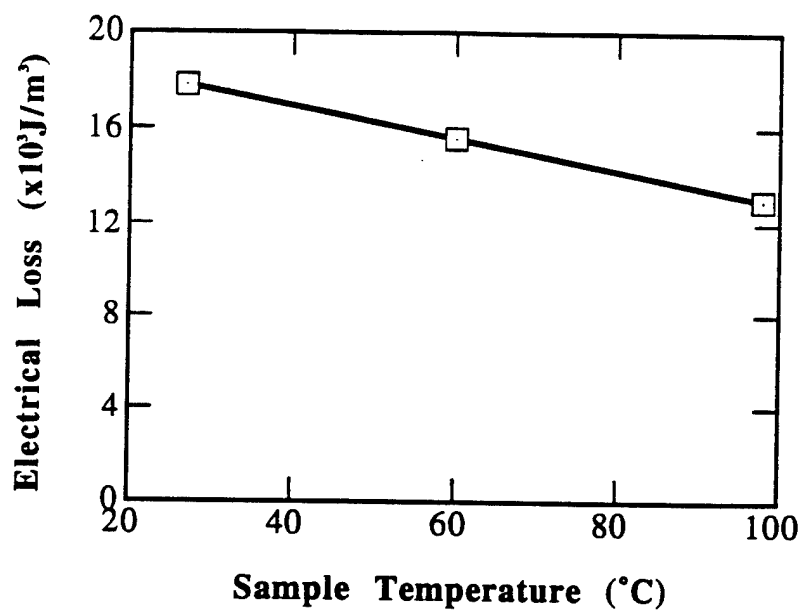


Fig. 7. P-E hysteresis loss as a function of sample temperatures.
(3 kV/mm, 300 Hz)

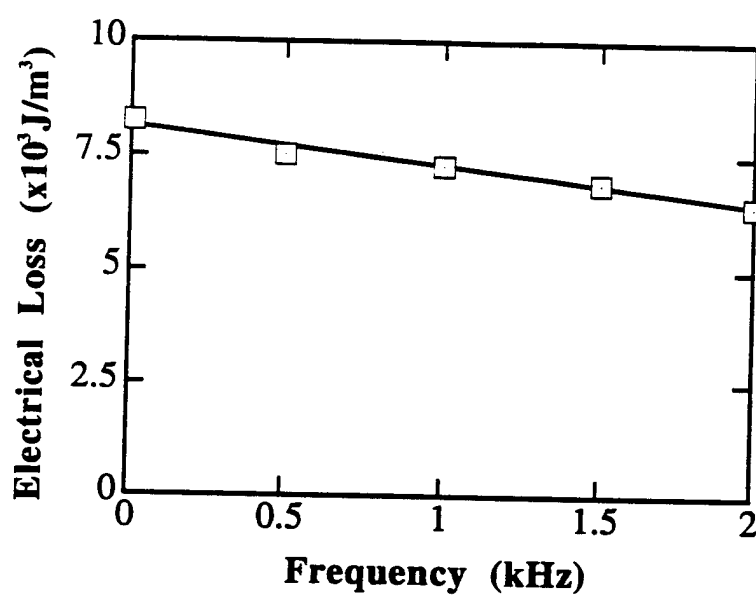


Fig. 8. P-E hysteresis loss as a function of frequency.
($T = 25\text{ }^{\circ}\text{C}$, $E = 2\text{ kV/mm}$)

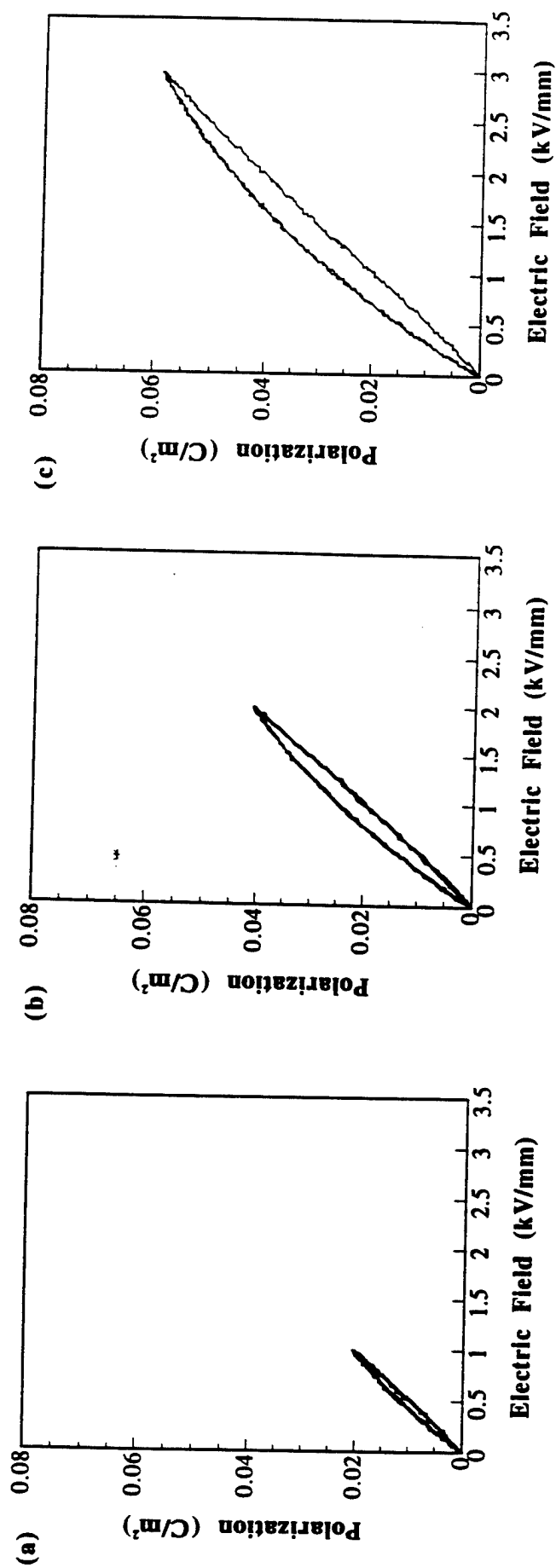


Fig. 9. P-E hysteresis loops of various applied electric field: (a) 1kV/mm, (b) 2kV/mm, (c) 3kV/mm. ($T=25^{\circ}C$, $f=300Hz$)

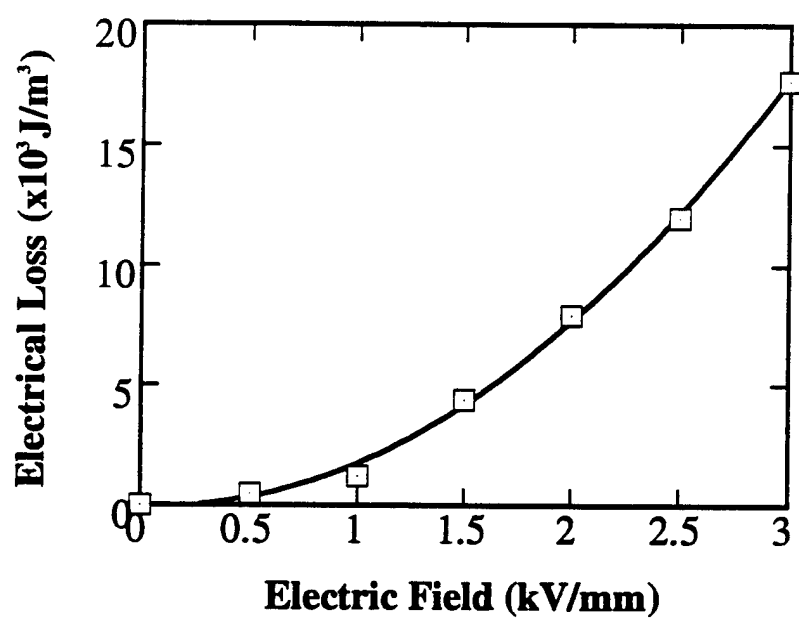


Fig. 10. P-E hysteresis loss as a function of electric fields.
($T = 25^\circ\text{C}$, $f = 300 \text{ Hz}$)

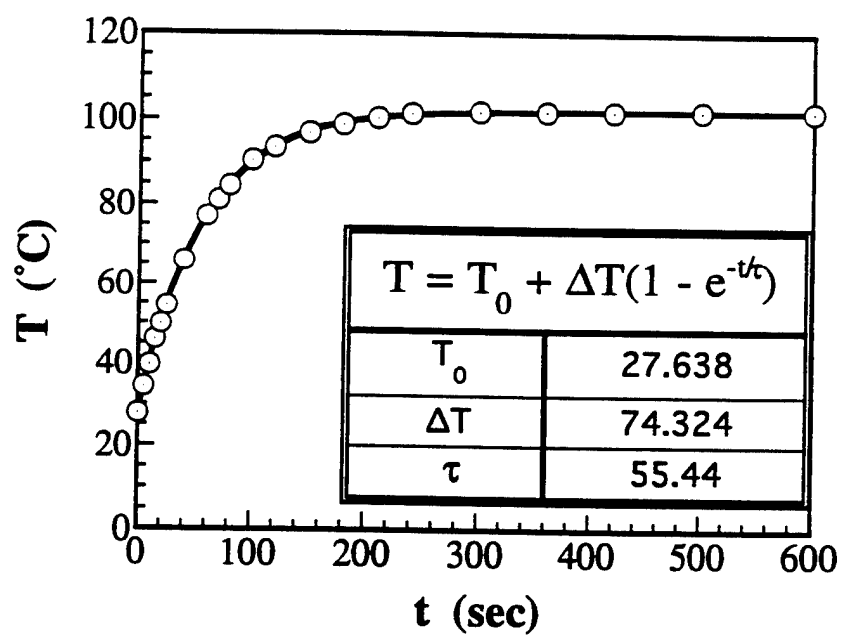


Fig. 11. Curve fit with the equation $T=T_0+\Delta T(1-e^{-t/\tau})$. (Data from the actuator with dimension of 7x7x2 mm, driven under 3 kV/mm, 300 Hz)

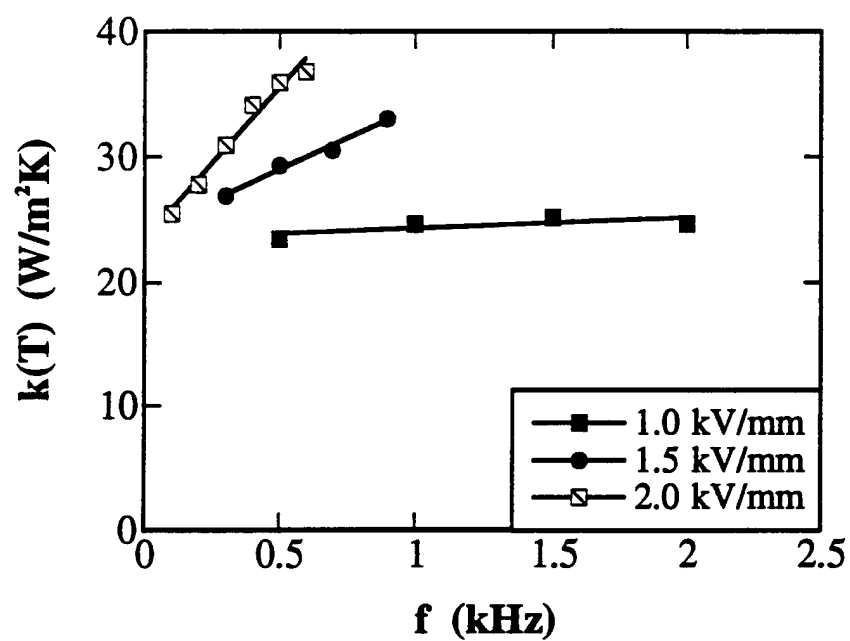


Fig. 12. Overall heat transfer coefficient $k(T)$ as a function of frequency (data from the actuator with dimension of $7 \times 7 \times 2 \text{ mm}$).

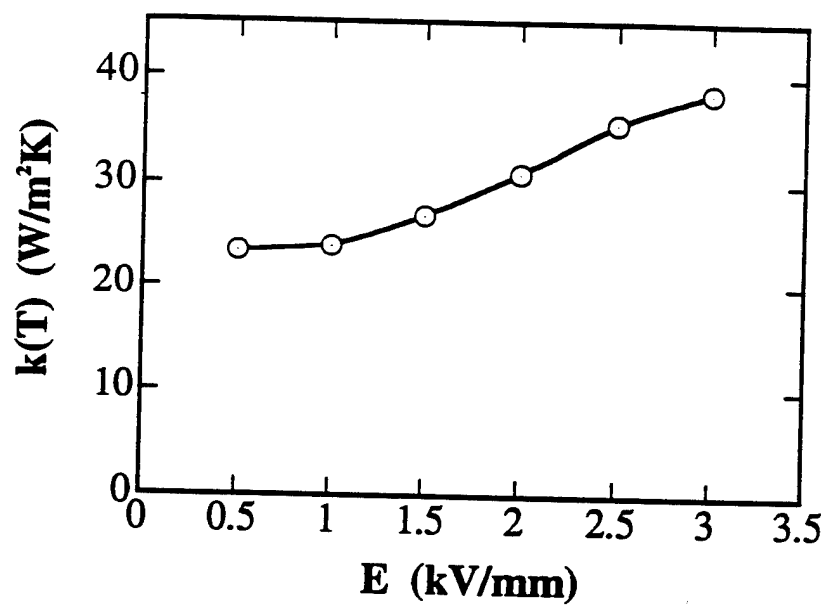


Fig. 13. $k(T)$ as a function of applied electric fields (300 Hz, data from the actuator with dimension of 7x7x2 mm).

APPENDIX 47

REVIEW: PHOTOSTRICTION AND ITS APPLICATIONS

Kenji Uchino
International Center for Actuators and Transducers
Materials Research Laboratory, The Pennsylvania State University
University Park, PA 16802

ABSTRACT

Photostriction in ferroelectrics arises from a superposition of photovoltaic and inverse piezoelectric effects. $(\text{Pb,Lu})(\text{Zr,Ti})\text{O}_3$ ceramics doped with WO_3 exhibit large photostriction under irradiation of near-ultraviolet light, and are applicable to remote control actuators and photoacoustic devices. Using a bimorph configuration, a photo-driven relay and a micro walking device have been developed, which are designed to start moving as a result from the irradiation, having neither electric lead wires nor electric circuits. The mechanical resonance of the bimorph was also induced by an intermittent illumination of purple-color light; this verified the feasibility of the photostriction to "photophone" applications.

Keywords: *Photostriction, Photovoltaic effect, Piezoelectricity, Bimorph, Photoacoustic, Photophone, Mechanical resonance*

INTRODUCTION

Photostrictive effect is a phenomenon in which strain is induced in the sample when it is illuminated. This effect is focused especially in the fields of micromechanism and optical communication.

With decreasing the size of miniature robots/actuators, the weight of the electric lead wire connecting the power supply becomes significant, and remote control will definitely be required for sub-millimeter devices. A photo-driven actuator is a very promising candidate for micro-robots. On the other hand, the key components in the optical communication are a solid state laser as a light source, an optical fiber as a transfer line, and a display/ a telephone as a visual/audible interface with the human. The former two components have been developed fairly successfully, and the photo-acoustic device (i. e. an optical telephone or a "photophone") will be eagerly anticipated in the next century.

Photostrictive devices which are actuated when they receive the energy of light will be particularly suitable for use in the above-mentioned fields. In principle, the photostrictive effect arises from a superposition of a photovoltaic effect, where a large voltage is generated in a ferroelectric through the irradiation of light,¹⁾ and a piezoelectric effect, where the material expands or contracts under the voltage applied. It is noteworthy that this photostriction is neither the thermal dilatation nor the pyroelectrically-produced strain associated with a temperature rise due to the light illumination. Also the photovoltaic effect mentioned here generates a greater-than-band-gap voltage (several kV/cm), and is quite different from that based on the p-n junction of semiconductors (i. e. solar battery).

This paper describes the details of the fundamental photostrictive effect in $(\text{Pb},\text{La})(\text{Zr},\text{Ti})\text{O}_3$ ceramics first, then introduces its applications to a photo-driven relay, a micro walking machine and a photophone, which are designed to function as a result of irradiation, having neither lead wires nor electric circuits.

PHOTOSTRICTIVE PROPERTIES

PRINCIPLE

The main features of the "bulk" photovoltaic effect are summarized as follows:

- 1) This effect is observed in a uniform crystal or ceramic having noncentric symmetry, and is entirely different in nature from the p-n junction effect observed in semiconductors.
- 2) A steady photovoltage/current is generated under uniform illumination.
- 3) The magnitude of the induced voltage is greater than the band gap energy of the crystal.

Although the origin of this photovoltaic effect has not been clarified yet, the key point to understand it is the necessity of both *impurity doping* and *crystal asymmetry*. Figure 1 illustrates one of the proposed models, the electron energy band model proposed for $(\text{Pb},\text{La})(\text{Zr},\text{Ti})\text{O}_3$.^{2,3)} The energy band is basically generated by the hybridized orbit of p-orbit of oxygen and d-orbit of Ti/Zr. The donor impurity levels induced in accordance with La doping (or other dopants) are present slightly above the valence band. The transition from these levels with an asymmetric potential due to the crystallographic anisotropy may provide the "preferred" momentum to the electron. Electromotive force is generated when electrons excited by light move in a certain direction of the ferroelectric crystal, which may arise along the spontaneous polarization direction.

The asymmetric crystal exhibiting a photovoltaic response is also piezoelectric in principle, and therefore, a photostriction effect is expected as a coupling of the bulk photovoltaic voltage (E^{ph}) with the piezoelectric strain constant (d).

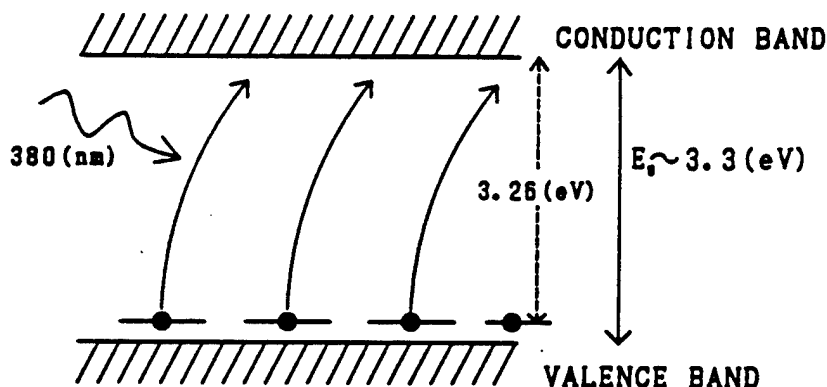


Figure 1 Energy band gap model of excited electron transition from impurity level in PLZT.

INSTRUMENTATION

The radiation from a high-pressure mercury lamp was passed through infrared-cut optical filters. The light with the wavelength peak around 370 nm, where the maximum photovoltaic effect of PLZT is obtained, was then applied to the sample. A xenon lamp was also used to measure the wavelength dependence of the photovoltaic effect. The light source was monochromated by a monochromator to 6 nm HWHM.

The photovoltaic voltage under illumination generally reaches several kV/cm, and the current is on the order of nA. The induced current was recorded as a function of the applied voltage over a range -100 V to +100 V, by means of a high-input impedance electrometer. The photovoltaic voltage and the current were determined from the intercepts of the horizontal and the vertical axes, respectively. The data are shown in Fig. 2.³⁾ Photostriction was directly measured by a differential transformer or an eddy current displacement sensor.

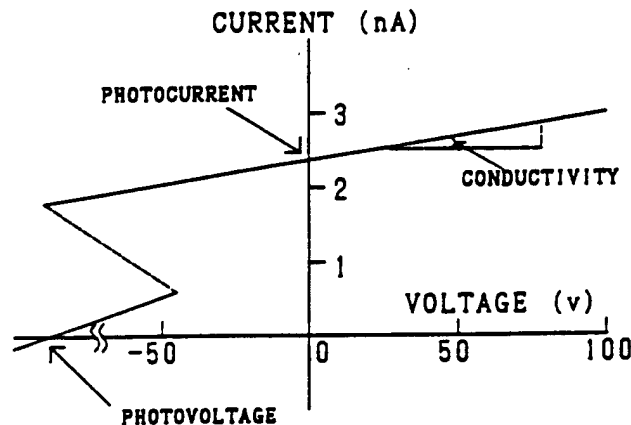


Figure 2 Photocurrent measured as a function of applied voltage under illumination.

MATERIALS RESEARCH

The figure of merit of the photostriction is evaluated by the product of the photovoltaic voltage (E^{ph}) and the piezoelectric coefficient (d). PZT based ceramics are currently focused because of their excellent piezoelectric properties, i. e. high d values. PLZT is one of such materials, which is also famous as a transparent (good sintered without pores) ceramic applicable to electrooptic devices.

PLZT ($x/y/z$) samples were prepared in accordance with the following composition formula:



Figures 3(a) and 3(b) illustrate the contour maps of the photovoltaic response and the piezoelectric strain constant d_{33} on the PLZT phase diagram.^{4,5)} The d_{33} shows the maximum around the morphotropic phase boundary (MPB) between the tetragonal and rhombohedral phases, and increases gradually with increasing the La concentration up to 9 mol %. On the contrary, the photovoltage exhibits the maximum also around the MPB, but in the tetragonal region with 3 mol % of La. The largest product $d_{33} \cdot E^{ph}$ was obtained with the composition (3/52/48).

The interrelation of the photovoltaic current with the remanent polarization for the PLZT family is very intriguing (Fig. 4).⁶⁾ The average remanent polarization exhibiting the same magnitude of photocurrent differs by 1.7 times between the tetragonal and rhombohedral phases; this suggests the photo-induced electron excitation is related to the (0 0 1) axis-oriented orbit, i. e. the hybridized orbit of p-orbit of oxygen and d-orbit of Ti/Zr.

Impurity doping on PLZT also affects the photovoltaic response significantly.³⁾ Figure 5 shows the photovoltaic response for various dopants with the same concentration of 1 atomic % into the base PLZT (3/52/48) under an illumination intensity of 4 mW/cm² at 366 nm. The dashed line in Fig. 5 represents

the constant power curve corresponding to the non-doped PLZT (3/52/48). Regarding the photostriction effect, it is known that as the photovoltaic voltage increases, the strain value increases, and with increasing photocurrent, there is an increase in the overall response. The photovoltaic response is enhanced by donor doping onto the B-site (Nb^{5+} , Ti^{5+} , W^{6+}). On the other hand, impurity ions substituting at the A-site and/or acceptor ions substituting at the B-site, whose ionic valences are small (1 to 4), have no significant effect on the response. Figure 6 shows the photovoltaic response plotted as a function of at.% of WO_3 doping concentration.⁷⁾ Note that the maximum power is obtained at 0.4 at.% of the dopant.

Even when the composition is fixed, the photostriction still depends on the sintering condition or the grain size.⁵⁾ Figure 7 shows the dependence of the photostrictive characteristics on the grain size. The smaller grain sample is preferable, if it is sintered to a high density.

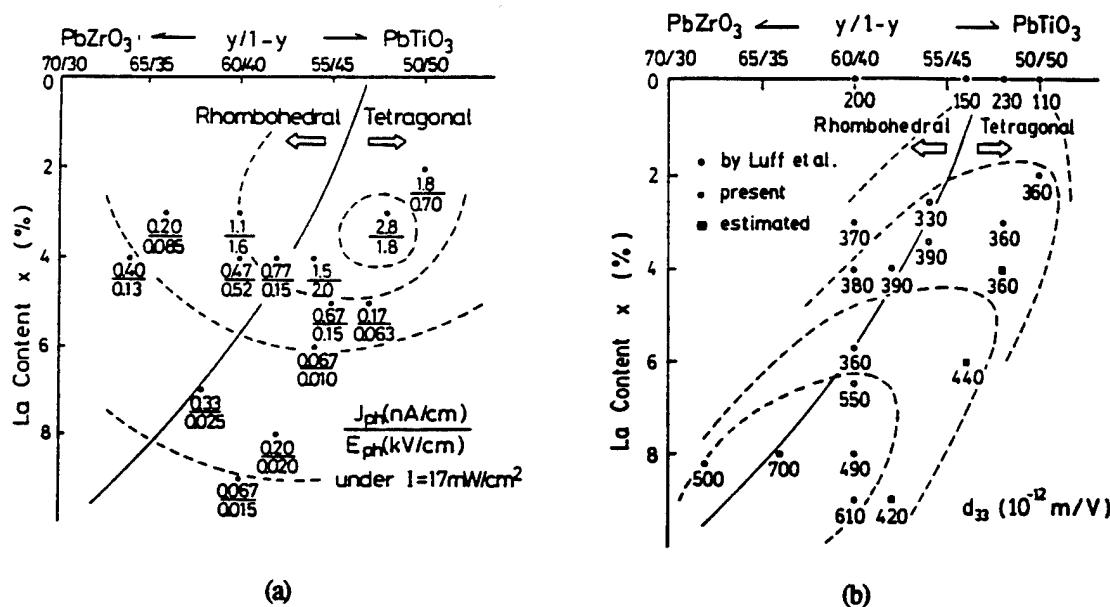


Figure 3 Photovoltaic response (a) and piezoelectric constant d_{33} (b) of PLZT plotted on the phase diagram near the morphotropic phase boundary between the tetragonal and rhombohedral phases.

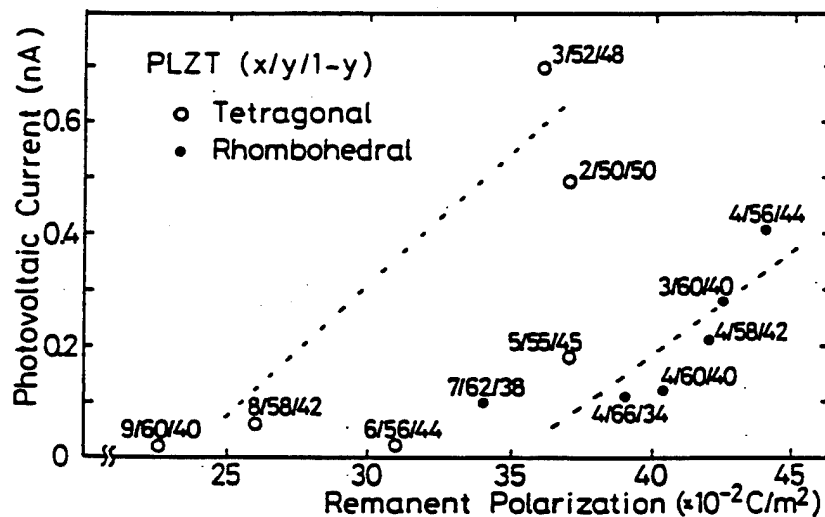


Figure 4 Interrelation of photovoltaic current with remanent polarization in PLZT family.

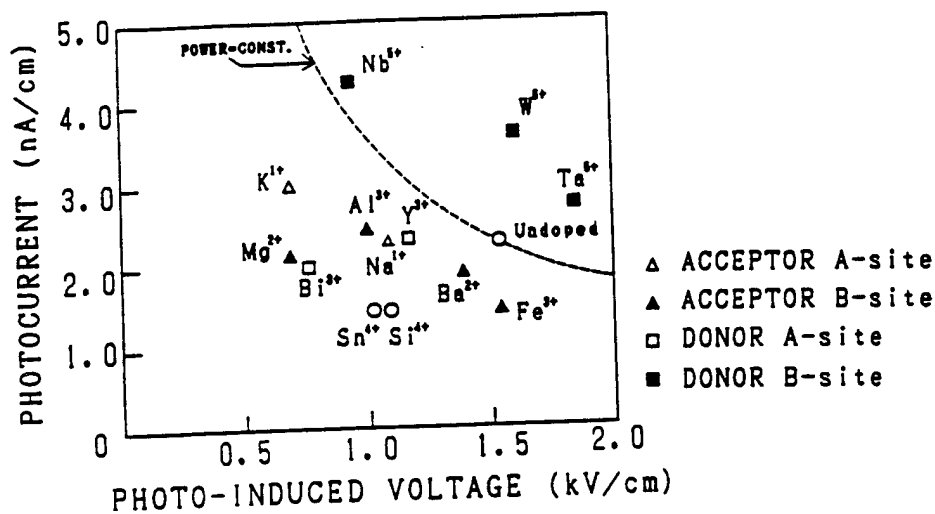


Figure 5 Photovoltaic response of PLZT for various impurity dopants (illumination intensity: 4mW/cm^2).

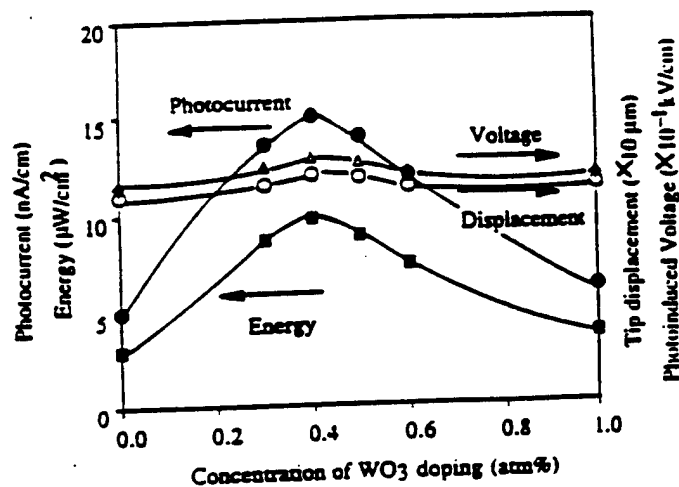


Figure 6 Photovoltaic current, voltage, power and tip displacement of a bimorph specimen as a function of dopant concentration in WO_3 doped PLZT (3/52/48).

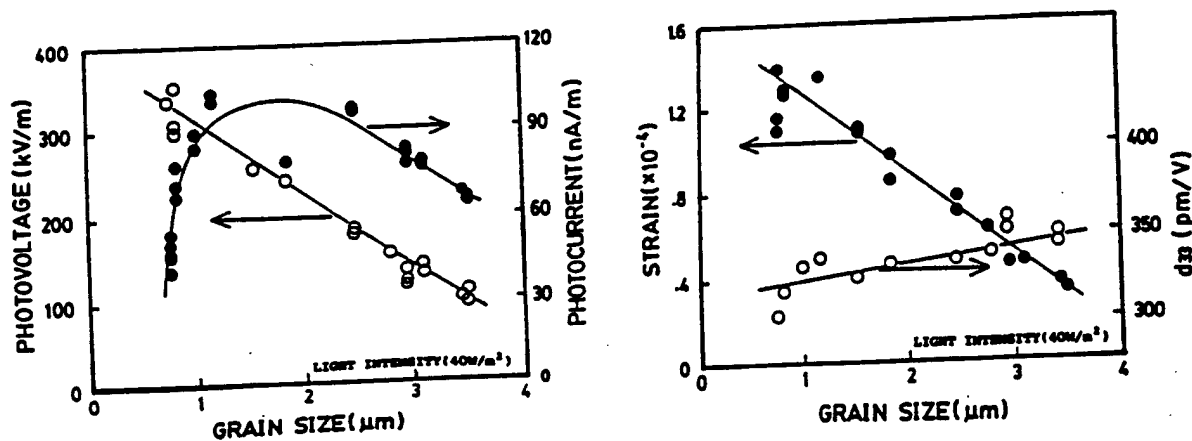


Figure 7 Grain size dependence of photostrictive characteristics in PLZT (3/52/48).

EFFECT OF LIGHT POLARIZATION DIRECTION

Effect of the light polarization direction on the photovoltaic phenomenon was investigated on the polycrystalline PLZT, using an experimental setup shown in Fig. 8(a).⁸ This experiment is important when the photostriction is employed to "photophones", where the sample is illuminated with the polarized light traveling through an optical fiber. The rotation angle θ was taken from the vertical spontaneous polarization direction, as shown in Fig. 8(a). Even in a polycrystalline sample, both the photovoltaic voltage and current provided the maximum at $\theta = 0$ and 180 deg and the minimum at $\theta = 90$ deg (Fig. 8(b)); this also indicates that the contributing electron orbit may be the p-d hybridized orbit mentioned above.

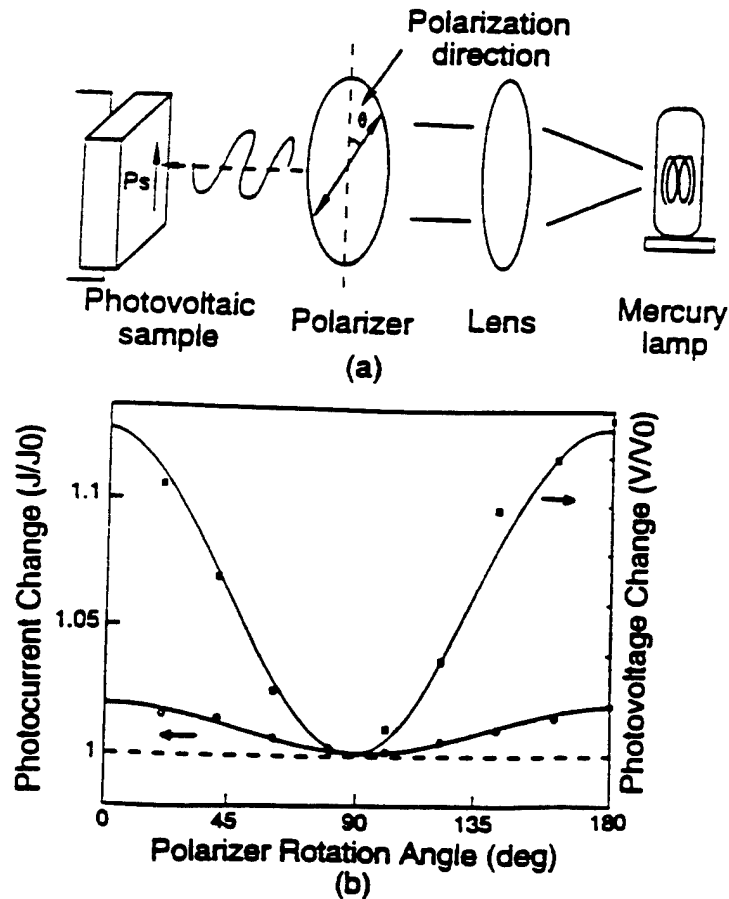


Figure 8 (a) Measuring system of the dependence of photovoltaic effect on light polarization direction, and (b) photovoltaic voltage and current as a function of the rotation angle.

DISPLACEMENT MAGNIFICATION MECHANISM

Since the maximum strain level of the photostriction is only 0.01 % (this corresponds to $1 \mu\text{m}$ displacement from a 10 mm sample), we need to consider a sophisticated magnification mechanism of the displacement. We employed a bimorph structure, which is analogous to a bimetal consisting of two metallic plates with different thermal expansion coefficients bonded together to generate a bending deformation according to a temperature change. Two PLZT plates were pasted back to back, but were placed in opposite polarization, then connected on the edges electrically, as shown in Fig. 9.³ A purple light (366 nm) was shined to one side, which generated a photovoltaic voltage of 7 kV across the length. This caused the PLZT plate on that side to expand by nearly 0.01 % of its length, while the plate on the other (unlit) side contracted due to the piezoelectric effect through the photovoltage. Since the two plates were bonded together, the whole device bent away from the light. For this 20 mm long and 0.35 mm thick bi-plate, the displacement at the edge was $150 \mu\text{m}$, and the response speed was a couple of seconds.

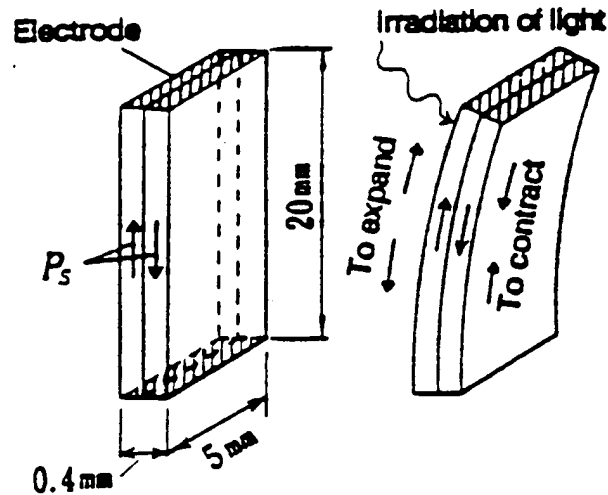


Figure 9 Structure of the photo-driven bimorph and its driving principle.

DEVICE APPLICATIONS

In this section we will introduce the applications of photostriction to a photo-driven relay, a micro walking machine and a photophone, which are designed to function as a result of irradiation, having neither lead wires nor electric circuits.

PHOTO-DRIVEN RELAY

A photo-driven relay was constructed using a PLZT photostrictive bimorph as a driver which consists of two ceramic plates bonded together with their polarization directions opposing each other (Fig. 10).³⁾ A dummy PLZT plate was positioned adjacent to the bimorph to cancel the photovoltaic voltage generated on the bimorph. Utilizing a dual beam method, switching was controlled by alternately irradiating the bimorph and the dummy. The time delay of the bimorph that ordinarily occurs in the off process due to a low dark conductivity could be avoided, making use of this dual beam method. Figure 11 shows the response of a photostrictive bimorph made from PLZT doped with 0.5 at% WO_3 under an illumination intensity of 10 mW/cm^2 . The amount of displacement observed at a tip of the bimorph (20 mm long and 0.35 mm thick) was $\pm 150 \mu\text{m}$. A snap action switch was used for the relay. Switching by a displacement of several tens of micron was possible with this device. The on/off response of the photo-driven relay is shown in Fig. 12. The typical delay time was 1 - 2 seconds.

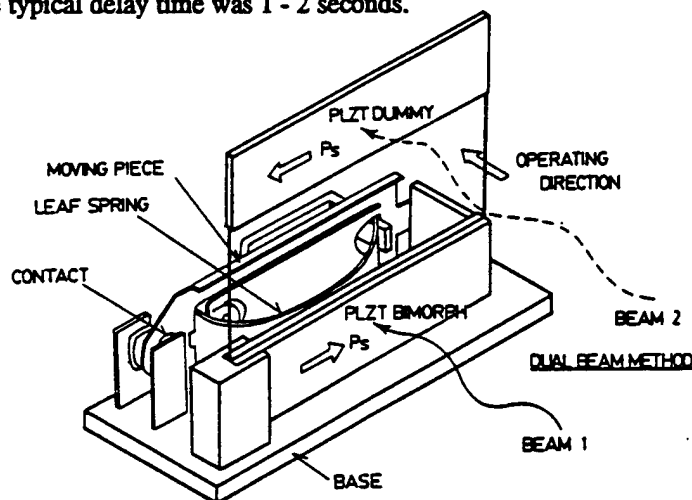


Figure 10 Structure of the photo-driven relay.

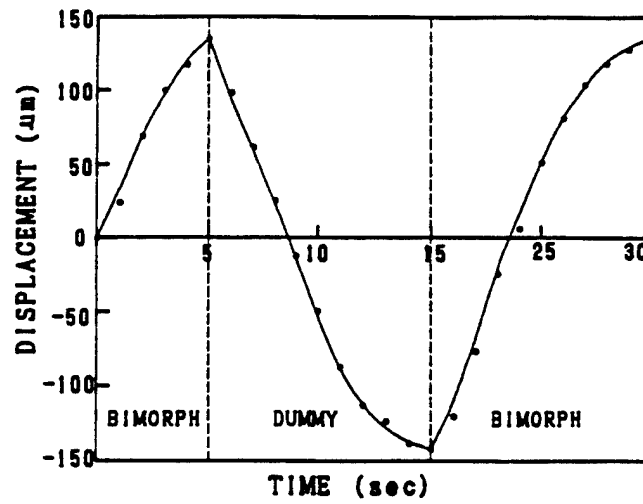


Figure 11 Tip deflection of the bimorph device made from WO_3 0.5 at.% doped PLZT under a dual beam control (illumination intensity: 10 mW/cm^2).

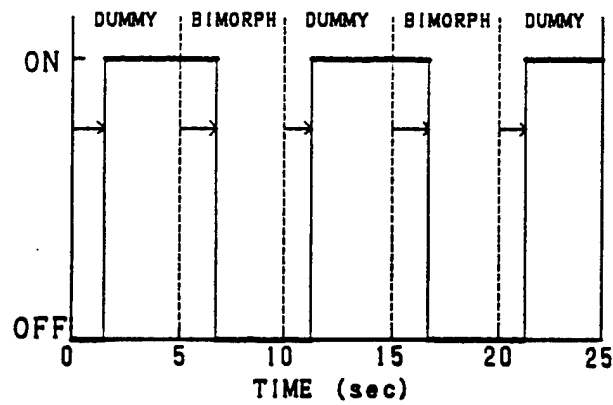


Figure 12 On/off response of the photo-driven relay.

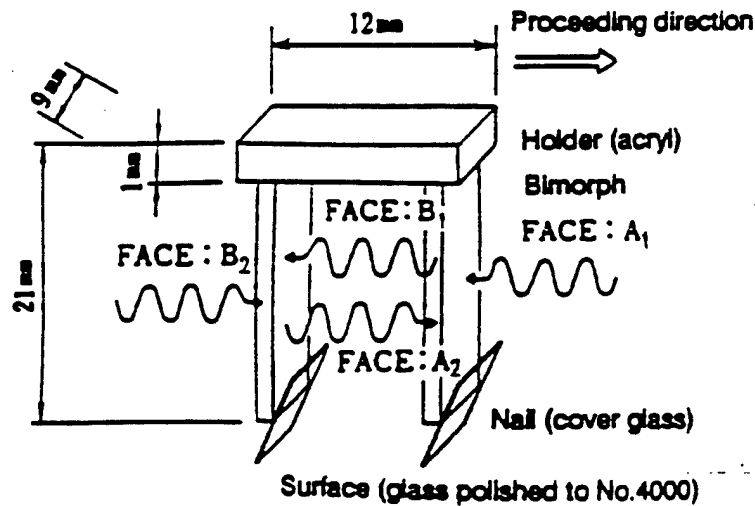


Figure 13 Structure of the photo-driven micro walking machine, and the irradiation directions.

MICRO WALKING DEVICE

A photo-driven micro walking machine has also been developed using the photostrictive bimorphs.⁹⁾ It was simple in structure, having only two ceramic legs (5mmx 20mmx 0.35mm) fixed to a plastic board (Fig. 13). When the two legs were irradiated with purple light alternately, the device moved like an inchworm. The photostrictive bimorph as a whole was caused to bend by $\pm 150 \mu\text{m}$ as if it averted the radiation of light. The inchworm built on a trial basis exhibited rather slow walking speed (several tens $\mu\text{m}/\text{min}$) as shown in Fig. 14, since slip occurred between the contacting surface of its leg and the floor. The walking speed can be increased to approximately 1 mm/min by providing some contrivances such as the use of a foothold having microgrooves fitted to the steps of the legs.

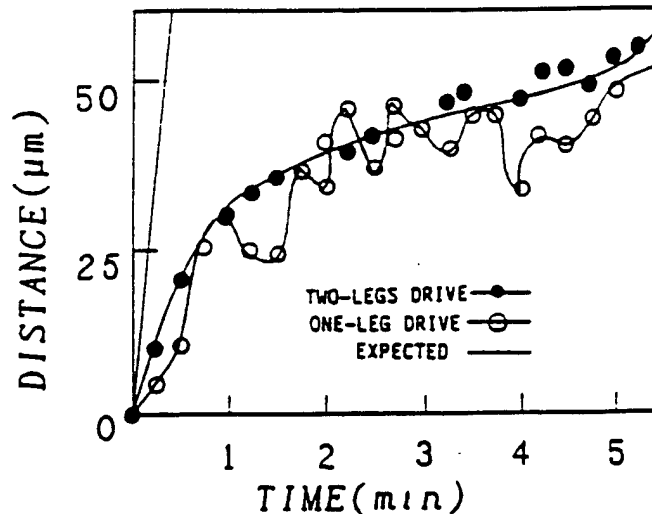


Figure 14 Position change of the photo-driven micro walking machine with time.

PHOTOPHONE

The technology to transmit voice data (i. e. a phone call) at the speed of light through lasers and fiber optics has been advancing rapidly. However, the end of the line — interface speaker — limits the technology, since optical phone signals must be converted from light energy to mechanical sound via electrical energy at present. The photostriction may provide new photoacoustic devices.

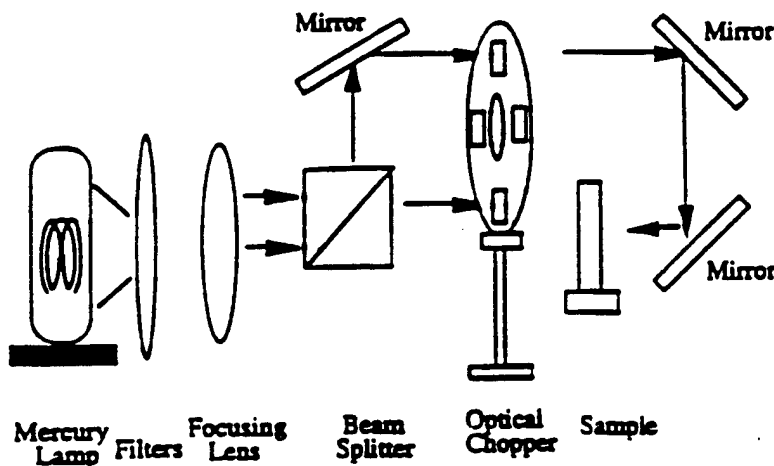


Figure 15 Experimental setup for the photo-induced mechanical resonance measurement.

Photo-mechanical resonance of a PLZT ceramic bimorph has been successfully induced using chopped near-ultraviolet irradiation, having neither electric lead wires nor electric circuits.¹⁰⁾ A thin cover glass was attached on the photostrictive bimorph structure to decrease the resonance frequency so as to easily observe the photo-induced resonance. Figure 15 shows the experimental setup with an optical chopper. A dual beam method was used to irradiate the two sides of the bimorph alternately; intermittently with a 180 deg phase difference. The mechanical resonance was then determined by changing the chopper frequency.

The tip displacement of the thin-plate-attached sample as a function of chopper frequency is presented in Fig. 16. Photo-induced mechanical resonance was successfully observed. The resonance frequency was about 75 Hz with the mechanical quality factor Q of about 30. The maximum tip displacement of this photostrictive sample was about 5 μm at the resonance point, smaller than the level required for audible sound. However, the achievement of photo-induced mechanical resonance in the audible frequency range suggests the promise of photostrictive PLZT bimorph-type devices as photo-acoustic components, or "photophones", for the next optical communication age.

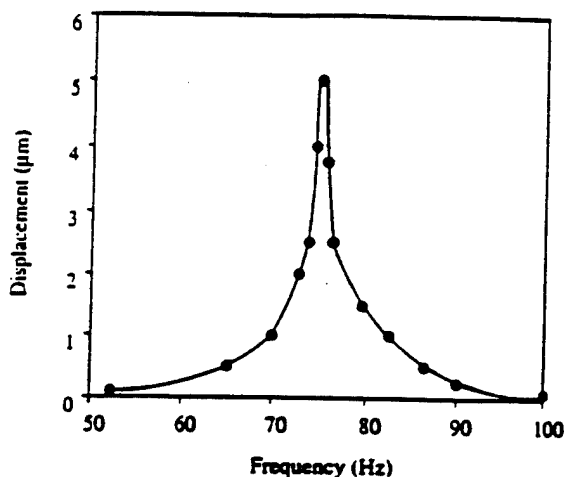


Figure 16 Photo-induced mechanical resonance behavior of the PLZT bimorph.

CONCLUSION

Photostrictive actuators can be driven only by the irradiation of light, so that they will be suitable for use in actuators, to which lead wires can hardly be connected because of their ultra-small size or of their employed conditions such as ultra-high vacuum or outer space. The photostrictive bimorphs will also be applicable to "photophones." The new principle actuators have considerable effects upon the future micro-mechatronics.

This work was partly supported by US Army Research Office through Contract No. DAAL 03-92-G-0244.

REFERENCES

1. V. M. Fridkin, *Photoferroelectrics*, Ed. by M. Cardona, P. Fulde, H. -J. , Queisser, Solid State Sciences 9, Springer-Verlag, New York (1979).
2. A. M. Glass, D. von der Linde, D. H. Austin and T. J. Negran, *J. Elec. Mater.*, 4 [5], 915 (1975).
3. M. Tanimura and K. Uchino, *Sensors and Materials*, 1, 47 (1988).
4. K. Uchino, M. Aizawa and Late S. Nomura, *Ferroelectrics*, 64, 199 (1985).
5. T. Sada, M. Inoue and K. Uchino, *J. Ceram. Soc. Jpn.*, 5, 545 (1987).
6. K. Uchino and M. Aizawa, *Jpn. J. Appl. Phys.*, 24, Suppl. 24-3, 139 (1985).
7. S. Y. Chu, Z. Ye and K. Uchino, *J. Adv. Performance Mater.* [in press].
8. S. Y. Chu, Z. Ye and K. Uchino, *Smart Mater. Struct.*, 3, 114 (1994).
9. K. Uchino, *J. Rob. Mech.*, 1, 124 (1989).
10. S. Y. Chu and K. Uchino, *Proc. 9th Int'l Symp. Appl. Ferroelectrics*, State College (1994)[in press].

APPENDIX 48

PHOTO-ACOUSTIC DEVICES USING (Pb,La)(Zr,Ti)O₃ CERAMICS

Sheng-Yuan Chu and Kenji Uchino
International Center for Actuators and Transducers
Intercollege Materials Research Laboratory
The Pennsylvania State University, University Park, PA 16802

Abstract -- Photostriction in ferroelectrics arises from a superposition of photovoltaic and inverse piezoelectric effects. This phenomenon provides promise for photo-acoustic devices, when the response has been sufficiently improved. In this paper, B-site donor doping was investigated in (Pb, La)(Zr, Ti)O₃ based ceramics with the aim of improving the response speed. Using a PLZT bimorph configuration, a photoacoustic device was trially fabricated, and the fundamental mechanical resonance was observed under intermittent illumination of purple-color light, having neither electric lead wires nor electric circuit.

INTRODUCTION

Photostrictive effect is a phenomenon in which strain is induced in the sample when it is illuminated. This effect is focused especially in the field of optical communication, where the key components are solid state lasers as a light source, optical fibers as a transfer line, and displays/telephones as a visual/audible interface with the human. The former two components have been developed fairly successfully, and the photo-acoustic device (i. e. optical telephone or "photophone") will be eagerly anticipated in the next century. Photostrictive devices which function when they receive the energy of light will be particularly suitable for use in the above-mentioned fields.

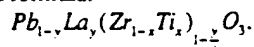
In principle, the photostrictive effect is the superimposing of a photovoltaic effect, where a large voltage is generated in ferroelectrics through the irradiation of light, and a piezoelectric effect, where the material expands or contracts from the voltage applied. The photovoltaic effect mentioned here generates a greater-than-band-gap voltage, and is quite different from that based on the p-n junction of semiconductors (i. e. solar battery).¹⁻³ It is generated when electrons excited by light move in a certain direction of the ferroelectric crystal due to the spontaneous polarization (i. e. crystallographic anisotropy).

So far, most of the studies on the photovoltaic effect have been made on single crystals to clarify the origin of the effect.¹⁻³ However, our research group has been focusing on polycrystalline samples such as PbTiO₃-based^{4,5} and Pb(Zr, Ti)O₃-based ceramics^{6,7} from a practical application point of view. High photovoltage (≈ 1 kV/cm) generators with relatively quick response (≈ 10 sec) have been developed in the (Pb, La)(Zr, Ti)O₃ (PLZT) system. Moreover, bimorph-type photostrictive elements could exhibit large tip deflections under UV light illumination.^{6,7}

In this paper, the photovoltaic effect in PLZT(3/52/48) based ceramics has been investigated as a function of B-site donor dopants. Then, using the PLZT bimorph, a photoacoustic device was trially fabricated, and the fundamental mechanical resonance was observed under intermittent illumination.

SAMPLE PREPARATION

PLZT (x/y/z) samples were prepared in accordance with the following composition formula:



Since the photostriction figure of merit is defined as the product of the photovoltaic voltage and piezoelectric coefficient ($x_{ph} = d_{33} \times E_{ph}$), PLZT(3/52/48) was selected due to its optimum photostrictive response within the PLZT system.⁶ According to our preliminary study on impurity doping,⁷ WO₃ doped PLZT ceramics were prepared.

Ceramic powders were prepared by a conventional mixed oxide technique. PbCO₃, La₂O₃, ZrO₂, TiO₂ and WO₃ were weighed in the appropriate proportions and mixed in a ball mill for 2 days using ethanol and zirconia grinding media. 0.5 wt% excess PbCO₃ was added to compensate for weight loss during calcination and sintering. The slurry was dried, then calcined in a closed alumina crucible at 950 °C for 10 hours. The calcined powder was ball-milled again for 48 hours. The samples were sintered in sealed alumina crucibles at 1270 °C for 2hrs. A PbO rich atmosphere was maintained with lead zirconate powder to minimize lead loss during sintering. Sintered samples were cut, polished and electroded with silver paste. Finally, each sample was poled at 15 kV/cm in silicone oil at 120°C.

The poled PLZT ceramics were used to make bimorph actuators. The elements were 20 x 4 x 0.15 mm³; the 4 x 0.15 mm² surface was electroded with silver paste and silver wires were attached. The bimorph actuator consisted of two bonded oppositely-poled ceramic plates (refer to Fig. 2).

IMPURITY DOPING EFFECT

Impurity doping on PLZT affects the photovoltaic response significantly.⁷ Regarding the photostriction effect, it is known that as the photovoltaic voltage increases, the strain value increases, and

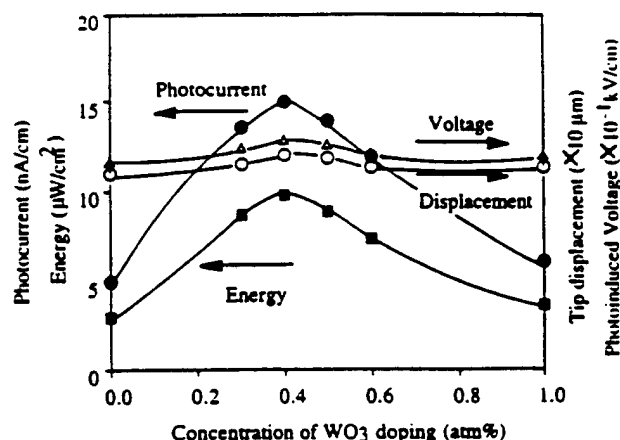


Fig. 1 Changes in photovoltaic current, voltage, power and tip displacement as a function of dopant WO₃ concentration in PLZT (3/52/48).

with increasing photo-current, there is an increase in the overall response. The photovoltaic response is enhanced by donor doping onto the B-site (Nb^{5+} , Ti^{5+} , W^{6+}). On the other hand, impurity ions substituting at the A-site and/or acceptor ions substituting at the B-site, whose ionic valences are small (1 to 4), have no effect on the response.

Figure 1 shows the photovoltaic current, photovoltaic voltage, photo-induced tip displacement and stored energy ($P=(1/2) I_{\text{max}} \times V_{\text{max}}$) in PLZT 3/52/48 samples plotted as a function of atm % of WO_3 doping concentration. It was found that higher photovoltaic response can be obtained in WO_3 doped samples. The photovoltaic voltage reaches 1 kV/mm, and the current is on the order of nA. The maximum of the saturated tip displacement was about 120 μm for 0.4 atm% WO_3 doped samples. The displacement of 30 μm could be obtained in one second under a light intensity of 4 mW/cm^2 ($\lambda = 370 \text{ nm}$).

PHOTO-ACOUSTIC MEASUREMENT

The mechanical resonance frequency of this bimorph sample can be estimated according to the equation:

$$f_r = 0.158 \times \frac{t}{l^2} \sqrt{\frac{1}{\rho s_{11}^E}} \quad (1)$$

where t and l are the thickness and length of the bimorph sample, respectively, ρ is the density and s_{11}^E is the elastic compliance of the ceramic. The calculated resonance frequency of the PLZT based bimorph, ($\rho = 7.9 \text{ g}/\text{cm}^3$ and $s_{11}^E = 16 \times 10^{-12} \text{ m}^2/\text{N}$), was about 3 kHz: too high for photo-induced resonance measurements. Therefore, a thin cover glass was attached to the bimorph sample to reduce the resonance frequency, as shown in Fig. 2. Initially, to determine the electromechanical resonance behavior, an ac. voltage was applied to the bimorph, and the tip displacement was monitored by changing the drive frequency, using the experimental setup shown in Fig. 3. Figure 4 shows the mechanical resonance characteristics obtained from this experiment. The resonance frequency was $\sim 79 \text{ Hz}$ with a mechanical quality factor Q of ~ 30 . The maximum displacement of this thin-plate attached sample was about 14 μm at 80 Vp-p.

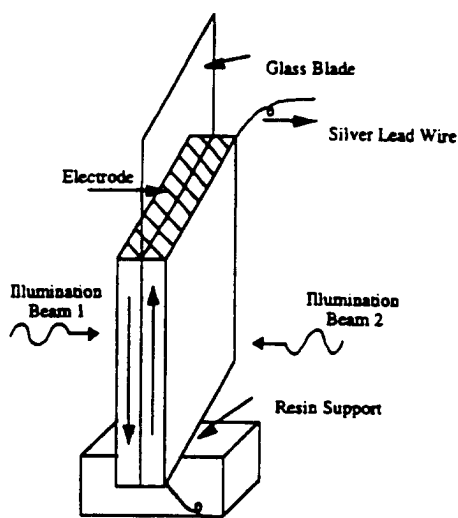


Fig.2 Configuration of a thin-plate attached photo-acoustic bimorph.

Then, the photo-induced mechanical resonance was measured using the system shown in Fig. 5. Radiation from a high-pressure mercury lamp (Ushio Electric USH-500D) was passed through a UV bandpass filter (Oriel Co., No.59811), an IR blocking filter (Oriel Co., No.59060), an optical focusing lens and an optical chopper to provide intermittent sample irradiation. A wavelength peak of 370 nm, where the maximum photovoltaic effect of PLZT is obtained, was used. A dual beam method was used to irradiate the two sides of the bimorph alternately.⁷⁾ Two beams, A and B, were chopped so as to cause a 180 degree phase difference as illustrated

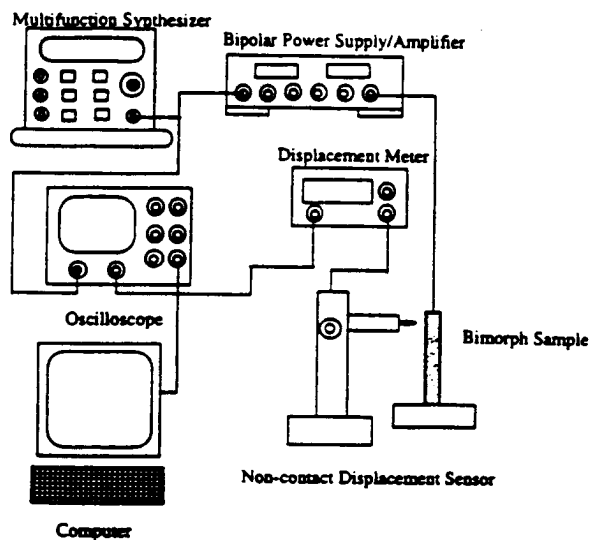


Fig.3 Experimental setup for the electro-mechanical resonance measurement.

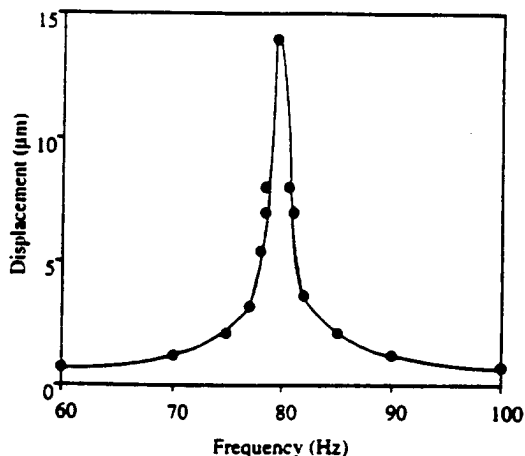


Fig.4 Electromechanical resonance behavior of the PLZT bimorph.

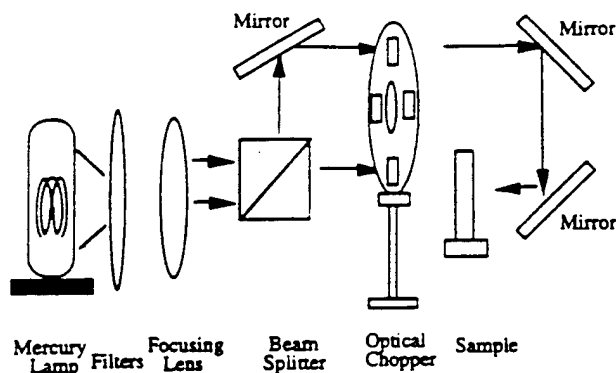


Fig.5 Experimental setup for the photo-induced mechanical resonance measurement.

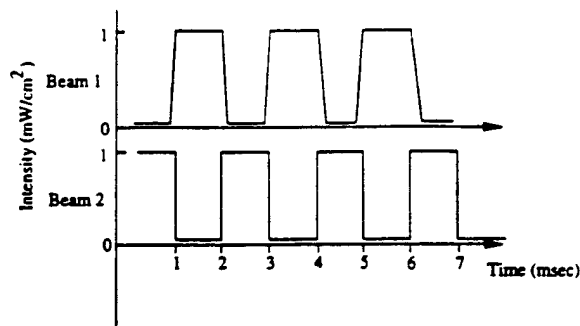


Fig.6 Wave forms for the two beams for illuminating the bimorph sample.

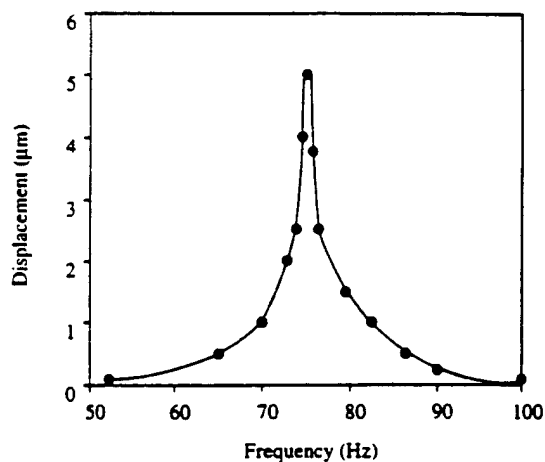


Fig.7 Photo-induced mechanical resonance behavior of the PLZT bimorph.

in Fig. 6. The slow recovery because of the low dark conductivity was overcome using this dual beam method. The mechanical resonance was then determined by changing the chopper frequency.

The tip displacement of the thin-plate-attached sample as a function of chopper frequency is presented in Fig. 7. Photo-induced mechanical resonance was successfully observed. The resonance frequency was about 75 Hz with the mechanical quality factor Q of about 30; in good agreement with the previous electromechanical data. The maximum tip displacement of this photostrictive sample was about 5 μm of resonance.

CONCLUSION

Photo-mechanical resonance of a PLZT ceramic bimorph actuator has been successfully induced using chopped UV irradiation, having neither electric lead wires nor electric circuit. A thin cover glass was attached on the bimorph structure to decrease the resonance frequency so as to easily observe the photo-induced resonance. The resonance frequency was 75 Hz with a mechanical quality factor Q of about 30 under dual beam operation. The maximum tip displacement of this sample was about 5 μm , smaller than the level required for audible sound. However, the achievement of photo-induced mechanical resonance in the audible frequency range suggests the promise of photostrictive PLZT bimorph-type devices as photo-acoustic components, or "photophones", for the next optical communication age.

ACKNOWLEDGEMENT

This work is supported by Army Research Laboratory (ARL), No. DAALO3-92-G-0244.

REFERENCES

- [1] V. M. Fridkin, "Photoferroelectrics", Ed. by M. Cardona, P. Fulde, H. -J. Queisser, Solid State Sciences, New York, (1979), pp. 85.
- [2] A. M. Glass, D. von der Linde, D. H. Austin and T. J. Negran, *J. Elec. Mat.* 4 [5], 915-943 (1975).
- [3] V. M. Fridkin and B. N. Povov, *Sov. Phys. Usp.*, 21(12), 981-991 (1978).
- [4] K. Uchino, Y. Miyazawa and S. Nomura, *Jpn. J. Appl. Phys.*, 21, [12], 1671-1674 (1982).
- [5] K. Uchino, Y. Miyazawa and S. Nomura, *Jpn. J. Appl. Phys. Suppl.* 22-2, 102-105 (1983).
- [6] T. Sada, M. Inoue and K. Uchino, *J. Ceram. Soc. Jpn.*, 5, 545 (1987).
- [7] M. Tanimura and K. Uchino, *Sensors and Materials*, 1, 47-56 (1988).

INTEGRATION ISSUES

APPENDIX 49

Zig-Zag Piezoelectric Actuators: Geometrical Control of Displacement and Resonance

M. G. MATSKO, Q. C. XU AND R. E. NEWNHAM

Materials Research Laboratory, The Pennsylvania State University, University Park, PA 16802

ABSTRACT: The Zig-Zag actuator is a hybrid design combining bimorph and multilayer characteristics that is capable of producing and sensing usable motion in two dimensions. The mechanical impedance can be optimized by changing the angle between the legs and the actuator's working parameters controlled by changing the driving voltage and its frequency. Two interesting features of this actuator are its performance as a linear motor and its ability to drive a load in two directions.

INTRODUCTION OF BASIC PRINCIPLES

PIEZOELECTRIC micropositioners are of increasing importance because of their ability to move objects electromechanically (Unchino, 1993). This capability bridges the electronic and structural ceramics fields, and produces tiny displacements with high-speed and precision. Adaptive optic systems incorporate positioning instruments that require both precision and accuracy, while other actuators are incorporated in devices that utilize their resonating ability, as in buzzers and timing instruments.

Piezoelectric materials are important as smart materials because they have both sensing and actuating abilities (Newnham and Ruschau, 1991). They can convert electrical energy into mechanical energy through the converse piezoelectric effect, and mechanical energy into electrical energy through the direct effect (Jaffe et al., 1971).

Several questions must be answered before incorporating a piezoelectric actuator into a specific instrument. How much displacement is required? How much force must the actuator exert? Is a resonance effect required? When the actuator is asked to supply a relatively small displacement with a high force, a multilayer stack is often used [Figure 1(a)]. When a larger displacement is required and a lower force can be tolerated, a bimorph or bender is used [Figure 1(b)]. Both of these forms may be driven in resonance, or at low frequency displacement modes.

In an effort to optimize the advantages of both geometries, a hybrid design was conceived. The Zig-Zag actuator appears advantageous for certain applications with intermediate requirements. It possesses a geometry that gives both good displacement and good force. Additionally, the Zig-Zag actuator exhibits two-dimensional movement with controllable vertical and horizontal components that include intermediate angle directions. Primary applications will be in linear motors and two-dimensional positioning and sensing devices, with an array of Zig-Zag actuators performing

transport or positioning functions. The present investigation involves the measurement of displacement and resonance characteristics for several geometries of the Zig-Zag actuator. A schematic diagram of the Zig-Zag actuator is shown in Figure 1(c).

ACTUATOR

Zig-Zag actuators with contact angles of 90° and 30° are shown in Figure 1(c). The limits of the actuator are defined by the bimorph and multilayer devices of the same composition and linear dimensions. The relationship between displacement and contact angle from 0° to 180° is related to the governing equations for a bimorph [Equation (1)], and a multilayer stack [Equation (2)] (Buchanan, 1986). At an angle of 0° the multilayer stack equation will have no contribution, and at an angle of 180° the bimorph equation will have no contribution.

$$D = 3/2 d_{31} V (L^3/T^3) \quad (1)$$

$$D = d_{31} V (L/T) \quad (2)$$

where

D = displacement
 d_{31} = transverse charge coefficient
 V = voltage
 L = length
 T = thickness

These two equations can be related by a sine/cosine interaction relationship that would result in each of the equations dropping out at their respective angles. The resulting relationship may be represented by Equation (3). This implies the Zig-Zag equation must revert to Equation (1) at 0° and Equation (2) at 180°.

$$D = A \cos^n (Q/2) + B \sin^n (Q/2) \quad (3)$$

Associate Editor: K. Reifsnider.

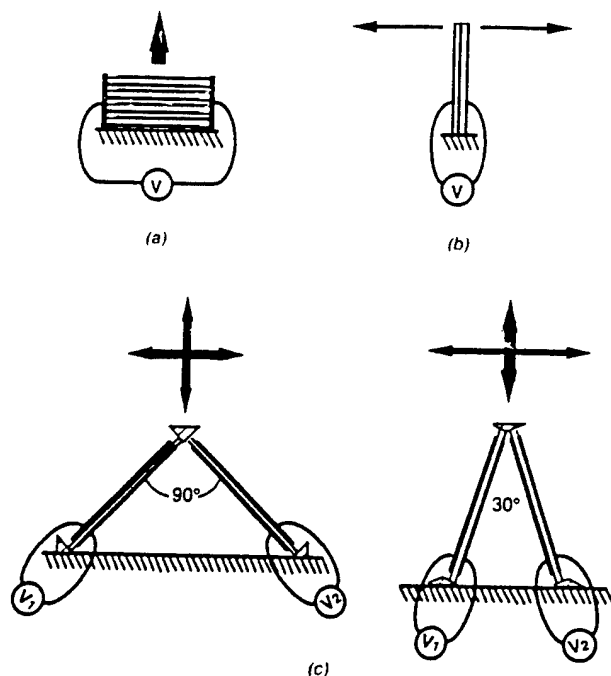


Figure 1. (a) Multilayer, (b) bimorph, (c) Zig-Zag actuator (90° and 30° geometries).

where

$$A = 3/2 d_{31} V(L^3/T^3)$$

$$B = d_{31} V(L/T)$$

Q = angle between legs

n, p = adjustable exponents

To demonstrate this behavior, a test apparatus was constructed that allowed several different geometries. The principal geometrical factor is the angle at which the legs are attached as illustrated in Figure 1(c). Experiments were carried out at three angles: 30°, 45°, and 90°.

PIEZOELECTRIC LINEAR MOTOR

The required motion for a linear motor can be achieved by driving one leg with a sine wave and the other leg with a sine wave that is 90° out of phase. If the second leg is 90° ahead of the first, the resulting motion will be clockwise, and will move the load from right to left. If the second leg is 90° behind the first the resulting motion will be counter-clockwise and the load will be moved from left to right. A schematic view of the resulting motion when the actuator is driven in this manner is shown in Figure 2. The Zig-Zag design allows the mechanical impedance of the actuator to be adjusted to the specific application by changing the angle between the legs.

EXPERIMENTAL PROCEDURE AND RESULTS

To fabricate the Zig-Zag actuator, the legs were cut from a large commercial disk of PZT 8. Each leg was approximately 1 mm thick, 45 mm long, and 10 mm wide. The plates were polished and electroded with silver termination paint and sintered at 600°C. This sintering had a two-fold effect: first it bonded the silver electrode to the PZT ceramic and densified it, and secondly it removed any previous poling orientations and restored the PZT to its randomized domain structure. The electroded PZT plates were then poled in a Neslab Exacal high temperature oil bath with a Trek cur-a-trol H.V. power supply model 610A. Poling conditions were approximately 125°C for 15 minutes with an applied field of 2.5 kV/cm. The d_{33} measurements were taken with a Berlincourt Piezo d_{33} Meter to ensure good poling. The effect of aging was checked by measuring d_{33} one week later.

The admittance of the PZT plate was measured as a function of frequency using a computer-controlled Hewlett-Packard 3577A Network Analyzer. This information was used to classify the plates into pairs having similar resonance and antiresonance peaks.

The PZT plates were bonded to the metal wedges using a strong two-component room temperature epoxy. Due to concerns about the epoxy absorbing the motion of the actuator, a second design was also constructed that mechanically-clamped the PZT plates. Wire leads were soldered to the electrodes to ensure good contacts.

Displacement measurements were made with the LVDT system and an eddy-current sensor. The direction of the electric field and measuring device were alternated to measure movement in both directions (Table 1). The field was applied in a DC fashion ranging from 0 to 1100 V/mm.

An aluminum bar suspended on ball bearings was used as a load in testing the actuator as a linear motor (Figure 3). The height of the actuator was adjusted using a micropositioner.

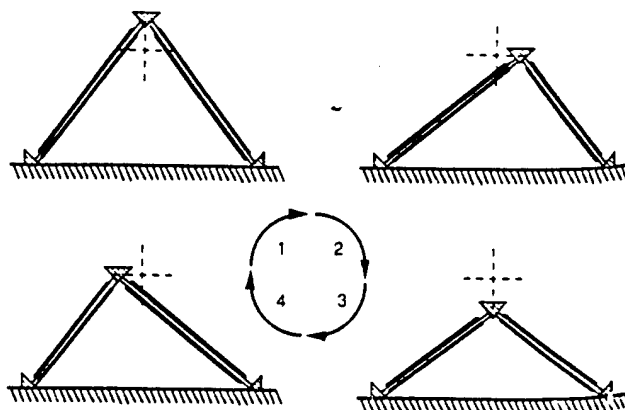


Figure 2. Zig-Zag actuator being driven by sine and cosine voltages.

Table 1. Displacement versus angle and direction of measurement and applied electric field of 1100 V/mm (epoxy design).

Leg Separation Angle	Measured Longitudinal Displacement (μm)		Measuring Shear Displacement (μm)	
	In Phase	Out of Phase	Out of Phase	In Phase
90°	6.8	2.7	7.4	2.5
45°	5.3	1.6	18.9	0.6
30°	3.5	1.3	28.6	1.0

The appropriate fields for circular motion were produced with an NF Electronic Instruments 1930A multifunction synthesizer, an NF 1933A phase shifter, two NF 4010 high speed power amplifiers, and a Tektronix 2445A 150 MHz oscilloscope (Figure 3). This allowed control over the frequency of the applied functions as well as their relationship to one another. The optimum driving frequency was experimentally determined to be $\approx 6\text{--}7$ kHz with a sine wave (± 100 V). At these frequencies, the Zig-Zag actuator drove the load at approximately 1 cm per second in both the forward and reverse directions. The impedance spectrum of the Zig-Zag actuator was measured with respect to frequency and geometry, using the same equipment used to measure the single plates.

DISCUSSION

In constructing the Zig-Zag actuator, poled plates were paired together by matching resonance and antiresonance peaks from a plot of the admittance spectrum. Matching the legs in this manner helped to compensate for problems associated with variations in poling and thickness. Several Zig-Zag actuators were constructed using different sets of PZT plates. The aging effects that occurred in PZT proved negligible compared to other parameters in the experiment.

Poling of the individual plates must be done in such a way that allows them to be matched in pairs. The displacements produced by the two legs must be equal, otherwise, the actuator wastes much of its displacement capabilities.

Design modifications of the metal parts of the actuator were carried out to combat several problems. The movement of the PZT plates in some directions may only be a few microns. Consequently, a major concern was the ability to measure the movement of the actuator. If the epoxy used to bond the legs was too "soft," the motion of the actuator may be absorbed in the epoxy, making it unmeasurable. The epoxy used in our experiments had substantial tensile strength, but relatively low shear strength. This meant that the epoxy should be subjected to as little shear stress as possible. To alleviate most of the shear stresses the metal base and top had to meet the PZT legs perpendicularly. Metal wedges were used on the base and top to avoid cutting the legs on an angle. An angular cut would subject the epoxy to shear stresses. The masses of the base and the top were also of some concern. The ratio of the bottom to the top had to be high enough that the base would not move. If they both moved, no accurate measurements could be made. The top had to have sufficient mass to offset the effect of the wire leads, and yet be small enough so as not to place too much stress on the epoxy. A few problems arose in the construction of the actuator, especially with the epoxy. The epoxy

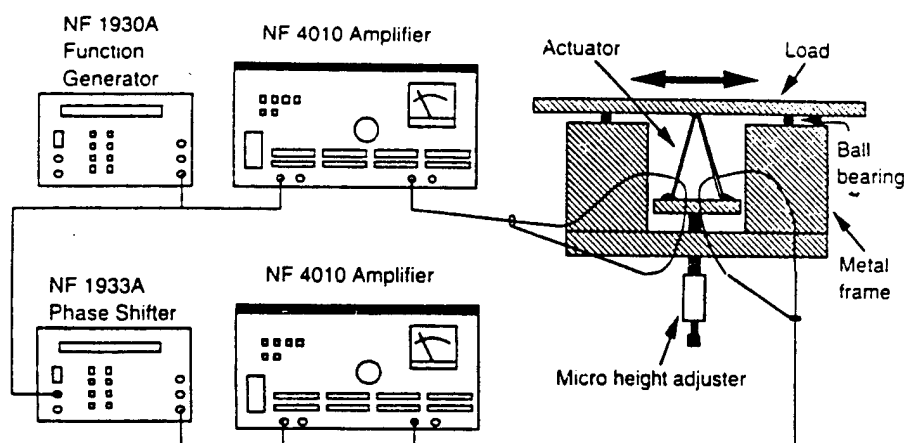


Figure 3. Linear motor driving setup.

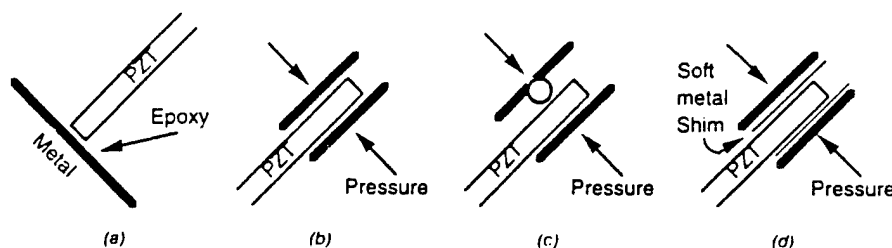


Figure 4. Attaching methods: (a) perpendicular epoxy, (b) plate/plate, (c) point/plate, (d) plate/plate with soft metal shims.

used in this study, ECCOBOND, was manufactured by Emerson & Cuming. It is a two-component system that cures at room temperature, and to assist the bonding, some pressure is necessary. The required pressure was produced by a C-clamp. When the applied pressure was removed, the epoxy had a tendency to expand, followed by cracking and failure. This was compensated for by slightly adjusting the composition of the epoxy and optimizing the applied pressure.

Because of the tendency of the plates to fail using the perpendicular epoxy method [Figure 4(a)], a clamping method was developed. The plate/plate clamping method [Figure 4(b)], required careful machining to avoid torsional stresses that might fracture the ceramic plates. To eliminate these stresses two approaches were examined. One approach was a point and plate clamp rather than a plate/plate design, as shown in Figure 4(c). A second idea was to use a soft metal shim that plastically deforms, pressing on the PZT plate over a wide area [Figure 4(d)]. Of these four designs examined, the plate/plate with soft metal shim gave the best frictional force and lowest motion loss due to slippage. This design also resulted in the fewest failures due to torsional stresses encountered during construction.

The frequency at which the actuator operates best depends on several factors. These factors include the properties of the PZT plates, the geometry of the plate and the actuator, and the mass of the metal parts. The properties of the PZT plates that must be considered are its density, mechanical coupling coefficient, compliance, and electrode length to total length ratio. All of these factors play a role in the resonance spectrum of the actuator and its usefulness as a linear motor. Relatively small changes in the construction of the actuator resulted in large changes in the optimum driving frequency.

The largest problem yet to be overcome is that of attaching the PZT legs to the metal parts. Finding the best method of joining the parts, to give the highest frictional forces with the fewest construction failures, is difficult. If the connection is too weak, the actuator motions are not transmitted to the base, producing an error in the measurements. If the connection is too strong, the ceramic may crack, again re-

ducing the motion. These coupling problems are amplified when the device is driven at resonance.

FUTURE WORK

The Zig-Zag actuator can also take advantage of the direct piezoelectric effect, and be used as a two-dimensional sensor. In this way the actuator can sense and transmit information about the direction and displacement of an applied force. The phase, magnitude and frequency spectrum of the sensor signals determine the direction and force or displacement of the stimuli.

CONCLUSIONS

This investigation provides a preliminary study of the construction and the effects of geometry on the Zig-Zag actuator. The Zig-Zag transducer has performed well as a linear motor and in the future may function as a two-dimensional sensor, as well as a two-dimensional actuator.

ACKNOWLEDGEMENTS

Portions of the work were performed using equipment in the laboratory of Professor K. Uchino. Completion of this phase of the project was made possible with funds from Navy Contract No. N00014-92-J-2765.

REFERENCES

- Uchino, K. 1993. "Ceramic Actuators: Principles and Applications", *MRS Bulletin XVIII*, 4:42-48.
- Newnham, R. E. and G. R. Ruschau. 1991. "Smart Electroceramics", *Journal American Ceramic Society*, 74(3):463-480.
- Jaffe, W., R. Cook and H. Jaffe. 1971. *Piezoelectric Ceramics*. Marietta, Ohio: Academic Press.
- Buchanan, R. C. 1986. *Ceramic Materials for Electronics*. New York: Marcel Dekker, Inc.

APPENDIX 50

Presented at the SPIE's 1996 Symposium on

Smart Structures and Materials

26-29 February 1996

San Diego, California USA

Paper No. 2717-33

Piezoelectric air transducer for active noise control

Baomin Xu, Qiming Zhang, V. D. Kugel and L. E. Cross

Intercollege Materials Research Laboratory, Pennsylvania
State University, University Park, PA 16802

ABSTRACT

A new type of piezoelectric air transducer has been developed for active noise control and other air acoustics applications. The transducer is based on the composite panel structure of a bimorph-based double amplifier, that is, two parallel bimorphs or bimorph arrays with a curved cover plate as an active face attached to the top of the bimorphs. The electro-mechanical and electro-acoustic properties of the double amplifier structure and the transducer are investigated in this paper. The displacement of the cover plate of the double amplifier structure can reach millimeter scale with a relatively low driving voltage, which is more than ten times larger than the tip displacement of bimorphs. The sound pressure level (SPL) of the transducer can be larger than 90dB (near field) in the frequency range from 50 to 1000Hz and be larger than 80dB (far field) from 200Hz to 1000Hz, with the largest value more than 130dB (near field). Because of its light weight and panel structure, it has the potential to be used in active noise control.

Keywords: piezoelectric transducers, bimorphs, double amplifier structure, air acoustics, active noise control

1. INTRODUCTION

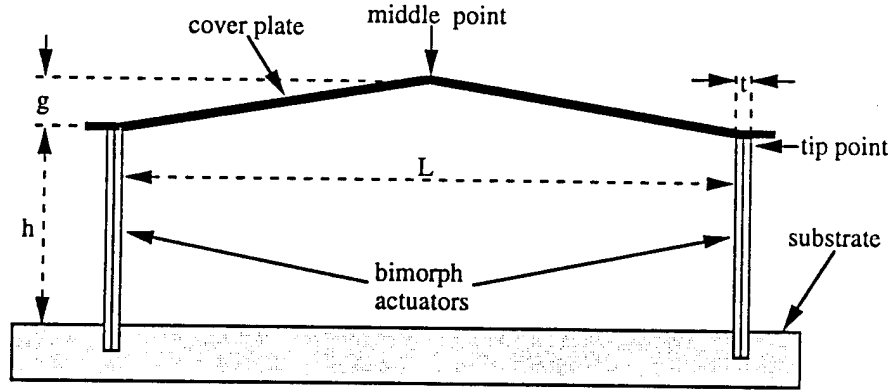
The electromechanical transducers based on piezoelectric materials have been widely used for many decades. However, most of these transducers are used in the areas of ultrasonics and underwater acoustics.¹ It is still difficult to apply piezoelectric materials or devices in air acoustics, especially at low frequency range. On the other hand, because of their unique properties, such as high electromechanical coupling efficiency, the ability of both sensing and transmitting, low loss, light weight and panel structure, it is highly desirable to use piezoelectric transducers at low frequency range and active noise control.²

There are two main problems to be solved to apply piezoelectric transducers in air acoustics and active noise control. One is that the displacement must be much larger than that of the common ceramic actuators because the radiated acoustic energy is proportional to the square of the displacement amplitude.³ Another one is that the acoustic impedance should be matching to air to ensure an effective acoustic flow from the transducer to the medium.

Among all the piezoelectric actuators, bimorph type actuators generate the largest displacement (tip displacement).⁴ However, the displacement is still not large enough to be used in air acoustics at low frequency range. In this paper, a new type of piezoelectric transducer based on the idea of bimorph-based double amplifier structure is presented. The displacement generated by the double amplifier structure can be more than ten times larger than the tip displacement of bimorphs. The acoustic impedance matching between the transducer and air can be obtained by carefully choosing the cover plate (active face) materials and its geometric configurations. As a result of these new designs, the transducer is promising to be used in active noise control as a sound transmitter.

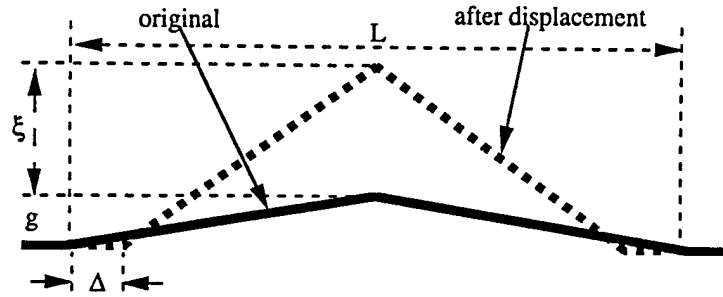
2. DESIGN PRINCIPLES

The basic configuration of the bimorph-based double amplifier structure is shown in Fig. 1. The structure mainly consists of two parallel bimorphs with a curved (triangle shape) cover plate as an active face attached to the top of the bimorphs. Higher displacement is achieved by changing the tip displacement of bimorphs to a flexural motion of the cover plate. That is, when the bimorphs vibrate horizontally, the cover plate vibrates vertically with larger amplitude. Fig. 1(b) is the schematic of the displacement of the cover plate and bimorph actuators. From the geometric consideration, the vertical displacement of the middle point on the cover plate can be described as:



L: distance between bimorphs h: height of bimorphs
t: thickness of bimorphs g: height of the cover plate

(a) Cross section of the double amplifier structure



Δ : tip displacement of bimorphs ξ : displacement of the middle point of the cover plate

(b) Displacement of the double amplifier structure

Fig. 1. Configuration of the Bimorph Based Double Amplifier Structure

$$\xi = \sqrt{g^2 + L \cdot \Delta} - g \quad (1)$$

where ξ is the displacement of the middle point;
g is the height of the cover plate;
L is the distance between bimorph actuators;
 Δ is the tip displacement of bimorphs.

We define the amplification factor of the displacement as:

$$\alpha = \frac{\text{middle point displacement of cover plate}}{\text{tip displacement of bimorph}} = \frac{\xi}{\Delta}$$

so,

$$\alpha = \frac{\sqrt{g^2 + L \cdot \Delta} - g}{\Delta} \quad (2)$$

If $L \cdot \Delta \ll g^2$, then

$$\sqrt{g^2 + L \cdot \Delta} \approx g \left(1 + \frac{L \cdot \Delta}{2g^2} \right) = g + \frac{L \cdot \Delta}{2g}$$

Therefore,

$$\xi = \frac{L \cdot \Delta}{2g} \quad (3)$$

and,

$$\alpha = \frac{\xi}{\Delta} \approx \frac{L}{2g} \quad (4)$$

This is why the displacement of the cover plate is much larger than the tip displacement of bimorphs.

Shown in Fig. 2 is the transducer constructed from the bimorph-based double amplifier structure. Instead of two parallel bimorphs, two parallel bimorph arrays are used here and the cover plate is fixed on the top of the bimorph arrays so that larger radiation area is obtained. Loudspeaker paper is chosen as the cover plate because of its excellent mechanical and acoustic properties and light weight. The other two lateral faces were also sealed by loudspeaker papers so that the transducer can work effectively as a monopole source.⁵

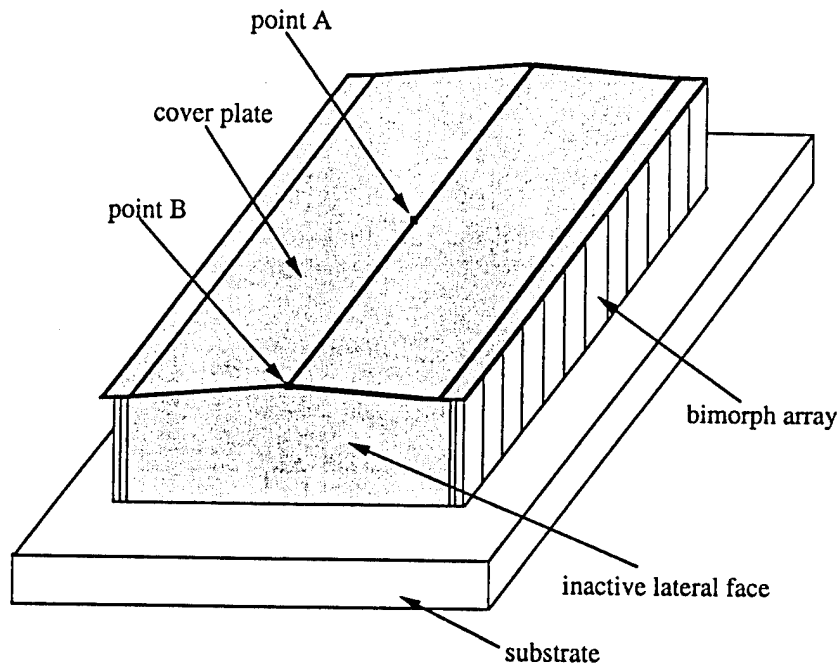


Fig. 2. Configuration of the Double Amplifier Transducer

3. SAMPLE PREPARATION AND MEASUREMENT TECHNIQUE

Bimorph actuators can be operated in series (the poling directions of the two piezoelectric plates are opposite) or in parallel (the poling directions of the two piezoelectric plates are consistent) configurations. All the bimorphs used in this paper are in parallel structure. They are made from a kind of PZT 5H type piezoelectric material⁶ and the dimensions are 20.0mm X 7.0 X 1.0mm. The loudspeaker paper is from Nu-Way Company with the thickness of 0.56mm.⁷ The experiments were conducted both on the double amplifier structures and the transducer. For the double amplifier structure experiment, the bimorphs are mechanically clamped at one end, and the cover plate is fixed on the top of bimorphs by super glue. The displacement of middle point and tip point are measured by using MTI 2000 Fotonic Sensor⁸ under quistatic and dynamic conditions. Fig. 3 is the schematic drawing of the measurement setup. The resonant frequency of the structure was determined by an HP-4194 Impedance Analyzer. For the transducer study, the bimorph arrays were fixed in the slots on the plastic substrate by super glue. The displacement at the central point (point A in Fig. 2) of the cover plate and at the intersection point of the central line and edge of the cover plate (point B in Fig. 2) was measured. The sound pressure level of the transducer was also studied in an anechoic chamber by using B & K 4135 type condenser microphone.⁹ In measurement, the

Don't forget to check the voltage and current levels to be not too high. The measurement is done in the air.

transducer is baffled in a large rigid plane and the measurement points are on the axis which goes through the central point and perpendicular to the substrate as shown in Fig. 4. The distances between the measurement points and the central point are 5.0mm and 1.0m respectively. The former situation is called near field and the latter is far field.¹⁰

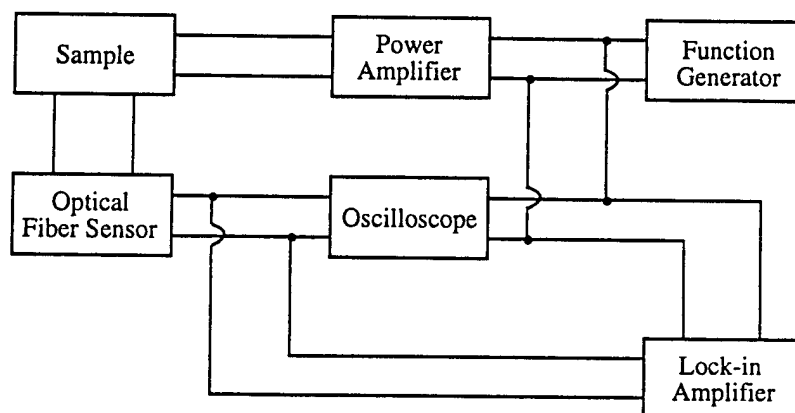


Fig. 3. Schematic Drawing of the Displacement Measurement Setup

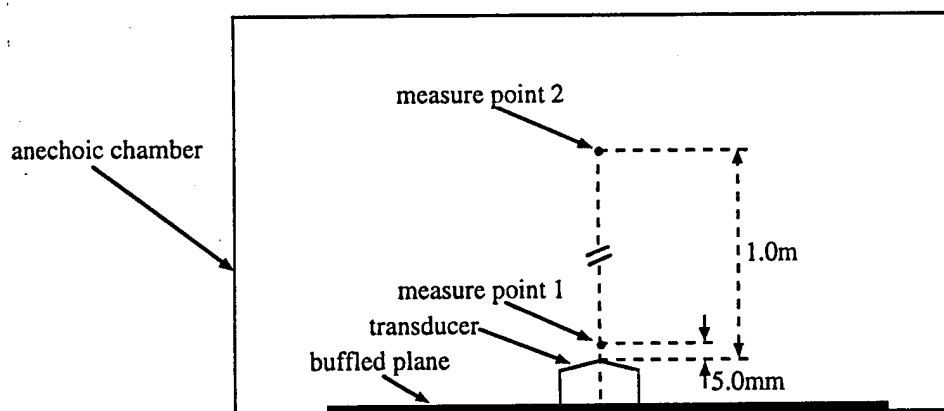


Fig. 4. Schematic Drawing of Sound Pressure Level Measurement Setup

4.RESULTS AND DISCUSOINS

4.1. Displacement and resonant frequency of the double amplifier structures

The dependence of the middle point displacement and amplification factor on the height of the cover plate was evaluated under quistatic condition (driving frequency = 1Hz) for the double amplifier structures with $L = 50.0\text{mm}$ and 60.0mm (see Fig. 1) respectively, and the results were presented in Fig. 5. As the height of cover plate g decreases, the middle point displacement increases first, and then decreases. The largest displacement was obtained when the distance between bimorphs was 50mm and the height of cover plate was 1.0mm . The largest displacement can reach $450\mu\text{m}$ (0.450mm) with a driving voltage of 100V (peak-peak value). Fig. 5 also reveals that the amplification factor always increases as the height of the cover plate is reduced. The amplification factor can reach more than ten easily. When the driving voltage is 100V (peak-peak value), the tip displacement of the bimorphs without loading is $37.63\mu\text{m}$, which is called free tip displacement.¹¹ Hence the middle point displacement can be more than ten times larger than the free tip displacement of the bimorphs. Fig. 6 shows the

displacement of the middle point as a function of the driving voltage. The displacement of the middle point increases almost linearly with the driving voltage. It is expected that the displacement of the middle point can reach about 1.5mm when the driving voltage is raised to 300V (peak-peak value) or 110V (rms value).

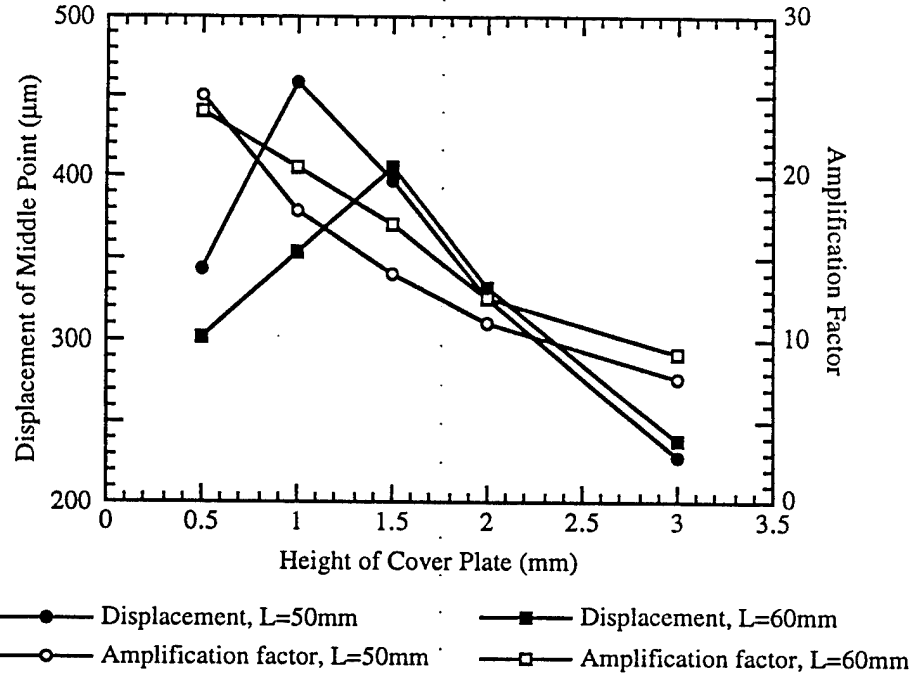


Fig. 5. Displacement and Amplification Factor of the Double Amplifier Structure ($f=1\text{Hz}$, $V_{p-p}=100\text{V}$)

Equations (1) to (4) show that the middle point displacement should always increase as the cover plate height is reduced, so does the amplification factor. However, when the height of the cover plate decreases, the effective loading of the cover plate will increase, and a larger force is needed to push the cover plate. The relationship between the generated force and tip displacement of bimorph can be described as:¹²

$$F = \frac{Y_c t^3 w}{4h^3} \left(\frac{3d_{31} h^2 E}{2t} - \Delta \right) \quad (5)$$

where Y_c is Young's modules of ceramic material;
 d_{31} is piezoelectric constant of ceramic material;
 w is width of bimorph;
 E is applied electric field.

When a larger force is needed, the tip displacement of bimorph will reduce. Therefore, when the height of cover plate decreases, there are two competing factors which influence the middle point displacement of the cover plate. One is that the middle point displacement will increase according to the geometric relationship, so does the amplification factor. Another one is that the tip displacement of bimorph will decrease, which will reduce the middle point displacement. Therefore, there is an optimum point where the maximum value of the middle point displacement is obtained. However, the amplification factor will always increase when the cover plate height decreases as long as the geometric relationship is valid. The similar situation will happen when the distance between the bimorphs is changed.

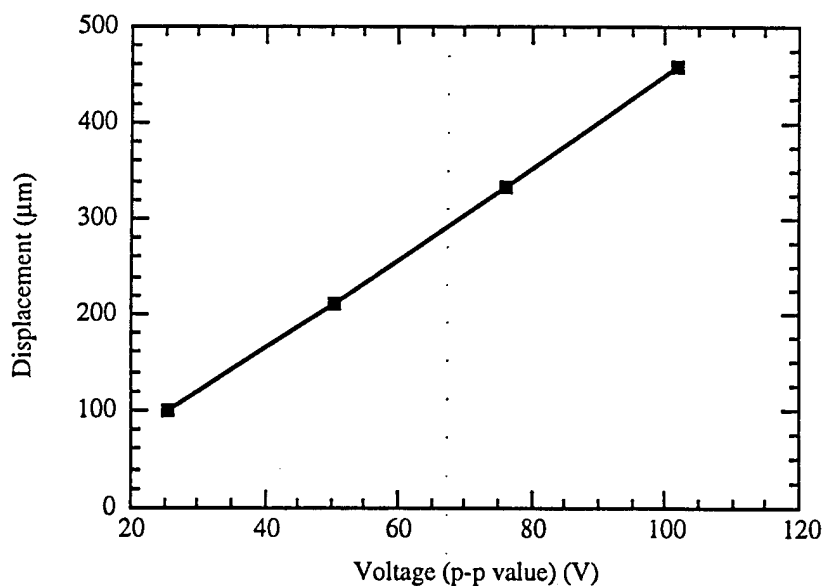


Fig. 6. Displacement of the Middle Point as a Function of Driving Voltage ($f=1\text{Hz}$, $L=50\text{mm}$, $g=1.0\text{mm}$)

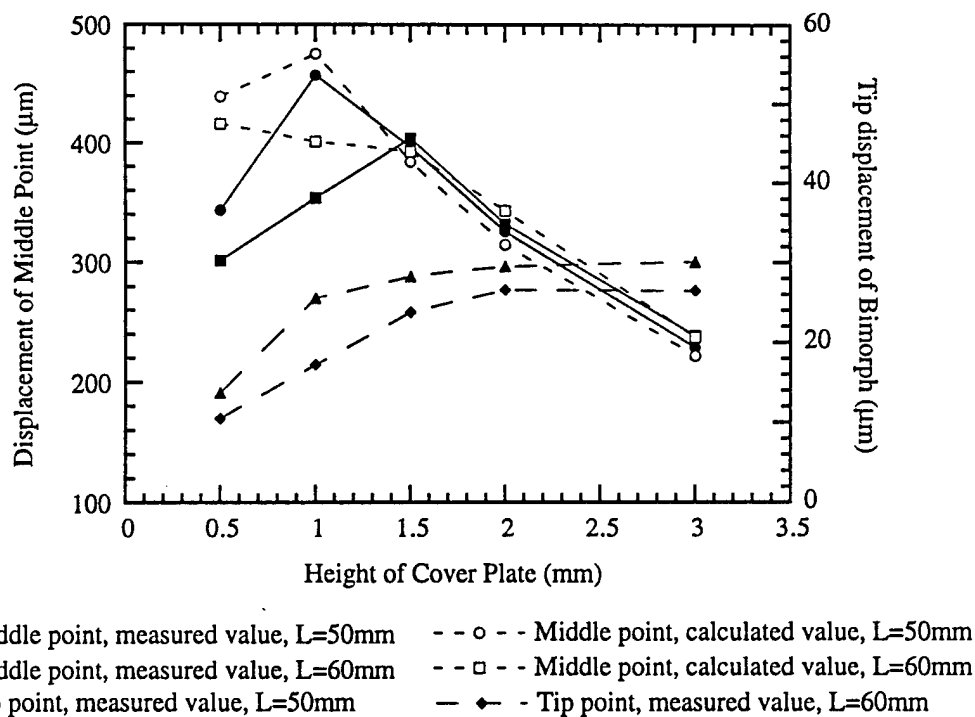


Fig. 7. Displacement of the Double Amplifier Structure ($f=1\text{ Hz}$, $V_{p-p}=100\text{V}$)

Besides these two factors, there is an additional factor should be considered is the buckling of the cover plate. If the buckling of the cover plate happens, the geometric relationship (equation (1)) will not be hold, and the middle point displacement of cover plate will become smaller.

The tip displacement of bimorphs, the measured displacement of the middle point, and the calculated displacement of the middle point according to equation (1) are presented in Fig. 7. The tip displacement decreases rapidly when g is below 1.0mm for $L = 50.0\text{mm}$ and 1.5mm for $L = 60.0\text{mm}$, which results in a decrease in the middle point displacement. When g is larger than 1.0mm for $L = 50\text{mm}$ and 1.5mm for $L = 60\text{mm}$, there is no buckling of the cover plate since the calculated middle point displacement is nearly the same as the measured value. Below these values buckling of the cover plate occurs.

The dependence of the resonant frequency on the height of the cover plate is shown in Fig. 8 for $L = 50.0\text{mm}$ and 60.0mm . For this amplifier structure, the cover plate can be considered as an effective mass loading attached on the top of the bimorph beams, which reduces the resonant frequency of the bimorph beams.¹³ As the height of the cover plate decreases and the distance between bimorphs increases, the effective loading of the cover plate increases, resulting in a decrease of the resonant frequency. This is consistent with the experimental results.

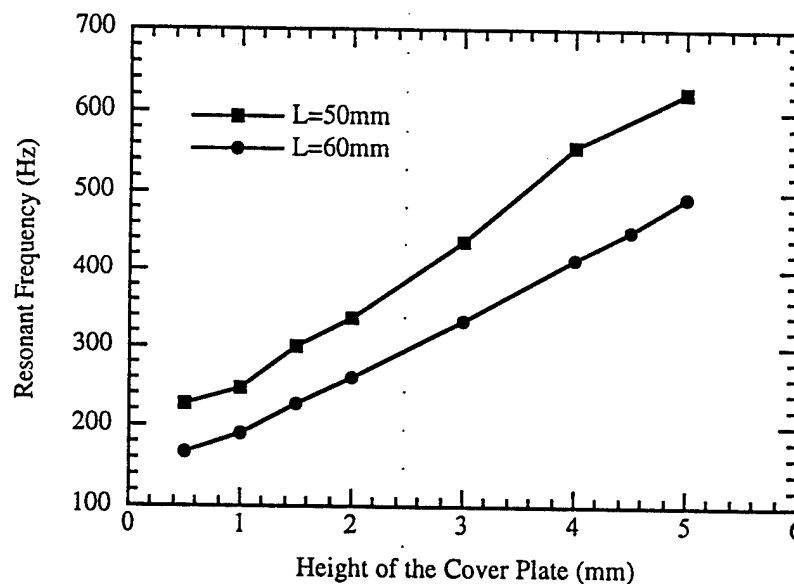


Fig. 8. Resonant Frequency of the Double Amplifier Structure

The relationship between the displacement and frequency is shown in Fig. 9 for $L = 50.0\text{mm}$, $g = 1.0\text{mm}$. From the comparison of the tip displacement of bimorphs, the calculated displacement of middle point, and the measured displacement of middle point, it can be concluded that the cover plate can keep its shape from buckling during vibration in the frequency range up to about two times of the resonant frequency, that is, the transducer can work effectively in the frequency range up to the two times of the resonant frequency.

4.2. Displacement and sound pressure level of the double amplifier transducer

Based on the experimental results and analyses of the double amplifier structures, the bimorph-based double amplifier transducer was constructed. The dimensions of the transducer are:

- the distance between the bimorphs $L = 50.0\text{mm}$;
- the height of the cover plate $g = 3.5\text{mm}$;
- the width of the bimorph arrays $W = 60.0\text{mm}$;
- the height of bimorphs $h = 18.0\text{mm}$.

Therefore, this transducer can be expected to work effectively up to 1000 Hz, which is the frequency range desirable for the active noise control.

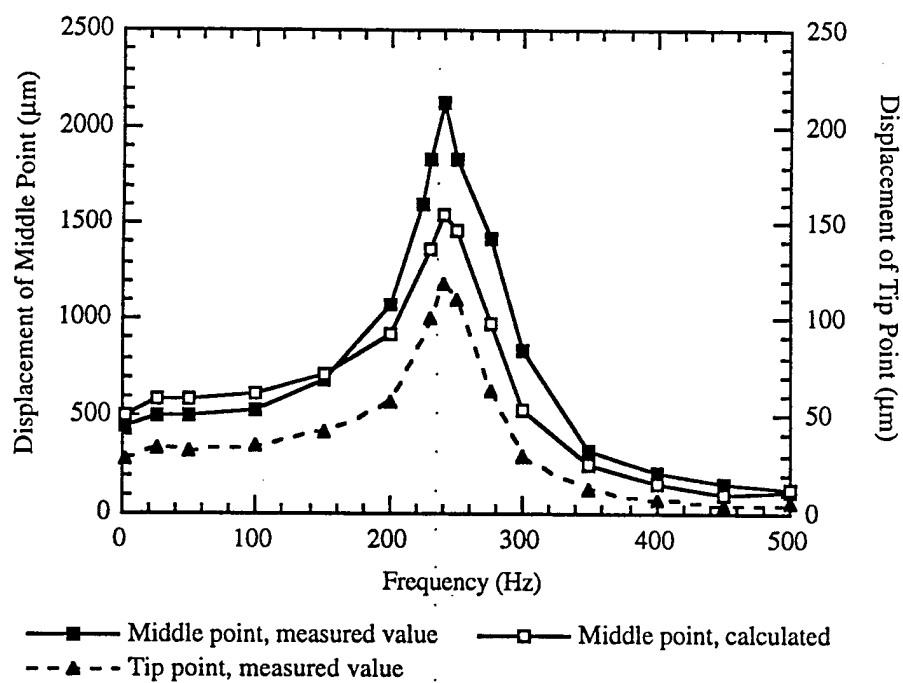


Fig. 9. Dependence of the Displacement on Frequency ($L=50\text{mm}$, $g = 1.0\text{mm}$, $V_{p-p} = 100\text{V}$)

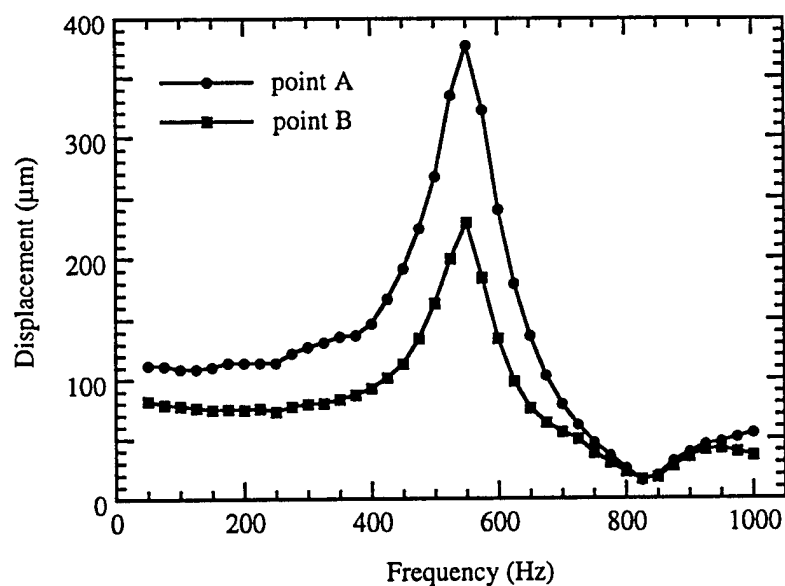


Fig. 10. Frequency Dependence of the Displacement of the Transducer ($V_{p-p} = 100V$)

The dependence of the displacement of the point A and point B of the cover plate (see Fig. 2) on frequency is shown in Fig. 10. Due to clamping effect of the two lateral faces which are made of loudspeaker paper and are inactive, and due to the loading effect of the air in the closed chamber of the transducer, the displacement of point A is some smaller than that of the middle point displacement of the double amplifier structure with the same L and g values, and the displacement of point B is smaller than that of point A, but the displacement of the cover plate is still much larger than the tip displacement of bimorphs. The height of the peak in the resonant frequency also becomes weaker and smooth due to these clamping and loading effects.

The frequency dependence of the sound pressure level (SPL) was presented in Fig. 11. The SPL of the near field can be larger than 90dB in the frequency range from 50 to 1000Hz, and the largest value can reach more than 130dB. For the far field, the SPL can reach more than 80dB when the frequency is higher than 200Hz, which is suitable for active noise control. Larger SPL value can be easily obtained by increasing the width of the bimorph arrays. Another approach to get larger SPL value is to construct the transducer with multi-double amplifier structure, as shown in Fig. 12.

5. CONCLUSIONS

Bimorph-based double amplifier structure and the transducer based on this structure have been constructed and studied in this paper. It was demonstrated that with relatively low voltage, the displacement of the active face can reach millimeter scale, which is more than ten times larger than the tip displacement of bimorphs. The sound pressure level of the piezoelectric transducer can be larger than 90dB (near field) between 50 to 1000Hz and 80dB (far field) between 200 to 1000Hz. And the largest value can reach 130dB (near field). Because of its light weight and panel structure, it is potential to use this new piezoelectric air transducer in active noise control.

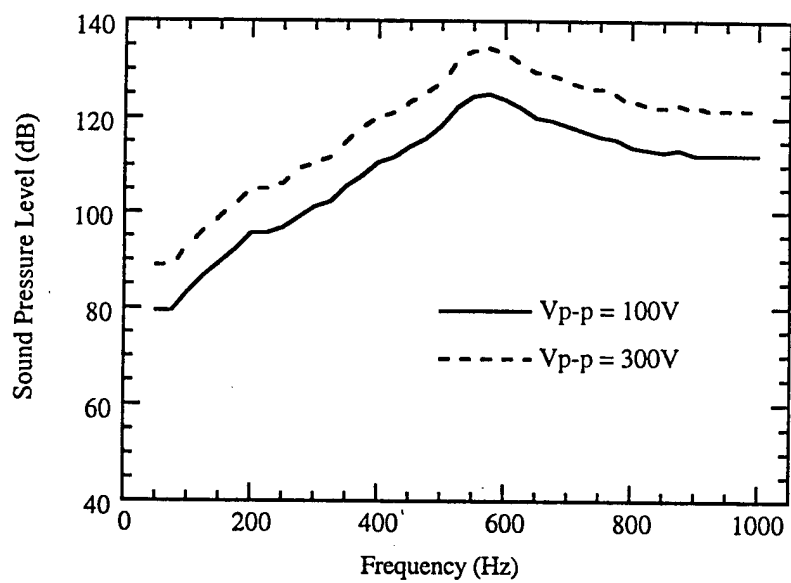
As the first result of the bimorph-based double amplifier transducer, further improvements in transducer performance are expected using improved materials and design. Instead of bimorph, some other ceramic actuators such as unimorph or monomorph can also be used in the double amplifier structure and transducer design.

6. ACKNOWLEDGMENT

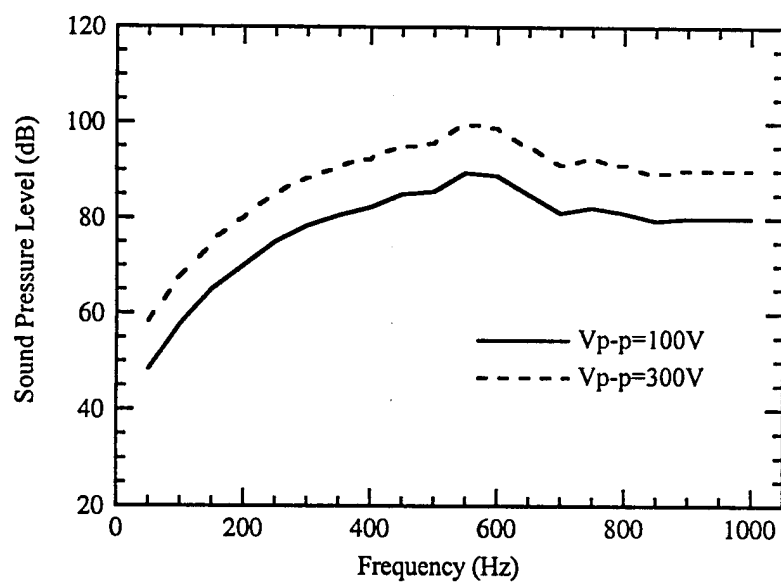
This work was supported by the Office of Naval Research under the contract No. N00014-94-1-1140.

7. REFERENCES

1. L. E. Cross and K. H. Hardtl, "Ferroelectrics," in *Piezoelectricity*, Ed. by C. Z. Rosen, B. V. Hiremath and R. E. Newnham, pp.1-31, American Institute of Physics, New York, 1992.
2. E. K. Dimitriadis and C. R. Fuller, "Active control of sound transmission through elastic plates using piezoelectric actuators," *AIAA Journal*, Vol. 29, pp. 1771-1777, 1991.
3. L. L. Beranek, *Acoustics*, Chapter 4, the Acoustical Society of America, New York, 1993.
4. K. Uchino, *Piezoelectric/Electrostrictive Actuator*, Chapter 4, Morikita Publishers, Tokyo, Japan, 1986.
5. D. E. Hall, *Basic Acoustics*, Chapter 11, Harper & Row Publishers, New York, 1987.
6. PZT 3203HD Piezoelectric Materials, Motorola Company, Albuquerque, New Mexico.
7. NW 2200A Loudspeaker Paper, Nu-Way Speaker Products, Antioch, Illinois.
8. MTI-2200 Fonic Sensor, MTI Instruments, Latham, New York.
9. Cartage Type 4135 1/4" Condenser Microphone, Bruel & Kjaer Instruments, Marlborough, Massachusetts.
10. L. E. Kinsler, A. R. Frey, A. B. Coppens and J. V. Sanders, *Fundamentals of Acoustics*, 3rd Edition, Chapter 8, John Wiley & Sons, New York, 1982.
11. J. K. Lee and M. A. Marcus, "The deflection-bandwidth product of poly(vinylidene fluoride) benders and related structures," *Ferroelectrics*, Vol. 32, pp. 93-101, 1981.
12. J. G. Smits, S. I. Dalke and T. K. Cooney, "The Constituent equations of piezoelectric bimorphs," *Sensors and Actuators A*, Vol. 28, pp. 41-61, 1991.
13. D. J. Gorman, *Free Vibration Analysis of Beams and Shafts*, Chapters 1 and 2, John Wiley & Sons, New York, 1975.



(a) Near field



(b) Far field

Fig. 11. Sound Pressure Level of the Transducer

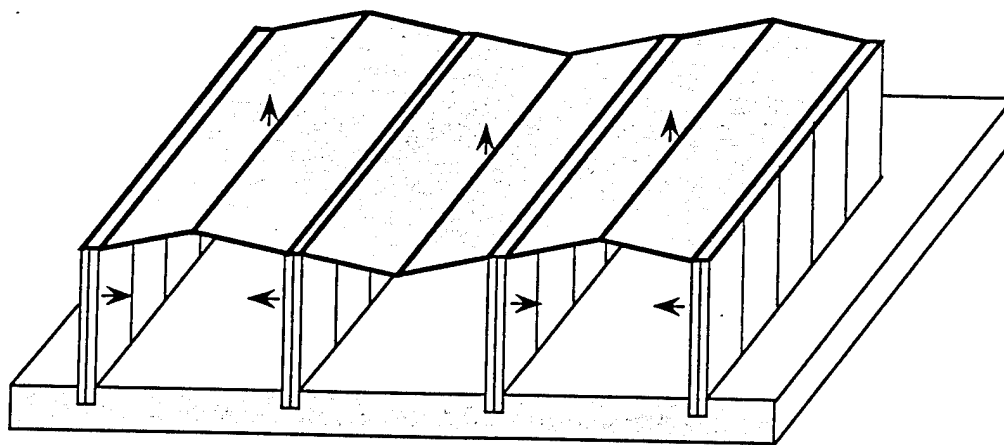


Fig. 12. Configuration of the Transducer Constructed from Multi-Double Amplifier Structure (the arrows represent the moving direction)

APPENDIX 51

UNDERWATER ACOUSTIC ABSORPTION BY COLLOCATED SMART MATERIALS

S. KUMAR, A. S. BHALLA and L. E. CROSS

**Materials Research Laboratory, The Pennsylvania State University
University Park, PA, USA**

Abstract: Collocated smart structures provide the most effective technique of influencing the stimuli. Such systems can also be used for absorbing underwater acoustic waves. A collocated system is designed by mounting piezoelectric sensor on a multilayer PZT discs stack. Using PZT sensor for narrowband response and modified lead titanate sensor for broadband response, the effectiveness of these smart structures in absorbing acoustic waves is experimentally determined by using an acoustic tube.

INTRODUCTION

It has been shown that collocated smart structures can be used in active vibration control and removal of energy from the vibration field [1,2]. These collocated systems for vibration control are designed by directly mounting a piezoelectric sensor on multilayer stack of piezoelectric (generally PZT) thin discs. The piezoelectric thin discs in the actuator are mechanically in series and electrically in parallel so that displacements of each disc adds up. If the sensor voltage, which develops due to pressure change on the sensor surface, is amplified, inverted in phase and applied to the actuator, the dynamic compliance of the sensor-actuator composite can be controlled and used in active vibration control. The material properties play a crucial role in the designing of the systems. For example to obtain a narrowband response from a simple collocated system, a PZT sensor can be used. But for broadband response, there are restrictions on choice of sensor material. A modified lead titanate sensor is required to obtain broadband response from a simple collocated system. In these systems there is a very strong field coupling between the sensor and the actuator and therefore they are quite difficult to design because of stability considerations. However, they provide the most effective technique of controlling the field since sensing and actuating takes place at the same point. It should also be pointed out that

by moving the sensor surface by electronic feedback to the actuator, the acoustic impedance of the smart material (sensor-actuator composite) can be controlled. This presents the opportunity of using these smart systems for underwater acoustic absorption and therefore making them useful in many applications. In this work we investigate the underwater acoustic absorption by collocated smart materials.

Experimental

Figure 1 shows the collocated smart system which has been used to absorb energy from underwater acoustic waves. For this investigation, an acoustic tube experiment was set up as shown in fig. 2. A 3 feet long aluminum tube with 3 inch internal diameter and 0.5 inch wall thickness was used as an acoustic tube.

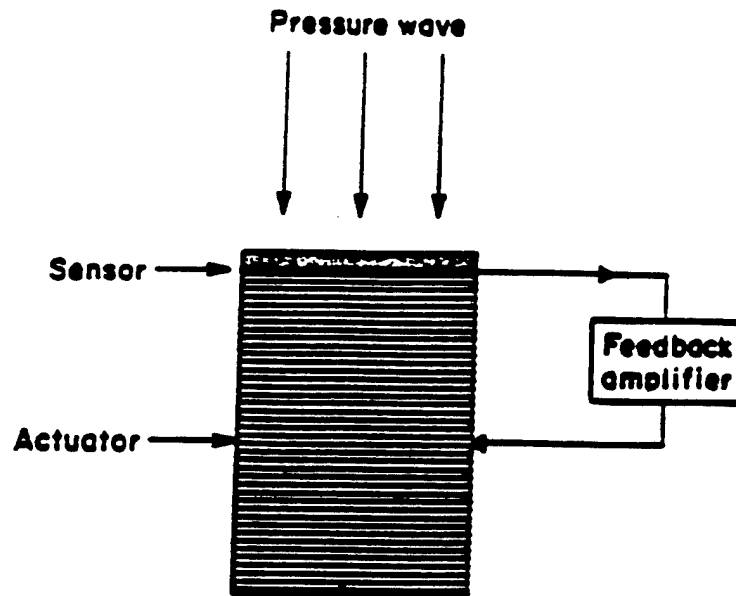


FIGURE 1. Collocated Smart Material.

Standard navy transducer J9, which operates at low frequencies, was placed on one side of the acoustic tube and a cell as shown in fig. 3, was designed to house sensor-actuator combination. The cell was placed on the other side of the acoustic tube. A solid aluminum cone was joined to the sensor in the cell to increase the effective area of the sensor. The cell was filled with castor oil so that the gap between the rubber diaphragm and the aluminum cone contain castor oil which would provide acoustic coupling between the diaphragm and the cone. Because of air bubble problems the cell design was changed to remove castor oil. The rubber diaphragm was glued directly to the aluminum cone.

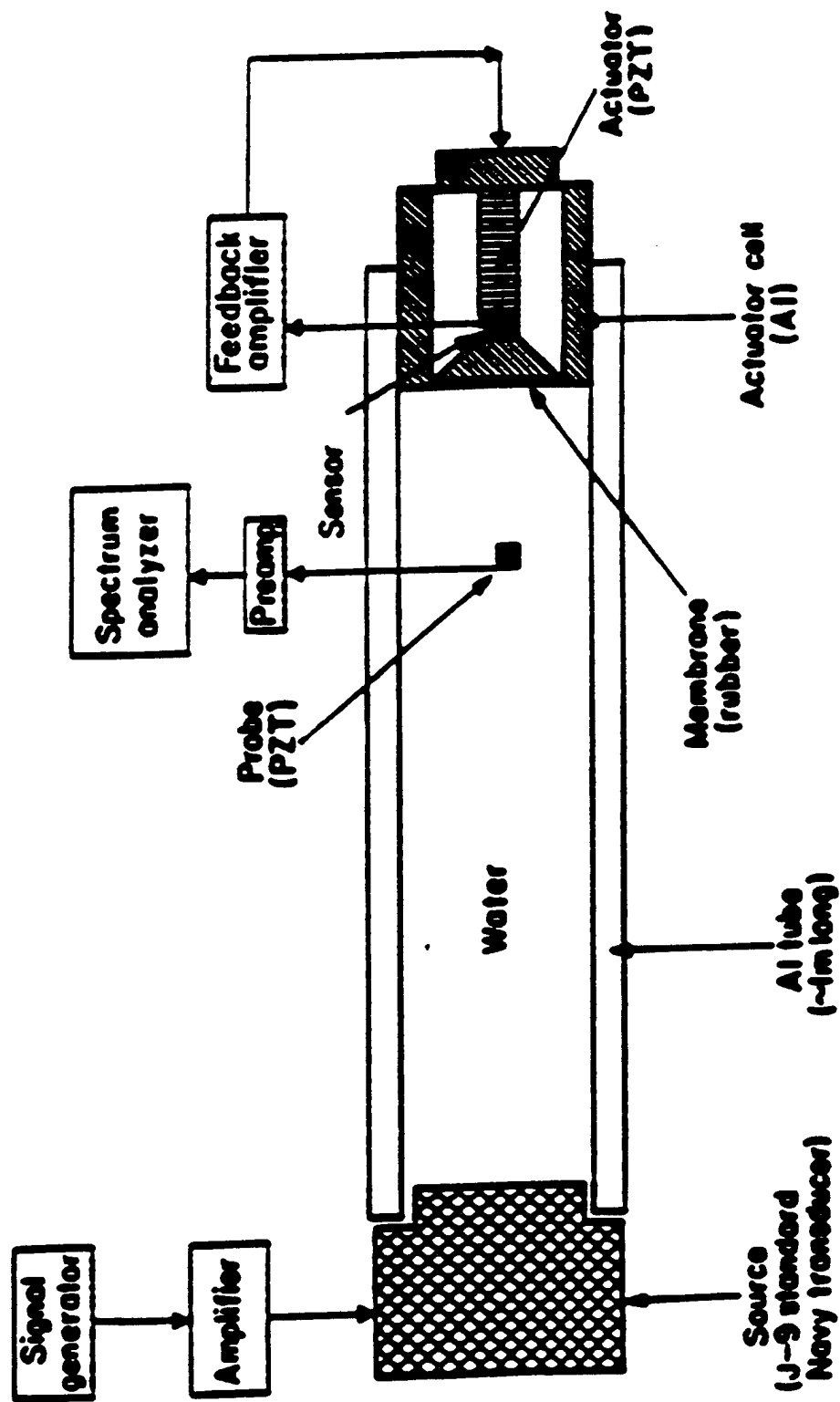


FIGURE 2. Acoustic tube set up for underwater acoustic wave absorption measurement.

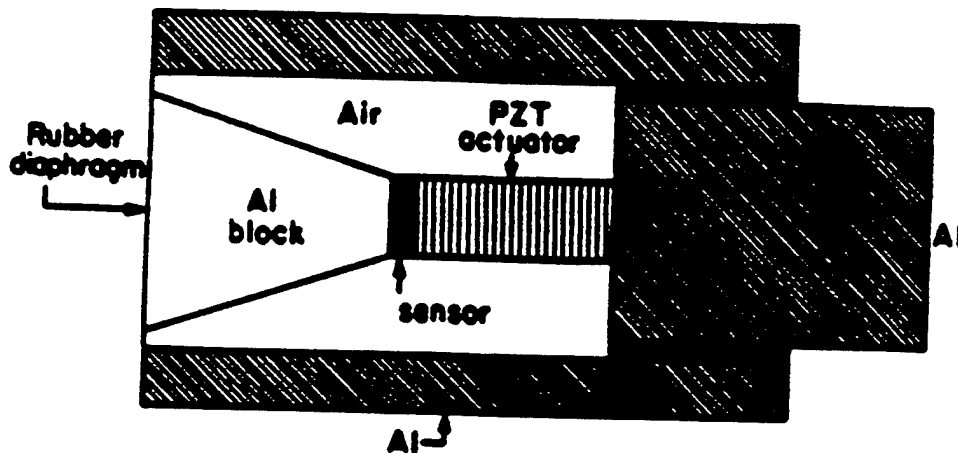


FIGURE 3. Cell containing collocated sensor actuator combination. A low noise preamplifier is housed in a cavity in the aluminium block behind the actuator.

Narrowband Response

In this case a PZT disc was used as a sensor in sensor-actuator smart composite and a high Q bandpass filter was placed in the feedback circuit. Assuming that diameter of the tube is small compared to the wavelength so that plane wave propagates in the tube, the pressure as a function of length in the acoustic tube can be calculated by solving the well known Helmholtz equation and applying the appropriate boundary conditions. This assumption is clearly valid for the low frequencies used in the experiment. In the experimental set up, provision was made to monitor the pressure along the axis of the tube by placing very small pressure sensors through very small holes in the wall of the tube. The acoustic tube was lowered in the water tank and filled with water so that whole acoustic tube with J9 and cell on its sides was submerged in the water. Care was taken to remove all air bubbles from the acoustic tube. The signal from the sensor was amplified, passed through the bandpass filter which was tuned to the J9 frequency, inverted in phase and applied to the actuator. The effect of the sensor-actuator combination on the pressure along the axis of the tube could not be seen due to small applied voltages to the actuator. Alternatively, the sensor voltage was monitored with and without feedback applied to the actuator. The frequency of the standard transducer J9 was changed and the bandpass filter in the feedback circuit was tuned to the same frequency. Figure 4 shows the effect of feedback on the sensor voltage. The reduction in sensor voltage when feedback was applied implies that the smart material partially absorbed the incident acoustic wave.

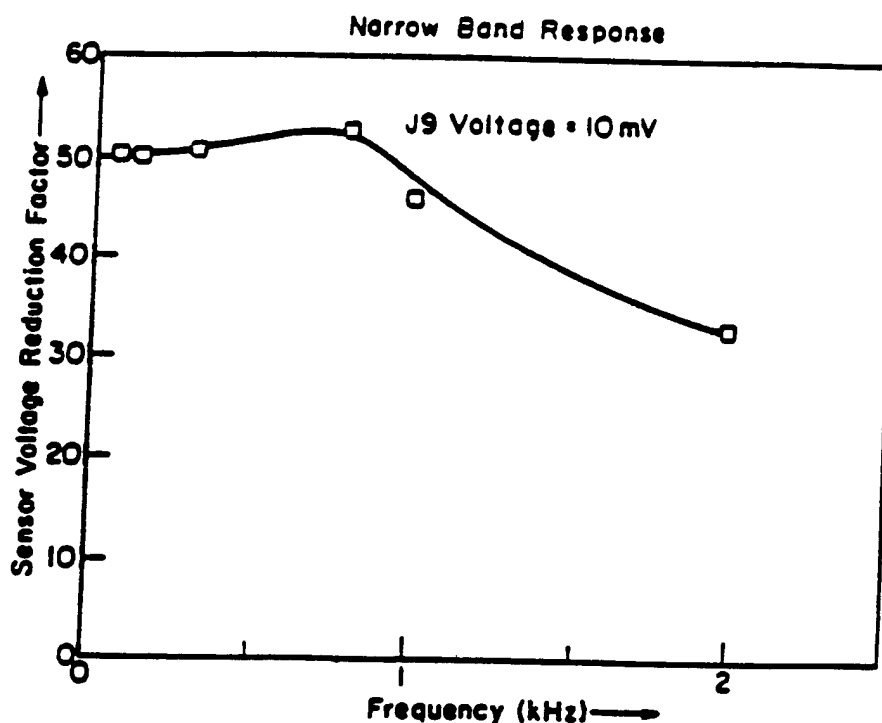


FIGURE 4. Narrowband response of the collocated sensor-actuator combination for the under water acoustic absorption.

Broadband Response

The PZT sensor was replaced with modified lead titanate sensor in the cell and the high Q bandpass filter was removed from the feedback circuit. The feedback circuit used in this system is described elsewhere [2]. The sensor voltage was monitored with and without feedback to the actuator. The frequency of transducer J9 was changed and sensor voltage again monitored. Figure 5 shows the broadband response of the smart system.

RESULTS AND DISCUSSION

Figure 4 shows the narrowband response in which the ratio of sensor voltage without and with feedback applied to the actuator as function of frequency is plotted. Higher reduction factor implies higher effectiveness of the smart system since the sensor voltage is a measure of acoustic impedance of the smart system. The reduction factor obtained is about 50 at low frequencies dropping to about 35 around 2 kHz. The drop in sensor voltage reduction factor is expected since response time of the actuator comes into picture.

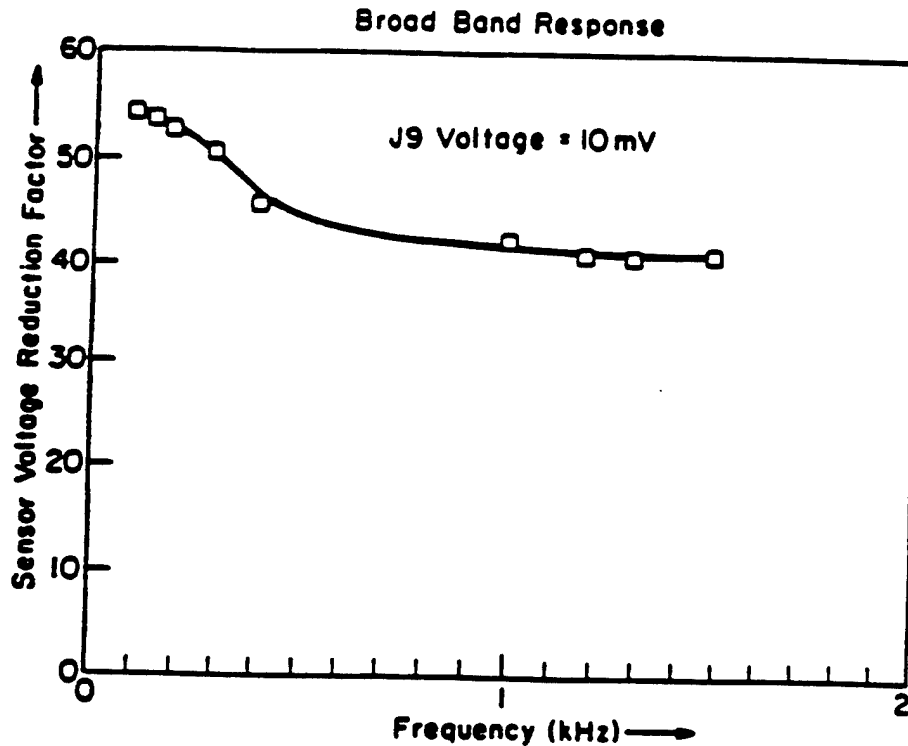


FIGURE 5. Broadband response of the collocated sensor-actuator combination for the underwater acoustic absorption.

The broadband response of the smart system is obtained without using a higher order filter in the feedback circuit. This design is possible because of low planar coupling coefficient of modified lead titanate. Again the sensor voltage reduction factor is seen to be 55 at low frequencies dropping to 40 at 1.5 kHz. This is a broadband response of the smart system since there is no bandpass filter in the feedback circuit and only J9 frequencies are changed keeping the J9 voltage same at each frequency. These results for narrowband and broadband response show that it is possible to control the acoustic impedance of the smart structures and remove energy from the incident acoustic waves.

REFERENCES

1. S. Kumar, A. S. Bhalla, L. E. Cross. " Smart Ceramics for Acoustic and Vibration Control." *J. Intelligent Material Systems and Structures*, Vol. 5, No. 5, 678-682 (1994).
2. S. Kumar, A. S. Bhalla, L. E. Cross. " Broadband Vibration Control Using Smart Ceramics." *J. Intelligent Material Systems and Structures*, Vol. 5, No. 5, 673-677 (1994).

APPENDIX 52

Dynamic Characteristics of Rainbow Ceramics

Catherine Elissalde and Leslie Eric Cross*

Materials Research Laboratory, The Pennsylvania State University, University Park, Pennsylvania 16802

The piezoelectric resonance behavior of end-clamped bimorph structures made from the rainbow monolithic ceramic have been evaluated. Thickness, width, width flexure, and length bending modes have been identified and measured. Using a very crude model in which the cermet component of the rainbow is assumed to have the same density \times elasticity product as the bulk, surprisingly good agreement is obtained between observed and calculated frequency behavior. By appropriate processing it is possible to delaminate the bimorph, and work is now in progress to measure the properties of the two separate phases so that a proper composite resonator model may be developed.

I. Introduction

PIEZOELECTRIC and electrostrictive materials are used in a wide range of applications. Especially smart materials have aroused increasing interest. To improve the performance of piezoelectric materials (higher strain or higher displacement), new structures such as flexensional structures or "moonie" are developed.¹ Recently a new type of monolithic ceramic bender, known as "rainbow" (reduced and internally biased oxide wafer), was developed by Haertling.² This material presents a number of advantages and in particular the possibility to generate very high displacements.² The piezoelectric material response depends not only on its piezoelectric properties but also on elastic and dielectric parameters. Elastic bodies show resonances, and the resonance method is convenient for evaluating such properties. In this way, the purpose of this work is to study the resonant behavior of rainbow materials. A good

knowledge of the frequency characteristics is, indeed, essential for many types of applications.

II. Experimental Procedure

(1) Sample Preparation

Rainbow piezoelectric PZT (lead zirconate titanate) materials were prepared using a conventional mixed oxide process. During the processing, an additional important step for the rainbow is the high-temperature chemical reduction of one surface of the wafer.² The thickness of the reduced layer is 1/3 to 1/2 of the sample thickness. This single-sided reduction introduces a stress in the ceramic and the rainbow becomes a dome-shaped wafer.

The rainbow actuators were supplied by Aura Ceramics, Inc. The dimensions of the initial wafer were the following: 50.8 mm in diameter and 0.76 or 0.38 mm in thickness. A motional diamond saw was used to generate the rainbow cantilever used for our experiments. One end of the sample was then clamped in a plastic support using 5 Minute Epoxy glue, and the other end was free.

(2) Frequency Measurements

Frequency measurements were performed using an HP4194 A impedance/gain-phase analyzer which covers a frequency range of 100 Hz to 40 MHz. A preliminary calibration was conducted (open and short circuit). On account of the initial bent shape of the rainbow and thus because of the high sensitivity of the sample measurement, two different cells were used. Both were connected to a test fixture with the four terminals attached directly to the terminals of the analyzer (BNC connectors). The so-called "soft cell" (SC) consisted of an HP16047 C test fixture. The so-called "hard cell" (HC) was made up of a clip mounted on an HP16047 A test fixture. For each cell, the contact was near the clamped end of the rainbow cantilever.

The reduced layer on the concave side of the rainbow served as one of the electrodes but it was also possible to electrode it

G. H. Haertling—contributing editor

Manuscript No. 192775. Received March 8, 1995; approved June 5, 1995.
*Member, American Ceramic Society.

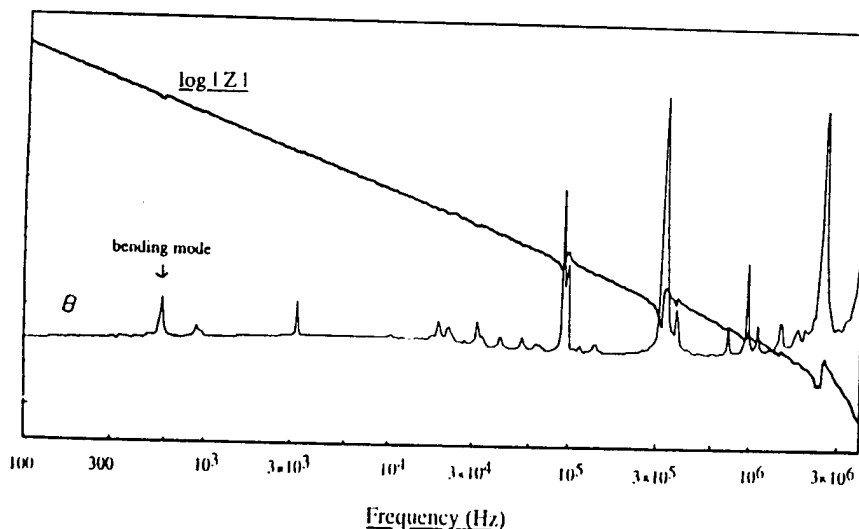


Fig. 1. Impedance spectrum of rainbow cantilever ($L = 25.5$ mm, $w = 5$ mm, $t = 0.76$ mm).

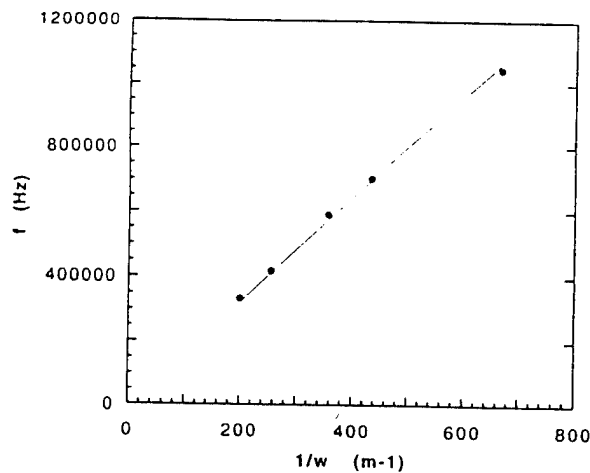


Fig. 2. Resonant frequency of lateral extensional mode vs width ($t = 0.76$ mm): (●) f_{expt} , (—) f_{calc} .

to ensure a good contact. In fact, the results of these impedance measurements were not affected if only the top side or if both sides were electroded.

Temperature measurements were performed using a metallic cell, a hot plate PC-35, and a model DRC 80-C temperature controller.

III. Results

(1) Resonance Modes

Four resonant modes were observed in the rainbow cantilever with one end clamped. The resonances appeared in the frequency range 100 Hz to 4 MHz. As an example, Fig. 1 shows the impedance spectrum obtained. The lowest resonant mode is the bending mode. The value of the corresponding resonant frequency depends on both length and thickness. At high frequency ($f > 2$ MHz), the fundamental thickness mode can be observed. In a conventional plate thickness resonance, the frequency of the fundamental is given by

$$2f_p t = \sqrt{\frac{C_{11}^D}{\rho}} \quad (1)$$

where f_p is the parallel resonance frequency, t the plate thickness, ρ the density ($\rho = 7.5 \times 10^3$ kg/m³), and C_{11}^D the elastic stiffness at constant dielectric displacement. For the bimorph

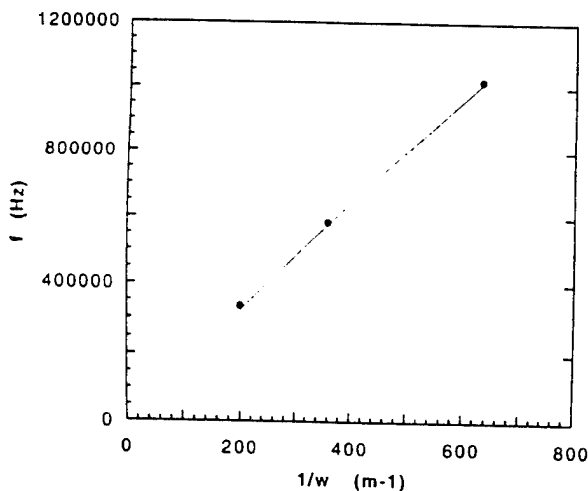


Fig. 3. Resonant frequency of lateral extensional mode vs width ($t = 0.38$ mm): (●) f_{expt} , (—) f_{calc} .

Table I. Measured Resonant Frequency of Rainbow Cantilever¹

	Resonant frequency (Hz)		
	$w = 5$ mm	$w = 2.8$ mm	$w = 1.5$ mm
$t = 0.76$ mm	93 732	274 861	678 755
$t = 0.38$ mm	52 046	158 197	426 264

¹ $L = 19.7$ mm.

structure of the rainbow, there are two materials involved, the unreduced PZT ceramic and the lead-based cermet of the reduced region. As a first approximation, assuming that the cermet behaves elastically like the PZT, the value obtained from experimental results is about $C_{11}^D = 14.4 \times 10^{10}$ N/m² ($f_p = 2.6$ MHz). Such a value is effectively the same as the value for common piezoelectric ceramics.

The frequency of the resonant mode observed close to 3×10^5 Hz in Fig. 1 depends only on the width of the sample and thus corresponds to the lateral extensional mode of the cantilever. Again, assuming the cermet behaves like PZT we could expect the frequency to be given by

$$f_e = 0.5(1/w) \sqrt{\frac{C_{11}^E}{\rho}} \quad (2)$$

where w is the width of the sample, ρ the density, and C_{11}^E the effective elastic constant measured at constant field. The mechanical conditions are $S_1 = 0$, $T_2 = 0$, and $C_{11}^E = 1/S_{11}^E(1 - \sigma^2)$.³

Figures 2 and 3 represent the measured frequency versus width for 0.76 and 0.38 mm thick rainbows. The plots clearly verify the $1/w$ dependence and from the slope a value of $S_{11}^E = 14.94 \times 10^{-12}$ m²/N is obtained assuming that the value of the Poisson ratio, σ , is that of PZT, i.e., $\sigma = 0.36$. Such a S_{11}^E value is in the range expected for softer PZT compositions.

For the resonance observed near 9×10^4 Hz (Fig. 1) the most probable origin is a width bending mode as the frequency scales with both width and thickness, but not with length of the rainbow. Table I lists the measured resonance frequencies as a function of these two controlling dimensions.

(2) Bending Mode

In this study we have focused our attention on the lowest frequency resonant mode, namely the bending mode. Figure 4 shows the measured bending resonant frequency versus the ratio t/L^2 of the cantilever. By changing the length, the frequencies of the other resonant modes remain constant. Again, using the assumption of a homogeneous ceramic, the resonant frequency of a cantilever (one end clamped and the other free) can be expressed as

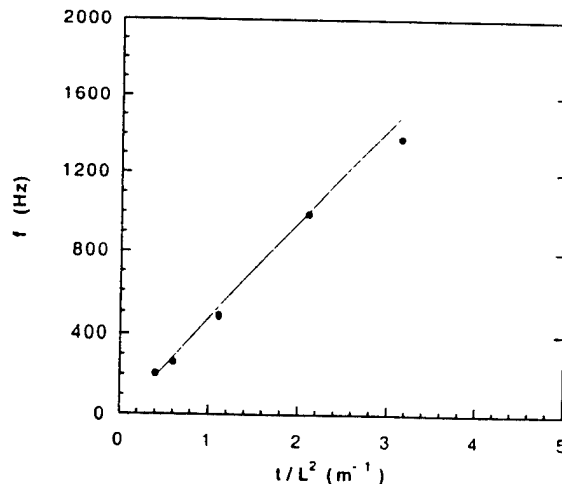
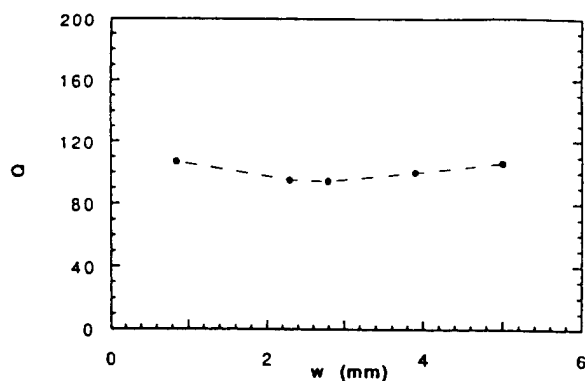


Fig. 4. Resonant frequency of bending mode vs t/L^2 : (●) f_{expt} , (—) f_{calc} .

Fig. 5. Q vs width.

$$f_r = \frac{m^2}{2\pi\sqrt{12}}(t/L^2) \frac{1}{\sqrt{\rho S_{11}^E}}$$

where L is the length of the sample and m the eigenvalue of the resonant mode. The fundamental resonant frequency corresponds to a value of $m = 1.875^4$ and

$$f_r = 0.16(t/L^2) \frac{1}{\sqrt{\rho S_{11}^E}} \quad (3)$$

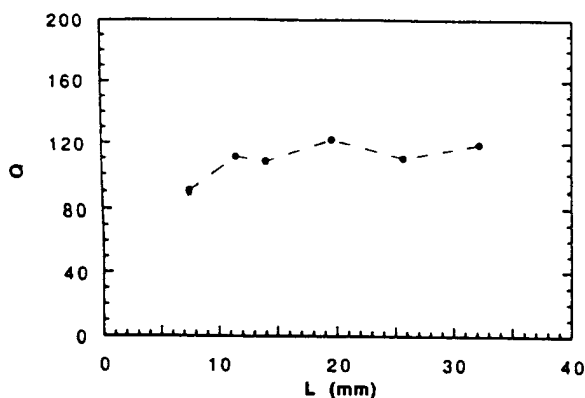
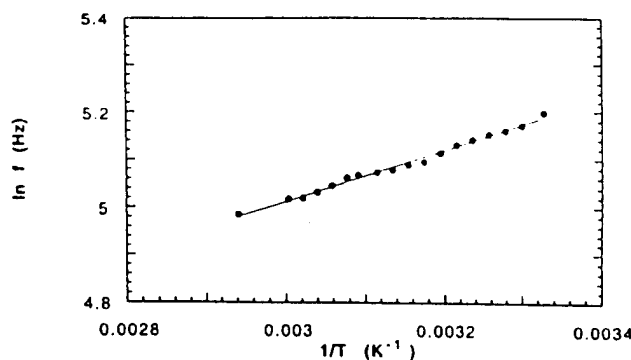
From experimental values, the obtained elastic compliance is about $15 \times 10^{-12} \text{ m}^2/\text{N}$ (Fig. 4). There is not a significant difference using one or the other of the cells. Moreover, it is interesting to notice that even if the reduced layer is not electroded, the measured resonant frequency remains the same.

The sharpness of the impedance-frequency peak in the neighborhood of the resonance is controlled by losses in material. Near the resonance the dominant factor is probably related to mechanical losses. The mechanical quality factor, Q , is thus an important parameter to determine the impedance-frequency characteristics of resonating systems. It also gives an idea of the usable bandwidth. Q is obtained from a determination of the minimum impedance $|Z_m|$ at resonance. Q is given by the relation

$$Q = 1/[4\pi(C_0 + C_1)(f_p - f_s)|Z_m|] \quad (4)$$

where $C_0 + C_1$ is the capacitance measured at low frequency, and f_p and f_s are the frequencies corresponding to the maximum values of the resistance R and the conductance G , respectively. For the rainbow cantilever, the calculated Q value is close to 100. There is not a precise evolution of Q as a function of width and length (Figs. 5 and 6). Considering the restricted sensitivity of the measurement, it is reasonable to conclude in favor of an average value.

In order to complete the characterization of the bending mode in the rainbow cantilever, measurements as a function of

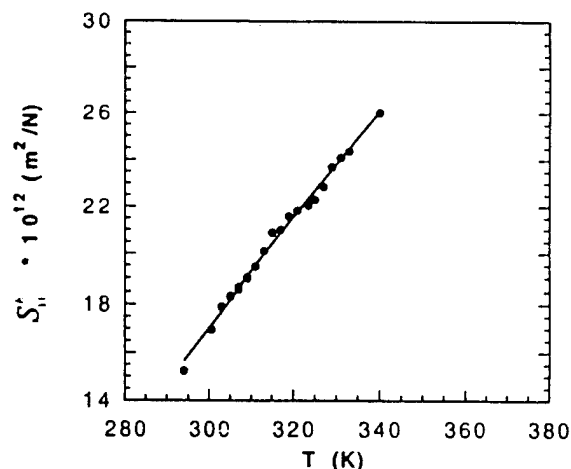
Fig. 6. Q vs length.Fig. 7. Temperature dependence of resonant frequency of the bending mode ($L = 32.27 \text{ mm}$, $w = 5 \text{ mm}$, $t = 0.38 \text{ mm}$).

temperature were performed. The temperature range was from room temperature to 340 K. As an example, the temperature dependence of the frequency of the bending mode is shown in Fig. 7. For all the samples, a decrease of frequency is observed when the temperature increases. The corresponding variation of the resonant frequency can be well fitted using a law-type such as $\ln f = A + B(1/T)$ (A and B are constants). Using Eq. (3) it is also possible to determine the temperature dependence of the elastic compliance. In each case, S_{11}^E increases linearly with increasing temperature. The curve fit is a straight line (Fig. 8).

It is perhaps surprising that the assumption of a homogeneous ceramic in describing the elastic and density properties works very well and is probably adequate for many engineering purposes. Given the fact that oxygen is lost from the ceramic during the reduction process and that the resulting cermet puts the ceramic under compression, one would expect a higher density in this component. Possibly this change is partially compensated by a reduction in stiffness due to the metallic phase. We note that in some cases it is possible to cause a delamination between the ceramic and the cermet phases, so that with the possibility of explaining the elastic and density behavior of the two separate phases, it will be possible to model more exactly the precise behavior of this composite resonator.

IV. Summary

The frequency behavior of rainbow cantilevers has been studied in a large frequency range (100 Hz to 4 MHz). Different modes of resonance have been observed. The stronger corresponds to the thickness mode and appears at high frequency ($f > 2 \text{ MHz}$). At low frequency, the bending mode can be characterized by an impedance-frequency peak with a value of

Fig. 8. Temperature dependence of S_{11}^E ($L = 32.27 \text{ mm}$, $w = 5 \text{ mm}$, $t = 0.38 \text{ mm}$).

Q close to 100. The corresponding resonant frequency increases when the length of the cantilever decreases and is also dependent on temperature. The behavior has been modeled on the simple assumption that the rainbow cermet has elastic and density properties similar to those of the bulk ceramic and there is surprisingly good agreement between measured and predicted properties. The temperature dependence of the resonance suggests that the S_{11}^E has a linear variation with temperature.

Using separated cermet and ceramic elements, measurements are now in progress to characterize exactly the separate phases

so that a more precise composite resonator model can be developed.

References

- ¹Y. Sugawara, K. Onitsuka, S. Yoshikawa, Q. Xu, R. E. Newham, and K. Uchino, "Metal-Ceramic Composite Actuators," *J. Am. Ceram. Soc.*, **75** [4] 996-98 (1992).
- ²G. H. Haertling, "Rainbow Ceramics—A New Type of Ultra-High-Displacement Actuator," *Bull. Am. Ceram. Soc.*, **73**, 93-96 (1994).
- ³T. Ikeda, *Fundamentals of Piezoelectricity*, Oxford University Press, New York, 1990.
- ⁴W. P. Mason, *Electromechanical Transducers and Wave Filters*, D. Van Nostrand Co., New York, 1942.

PROCESSING STUDIES

APPENDIX 53

Tunable Electric Field Processing of Composite Materials

CHRISTOPHER P. BOWEN, THOMAS R. SHROUT, ROBERT E. NEWNHAM AND CLIVE A. RANDALL*
Intercollege Materials Research Laboratory, The Pennsylvania State University, University Park, PA 16802

ABSTRACT: Using the dielectrophoretic effect, it is possible to fabricate polymer/ceramic composite materials in which the filler phase can be manipulated to form a desired microstructure. This is performed via the application of an electric field to a colloidal suspension consisting of a filler material dispersed in a fluid polymer medium. Field induced dipole-dipole interactions cause particles to experience a mutual interaction resulting in distinct particle chains which align parallel to the applied electric field direction. This chained microstructure can then be "frozen in" by cross-linking the polymer matrix. The chaining phenomena is dependent on both the magnitude and the frequency of the applied field. Optimum assembly conditions for this process are determined via optical microscopy and electrorheological measurements. The dielectrophoretic assembly process also has the advantage of *in-situ* quality control through dielectric measurements. Both the degree of alignment and the batch uniformity can be confirmed via dielectric measurements. By varying the applied field and frequency, chain coarseness can be manipulated giving rise to the ability to "tune" the properties of the composite. The dielectrophoretic assembly process is projected to be utilized for electrical, structural and thermal composite applications.

INTRODUCTION

MANY of today's adaptive materials are based on composite systems (Newnham, 1989, 1986a, 1986b). A composite is a multiphase material which exhibits properties unattainable in any of the isolated constituent phases. The properties of composite materials are controlled through materials selection, volume fraction of filler, percolation behavior and connectivity. For the typical case of a polymer matrix-ceramic filler composite, we introduce a novel assembly technique which allows manipulation of the ceramic filler phase during the manufacturing process. This assembly involves the induction of dipole-dipole interactions between the second phase filler particulates under both alternating and direct current electric fields, a phenomena known as dielectrophoresis (Pohl, 1978). The result is a unidirectional alignment of the filler material in the polymer matrix.

The dielectrophoretic assembly is suited to a variety of thermoset polymers and filler materials. Optimum assembly conditions have been determined via electrorheological behavior and *in-situ* microscopy (Bowen, et al., 1994). Dielectric property and impedance changes (suitable for quality control monitoring of the composite assembly process) are also projected to be a useful means to determine the optimum assembly conditions. The potential of this processing methodology is not yet fully realized. Target applications include electronic, structural and thermally conductive composite materials. This paper will discuss the background, theory, and important parameters of the dielec-

trophoretic processing technique with emphasis on electrical composites.

BACKGROUND

Before beginning the discussion of dielectrophoretic processing, it is useful to clarify some basic definitions and terms that will be used in the characterization this class of composite.

Connectivity

In composite materials, there exists a classification system to describe the architecture of the component phases. This classification system is designated as the connectivity of the composite material. Connectivity describes the number of dimensions a phase in a composite material is continuous in. Newnham (1986b) developed a self-consistent nomenclature to describe the connectivity of composite materials. He showed that for a given number of components (n), there is a finite set of connectivity patterns given by the expression:

$$\frac{(n+3)!}{3!n!} \quad (1)$$

For example, with a diphasic composite material (a matrix phase and a single filler phase), $n = 2$, resulting in a possible 10 connectivity patterns (Newnham, Skinner and Cross, 1978). The convention is to make the first term of the connectivity pattern description equal to the number of dimensions in which the filler is continuous while the

*Author to whom correspondence should be addressed.

second term refers to the number of dimensions in which the matrix is continuous. For a 0-3 connectivity, the filler phase is completely discontinuous while the matrix phase is continuous in all three directions (e.g., a well dispersed powder in a polymer matrix). This differs from a 1-3 connectivity where the filler is continuous in one dimension and the matrix is continuous in all three dimensions (e.g., parallel rods in a polymer matrix). By carefully choosing a process which results in a desired connectivity, the directional anisotropy and magnitude of properties in a composite can be precisely engineered.

Percolation Theory

Percolation theory is the means used to explain how the properties of a composite material are altered by changing the volume fraction of the filler phase (Zallen, 1983). For simplicity in describing percolation theory, a metal powder will be considered and the composite property of conductivity will be examined. Intuitively, at low volume fractions of filler, the conductivity of the composite material will be low, approximately equal to that of the polymer matrix. A schematic of a low volume fraction composite material is given in Figure 1(a). As more and more metal particles are added, they begin to crowd together and come in contact with each other until, at high volume fractions, conducting pathways exist through the polymer matrix. The conducting microstructure is shown schematically in Figure 1(b). This results in a composite conductivity that is governed by the conductivity of the metal filler.

The change in conductivity as a function of increasing volume fraction metallic filler is schematically plotted in Figure 1(c). The volume fraction of filler at the inflection point in the curve is defined as the percolation limit or "critical" volume fraction of filler. This inflection point exists at a volume fraction of filler where the particulates are

crowded together enough such that they just begin to touch each other and form conducting pathways through the composite. The "critical" volume fraction of filler is not a fixed quantity and will vary with the filler particle size, size distribution and morphology. A more detailed discussion of percolation theory as it applies to conductive composites can be found in McLachlan et al., (1990) and Janzen (1975), but the point to be noted here is that by changing the volume fraction of the filler material in the composite, properties can be altered and effectively tuned to meet certain design parameters. This tuning effect is utilized in applications such as piezoresistors and both positive and negative temperature coefficient resistors (Newnham, 1989).

PROCESSING TECHNIQUES UTILIZED FOR COMPOSITE MATERIALS

Because the electronics industry is driven to obtain increasingly higher volumetric efficiencies from devices, smaller filler materials must be manufactured. Fabrication of functional composites on a micron-submicron scale makes processing very difficult and is the driving force in the search for more sophisticated processing techniques. This section is intended to give a brief look at relevant processes currently utilized in the fabrication of electronic composite materials.

Low Connectivity Processing Techniques (0-3 Connectivity)

One of the most common architectures in electronic composite materials is the 0-3 connectivity. This type of composite is generally used for piezoelectric transducer applications (electrical to mechanical energy conversion and vice versa) such as those used in pressure sensors. The 0-3 composite is attractive not only for its property enhancement advantages (higher effective d_{33} , piezoelectric coefficient and better acoustical impedance matching) but for its ease in processing as well.

Composites of the 0-3 type are usually fabricated through a high-shear mixing process that disperses a ceramic or metal powder uniformly into an uncured thermoset or heated thermoplastic polymer matrix. Typical means of high shear mixing range from an automated, large scale mixer (such as a 3-roll mill) to laboratory scale mortar and pestle mixing. Usually, 0-3 composite materials are processed as sheets which are easily mass produced (Baker, Moore and Petroff, 1991). However, these sheets can contain large density gradients and heterogeneities due to segregation effects of incomplete mixing.

Electric Field Processing

Electric fields have been used in the processing of composite materials mainly for producing specific orientations of filler materials within a polymer matrix. Electric fields

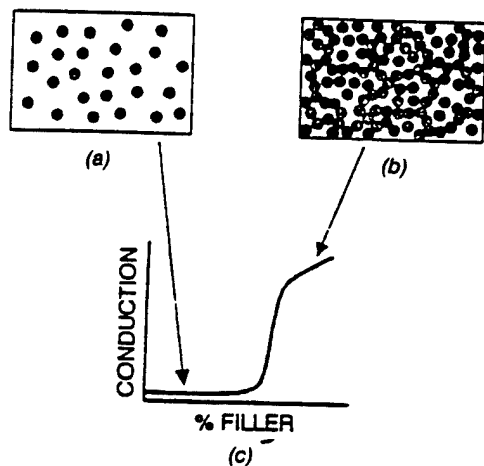


Figure 1. (a) Schematic of composite microstructure at low volume fraction filler; (b) schematic of composite microstructure at high volume fraction filler; (c) schematic of the percolation curve for a metal filled polymer composite.

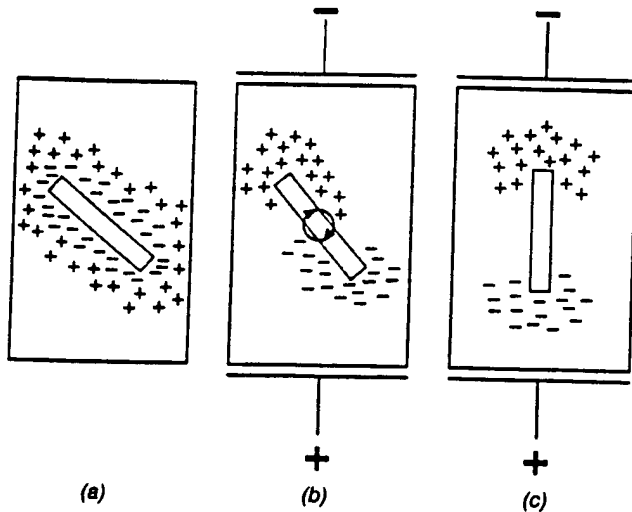


Figure 2. (a) Schematic showing charge double layer in the absence of an applied electric field; (b) on the application of an electric field, the charge will separate and migrate towards the electrode of opposite charge, effectively forming a macroscopic dipole; (c) as the charge is pulled by the electrodes, it acts to rotate the fiber into an orientation where the charges can be closest to the electrodes, i.e., aligned parallel to the applied field direction.

can be used to orient polar crystals and fibers (via induced dipolar interactions), to deposit thin coatings (via electrophoretic effects) and to induce particulate chaining within a matrix polymer (via the dielectrophoretic effect) (Tada et al., 1993; Sarkar et al., 1992; Bowen et al., 1994).

Orientation of fibers and polar crystals into a quasi 1-3 connectivity can be accomplished through dipolar interactions with an applied electric field. When an electric field is applied to a fiber, charge on the filler surface will migrate to the region nearest the opposite charged electrode. The fiber will rotate and align its long axis parallel to the applied field direction as a result of the redistribution of charge. This phenomena is shown schematically in Figure 2.

The electrophoretic effect involves the migration of charged particles in an electric field. If a particle obtains a positive charge in a suspension and an electric field is applied, the particle will migrate toward the negatively charged electrode. In a colloidal system, a thin coating of particles can be deposited on the surface of an electrode utilizing the electrophoretic concept. By depositing alternating layers of particles (alumina and zinc oxide, for example), laminate composite structures (2-2 connectivity) can be produced (Sarkar, Haung and Nicholson, 1992). The variables affecting electrophoretic deposition include the magnitude of the applied electric field, the surface charge on the particles (variable by altering pH when using aqueous systems), viscosity of the suspension medium and the duration of the applied field (longer times will facilitate the deposition of a greater number of particles and hence, thicker films).

The dielectrophoretic effect can be used to induce an attractive potential between particles in a suspension resulting

in a quasi 1-3 connectivity. This effect is currently being researched as an assembly technique for composite materials and will be exclusively addressed in the remainder of this paper.

THE DIELECTROPHORETIC EFFECT AS A COMPOSITE ASSEMBLY TECHNIQUE

While dielectrophoresis has been recognized since 1949, it was generally utilized as a separation technique by mineralogists and biologists (Pohl, 1978; Winslow, 1949). Only recently has the dielectrophoretic effect been recognized as a useful means of assembling composite materials (Randall et al., 1993). Through the mutual dielectrophoretic effect, quasi 1-3 composites can be fabricated such that the separation phenomena is suppressed, yielding a composite material with minimized structural disorder.

Dielectrophoretic Effect—Background Information

When a single particle suspended in a fluid medium is exposed to an electric field, two phenomena can possibly occur: (1) electrophoresis and (2) dielectrophoresis. Electrophoresis was defined earlier as the translational motion of charged matter within any electric field (uniform or non-uniform). Dielectrophoresis will be defined as translational motion of neutral matter caused by the induction of a polarization in a non-uniform electric field (Pohl, 1978). Both of these effects are shown in Figure 3. The major differences between the electrophoretic and dielectrophoretic effects are given as:

1. The dielectrophoretic effect is not dependent on the sign of the applied electric field whereas the electrophoretic effect is dependent on both the field direction and the sign of the particle charge.
2. The dielectrophoretic effect is proportional to the particle volume and, as such, is more pronounced as particle size increases. However, the electrophoretic effect is relatively independent of particle size.
3. Dielectrophoresis usually requires very divergent non-

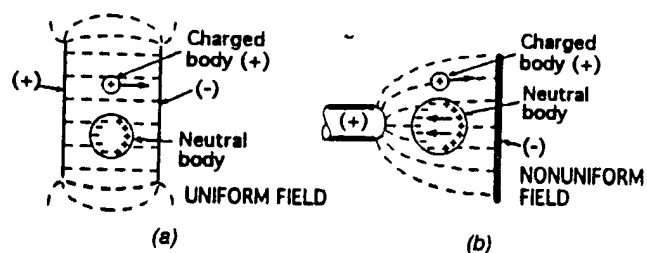


Figure 3. Schematic showing the phenomena of dielectrophoresis for a single particle in suspension. Figure (a) shows that a neutral body will be simply polarized in a uniform electric field and no translation will occur. Figure (b) shows that, for the nonuniform case, the neutral particle will migrate to the region of higher field concentration. (After Pohl).

uniform electric fields for pronounced effects while electrophoresis is observed in both uniform and non-uniform electric fields.

A special case arises when more than one particle is considered in the suspension. Consider two particles having a higher dielectric constant than the suspension medium (i.e., a higher polarizability) and in close proximity to each other. When a uniform electric field is applied to the suspension, it is perturbed in a manner consistent with that shown in Figure 4(a). Hence, a non-uniform electric field is generated in the gap between the two particles. Since the particles are already polarized by the field [Figure 4(b)], the non-uniform perturbation acts to pull the particles together. A semi-quantitative model for the mutual agglomeration is explained in the next section.

When many particles are present in the suspension, the mutual dielectrophoretic effect acts to cause particles to attract each other and agglomerate unidirectionally to form chains parallel to the applied field direction. This is shown schematically in Figure 5. With this chained microstructure, the composite achieves percolation at a much lower volume fraction filler than the simple dispersion case. However, the percolation of properties is anisotropic, with property enhancements occurring along the chained direction.

Interaction Potential Theory of Colloidal Suspensions

If a two particle suspension is considered, the interaction potential can be explained by the DLVO colloidal stability expression given as:

$$V(r) = 2\pi\epsilon_0\epsilon_f a \zeta^2 \ln [1 + \exp(-\chi r)] - \frac{Aa}{12r} \quad (2)$$

where $V(r)$ = total interaction potential, ϵ_0 = permittivity

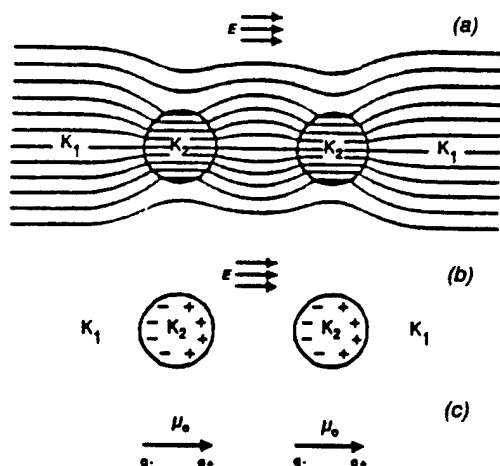


Figure 4. (a) Effect on field when two particles in a medium are close and their dielectric constant, K_2 , exceeds that of the medium, K_1 ; (b) excess polarization produced in two particles subject to an external electric field when $K_2 > K_1$; (c) effective dipoles, showing their attractive nature. (After Pohl).

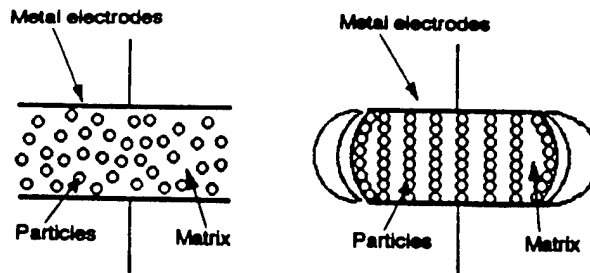


Figure 5. Schematic showing the unidirectional agglomeration phenomena. At zero applied field, the particles stay in a dispersed state. Upon the application of an external electric field, dipole-dipole interaction causes particle chains parallel to the applied field direction.

of free space, ϵ_f = dielectric constant of the medium, a = spherical particle radius, ζ = Zeta potential, χ = Debye reciprocal length, r = interparticle distance, and A = Hamaker constant (Reed, 1988).

The first term in Equation (2) represents a repulsive potential due to the Stern and Gouy-Chapman charge layers surrounding a particle in suspension (Figure 2 schematically shows charge layers around a fiber morphology). The second term is an attractive potential based on van der Waals forces of attraction. When typical values for particles suspended in an uncured polymeric matrix are chosen and input into Equation (2), a plot (Figure 6) showing the interaction potential curves can be generated. Numerical values used in the calculations for Figure 6 can be found in Table 1. These values are based on physical measurements and approximated variables owing to the incomplete database for non-aqueous media. These values are suitable, however, to qualitatively describe the effects of electric field strength on the colloidal stability of ceramic particulates suspended in an uncrosslinked polymer. Figure 6 shows that there is a critical separation distance at which the two

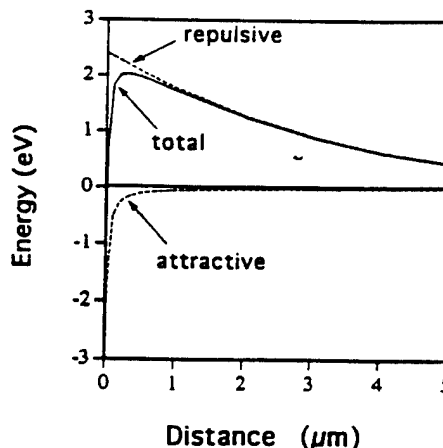


Figure 6. Calculated interaction potential versus separation distance according to the classical colloidal stability equation for SrTiO_3 in an uncured polymer.

Table 1. Values used in the calculation of Figure 6.

ϵ_f	= 4 (typical of polyurethane at room temperature)
ϵ_p	= 300 (typical of bulk SrTiO_3)
a	= 1 μm (typical particle size for powders)
ζ	= 50 mV (approximated)
κ	= 400,000 1/m (approximated)
A	= $1\text{E-}19$ J (typical Hamaker constant)

particles must overcome an energy barrier in order for agglomeration to occur.

When the effects of an electric field applied to the suspension are considered, a third term is introduced. This term is the quadruple solution to the Laplace equation and is included in the interaction potential equation to yield:

$$V(r) = 2\pi\epsilon_0\epsilon_f a^2 \zeta^2 \ln [1 + \exp(-\kappa r)] - \frac{Aa}{12r} + \frac{v(1 - 3\cos^2\theta)}{r^3} \quad (3)$$

where

$$v = \frac{(\beta a^3 \epsilon_f E_{loc})^2}{\epsilon_f} \quad \text{and} \quad \beta = \frac{\epsilon_p - \epsilon_f}{\epsilon_p + 2\epsilon_f}$$

where θ = orientation angle of particles, r = interparticle distance, β = effective polarizability, a = particle radius, ϵ_f = dielectric constant of the suspending fluid, ϵ_p = dielectric constant of the particles and $E_{loc} \approx E_{applied}$ (Halsey, 1992). As can be seen, the Laplace term is dependent on the square of the applied electric field and on the difference between the dielectric constants of the particle and the suspending medium. Hence, if the applied field is increased or if higher permittivity filler material is utilized, the attractive potential between the particles will increase.

The modified interaction potential Equation (3) can be solved and plotted for differing field conditions as found in Figure 7. As the applied field is increased, the barrier to agglomeration is reduced and particles at larger separation distances will experience an attractive potential. Figure 7 also shows that the equilibrium interparticle spacing varies with the magnitude of the electric field. Utilizing this calculated dependence of the particle spacing on the magnitude of the applied field, adaptive composite materials can be produced with properties that will depend on the applied processing conditions.

The orientation angle dependence of Equation (3) shows why, fundamentally, the particles form distinct chains exclusively along the electric field direction. The orientation angle (θ) is defined as the angle formed between a vector parallel to the applied field and a vector connecting the centers of two particles in suspension (see Figure 8). The contribution to the attractive interaction potential is maximized when $\theta = 0^\circ$. At a critical angle of approximately 55° , the dipole-dipole potential switches from an attractive

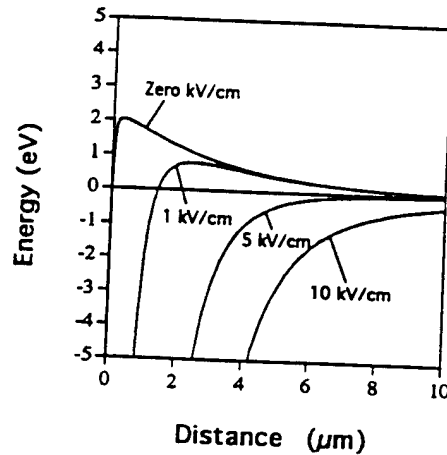


Figure 7. Calculated interaction potential versus separation distance according to the modified classical colloidal stability equation for SrTiO_3 in an uncured polymer at varying electric field intensities. The variables are from Table 1 with the exception of the applied electric field strengths (typical of those actually used) and θ (taken to be 0°).

to a repulsive potential. Hence, particles existing at an orientation greater than 55° (those particles existing approximately perpendicular to the applied field) will experience a repulsive potential. The result is the formation of distinct chains parallel to the applied field direction. Figure 9 shows the interaction potential at varying orientation angles and it can be seen that an essentially infinite barrier to agglomeration exists at angles greater than 55° to keep particles separated in the direction perpendicular to the applied field.

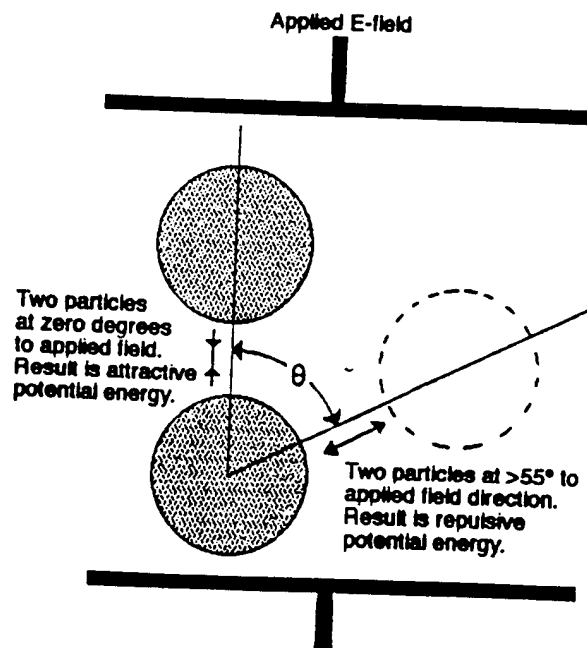


Figure 8. Schematic of the orientational relationship of the interaction potential under an applied electric field. At angles greater than 55° , a repulsive potential exists which aids in the formation of the distinct chained microstructure.

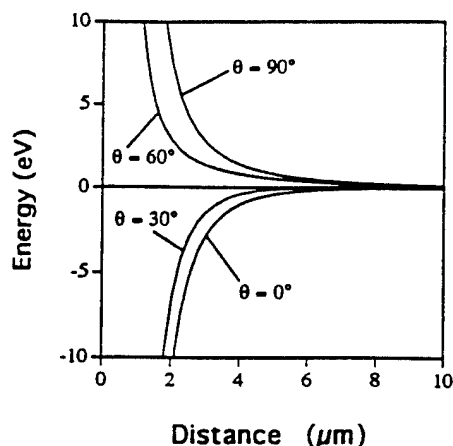


Figure 9. Calculated interaction potential versus separation distance according to the modified classical colloidal stability equation for SrTiO_3 in an uncured polymer at varying orientations. There is an enormous ($1\text{E} + 14\text{ eV}$) barrier to agglomeration for the 60° and 90° orientation angles. This can essentially be considered an infinite barrier to agglomeration resulting in a minimum equilibrium separation of particles perpendicular to the applied field. The applied electric field is taken to be 5000 v/cm in this calculation.

MATERIALS ISSUES FOR DIELECTROPHORETIC ASSEMBLY OF COMPOSITE MATERIALS

When choosing materials to fabricate composites, one must consider components that best suit the composite application. Careful considerations must be taken to control properties such as electrical and thermal conductivity, thermal stability, mechanical strength, mechanical stiffness and piezoelectric coefficient. Through the combination of the chosen filler and matrix materials, one can achieve composite properties which are unattainable in the isolated constituent phases.

Matrix Materials

There are several general requirements necessary for the matrix materials in the dielectrophoretic assembly of composites. The first requirement is that the matrix must be an insulating material of low dielectric constant that can easily transform from a liquid-like to a solid state (crosslinked or vitrified). The liquid-like state is necessary to suspend and align particles while the solid state is necessary to "freeze in" the oriented structure to produce a useful device. The matrix must be insulating in order to allow the generation of a polarization field (driving force for the chaining phenomena) and the dielectric constant is desired to be low so the effective polarizability, β in Equation (3), is maximized for a given particulate filler material. The second requirement is that the polymer matrix should have a high breakdown strength in the uncured state. The required breakdown strength of the polymer is dependent on the application envisioned. If it is desired to apply a 1 kV/mm field to process the composite, then the polymer should have

a breakdown strength of at least 1 kV/mm . If breakdown is occurring during the curing phase, local electric discharges will result in local thermal decomposition of the matrix. The result is a polymer which is damaged such that the crosslinking process is inhibited, thus ruining it as an acceptable matrix material. Thirdly, the viscosity of the uncured polymer matrix must be such that it is low enough to allow dielectrophoretic migration of particles into the chained microstructure but high enough to prohibit settling of the particles due to gravitational forces. Finally, the matrix should cure rapidly and easily (low temperatures) to allow for a rapid production rate and lower production costs.

The matrix materials utilized thus far are shown in Table 2. All of these polymers have supported dielectrophoretic assembly. A special note about the Norland optical adhesive (a UV curing polymer) is that it is limited to low volume fractions of filler material (≈ 0.05) and small thicknesses due to scattering conditions accompanying these two variables. If the volume fraction filler is too high for the desired thickness, the UV light necessary to cure the polymer will be scattered away at the surfaces and will not be able to penetrate and crosslink the center of the composite sample. Hence, the UV transmission of the composite must be accounted for when utilizing UV curing polymer matrices.

Filler Materials

Theoretically, any material with a dielectric constant higher than that of the matrix can be aligned and chained through the dielectrophoretic effect. Table 3 shows a list of insulators, semiconductors and metals which have been successfully aligned in a thermoset polymer matrix. Randall et al., (1992) showed that insulating particles are easily aligned, provided that their dielectric constant is greater than that of the matrix phase used [i.e., $\beta > 1$ in Equation (3)]. Fibrous filler morphologies are also capable of being aligned utilizing the dielectrophoretic assembly technique. Figure 10 shows PZT fibers aligned at approximately 0.1 and 0.005 volume fractions.

When conducting fillers are used, limitations associated with composite fabrication arise. The first limitation involves the elimination of the potential drop across the sample once the particles successfully chain. When the particles chain, the composite becomes conducting and the potential voltage drop (polarizing field) across the sample is de-

Table 2. Polymers and suppliers.

Polyurethane	Hysol-Dexter US0048
Silicone elastomer	Sylgard-184, Dow Corning Eccogel, Emerson-Cummings
Eccogel epoxy	Eccogel, Emerson-Cummings 1365
Epon epoxy	Epon 865 Shell
Norland Optical Adhesive	Norland-81

Table 3. Filler materials which have been successfully assembled in uncured thermoset polymers.

Insulators	Semiconductors	Metals
BaTiO ₃	YBa ₂ Cu ₃ O _{7-x}	Aluminum powder
PbTiO ₃	Graphite	Silver-coated resin balls
Pb(Zr,Ti)O ₃	SiC Fibers	
SrTiO ₃	ZnO	
Ba ₂ TiSi ₂ O ₇	V ₂ O ₅	
ZrO ₂		
TiO ₂		
SiO ₂ -balls		

stroyed. The polarizing field is the driving force for the chaining phenomena and without it, migration of particles to form chains will not occur. Recent studies have revealed that once the composite sample becomes conducting, a few chains will remain intact and keep the polarizing field at zero while the rest of the chains will relax and dissipate due to Brownian motion. Hence, a rapid cure polymer is necessary to freeze in the chained structure before it can drift apart. Recent progress with alignment in UV curable polymers has been promising, but more work is necessary.

The second limitation of using conducting filler materials is that the volume fraction of the filler materials must be less than the percolation limit (recall Background section). If the conducting powder is present in large enough quantities that the particles touch to create a conducting pathway through the material, there will be no chaining phenomena because the polarization field will never be established.

The third limitation of conducting fillers concerns electrical breakdown of the uncured polymer during assembly. As particles begin to form chains, the insulating gap between the particles becomes increasingly smaller. This creates an enormous energy density between the particles and can result in sparking or electrical discharge. This electric breakdown can slow and even prohibit the curing of the matrix due to thermal decomposition effects.

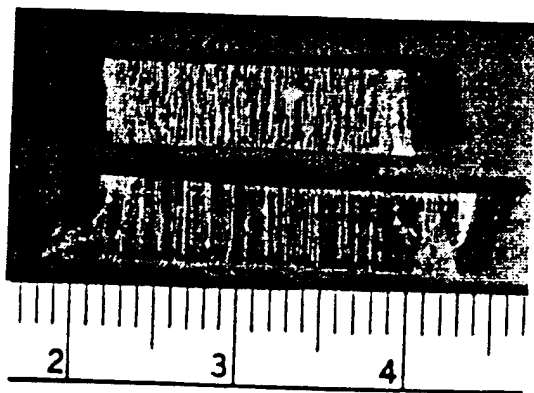


Figure 10. Photograph of PZT fibers (30 μm thick, 1 cm long) aligned in a polymer matrix at approximately 0.1 volume fraction (top) and 0.005 volume fraction (bottom).

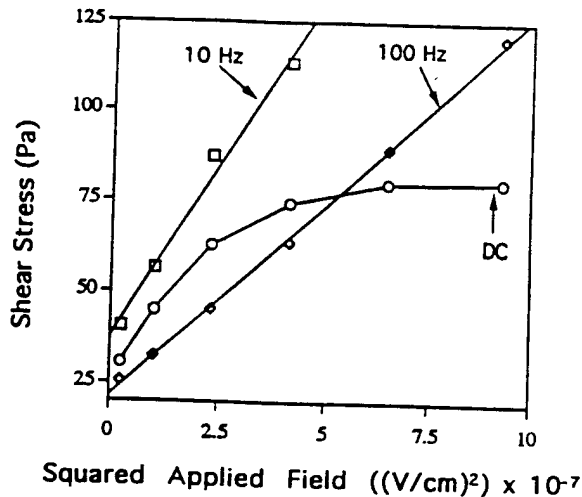


Figure 11. Shear stress vs. squared applied field for polyurethane + 0.2 volume fraction SrTiO₃ at a shear rate of 9.6 sec^{-1} (after Bowen, Bhalla, Newnham and Randall).

Ideal Dielectrophoretic Assembly Conditions for Composite Materials

Once the constituent materials have been selected, the focus of the assembly shifts to the process parameters. Based on the conditions placed on an individual system, the dielectrophoretically assembled composite can have a number of microstructures. The filler can exist in a dispersed state, well-defined chains, poorly-defined chains, and a turbulent flow state (Bowen et al., 1994).

While it was shown previously that the effects of the applied field magnitude have a great effect on the alignment of the particulate filler material, the frequency of the applied field also has an enormous impact on the microstructure of the final composite material (Bowen et al., 1994). Using a modified Brookfield viscometer, the forces of attraction between particles as a function of the applied electric field strength and frequency can be indirectly measured. The stronger the attractive forces between particles are, the harder it will be to move them past each other in a rotational viscometer. This will result in a higher shear stress being recorded for conditions which maximize the force of attraction between the suspended particulates (for complete experimental details see Bowen et al., 1994). Figure 11 shows a plot of the shear stress versus the square of the applied field at a constant shear rate for a polyurethane matrix with SrTiO₃ filler. When DC voltages are applied, an initial increase in the shear stress is seen, however, it diminishes with increasing field intensity. This is believed to be caused by the domination of the electrophoretic effect at high electric field strengths.

As can be seen for both the AC frequencies in Figure 11, the electrophoretic effect has been successfully suppressed [the plot has a linear dependence on E^2 as predicted by Equation (3)]. Also, Figure 11 clearly shows that the force of attraction between particles is highly frequency depen-

dent. For this system at a given electric field, there is a larger particulate force of attraction at 10 Hz than at 100 Hz. This shows that the composite architecture is adaptive based on the given set of assembly conditions (applied field intensity and frequency). Also, an optimum condition (which differs from system to system) exists to assemble a composite material via the dielectrophoretic technique (Bowen et al., 1994).

APPLICATIONS FOR DIELECTROPHORETICALLY ASSEMBLED COMPOSITE MATERIALS

Composite materials assembled utilizing the dielectrophoretic effect can be exploited in a number of potential applications. These materials may not only be used as electrical composite materials but as thermally conducting and structural composites as well. They also have the ability to achieve percolation at low volume fractions so less filler material is necessary. A chart showing the potential of dielectrophoretically assembled composites is given in Figure 12.

Electronic Composite Applications

As electronic composite applications is our original projected field of use for dielectrophoretically processed composite materials, many devices have been considered as potential candidates for this processing technique. The use of dielectric measurements is foreseen as a type of quality control on this class of materials. Through the use of dielec-

tric measurements, the degree of alignment as well as the uniformity of the composite architecture across large sample areas can be quantitatively determined. In the future it is envisioned that a microprocessor feedback loop can be coupled with the dielectric measurements to adjust the field and frequency conditions during composite fabrication to create an intelligent processing setup.

Hydrophones

Using the direct piezoelectric effect, piezoelectric ceramics based on $\text{Pb}(\text{Zr,Ti})\text{O}_3$ can be utilized as pressure sensors. However, the performance of these materials is limited in hydrostatic applications such as underwater acoustic sensing devices (hydrophones) due to transverse piezoelectric contributions. The limitations of the monolithic ceramic sensitivity can be overcome by combining the ceramic with a polymer to form a composite material. In the composite design, higher sensitivity levels are obtainable due to enhancements of the effective d_{33} coefficient via stress transfer from the polymer to the ceramic (Cao, Zhang and Cross, 1992). Also, the composite device has an acoustical and capacitive impedance closer to that of the water medium it is used in (due to the replacement of most of the ceramic with a polymer) so it will be more sensitive to subtle pressure gradients. The most sensitive hydrophones have been designed with a 1-3 connectivity which has the advantage of large d_{33} , easy poling conditions and good impedance matching to the working environment.

Hydrophones have also been utilized as biomedical transducers which allow ultrasonic imaging of internal organs. These biomedical devices require high frequency operation (≥ 1 MHz) in order to provide accurate and distinct images (Smith and Shaulov, 1988). To obtain these high frequencies, small scale hydrophone composites are required. The dielectrophoretic assembly technique provides a means to fabricate such devices on a much smaller scale than is currently possible.

PTC Thermistors

When processing conditions are applied to cause a conducting filler to chain such that the particles are touching, a positive temperature coefficient of resistivity composite material is created. This composite material will be conductive at low temperatures and insulating above a certain critical temperature. When the device is heated, the thermal expansion mismatch between the polymer and the filler material can cause the composite to become insulating (see Figure 13). Since the polymer matrix will have a much larger coefficient of thermal expansion than the filler material, it will, on heating, separate the conducting particles. This results in an insulating composite at high temperatures. Figure 14 shows a typical resistivity versus temperature response for such a composite device as given by Newnham (1989). A device such as this is useful in applications such as thermostats and temperature sensors.

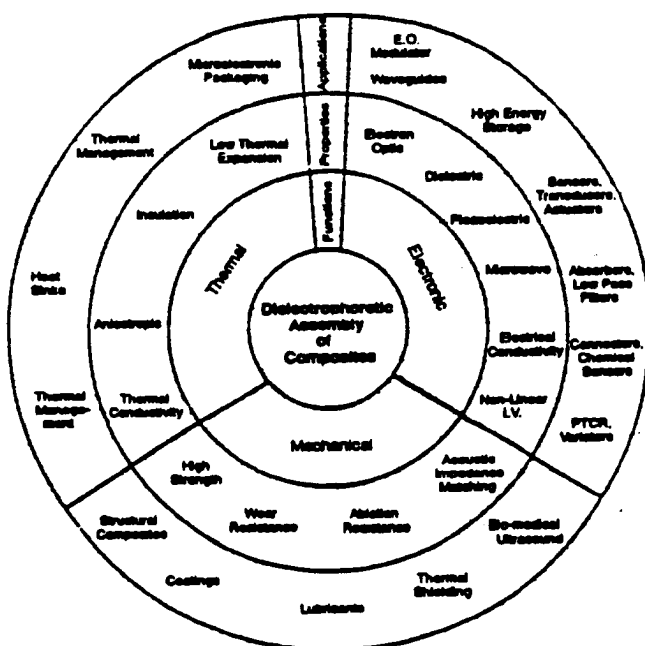


Figure 12. Potential applications for dielectrophoretically assembled composite materials. The circle chart is read from the center radially outwards with titles located at the top of each ring.

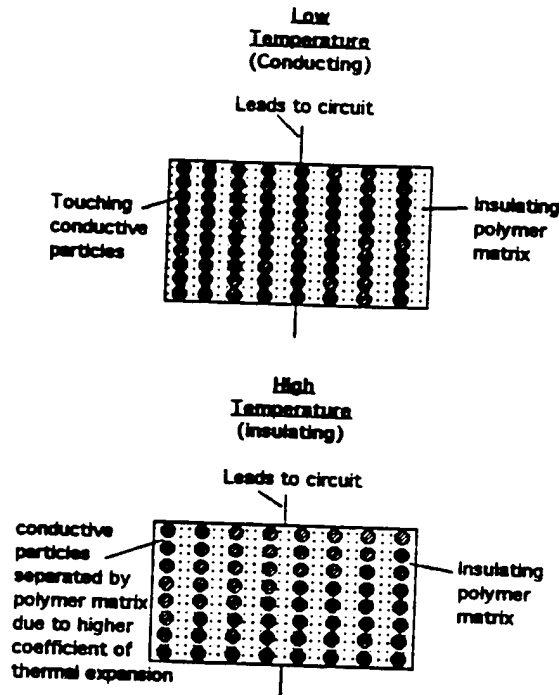


Figure 13. Schematic of the thermistor application.

Tunable Compliance Devices

It is anticipated that a device can be fabricated which alters its elastic compliance as a function of the magnitude of an applied electric field. By applying an electric field to a suspension of polarizable particles in an insulating fluid medium, the elastic compliance, and hence, the mechanical resonant frequency of the device should be altered. The resonant frequency should then be able to be tuned to a specific value by applying an appropriate voltage to the system according to the following expression:

$$f_R = \frac{1}{2t} \sqrt{\frac{c}{\rho}} \quad (4)$$

where ρ = density, c = elastic stiffness (voltage dependent) and t = thickness of the sample (Newnham and Ruschau, 1991). This device is shown schematically in Figure 15.

Structural Applications

The focus of the dielectrophoretic assembly of composite devices has recently expanded to differing particle morphologies and it has been shown that fibers will align with the electric field (recall Figure 10 where short fibers of PZT were aligned and chained). Hence, it is now anticipated that structural composites will benefit from the dielectrophoretic assembly technique. It is predicted that a bulk short fiber reinforced composite material can be processed such that all

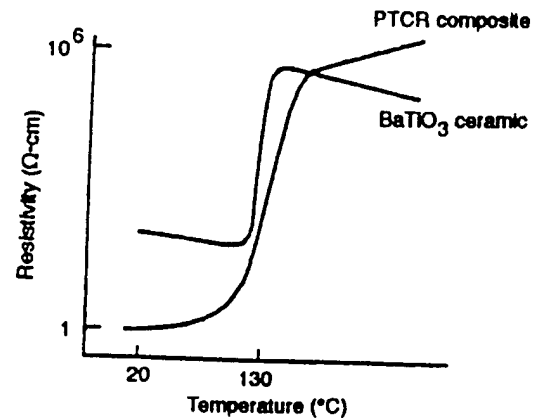


Figure 14. Plot of the PTC effect in a composite thermistor as compared to that in a BaTiO_3 ceramic (after Newnham, 1989).

the fibers are aligned in the same direction. This would give dramatic increases in composite properties over those attainable in a random chopped fiber system. As mentioned, this effect has only recently been identified and, as such, requires further study before any conclusions can be drawn.

Thermally Conducting Composites

Dielectrophoretic assembly of composite materials also has the potential of being used to produce composites utilized for their thermal conduction properties. A composite filled with a high thermal conductivity filler material (SiC) aligned using the dielectrophoretic effect will exhibit a high thermal conductivity in the chained directions while the thermal conduction in the transverse directions will be minimal. While the thermal expansion mismatch that is ex-

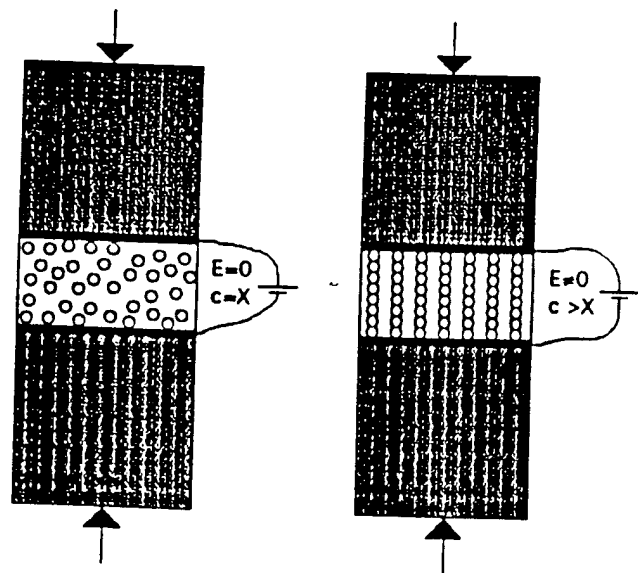


Figure 15. Schematic of the tunable compliance application. The electric field induced chains (right) will give the device a different elastic compliance than the dispersed case (left).

ploited in the composite PTC thermistor must be taken into consideration, it is projected that the working range of these devices can be controlled by the temperature used to cure the device.

Bhattacharya and Chaklader (1983) have shown thermally conductive composites are possible using the percolation effect. By using dielectrophoretic processing, the percolation limit should be able to be shifted so that the same thermal conductivity is possible at lower volume fractions of filler material. In addition, the thermal conductivity of a dielectrophoretically produced device will be anisotropic, having a higher thermal conductivity in the chained direction. As is the case with structural composite materials, the applications of dielectrophoretically produced thermal composites have only recently been realized so further study is required in this area.

SUMMARY

In this paper, a new, novel processing technique termed dielectrophoretic assembly has been introduced. It has been shown to be applicable to a wide range of matrix and filler materials, but limitations still exist. Different assembly conditions for composite fabrication were shown to have a dramatic effect on composite architecture, giving the composite its adaptive nature. With optimum assembly conditions applied, the composite consists of a filler material which is aligned unidirectionally in the matrix phase. This type of microstructure can be exploited in terms of its electrical, thermal and structural advantages. By varying the processing conditions, composite properties can be "tuned" to meet different design criteria. It is believed that once the materials science and engineering behind this processing technique is fully developed, dielectrophoretic assembly will become a powerful processing tool for the fabrication of functional composite materials.

REFERENCES

- Baker, W. E., E. M. Moore and T. E. Petroff. 1991. "PZT 0-3 Composites Using Acid Based Co-Polymers", *IEEE Proceedings* 1991, p. 309.
- Bhattacharya, S. K. and A. C. D. Chaklader. 1983. "Review on Metal-Filled Plastics. Part 2. Thermal Properties", *Polym. Plast. Technol. Eng.*, 20(1):35-39.
- Bowen, C. P., A. S. Bhalla, R. E. Newnham and C. A. Randall. 1994. "An Investigation of the Assembly Conditions of Dielectric Particles in Uncured Thermoset Polymers", *J. Mat. Res.*, 9(3):781-788.
- Cao, W., Q. M. Zhang and L. E. Cross. 1992. *J. Appl. Phys.*, 72(12).
- Halsey, T. C., 1992. "Electrorheological Fluids", *Science*, 258:761-764.
- Janzen, J. 1975. "On the Critical Conductive Filler Loading in Antistatic Composites", *J. Appl. Phys.*, 46(2):966-969.
- McLachlan, D. S., M. Blaszkiewicz and R. E. Newnham. 1990. "Electrical Resistivity of Composites", *J. Am. Ceram. Soc.*, 73(8):2187-2203.
- Newnham, R. E., D. P. Skinner and L. E. Cross. 1978. *Matl. Res. Bull.*, 13:525.
- Newnham, R. E. 1986a. *Ann. Rev. Mat. Sci.*, 16:47-68.
- Newnham, R. E. 1986b. *Ferroelectrics*, 68:1-32.
- Newnham, R. E. 1989. *Rep. Prog. Phys.*, 52:123-156.
- Newnham, R. E. and G. R. Rusheau. 1991. *J. Am. Ceram. Soc.*, 74:463-480.
- Pohl, H. A. 1978. *Dielectrophoresis*. Cambridge, London, New York and Melbourne: Cambridge University Press, pp. 34-47.
- Randall, C. A., S. Miyazaki, K. L. More, A. S. Bhalla and R. E. Newnham. 1992. "Structural-Property Relationships in Dielectrophoretically Assembled BaTiO₃ Nanocomposites", *Matl. Letters*, 15:26-30.
- Randall, C. A., D. V. Miller, J. H. Adair and A. S. Bhalla. 1993. "Processing of Electroceramic-Polymer Composites Using the Electrorheological Effect", *J. Mat. Res.*, 8(4):899-904.
- Reed, J. 1988. *Introduction to the Principals of Ceramic Processing*. New York, Chichester, Brisbane, Toronto and Singapore: John Wiley & Sons, p. 144.
- Sarkar, P., X. Haung and P. S. Nicholson. 1992. "Structural Ceramic Microlaminates by Electrophoretic Deposition", *J. Am. Ceram. Soc.*, 75(10):2907-2909.
- Smith, W. A. and A. A. Shaulov. 1988. *Ferroelectrics*, 87:309-320.
- Tada, H., Y. Saito, M. Hirata, M. Hyodo and H. Kawahara. 1993. "A Novel Switchable Glazing Formed by Electrically Induced Chains of Suspensions", *J. Appl. Phys.*, 73(2):489-493.
- Winslow, W. M. 1949. *J. Appl. Phys.*, 20:1137.
- Zallen, R. 1983. *The Physics of Amorphous Solids*. New York: Wiley.

APPENDIX 54

Characteristics of the electromechanical response and polarization of electric field biased ferroelectrics

Q. M. Zhang, J. Zhao, T. Shrout, N. Kim, and L. E. Cross
Intercollege Materials Research Laboratory, The Penn State University, University Park,
Pennsylvania 16802

A. Amin and B. M. Kulwicki
Texas Instruments Incorporated, Attleboro, Massachusetts 02703

(Received 6 September 1994; accepted for publication 7 December 1994)

The electromechanical and dielectric responses of ferroelectric materials near paraelectric-ferroelectric (PF) phase transitions are examined both experimentally and theoretically. It is shown that the type of PF transition, i.e., first order and continuous transitions, and diffused phase transition found in relaxor ferroelectrics, has marked effect on the electromechanical and dielectric response behavior for materials under electric field bias. It is demonstrated that an exceptionally large piezoelectric and electromechanical response can be achieved in materials with a first order PF transition. For example, in $\text{Ba}_{1-x}\text{Sr}_x\text{TiO}_3$ ($x \sim 0.35$) ceramics at room temperature, a piezoelectric d_{33} larger than 1500 pm/V with very little frequency dispersion can be obtained. © 1995 American Institute of Physics.

I. INTRODUCTION

Near a ferroelectric phase transition, the competition between two or more neighboring phases and structural instability make the material susceptible to external excitations and disturbances.^{1,2} As a result, a large change in material properties can be induced with small external driving forces. Many devices have been made and materials have been developed utilizing this unique feature of a ferroelectric material near a phase transition.³

In this article, the dielectric and electromechanical properties of a material near its associated ferroelectric-paraelectric (PF) phase transition, in particular in relation to the type of transition, including first order, continuous, and diffused phase transitions are examined. Information of this kind can be useful in the design and selection of materials for electromechanical actuator and sensor applications, pyroelectric IR detection, energy storage, etc. Experimental results from a series of $\text{Ba}_{1-x}\text{Sr}_x\text{TiO}_3$ ($x \sim 0.35$) polycrystalline samples, which show both first order and continuous transitions, and lead magnesium niobate-lead titanate (PMN-PT) ceramics, which show diffused phase transition (relaxor ferroelectrics), will be presented and the comparison between theoretical and experimental results will be made. From the results of $(\text{Ba,Sr})\text{TiO}_3$, it will be demonstrated that exceptionally large piezoelectric responses can be achieved in materials with a first order PF transition and the overall electromechanical response behavior for materials with a first order PF transition are comparable to those of PMN-PT-type relaxor materials.

II. RESULTS FOR MATERIALS WITH A FIRST ORDER AND SECOND ORDER PF TRANSITIONS

A. Phenomenological treatment of the transition behavior

Using Landau-Devonshire theory, the expressions for the electric field, mechanical stress, and temperature depen-

dence of the dielectric, piezoelectric coefficients, elastic compliance, and electromechanical coupling factor near both first order and continuous phase transitions can be derived for single crystal materials.² The results can also serve as a guideline for the experiments on polycrystalline materials.

The free energy for a PF transition from a cubic to a tetragonal ferroelectric phase can be written as

$$G = (1/2)\alpha P^2 + (1/4)\beta P^4 + (1/6)\gamma P^6 - Q_{11}X_3P^2 - Q_{12}(X_1 + X_2)P^2 - (1/2)s_{11}^P(X_1^2 + X_2^2 + X_3^2), \quad (1)$$

where P is the polarization, X_i are the mechanical stress tensors, $\alpha = \alpha_0(T - T_0)$, T is temperature, α_0 , β , γ are constants, Q_{ij} are the electrostrictive coefficients, and s_{11}^P are the elastic compliance under constant electric displacement. For most materials, Q_{ij} and s_{11}^P are nearly independent of temperature and electric field. In Eq. (1), the free energy for the state with $P=0$ is taken as zero. The difference between a first order transition and a continuous transition is reflected by the sign of β in Eq. (1). For a first order transition $\beta < 0$, and for a continuous transition $\beta > 0$ and the transition occurs at $T = T_0$.

From Eq. (1), the basic equations which describe the response behavior of a material in the transition region can be derived as follows:

$$E = \frac{\partial G}{\partial P} = \alpha P + \beta P^3 + \gamma P^5 - 2Q_{11}X_3P - 2Q_{12}(X_1 + X_2)P, \quad (2)$$

$$\epsilon = \frac{1}{[\alpha + 3\beta P^2 + 5\gamma P^4 - 2Q_{11}X_3 - 2Q_{12}(X_1 + X_2)]}, \quad (3)$$

$$d_{33} = 2Q_{11}\epsilon P = \frac{2Q_{11}P}{[\alpha + 3\beta P^2 + 5\gamma P^4 - 2Q_{11}X_3 - 2Q_{12}(X_1 + X_2)]}, \quad (4)$$

$$s_{33}^E = s_{11}^P + \frac{4Q_{11}^2 P^2}{[\alpha + 3\beta P^2 + 5\gamma P^4 - 2Q_{11}X_3 - 2Q_{12}(X_1 + X_2)]}, \quad (5)$$

$$k_{33}^2 = \frac{d_{33}^2}{\epsilon s_{33}^E}, \quad (6)$$

where E is the electric field applied in the 3 direction, ϵ is the dielectric permittivity, d_{33} is the piezoelectric charge coefficient, and k_{33} is the electromechanical coupling factor. The effect of mechanical stress on various material coefficients is equivalent to that of temperature. That is, the only effect of applying a mechanical stress X_j on a sample is to shift the transition temperature from the original T_0 to a new value of $T_0 + 2Q_{ij}X_j/\alpha_0$. Hence, mechanical stress terms are omitted in the following discussion.

For a continuous transition, when the external field is zero, at $T < T_0$,

$$P = \sqrt{\frac{\alpha_0(T_0 - T)}{\beta}}, \quad \epsilon = \frac{1}{2\alpha_0(T_0 - T)},$$

$$d_{33} = \frac{Q_{11}}{\sqrt{\beta\alpha_0(T_0 - T)}}. \quad (7)$$

Above T_0 , both P and d_{33} become zero. To calculate the variation of the material parameters, i.e., ϵ , d , etc., with temperature under a fixed dc bias field or with dc bias fields at a given temperature, Eqs. (2)–(5) are solved numerically. Presented in Fig. 1 are the material properties as a function of temperature under a fixed dc bias field for a material with a continuous PF transition. The parameters used are listed in Table I. Clearly, a dc bias field eliminates the critical behavior, that is, the material parameters no longer exhibit the $|T_0 - T|$ -type temperature dependence behavior, which leads to the anomalous dielectric and piezoelectric responses as shown in Eq. (7) and reduces the dielectric constant substantially. Consequently, the material does not exhibit a large piezoelectric coefficient and electromechanical coupling factor in the induced piezoelectric state.

In contrast, for materials with a first order transition, these material parameters will have a substantial increase as a dc electric bias field is applied. Without a dc bias electric field, a first order transition will occur at a temperature $T_u = T_0 + [(3\beta^2)/(16\alpha_0\gamma)]$.⁴ Under a dc bias field, a critical region will be induced near the critical field $E_c = [(6\beta^2)/(25\gamma)]P_c$. The polarization at the critical field is $P_c^2 = -(3\beta)/(10\gamma)$ and the critical temperature is at $T_c = T_0 + [(9\beta^2)/(20\alpha_0\gamma)]$.⁴ Near the critical point,

$$k_{33} \rightarrow 1, \epsilon \rightarrow |T - T_c|^{-1}, \quad \text{and} \quad d_{33} \rightarrow P_c |T - T_c|^{-1/2}, \quad (8)$$

hence, both ϵ and d exhibit singular behavior. In Fig. 2, the dependence of the dielectric constant, piezoelectric coefficient, and electromechanical coupling factor with various bias electric fields and temperature for a material with a first order transition is presented. The parameters used here are

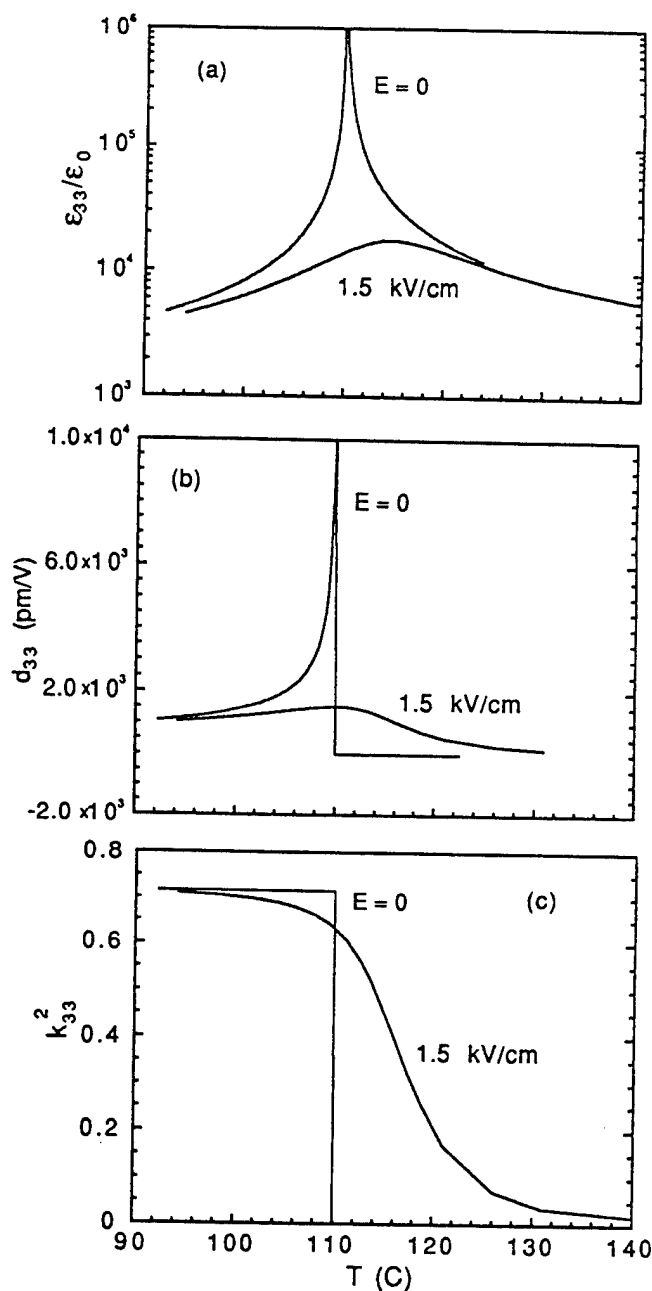


FIG. 1. (a) the dielectric constant; (b) the piezoelectric coefficient; and (c) the electromechanical coupling factor at different dc bias field as a function of temperature for a material with a continuous PF transition. The results are calculated based on Landau–Devonshire theory.

TABLE I. Parameters used in the theoretical calculation.^a

	α_0	β	γ	Q_{11}
Continuous transition	6.66×10^5	9.48×10^8	3.94×10^{10}	0.1
First order transition	6.66×10^5	-9.48×10^8	3.94×10^{10}	0.1

^aAll the parameters are in MKS units.

TABLE II. Characteristics of the BST ceramics.

	BST1	BST2	BST3
Composition (Ba/Sr/Ca)	58/32/10	67/33/0	59/31/10
Doping (Ho/Mn)	Undoped	0.5/0.1	0.5/0.1
Grain size (μm)	17	2.1	2.6

continuous phase transitions. The difference between the two types of transition is that for a material with a continuous PF transition, the dielectric and piezoelectric maximums will subside as the dc bias field increases, while for a first order PF transition, the peak values of these coefficients will increase with dc bias field up to a critical field, and then decrease. A stronger first order transition will lead to a higher critical bias field and larger temperature differences between T_c and T_{tr} . This behavior provides a convenient means to distinguish a first order transition from a continuous transition. Most importantly, a large piezoelectric coefficient and electromechanical coupling factor are expected for a material with a first order PF transition at temperatures near T_c under a critical dc bias field.

In most practical applications, the materials used are in polycrystalline form. The nonzero stresses existing at grain boundaries and random orientation of grains will broaden a first order transition. However, it should not change the conclusions reached above, that is, to have a high piezoelectric response and electromechanical coupling factor in the induced piezoelectric state, a material with a strong first order transition is preferred and a strong first order transition is marked experimentally by a large difference between T_{tr} and T_c .

B. Experimental results for $\text{Ba}_{1-x}\text{Sr}_x\text{TiO}_3$ ceramics

The ceramic $(\text{Ba,Sr})\text{TiO}_3$ (BST) was chosen for this study. The materials used have a PF transition near room temperature. Three different specimens, containing different levels of Ca as well as Ho and Mn dopants, were selected for the investigation. The characteristics of the materials are listed in Table II. These three types of specimens, as will be shown later in the paper, exhibit a continuous PF transition, a weakly first order transition, and a first order transition, respectively. Correspondingly, the specimens are designated as BST1, BST2, and BST3. The properties investigated are the dielectric permittivity ϵ_{33} , the piezoelectric coefficients d_{33} and d_{31} , and the polarization and longitudinal strain hysteresis loops at high driving fields. Both ϵ_{33} and d_{ij} were measured with and without dc electric bias field. Typical sample sizes in those measurements were $6 \times 5 \text{ mm}^2$ in area and 1 mm in thickness. For the dc biased dielectric constant measurements, samples with 0.15 mm thickness were used in order to obtain higher field levels.

In addition to polycrystalline samples, BaTiO_3 single crystal, which has a well defined first order PF transition, was also investigated. The high conduction under dc bias field at high temperatures, especially near the transition point, resulted in irregular temperature changes and hence no reliable results could be obtained.

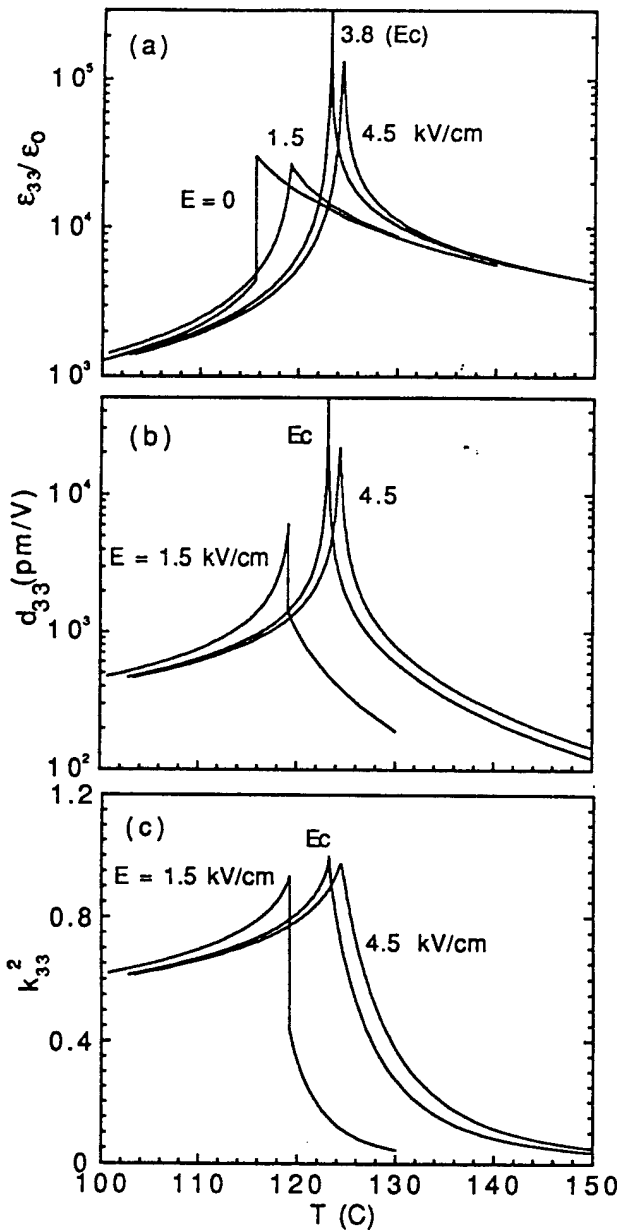


FIG. 2. (a) the dielectric constant; (b) the piezoelectric coefficient; (c) and the electromechanical coupling factor at different dc bias field as a function of temperature for a material with a first order PF transition. In (b) and (c), $E_c = 3.8 \text{ kV/cm}$. The results are calculated based on Landau-Devonshire theory.

those of BaTiO_3 single crystal which are also listed in Table I.⁴ These parameters are similar to those used in the calculation for the continuous transition above except β . The exceptionally large induced piezoelectric coefficient and large electromechanical coupling factor shown in Fig. 2 are in marked contrast to the relatively low electromechanical activity in the induced piezoelectric state of a material with a continuous transition (Fig. 1).

The results above can be summarized as: applying a dc bias electric field moves the piezoelectric and dielectric maximums to higher temperatures for both the first order and

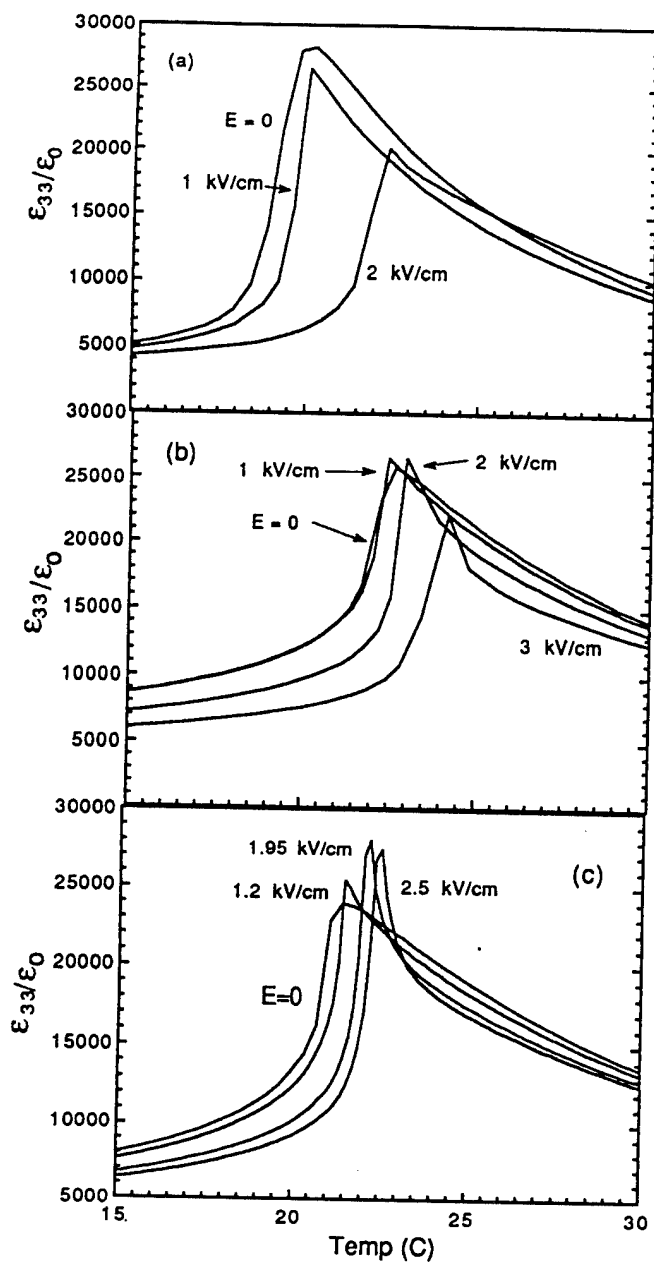


FIG. 3. The dc bias field dependence of the dielectric constant as a function of temperature for (a) BST1; (b) BST2; (c) BST3 near the PF transition region.

The dielectric constant was determined using a HP LCR meter (HP-4274A) in the frequency range from 0.1 to 100 kHz. The temperature control for this setup was made by a Delta temperature chamber. The piezoelectric coefficients and the strain hysteresis loops were measured using a laser dilatometer.⁵ The dilatometer is equipped with a temperature chamber covering the temperature range from near liquid nitrogen temperature to about 200 °C. The polarization hysteresis behavior (P/E) was acquired using a Sawyer-Tower circuit with a Delta temperature chamber to regulate the temperature.

Shown in Fig. 3 are the dielectric constant for the three

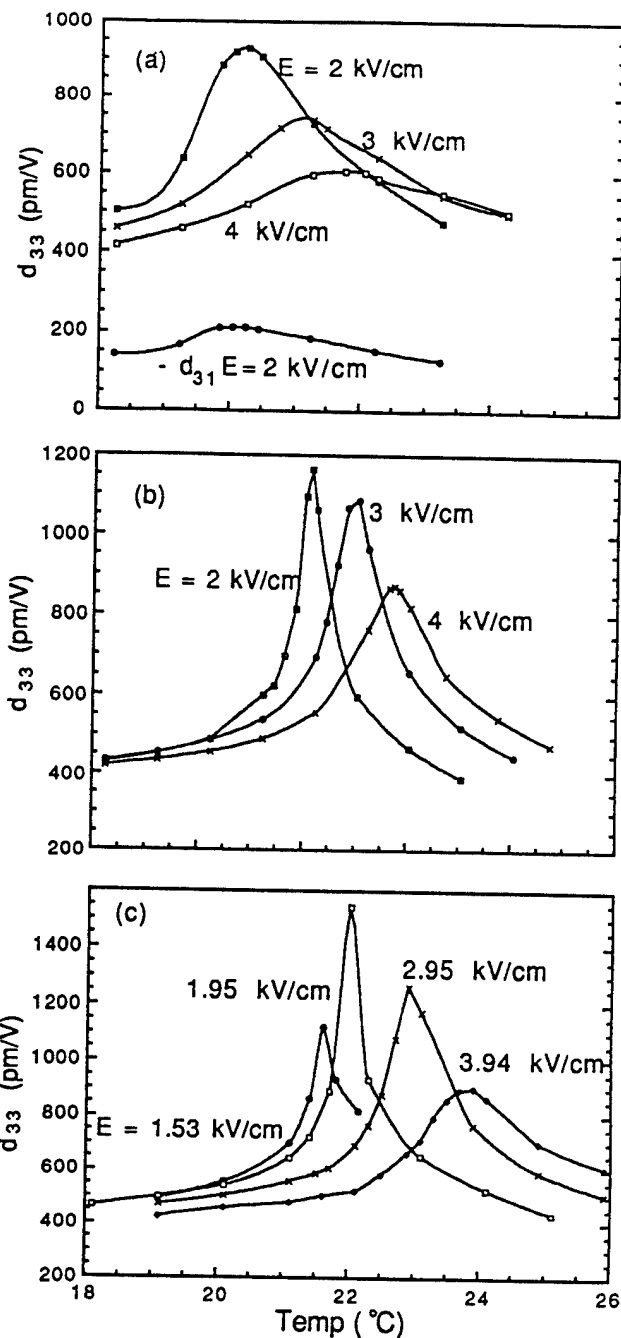


FIG. 4. The dc bias field dependence of the piezoelectric coefficients in the field tuned piezoelectric state as a function of temperature for (a) BST1; (b) BST2; (c) BST3 samples.

BST samples as a function of temperature acquired under different dc electric bias fields. For BST1, the peak value of the dielectric constant decreases progressively as the dc bias field increases, a typical characteristic for a continuous transition. For BST2, the dielectric constant maximum rises slightly with increased dc electric bias field, before dropping to lower values at higher dc bias fields. Therefore, the transition in BST2 is near the boundary between a first order and a continuous transition, i.e., near a tricritical point. In contrast, for BST3 samples, as the dc bias field increases, the

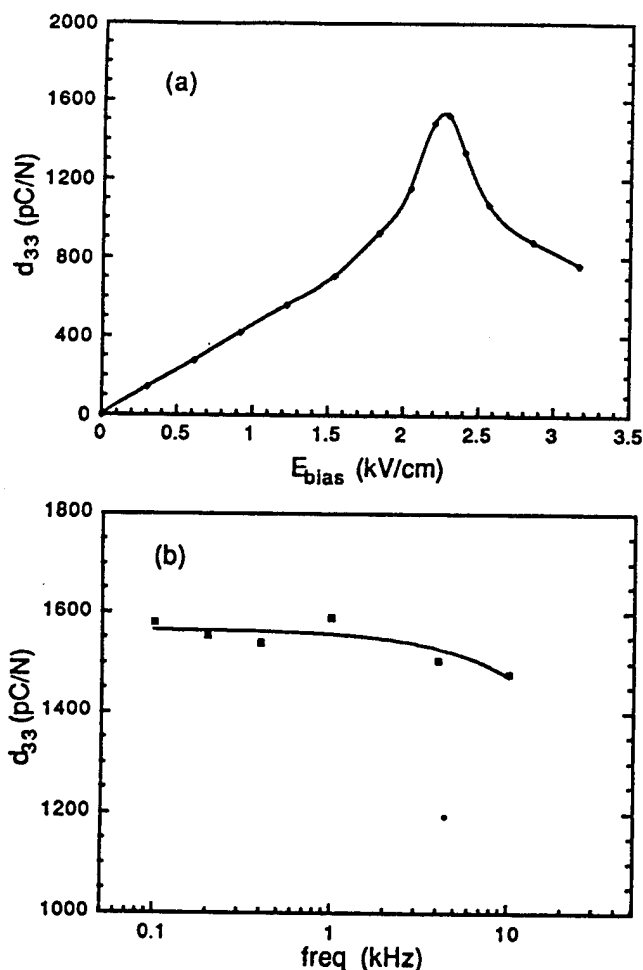


FIG. 5. The induced piezoelectric coefficient for BST3 (a) as a function of dc bias field; (b) as a function of frequency at a temperature=22.2 °C (the critical temperature).

dielectric constant maximum exhibits a marked increase. At the critical point (with $E_c = 1.95$ kV/cm), the dielectric peak reaches its maximum value and the transition behavior is very much like a continuous one. As the dc bias field increases further, the peak value of the dielectric constant subsides. These are the features expected for a first order transition as explained above using the phenomenological theory. The temperature difference between the critical point and the transition temperature at zero bias field for BST3 is about 1 °C, which is significantly smaller than that for pure BaTiO₃, in which this difference is about 9 °C.⁴ Substituting Ba with Sr apparently weakens the first order PF transition.

The piezoelectric constants for the three BST materials are shown in Fig. 4 determined at a frequency of 1 kHz. As the PF transition becomes more first order, the peak value of the induced piezoelectric constant increases, which is consistent with theoretical results. For BST1, the maximum induced d_{33} is found to be 925 pm/V and for BST2, 1150 pm/V. For BST3, which shows a clear first order transition, under the critical dc bias field (1.95 kV/cm), the induced d_{33} reaches 1550 pm/V. The frequency dependence of the induced piezoelectric constant was also characterized and is

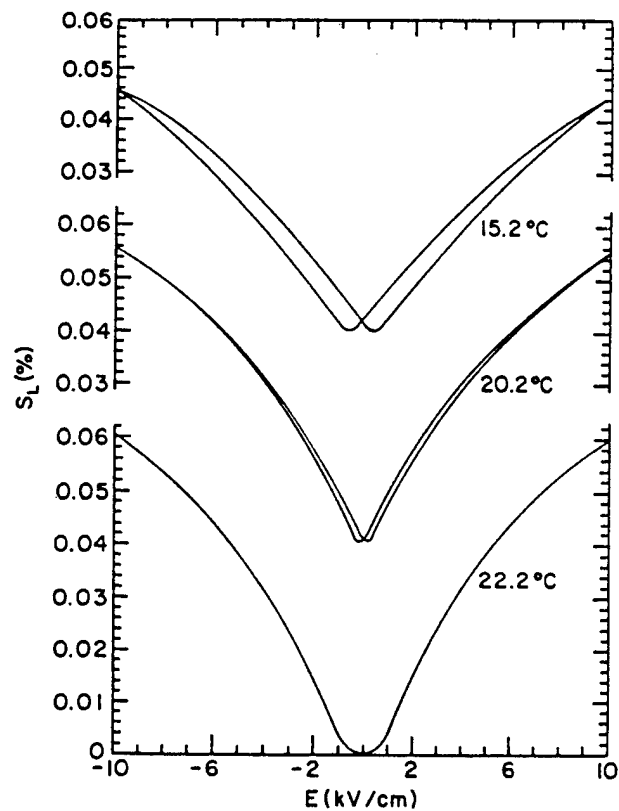


FIG. 6. The longitudinal strain hysteresis loop for BST3 at temperatures near the PF transition.

shown in Fig. 5 for BST3. The piezoelectric coefficient shows very little frequency dispersion compared with that of PMN-PT relaxor materials.⁶ As indicated in Eq. (8), a material with a strong first order PF transition, that is, a large $T_c - T_u$, will yield a large induced piezoelectric response and since in BST3, $T_c - T_u$ is only 1 °C, which is far smaller than that of BaTiO₃, significantly higher induced d_{33} value

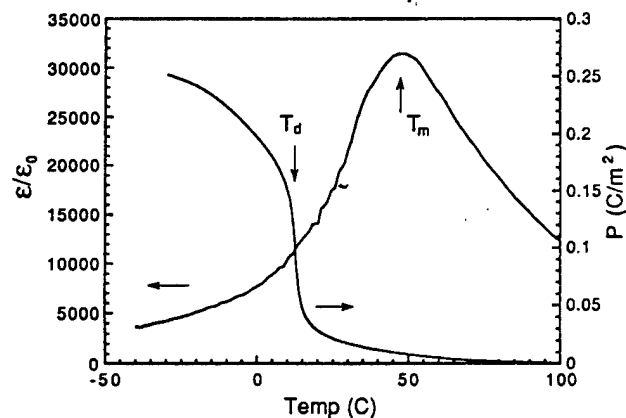


FIG. 7. The dielectric constant (at 1 kHz) and remanent polarization as a function of temperature for PMN-PT (0.9–0.1) near the diffused phase transition region. Notice the temperature difference between T_d and T_m .

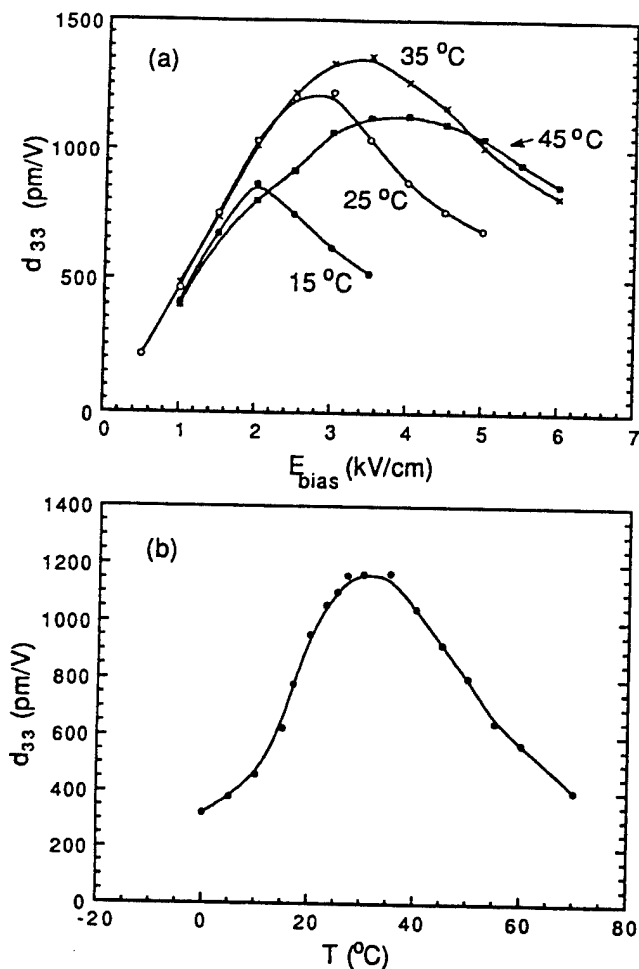


FIG. 8. (a) The piezoelectric coefficient of PMN-PT (0.9-0.1) as a function of dc bias field at different temperatures; (b) d_{33} as a function of temperature at $E_b=2.5$ kV/cm. All the measurements were made at 800 Hz frequency.

should be achievable for ceramics fabricated with larger $T_c - T_r$.

The strain hysteresis loop for BST3 was measured in the temperature range near the PF transition and the data are presented in Fig. 6, which were taken at a rate of one cycle per second. Near the phase transition temperature, a relatively high strain can be induced ($x_3=0.06\%$ under a 10 kV/cm driving field) with very little hysteresis. From the strain measurements, the electrostrictive coefficients Q_{11} and Q_{12} were determined for BST3 near the PF transition (22 °C) with $Q_{11}=0.043$ and $Q_{12}=-0.012$ m⁴/C², respectively. In the temperature range measured (from 15 to 26 °C), Q_{ij} is found to be nearly temperature independent. From Q_{11} , d_{33} can be evaluated using the relation $d_{33}=2Q_{11}\epsilon P$ and $d_{33}=1,600$ pm/V for BST3 at the critical point, where $P=7$ μ C/cm² (from the polarization hysteresis loop) and $\epsilon\epsilon_0=30\,000$ are used. This is very close to the d_{33} value directly measured.

III. RESULTS FROM RELAXOR MATERIALS (PMN-PT)

Owing to many unique features, ferroelectric relaxor materials, most notably the lead magnesium niobate-lead titan-

TABLE III. The comparison of BST samples and PMN-PT (0.9-0.1) sample.

	d_{33} (max) (pm/V)	E_{bias} (kV/cm)	FWHM (°C)
PMN-PT (0.9-0.1)	1350	3.3	40
BST1	925	2	6
BST2	1150	2	2
	865	4	9
BST3	1550	1.97	1.2
	900	3.94	10

ate $[(1-x)\text{PMN}-x\text{PT}]$ family, have become one of the most important transducer materials.⁷ In most applications, the material is operated in the temperature region near the broad dielectric constant maximum, termed as the diffused phase transition (DP) region. Typical data for the dielectric constant and the remnant polarization near the DP region are plotted in Fig. 7, which are taken from PMN-PT (0.9-0.1) composition. Besides the broad dielectric constant peak and its strong frequency dependent behavior (not shown in the figure), there is a large temperature difference between the dielectric constant maximum T_m and the depolarization temperature T_d where the remnant polarization decreases precipitously, a feature distinctively different from a regular first order and continuous PF transitions. The induced piezoelectric constant d in this type of material can be related approximately to the polarization P and dielectric permittivity ϵ through

$$d=2\epsilon QP, \quad (9)$$

where Q is the corresponding electrostrictive coefficient.⁶ The maximum induced piezoelectric constant will depend on $T_m - T_d$ which will be elucidated in the following section.

Unlike the first order and continuous PF transitions where the theoretical understanding is relatively well established, a rigorous theoretical treatment on the transition behavior in relaxor materials is still lacking. However, a coherent picture on this type of material is emerging⁷ and many of the properties can be understood qualitatively. For a relaxor material, like PMN-PT, many of its properties resemble those of random field system as well as those of spin glass.^{8,9} For a random field system, where the ferroelectric long range ordering is destroyed by the local random fields, the broad dielectric constant peak is related to the dynamics of the micropolar domains. Therefore, from the consideration of the dynamic scaling of a random field system,¹⁰ imposing a dc bias field on a relaxor material, which will increase the coherent length of the polar region, will reduce the dielectric constant maximum and broaden the dielectric constant peak (measured by the full temperature width at half peak maximum) as have been observed by many previous experiments.

One conclusion which can be drawn from Eq. (9) is that in order to have a large induced piezoelectric response in a material, it is necessary to have a large dielectric constant and polarization level concomitantly. The induced polarization will increase monotonically with the dc bias field, while at temperatures above T_d the dielectric constant subsides as the dc field increases due to the reasons presented. To induce a fixed polarization level P , a lower bias field is needed

when the temperature is closer to T_d . Therefore, the highest induced piezoelectric coefficient peak will be located at a temperature between T_m and T_d and a material with a smaller $T_m - T_d$ will have a larger induced piezoelectric response. On the other hand, if a small temperature variation of the induced piezoelectric coefficients is required, a material with a larger $T_m - T_d$ should be used.

Various characteristics of the induced piezoelectric response of PMN-PT (0.9–0.1), a typical relaxor material, at room temperature have been investigated by Pan *et al.*⁶ The data presented here are related to the temperature dependence behavior of the induced piezoelectric constant since the material properties are temperature sensitive. Shown in Fig. 8 are the field dependence of the induced piezoelectric coefficient at various temperatures measured at 800 Hz. The maximum induced d_{33} for this material is 1350 pm/V occurred at about 35 °C, which is between T_m and T_d (Fig. 7). Although the induced d_{33} at a constant dc bias field varies with temperature [Fig. 8(b)], the rate of the change is much smaller for PMN-PT (0.9–0.1) compared with those of BST samples. Since in most applications, a large induced d_{33} is highly desirable and the induced piezoelectric state is operated near the piezoelectric coefficient peak region, as a quantitative measure of the temperature changing rate, we introduce the notion of the full temperature width at half peak maximum (FWHM). In Table III, a comparison is made for BST samples and PMN-PT (0.9–0.1). The table reveals that there is a trade off between the maximum value and the temperature variation of the induced piezoelectric coefficient.

IV. SUMMARY

This article examined the characteristics of perovskite-type ferroelectric materials near the PF transition region. The

results demonstrate that by making use of the unique features of materials near a PF transition, a large electromechanical response can be achieved. For example, a d_{33} of 1550 pm/V with very little frequency dispersion has been obtained in the induced piezoelectric state in (BaSr)TiO₃ ceramic. It is also shown that there is a large difference in the way of the material properties responding to the dc bias electric field among a first order, a continuous, and a relaxor diffused transitions and this difference can be used to identify the type of a transition. The comparison among the materials with three types of transitions indicates that besides the relaxor materials, there are other materials having a large induced piezoelectric response and reasonable operation temperature range.

ACKNOWLEDGMENTS

The part of the work at Penn State University was supported in part by the Office of Naval Research and in part by a grant from the Texas Instruments Inc.

¹M. E. Lines and A. M. Glass, *Principles and Applications of Ferroelectrics and Related Materials* (Clarendon, Oxford, 1977).

²A. F. Devonshire, *Philos. Mag.* **3**, 85 (1954).

³B. Jaffe, W. R. Cook, and H. Jaffe, *Piezoelectric Ceramics* (Academic, London, 1971).

⁴F. Jona and G. Shirane, *Ferroelectric Crystals* (Dover, New York, 1993).

⁵Q. M. Zhang, S. J. Jang, and L. E. Cross, *J. Appl. Phys.* **64**, 6445 (1989).

⁶W. Y. Pan, W. Y. Gu, D. J. Taylor, and L. E. Cross, *Jpn. J. Appl. Phys.* **28**, 653 (1989).

⁷L. E. Cross, *Proceedings of the IUMRS, Iwakura, Tokyo*, 1993.

⁸Q. M. Zhang, W. Y. Pan, A. S. Bhalla, and L. E. Cross, *J. Am. Ceram. Soc.* **72**, 599 (1989).

⁹D. Viehland, M. Wuttig, and L. E. Cross, *Ferroelectrics* **120**, 71 (1991).

¹⁰V. Westphal, W. Kleemann, and M. D. Glinchuk, *Phys. Rev. Lett.* **68**, 847 (1992).

¹¹D. S. Fisher, *Phys. Rev. Lett.* **56**, 416 (1986).

APPENDIX 55

Electromechanical Properties of Relaxor Ferroelectric Lead Magnesium Niobate-Lead Titanate Ceramics

J. ZHAO, Q. M. ZHANG*, N. KIM and T. SHROUT

Intercollege Materials Research Laboratory, The Pennsylvania State University, University Park, PA 16802, USA

(Received April 6, 1995; accepted for publication July 17, 1995)

In this paper, the results of a recent investigation of the dependence of the induced piezoelectric activity on temperature, electric bias field, and frequency and the electrostrictive response in the relaxor ferroelectric lead magnesium niobate-lead titanate ceramics $((1-x)(\text{Pb}(\text{Mg}_{1/3}\text{Nb}_{2/3})\text{O}_3)-x(\text{PbTiO}_3))$ at compositions below 30% PT are presented. It was observed that the electrostrictive strain at temperatures near the dielectric constant maximum T_{max} increases monotonically with increased PT content. For PMN:PT at compositions near 30% PT, the electrostrictive strain under a 10 kV/cm electric field can reach about 0.15% with very little hysteresis. An exceptionally large piezoelectric response with an effective piezoelectric d_{33} coefficient in the electric field induced state of over 1,800 pC/N could be achieved for selected PMN:PT compositions and electric bias fields.

KEYWORDS: electrostriction, piezoelectricity, relaxor ferroelectrics, actuator and transducer, phase transition

1. Introduction

Electrostriction exists in all materials, however, it was not until the introduction of relaxor ferroelectric materials in the late seventies that this phenomenon began to attract attention for electromechanical transducer applications.^{1,2)} Compared with piezoelectric ceramics such as lead zirconate-titanate (PZT) ceramics, relaxor ferroelectric materials offer relatively high electric field induced strain ($\sim 0.1\%$) with a minimal hysteresis effect.³⁾ Moreover, since no poling process is involved, electrostrictive relaxor materials do not suffer strain aging or creep, as found in most piezoceramic materials, limiting their use in certain applications.⁴⁾

In general, an electrostrictive material can be operated either in the electrostrictive mode or in the electric field biased piezoelectric mode. In the former case, a large polarization and large electrostrictive coefficient are necessary for a material to exhibit a large electric field induced strain or electromechanical coupling. In the latter case, a DC electric bias field is applied onto the specimen to induce a bias polarization, analogous to the biased magnetostriction phenomenon, and the piezoelectric coefficient d_{33} (or d_{31}) is related to the polarization level P and the dielectric permittivity ϵ_{33} in the field biased state through approximately:

$$d_{33} = 2Q_{11}P\epsilon_{33} \quad (\text{or } d_{31} = 2Q_{12}P\epsilon_{33}) \quad (1)$$

where Q_{11} and Q_{12} are the longitudinal and transverse electrostrictive coefficients of the material, respectively. Clearly, a large polarization and a large dielectric constant in the induced piezoelectric state are required in order to have a large induced piezoelectric coefficient.

Relaxor ferroelectrics are characterized by their very broad dielectric constant peak. At temperatures near T_{max} (the temperature of dielectric constant maximum, which is frequency dependent), a large electrostrictive strain can be induced.⁴⁾ The high dielectric permittivity near T_{max} can also be utilized to improve the piezoelectric response in the induced piezoelectric state, as

indicated by eq. (1). For a relaxor ferroelectric, there is another characteristic temperature, the depolarization temperature T_d , which lies lower than T_{max} and also plays an important role in determining the electromechanical behavior of the material.

In this paper, the results of a recent experimental investigation on the electromechanical behavior, i.e. the electrostriction and electric bias field induced piezoelectricity, in PMN:PT relaxor ceramics will be presented. The electrostrictive behavior and induced piezoelectric effect of PMN:PT at low PT content (near 10% PT) has been studied earlier.^{1,5-7)} In the earlier studies, it was found that in 0.9PMN:0.1PT, a large electrostrictive strain of up to 0.1% could be induced with an electric field of 10 kV/cm. In addition, a large piezoelectric coefficient d_{33} in the field induced piezoelectric state of 0.9PMN:0.1PT was also demonstrated by Nakajima *et al.*, where the measurement was performed under near static condition.⁵⁾ More recently, Pan *et al.* investigated the induced piezoelectric effect in PMN:PT with low PT content (below 10% PT) at room temperature and showed that an electric field tunable piezoelectric state can be established in this type of material with a piezoelectric coefficient d_{33} as high as 1,000 pC/N, far above those obtainable in regular piezoelectric materials. However, in that study, the temperature dependence of the induced piezoelectricity was not characterized.⁶⁾

Shown in Fig. 1 is the phase diagram of PMN:PT. It is well known that at PT content below the morphotropic phase boundary (at about 30% PT), the material exhibits relaxor ferroelectric behavior.^{8,9)} Here, a brief discussion is presented concerning the general evolution behavior of the electrostrictive strain S and induced piezoelectric response with PT content. The discussion is based on eq. (1) for the piezoelectric response and the relation of $S = QP^2$ for the electrostrictive strain.

One interesting feature of Fig. 1 is that as PT content increases, the temperature difference $T_{\text{max}} - T_d$ decreases.^{9,10)} From the phenomenological theory, it can be shown that the energy barrier to induce a ferroelectric state decreases as the temperature approaches that of the ferroelectric-paraelectric transition from

*Corresponding author.

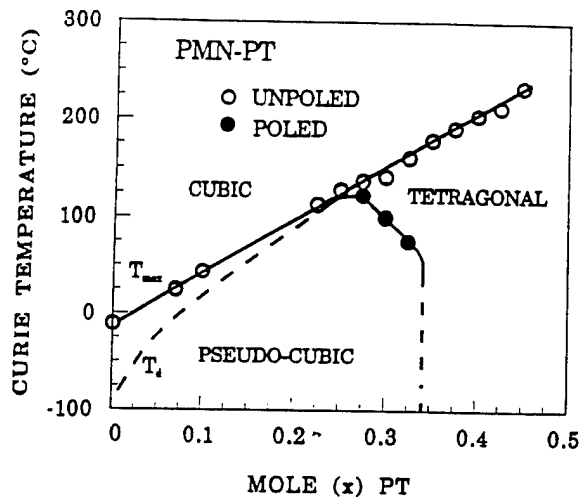


Fig. 1. Phase diagram of PMN:PT system.

above.¹¹⁾ Therefore, as temperature gets closer to T_d from above, the induced polarization P will increase for a given applied electric field. As a result, it is expected that the electrostrictive strain under a given electric field at temperatures near T_{max} will increase with PT content since T_{max} moves closer to T_d with increased PT content. By the same argument, the field biased piezoelectricity at temperatures near T_{max} should also increase. In addition, as will be shown later, the electrostrictive coefficients also increase with PT content, resulting in a further increase in the electromechanical response of the materials with increased PT content. On the other hand, as PT content increases, it is well known that the material moves progressively towards normal ferroelectrics,⁸⁾ which may cause increased hysteresis due to the increase in the energy barriers to switch polarization vectors among different equivalent states and hence, a reduction in the dielectric constant and consequently, a reduction of piezoelectricity in the field biased state. It is one of the objectives of this investigation to examine how these competing effects influence the electromechanical behavior of this family of material in the relaxor region (PT content less than 30%). In addition, the temperature and frequency dependence of the induced piezoelectricity and electrostriction was also characterized.

2. Experimental Procedure

The PMN:PT ceramics with different PT contents selected for this study are listed below: (1) 0.9Pb($Mg_{1/3}Nb_{2/3}$)O₃:0.1PbTiO₃, (2) 0.8Pb($Mg_{1/3}Nb_{2/3}$)O₃:0.2PbTiO₃, (3) 0.72($Mg_{1/3}Nb_{2/3}$)O₃:0.28PbTiO₃.

Among these three compositions, 0.9PMN:0.1PT exhibits typical relaxor behavior and 0.72PMN:0.28PT is very near the morphotropic phase boundary where the behavior of the material will be affected strongly by the increased normal ferroelectricity, and 0.8PMN:0.2PT is a composition between the two.

The ceramic samples across the series were prepared using the columbite precursor method as described by Swartz and Shrout.¹²⁾ In this processing, reagent grade

MgO and Nb₂O₅ are first reacted to form the columbite structure $MgNb_2O_6$ which is then reacted with PbO and TiO₂ to form $Pb(Mg_{1/3}Nb_{2/3})O_3:PbTiO_3$ compositions. Completion of the reactions was verified using X-ray diffraction, which was also used to determine the appropriate structure. After milling, the various powders were cold pressed to form disks, followed by sintering at temperatures near 1250°C for 4–6 h and then annealed in O₂ atmospheres at 900°C for about 6 h.

The weak field dielectric properties were determined with a HP multi-frequency LCR meter (HP4274) and the temperature dependence of the remanent polarization was characterized by the Byer-Roundy technique.¹³⁾ The dielectric properties at high driving fields were evaluated using a Sawyer-Tower circuit.¹⁴⁾ The piezoelectric coefficient d_{33} in the induced piezoelectric state and electrostrictive strain were measured by a double beam laser ultra-dilatometer, which was described in an earlier publication.¹⁵⁾

3. Experiment Results and Discussions

3.1 Dielectric constant and polarization data

The dielectric constant measured at 1 kHz and remanent polarization vs temperature for the three compositions are shown in Fig. 2. One salient feature of the data is that the temperature of maximum dielectric constant, T_{max} , does not coincide with the temperature of depolarization T_d , a feature distinctively different from normal ferroelectrics. The temperature difference $T_{max} - T_d$ decreases as the PT content increases, consistent with the earlier observations. With increased PT content, the dielectric peak sharpens, indicating a gradual approach toward normal ferroelectric behavior.

3.2 Electrostrictive behavior

The electrostrictive strain was characterized for these materials at temperatures near T_{max} since this is the region where the materials are most likely to be utilized as electrostrictive materials. Shown in Fig. 3 are the typical strain response curves acquired at 1 Hz. Very little hysteresis was observed. The data presented for 0.9PMN:0.1PT at room temperature is similar to that previously reported.⁶⁾ The materials with higher PT content exhibit larger electrostrictive strains. In Table I, the electrostrictive coefficients Q_{11} and Q_{12} at temperatures near T_{max} are presented. The data for PMN are taken from ref. 6. Apparently, the electrostrictive coefficients increase as PT content increases for the compositions investigated. In Fig. 4, the electrostrictive strains measured at T_{max} under 10 kV/cm electric field for the three compositions are compared.

Table I. The electrostrictive coefficients for PMN:PT relaxor ferroelectrics

Composition	Q_{11} ($10^{-2} \times m^4/C^2$)	Q_{12} ($10^{-2} \times m^4/C^2$)
PMN	1.9	-0.61
0.9PMN:0.1PT	2.0	-0.65
0.8PMN:0.2PT	2.24	
0.7PMN:0.3PT	2.5	-0.88

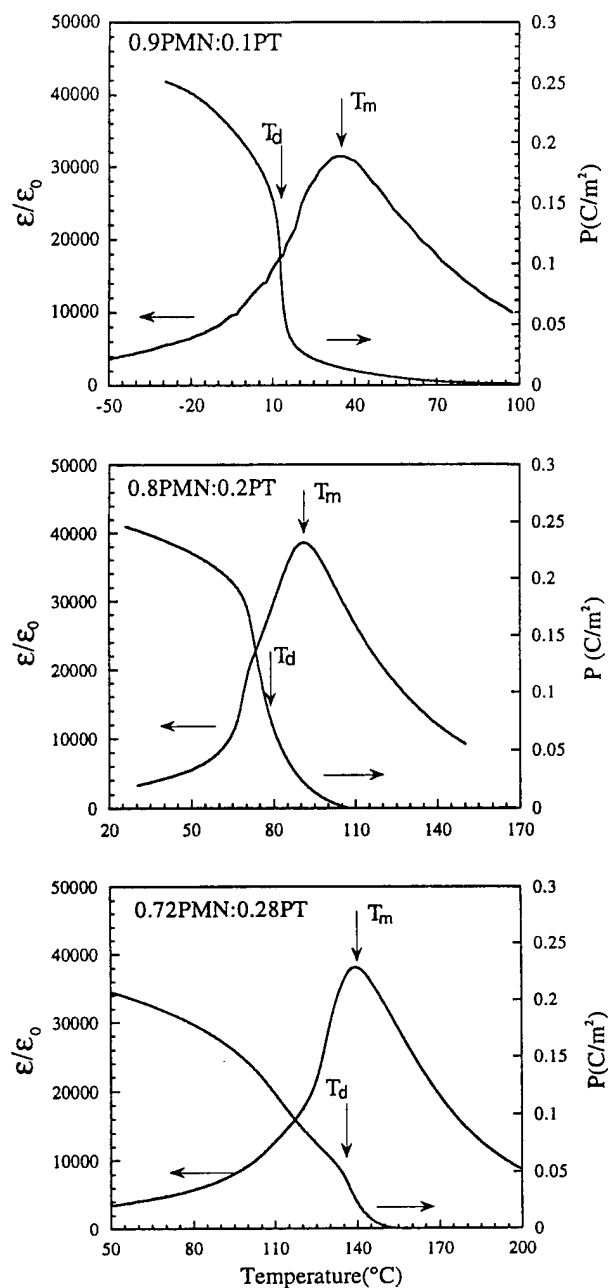


Fig. 2. The dielectric constant (at 1 kHz) and remanent polarization as a function of temperature for 0.9PMN:0.1PT, 0.8PMN:0.2PT, and 0.72PMN:0.28PT. The depolarization temperature T_d is defined as the temperature of the maximum of the derivative of polarization with temperature.

Also shown in the figure is the induced polarization under the same electric field at T_{\max} . Clearly, the rise in the electrostrictive strain S from 0.9PMN:0.1PT to 0.72PMN:0.28PT is caused by both the increase in the electrostrictive coefficients Q and the increase in the induced polarization P with PT ($S=QP^2$) the latter is a result of a smaller $T_{\max} - T_d$ at higher PT content.

3.3 Piezoelectric response in the electric field biased state

Presented in Fig. 5 are the induced piezoelectric

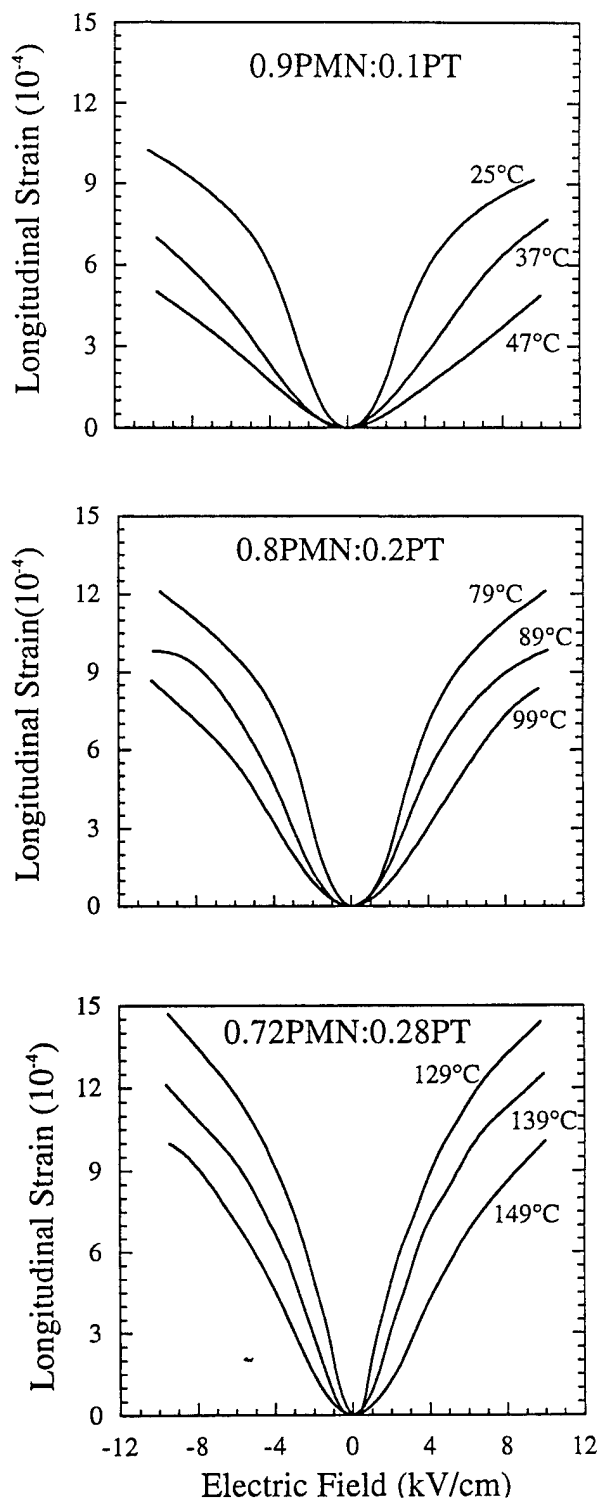


Fig. 3. The electrostrictive strain for 0.9PMN:0.1PT, 0.8PMN:0.2PT, and 0.72PMN:0.28PT at temperatures near T_{\max} . The measuring frequency is 1 Hz and the maximum electric field is 10 kV/cm.

coefficient d_{33} as a function of temperature and DC bias field measured with an AC field amplitude of 0.1 kV/cm at 1 kHz. For all three compositions, d_{33} increases and reaches a maximum with increasing DC bias field, after that, d_{33} drops as the DC bias field is further in-

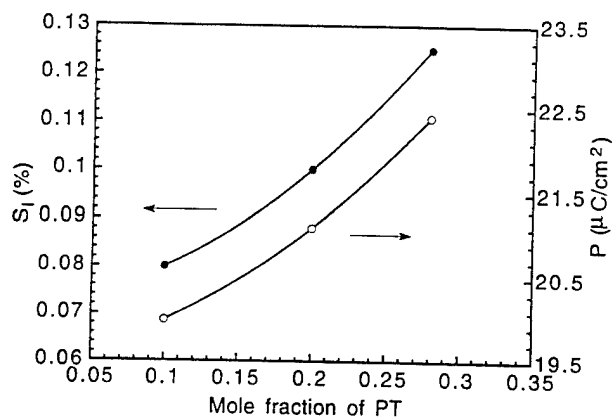


Fig. 4. The comparison of the electrostrictive strains and polarization measured at 1 Hz with 10 kV/cm electric field for 0.9PMN:0.1PT, 0.8PMN:0.2PT, and 0.72PMN:0.28PT. The black dots and open circles are the data points taken at their respective T_{\max} for the three compositions. The solid lines are drawn to guide the eye.

creased. This is expected because the polarization of the materials increases monotonically with DC bias field and will saturate at high DC bias field level, while the dielectric constant decreases with increasing DC bias field, as observed here and also in other investigations.^{10,16} It is the combination of the two effects, i.e., the polarization and dielectric permittivity, that determines how the induced piezoelectric response behaves.

For 0.9PMN:0.1PT composition, the maximum d_{33} in the induced piezoelectric state occurs at 35°, a temperature in between T_{\max} and T_d , which has a value about 1,360 pC/N. Increasing temperature above T_{\max} causes a reduction in the induced d_{33} .

The piezoelectric coefficient d_{33} for 0.8PMN:0.2PT in the field induced piezoelectric state is higher than those of 0.9PMN:0.1PT in the temperature region near their respective T_{\max} , as would be expected since $T_{\max} - T_d$ is smaller for 0.8PMN:0.2PT. The peak value of d_{33} for this composition reaches 1,820 pC/N, which is perhaps the highest d_{33} value ever obtained in a ceramic material.

However, as the PT content increases further, the induced piezoelectric coefficient d_{33} decreases as shown in the data for 0.72PMN:0.28PT even though $T_{\max} - T_d$ for this composition is further reduced. Plotted in Fig. 6 are a comparison of the maximum induced d_{33} in the three compositions, which is in sharp contrast with the data presented in Fig. 4.

Figure 7 shows the piezoelectric d_{33} coefficient at a fixed DC bias field as a function of temperature for the three compositions. The slow drop of d_{33} at the low temperature side of the d_{33} vs. temperature curve for 0.72PMN:0.28PT is due to the existence of the morphotropic phase boundary which increases the piezoelectric response, similar to the enhanced piezoelectric response occurred near the morphotropic phase boundary in PZT piezoceramics.

Figure 8 shows the induced piezoelectric d_{33} coefficient as a function of the driving field frequency

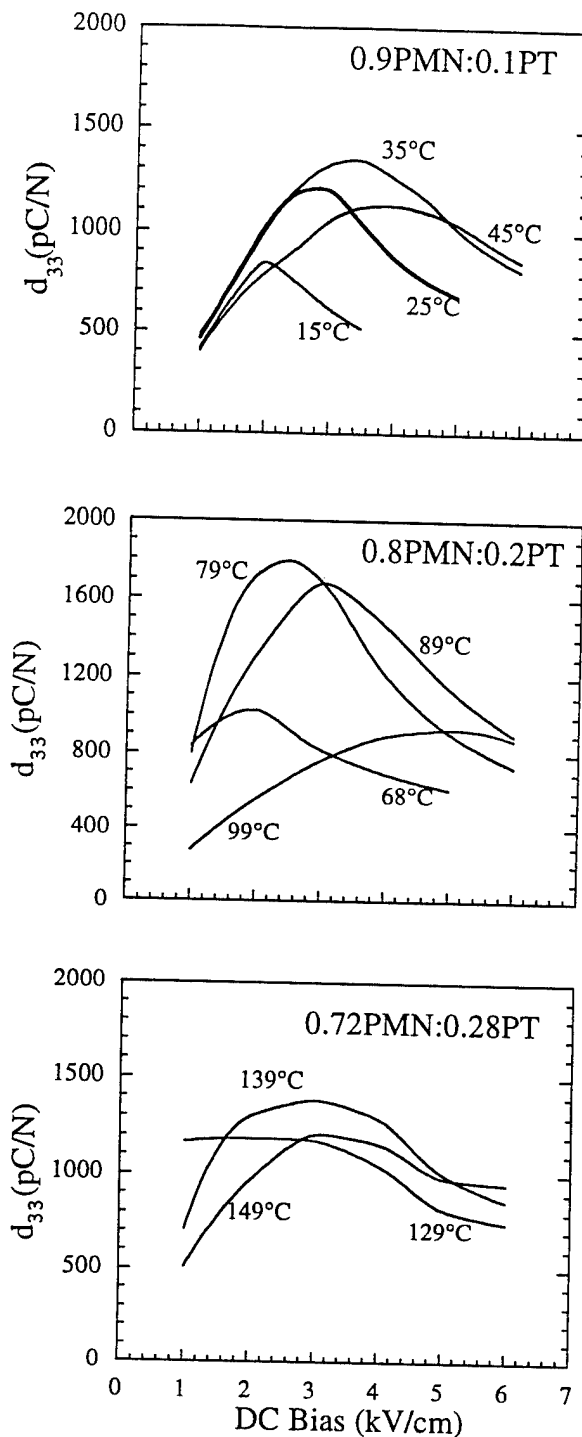


Fig. 5. The induced d_{33} coefficient at 1 kHz as a function of DC bias at different temperatures for 0.9PMN:0.1PT, 0.8PMN:0.2PT, and 0.72PMN:0.28PT.

for 0.8PMN:0.2PT (curve 1) measured at a bias field of 2.5 kV/cm and a temperature of 79°C. The significant dispersion of piezoelectric is due to well known dielectric dispersion which is not shown in Fig. 2. At low frequencies, the induced d_{33} for this composition approaches 2,000 pC/N. For the comparison, the data for 0.9PMN:0.1PT (curve 3), which were taken at 35°C and a bias field of 3 kV/cm, and for 0.72PMN:0.28PT

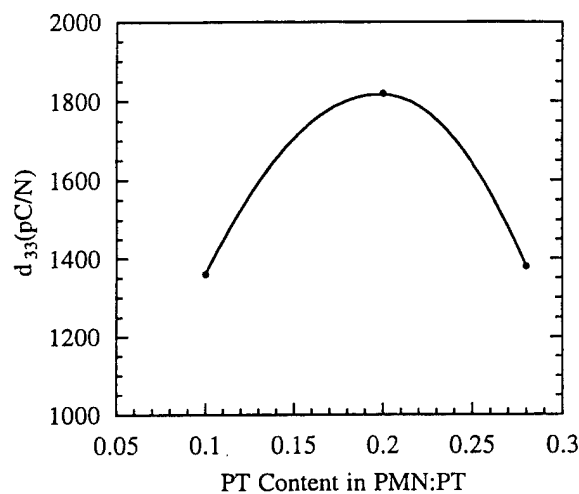


Fig. 6. The maximum electric field induced d_{33} for the three compositions investigated (measured at 1 kHz). The black dots are data points and solid line is drawn to guide the eye.

(curve 2), which were measured at 139°C and a bias field of 2.5 kV/cm, are also presented. The rise of d_{33} at 100 kHz for 0.72PMN-0.28PT is due to the piezoelectric resonance in the sample.

The increase of the electric field induced piezoelectric activity as PT content increases from 10% to 20% is consistent with a smaller $T_{\max} - T_d$ favoring a large induced piezoelectric activity. However, the drop in the induced piezoelectricity observed for PMN:PT at 28% PT content indicates that at higher PT content, the increased normal ferroelectric behavior in the material plays an important role in determining the induced piezoelectric response in the field induced state. To verify that, the driving field dependence of the dielectric response was measured for 0.9PMN:0.1PT and 0.72PMN:0.28PT at their respective T_{\max} and the results are presented in Fig. 9. Apparently, as the material approaches normal ferroelectric, the microhysteresis increases, which does not affect the electrostrictive strain at high driving field level but will affect the weak field material response behavior. Due to the increased probability of formation of macropolar domains at high DC bias fields, the reduction of the weak signal dielectric constant with DC bias field becomes more severe at high PT content, which results in a smaller d_{33} , as shown by eq. (1).

4. Summary

Exceptionally high piezoelectric response in the field induced state was observed in PMN:PT relaxor ferroelectrics. The maximum d_{33} observed here is 1820 pC/N at a frequency of 1 kHz for 0.8PMN:0.2PT composition, which is far above any piezoelectric d_{33} coefficient reported in any ceramic materials hitherto. The results here show that the induced piezoelectricity strongly depends on the operation temperature and frequency. Although the temperature difference $T_{\max} - T_d$ decreases with increased PT content, which should favor a large induced piezoelectricity at temperatures

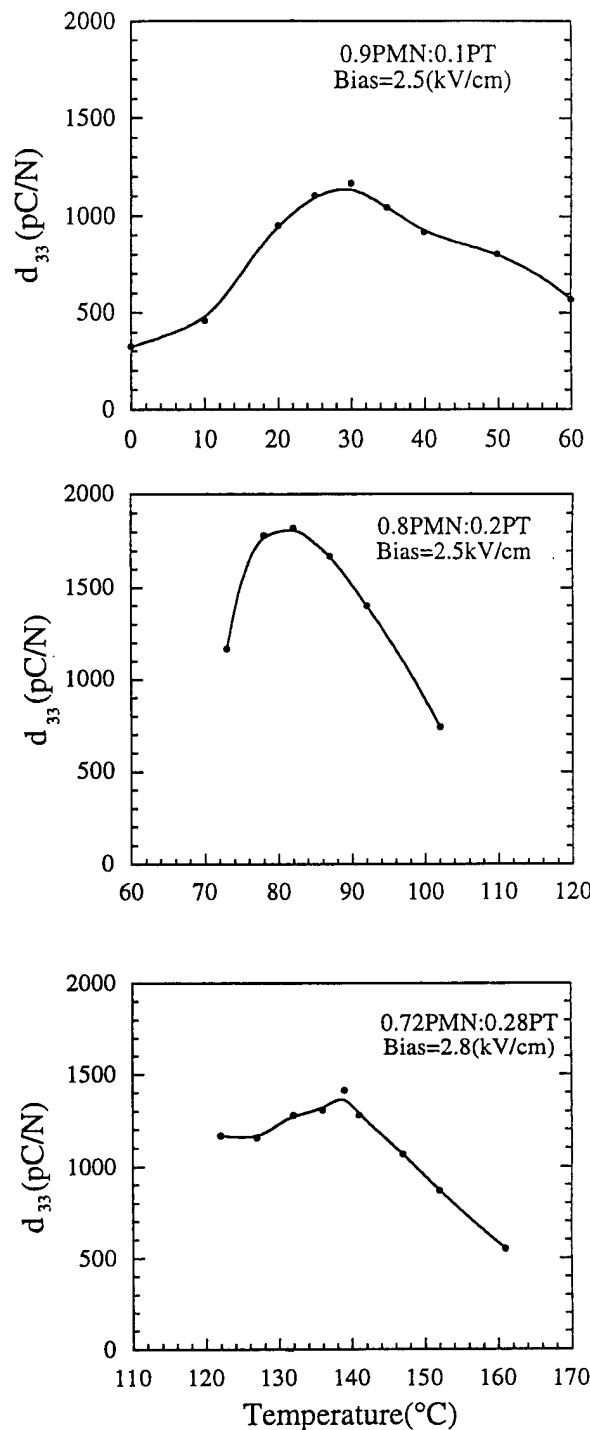


Fig. 7. The field induced d_{33} coefficient at 1 kHz and a fixed DC bias as a function of temperature for 0.9PMN:0.1PT, 0.8PMN:0.2PT, and 0.72PMN:0.28PT. The black dots are the data points and solid lines are drawn to guide the eye.

near T_{\max} for PMN:PT with high PT content, the gradual evolution towards normal ferroelectric behavior at high PT content will cause reductions in the field induced piezoelectricity due to increased amount of macro-domains at field biased states. As a result, the highest induced piezoelectricity occurs at a composition between the two ends and the data suggest that for

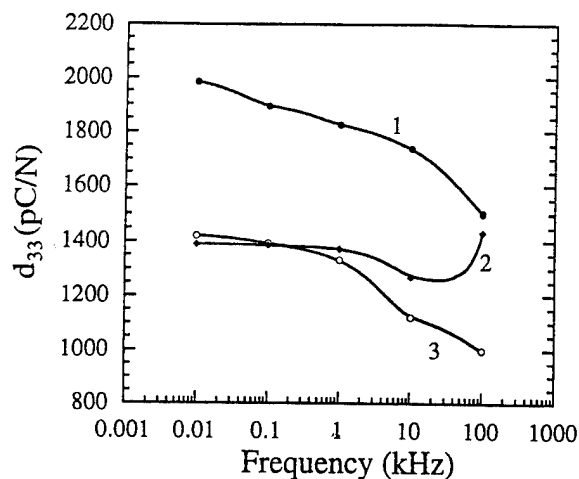


Fig. 8. The field induced d_{33} coefficient for the three compositions as a function of AC field frequency. For 0.8PMN:0.2PT (curve 1), the data were taken at 79°C and 2.5 kV/cm, for 0.9PMN:0.1PT (curve 3), it was at 35°C and 3 kV/cm, and for 0.72PMN:0.28PT (curve 2), it was at 139°C and 2.5 kV/cm. The black dots are the data points and solid lines are drawn to guide the eye.

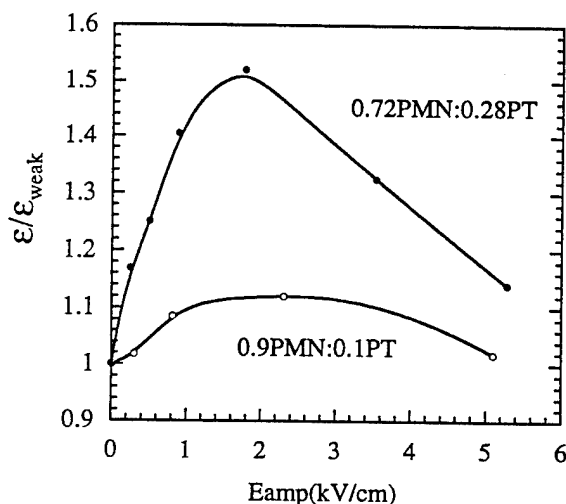


Fig. 9. The driving field amplitude dependence of the dielectric response for 0.9PMN:0.1PT and 0.72PMN:0.28PT measured at their respective T_{\max} . The data are plotted in the reduced unit where ϵ_{weak} is the dielectric permittivity measured at weak field (10 V/cm). There is a considerable increase in the dielectric response for 0.72PMN:0.28PT as the driving field amplitude increases in comparison with 0.9PMN:0.1PT. The black dots are the data points and solid lines are drawn to guide the eye.

PMN:PT, it is at a composition near 20% PT. On the other hand, the electrostrictive strain under high electric driving field (10 kV/cm) exhibits a steady increase with PT content, reflecting the steady increase of the electrostrictive coefficients and the reduction of $T_{\max} - T_d$ as the PT content increases.

Acknowledgment

This work was supported by Office of Naval Research and a grant from Tektronix Inc.

- 1) S. J. Jang, K. Uchino, S. Nomura and L. E. Cross: *Ferroelectrics* **27** (1980) 31.
- 2) K. Uchino, S. Nomura, L. E. Cross, S. J. Jang and R. E. Newnham: *J. Appl. Phys.* **51** (1981) 1142.
- 3) K. Uchino: *Am. Ceram. Bull.* **65** (1986) 647.
- 4) L. E. Cross: *Ferroelectrics* **76** (1987) 241.
- 5) Y. Nakajima, T. Hayashi, I. Hayashi and K. Uchino: *Jpn. J. Appl. Phys.* **24** (1983) 311.
- 6) W. Y. Pan, W. Y. Gu, D. J. Taylor and L. E. Cross: *Jpn. J. Appl. Phys.* **28** (1989) 653.
- 7) S. J. Jang: Ph. D. Thesis, The Pennsylvania State University, 1979.
- 8) S. W. Choi, T. R. Shrout, S. J. Jang and A. S. Bhalla: *Ferroelectrics* **100** (1989) 29.
- 9) T. R. Shrout and J. T. Fielding: *Proc. 1990 Ultrasonic Symp.* (1990) p. 711.
- 10) J. Fielding: Ph. D. Thesis, The Pennsylvania State University, 1993.
- 11) A. F. Devonshire: *Philos. Mag.* **3** (1954) 85.
- 12) S. L. Swartz and T. R. Shrout: *Mater. Res. Bull.* **17** (1982) 1245.
- 13) R. L. Ryer and C. B. Roundy: *Ferroelectrics* **3** (1972) 333.
- 14) Q. M. Zhang, W. Y. Pan, S. J. Jang and L. E. Cross: *J. Appl. Phys.* **64** (1989) 6445.
- 15) Q. M. Zhang, S. J. Jang and L. E. Cross: *J. Appl. Phys.* **65** (1989) 2807.
- 16) D. Viehland: Ph. D. Thesis, The Pennsylvania State University, 1991.

APPENDIX 56

Piezoelectric Properties of Fine Grain PZT Materials

M. J. Zipparo, K. K. Shung and T. R. Shrout

The Pennsylvania State University, University Park, PA 16801

Abstract: The piezoelectric properties of PZT materials were experimentally studied as a function of grain size (0.2 to 2.5 μm) at low frequencies (< 20 MHz) and vs. frequency (10 to 100 MHz) for a single fine grain size (1.0 μm). The piezoelectric properties were shown to decrease with decreasing grain size below 0.7 μm . The fine grain size properties vs. frequency were compared to commercially available materials. The new fine grain materials were found to be superior to commercial materials at very high frequencies. Also, it was possible to construct resonators of the new ceramics at much higher frequencies than was possible for the conventional materials.

INTRODUCTION

The properties of a transducer material play a vital role in determining the overall performance of an ultrasonic imaging system. Piezoelectric ceramic materials are used in a wide range of ultrasonic imaging applications. Multi-element arrays are generally used in the 5 to 10 MHz range, owing to good resolution with adequate penetration for general imaging which is achievable in this frequency range [1,2]. Higher frequency devices for specialized applications, where increased resolution is necessary and where the transducer can be placed very close to the region being imaged, have been introduced [3,4]. These devices are based on existing commercially available piezoelectric ceramics whose properties have been shown to decrease significantly with increasing frequency [5].

Current commercially available materials have an average grain size typically from 3 to 5 μm . Work by Arlt [6] has shown that at very high frequencies (> 100 MHz) a domain relaxation phenomenon leads to a decrease in piezoelectric properties and an increase in loss. He postulates that a similar effect due to the resonance of individual grains will influence the piezoelectric properties at much lower frequencies. The current work explores new materials which have been designed to have a microstructure whose average grain size (AGS) is smaller than 1.0 μm . Reducing the average grain size should push the domain relaxation and grain resonance effects to a higher frequency, resulting in improved high frequency piezoelectric properties and ultimately better images from systems which use the new materials.

In addition to material property considerations fine grain materials may provide an advantage in terms of manufacturability. The smaller grain size leads to an increased number of grains through the thickness of the material, perhaps leading to increased mechanical integrity of the ceramic, particularly for transducers operating at frequencies greater than 50 MHz where conventional materials provide few grains across the thickness of the material.

EXPERIMENTAL TECHNIQUE

Sample preparation

The effect of grain size on piezoelectric properties has been studied previously by Kim [7] where samples were prepared with grain sizes from 0.2 to 2.5 μm . Kim found that there was only a slight decrease in the piezoelectric constant, d_{33} , and the low frequency dielectric constant, ϵ_{33}^T , until the grain size was less than about 0.7 μm ; below this grain size the properties decreased considerably.

Thin plate samples of materials with grain sizes of 0.2, 0.8 and 2.5 μm were fabricated based on the work of Kim with thickness resonance frequencies less than 15 MHz. Based on these measurements the material with the best compromise between properties and grain size was chosen for analysis at high frequencies. For comparison purposes two commercial PZT5 type materials were also processed and tested at high frequency using the same method.

Samples were prepared by lapping of 1 cm diameter disks with an initial thickness of approximately 300 μm . Initial lapping utilized 12.5 μm Al_2O_3 powder suspended in a distilled water medium. Final lapping was done with 5.0 μm Al_2O_3 to give thickness resonators covering the range from 10 to 100 MHz. Samples prepared with a 0.03 μm final polish showed similar properties as those finished with the coarser powder so all samples were finished with the 5.0 μm powder.

After lapping to the desired thickness the disks were ultrasonically cleaned in acetone. A gold electrode was sputter deposited. The disks were then cut into squares so that the aspect ratio was between 20 and 40. This ensured that any lateral resonance would not interfere with the fundamental thickness mode. All samples, including the conventional materials, were then poled in a fluorinert bath at 60 degrees C for four minutes at an electric field of 40 kV/cm. The samples were allowed to age more than 24 hours before testing.

Piezoelectric property measurement

The piezoelectric properties of the samples were measured using the resonance method [8]. The properties of interest were: the thickness frequency constant, N_f ; the thickness coupling coefficient, k_t ; and the free dielectric constant, ϵ_{33}^T . The mechanical losses within the material were expressed as a mechanical quality factor, Q_m where a low Q_m corresponds to a high mechanical loss. The method of Ih and Lee [9] was used to calculate mechanical losses.

This method was chosen in favor of the IEEE standard method because of the error found in measuring the minimum impedance. This error was introduced by the resistance and inductance of the electrode which appeared in series with the impedance of the piezoelectric material. This effect was prominent because of the high frequencies where the measurements were performed.

All of the properties described above were calculated from electrical impedance measurements of a thin thickness resonator of known dimensions. The impedance was measured with an HP4194A impedance analyzer equipped with an HP41941B impedance probe adapter. The probe adapter, which allows measurements up to 100 MHz, was connected to a sample holder designed to not mechanically load small thin samples. The impedance analyzer was connected to a PC via a GPIB bus. This enabled the impedance measurements to be downloaded for ease of analysis.

The measurements were verified using the KLM model [10] with the addition of a mechanical loss term in the acoustic transmission lines. The calculated piezoelectric parameters were input into the modified KLM model to yield a simulated electrical input impedance which could be compared with the measured impedance to ensure the accuracy of the measured properties. Good agreement between the measured and simulated impedance confirmed that the measured piezoelectric parameters were accurate, as shown in figure 1 for the fine-grained PZT for both low and high resonance frequencies.

EXPERIMENTAL RESULTS

Properties vs. Grain Size

The low frequency (< 20 MHz) properties of the samples were tested for grain sizes of 0.2, 0.8 and 2.5 μm . Measurements shown in figure 2 confirmed that both the electromechanical coupling coefficient, kt , and the relative free dielectric constant, ϵ_{33}^T , maintained their values until grain size was below 0.8 μm . Based on these results a material with a 1.0 μm grain size was chosen for analysis at high frequencies.

The microstructure of the new fine-grained material (PZTFG) as well as that of two commercially available materials of a similar composition (PZT₁ and PZT₂) was analyzed using a scanning electron microscope (SEM). The results of the microstructure analysis are shown in figure 3. It is evident from the photos that the two commercial materials exhibit a grain size which is much larger than 1 μm , with PZT₁ having a slightly smaller AGS relative to PZT₂. Although the SEM photo of PZTFG is at a slightly lower magnification than that of the two commercial materials, it is clearly evident that the PZTFG has a much smaller AGS than either of the other two materials.

Properties vs. Frequency

The free dielectric constant, ϵ_{33}^T , was found to be essentially independent of frequency for all of the samples. This ensured that the samples were prepared without forming a large disturbed grain layer on the faces, as this would have been caused a marked decrease in the measured dielectric. Thus the variation of any other properties with frequency can be assumed to be due to the material itself rather than inadequate sample preparation.

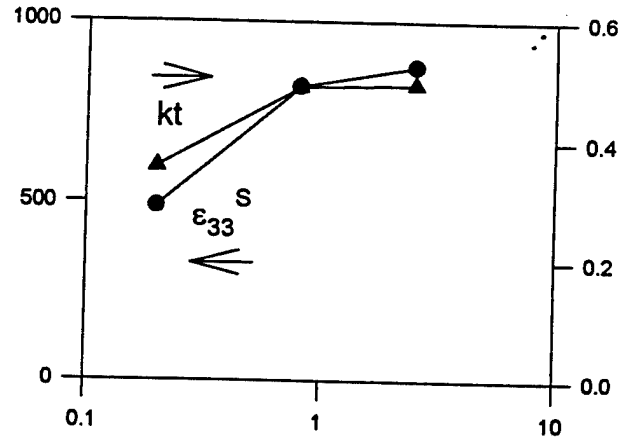


figure 2) piezoelectric properties vs. grain size

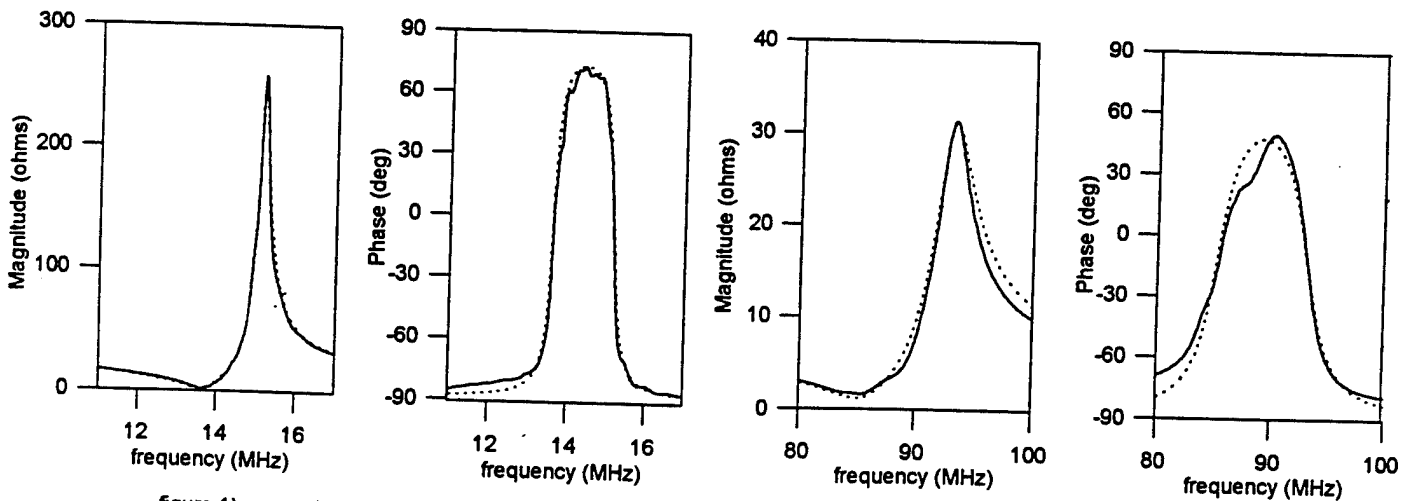


figure 1) comparison of measured (solid line) and modeled (dotted line) impedance magnitude and phase for fine-grained PZT

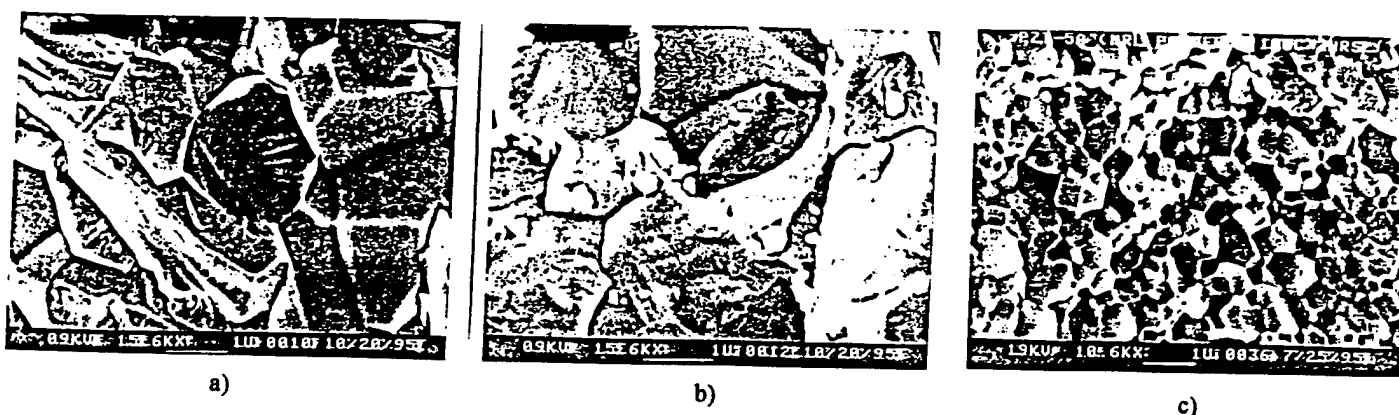


figure 3) SEM photos of a) PZT1, b) PZT2, c) fine-grained PZT

The piezoelectric properties of the various materials are shown vs. frequency in figure 4. Each point on the graph represents the average of up to three samples. It is important to note that for both commercial materials it was not possible to lap the disks to a thickness corresponding to a resonance above 80 MHz. For the PZT1 material the samples were too brittle and crumbled upon handling. Disks were lapped thin enough from the PZT2 material but they would not pole. Upon examination under an optical microscope it was found that tiny holes had formed through the disk. Owing to the relatively large grain size of the PZT2 material, grain pullout during lapping resulted in regions where upon sputtering there was a conductive path connecting the electrodes. This effect was not observed in the fine grain samples.

From figure 4a it is evident that the frequency constant, Nt , of the materials does not change appreciably as resonance frequency increases. Figure 4b shows that kt significantly decreases with frequency for the PZT1 material. This parallels the results

reported by Foster [5]. The fine-grained material was found to be as good as or slightly better than the PZT1 material at the lower frequencies, but at the higher frequencies the decrease in properties was less severe. The PZT2 material exhibited a slightly larger kt over the frequency range where resonators were fabricated using this material. However, resonators greater than 60 MHz could not be produced and there is likely a decrease in kt at higher frequencies.

The frequency dependence of Q_m for the three types of PZT is shown in figure 4c. Here the change in Q_m vs. frequency was found to be much steeper for the commercial materials than for the fine-grained material. The PZTFG material has a higher Q_m than the PZT2 material at all measured frequencies. Even though the PZT1 material has a higher Q_m at low frequencies, its steeper slope causes the PZTFG material to have a higher Q_m at frequencies greater than 70 MHz.

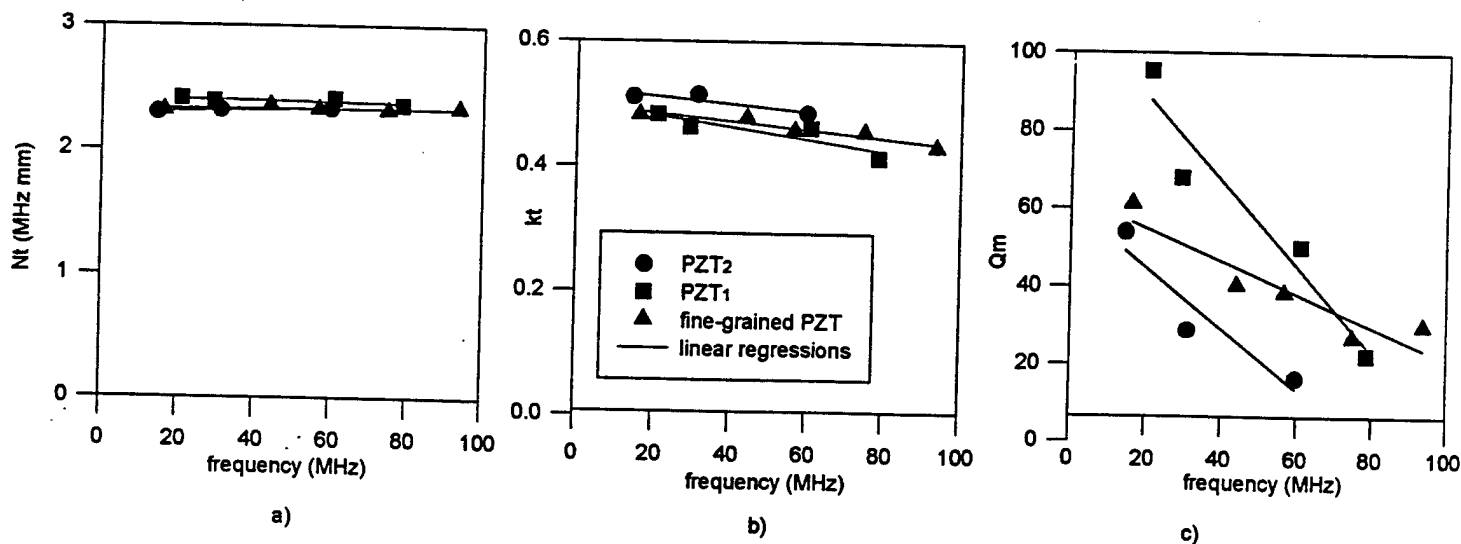


figure 4) Piezoelectric properties vs. resonance frequency

SUMMARY AND CONCLUSIONS

An experimental study has been performed in order to determine the piezoelectric properties of fine-grained PZT. No significant decrease in properties was observed until grain size falls below about 0.7 μm . A fine-grained material with an AGS about 1.0 μm was confirmed to be significantly finer than commercially available materials, which exhibited an AGS of 3 to 5 μm .

High frequency properties of the fine-grained and commercial materials were examined by preparing resonators of the appropriate thickness. The limitations of commercially available materials became apparent during processing, as it was not possible to prepare resonators greater than 80 MHz for the PZT1 material and 60 MHz for the PZT2 material. The fine-grained materials, however, allowed the preparation of plate thickness as thin as 15 μm , which corresponds to a thickness resonance of 155 MHz. Unfortunately the properties could not be measured at these frequencies due to limitations of the testing equipment.

Measurements up to 100 MHz showed improved performance of the fine-grained material at very high frequencies compared to larger-grained material. The change in both k_t and Q_m vs. frequency was lowest for the PZTFG material. The PZTFG material has a better k_t than the PZT1 material at all frequencies and a better Q_m above 70 MHz. While the PZT2 material does have a slightly higher k_t than PZTFG at low frequencies, it suffers from a low Q_m at all frequencies measured.

From a manufacturability and a performance point of view the fine-grained materials offer improvements compared to conventional materials for high frequency devices. The use of these new materials should ultimately lead to improved image quality for ultra-high resolution ultrasonic imaging systems.

REFERENCES

- [1] K. K. Shung, "General engineering principles in diagnostic ultrasound," IEEE En. Med. Biol. Mag., pp 7 - 13, Dec. 1987.
- [2] T. R. Gururaja, "Piezoelectrics for medical ultrasonics imaging," Amer. Ceram. So. Bull., vol 73, no. 5, pp 50 - 55, 1994.
- [3] K. A. Harasiewicz, et. al., "Ultrasound backscatter microscopy of articular cartilage in vitro," IEEE Ultrasonics Symposium Proceedings, pp 981 - 984, 1993.
- [4] D. H. Turnbull, et. al., "Ultrasound backscatter microscope for skin imaging," IEEE Ultrasonics Symposium Proceedings, pp 985 - 988, 1993.
- [5] F. S. Foster, "Characterization of lead zirconate titanate ceramics for use in high-frequency (20-80 MHz) transducers," IEEE Trans. Ultras. Fer. Freq. Cont., vol 38, pp 446 - 453, 1991.
- [6] G. Arlt, "Strong dielectric dispersion in ferroelectric ceramics at microwaves," Proc. 4th Intern. Conf. on Electronic Ceramics, pp 193 - 199, 1994.

[7] N. Kim, "Grain size effect on the dielectric and piezoelectric properties in compositions which are near the morphotropic phase boundary of lead zirconate-titanate based ceramics," Ph. D. dissertation, Penn State Univ., May 1994.

[8] IEEE Standard on Piezoelectricity, Std 176, 1978.

[9] J. Ih and B. Lee, "Attenuation coefficient of a piezoelectric resonator operating in a thickness mode," Electron. Lett., Vol. 22, pp 357 - 358, 1986.

[10] R. Krimholtz et. al., "New equivalent circuits for elementary piezoelectric transducers," Electron. Lett., Vol. 6, pp 398 - 399.

APPENDIX 57

Pb(Zr,Ti)O₃ [PZT] Fibers—Fabrication and Measurement Methods

SHOKO YOSHIKAWA,* ULAGARAJ SELVARAJ, PAUL MOSES, JOHN WITHAM, RICHARD MEYER AND THOMAS SHROUT
Materials Research Laboratory, The Pennsylvania State University, University Park, PA 16802

ABSTRACT: Fine scale lead zirconate titanate (PZT) and niobium substituted PZT (Nb-PZT) piezoelectric fibers were fabricated from sol-gel processed viscous "sol" using the "spinning" methodology developed for the continuous production of glass fibers. Subsequent drying and firing at above 750°C gave pure perovskite PZT and Nb-PZT fibers of 30 μm in average diameter. Further densification and grain growth were evident for fibers fired at 1250°C. Experimental methods for the determination of dielectric and polarization properties were developed to overcome inherent electric field difficulty relevant to fine scale fibers. The method to polarize fibers in a continuous manner was also demonstrated using 120 μm diameter extruded PZT fiber. The dielectric constant and polarization hysteresis values of the sol-gel derived fine fibers were comparable with that of bulk ceramics. Preliminary single fiber mechanical pull tests indicated that the tensile strength of 30 μm diameter PZT fibers were similar to that of bulk ceramics, being in the range of 35–55 MPa.

INTRODUCTION

LEAD zirconate titanate (PZT) piezoelectric ceramics' ability to efficiently convert electrical energy to mechanical and vice versa has made them attractive for both actuators and sensors in active control systems (Crawley and deLuis, 1987). This reversible transformation ability also makes piezoceramics viable candidates for passive vibration damping (Ramachandran et al., 1991; Hagood and von Flotow, 1991). For structural materials comprised of various fibers, i.e., glass and carbon, the incorporation of piezoelectric fibers is, therefore, inherently desired (Yoshikawa, 1992).

Previously, the fabrication of PZT fibers and/or rods has been driven by the need for high performance hydrophones (Klicker et al., 1981) and ultrasonic transducers (Gururaja et al., 1981). In such cases, PZT fibers/rods are fabricated simply by the dicing of bulk ceramics (Takeuchi and Nakaya, 1986), being limited to simple geometries on the order of a few millimeters in length and ~100 μm in cross section. Extrusion, the process by which a plasticized ceramic mass is passed through a die or orifice, provides the ability to fabricate meter length fibers with various cross-sectional geometries; however, they are again limited to diameters of ~100 μm (Park, 1991). For fibers with diameters less than 100 μm, non-conventional methods have been employed, including the impregnation of host fibers with a precursor solution (Waller et al., 1990) and hand drawing from a viscous sol (Seth, 1990; Chen et al., 1991; Selvaraj et al., 1992). Single strand fibers fabricated thus far have been limited to lengths of a few centimeters, being for dem-

onstration purposes only. No methods to polarize these free-standing fine fibers in longitudinal direction continuously have been established. PZT fibers are NOT "piezoelectric" unless electrically polarized (the term "poled" is commonly employed). Furthermore, little information regarding electrical and mechanical properties has yet to be reported.

It was the objective of this work to fabricate fine-scale PZT fibers using a "spinning" methodology developed for the continuous production of carbon and/or glass fibers. A further objective was to determine the electrical and mechanical properties of individual fibers prepared above.

EXPERIMENTAL PROCEDURE

PZT Fiber Fabrication

The advantages of sol-gel processing in the fabrication of ferroelectric thin films, i.e., compositional control, low-temperature densification and overall simplicity, make it the ideal methodology for the fabrication of fine-scale fibers. In the sol-gel process, a non-aqueous solution of precursors, generally alkoxides, is prepared with the metal cations in the desired stoichiometry, followed by controlled hydrolysis to form a "sol" and, subsequently, dried into a final gel-like structure.

The fabrication of PZT fibers in this work is outlined in Figure 1. As presented, two sources of the lead cation, lead (II) acetate trihydrate [Pb(CH₃COO)₂·3H₂O]¹ and lead (II) pentanedionate (lead acetylacetonate) [Pb(C₅H₇O₂)₂]² were used, the first having been initially employed (Selvaraj et al., 1992), and the latter proposed to give a more stable PZT

*Author to whom correspondence should be addressed.

¹Aldrich Chemical Co., Milwaukee, WI.

²Johnson Matthey Catalog Co., Ward Hill, MA.

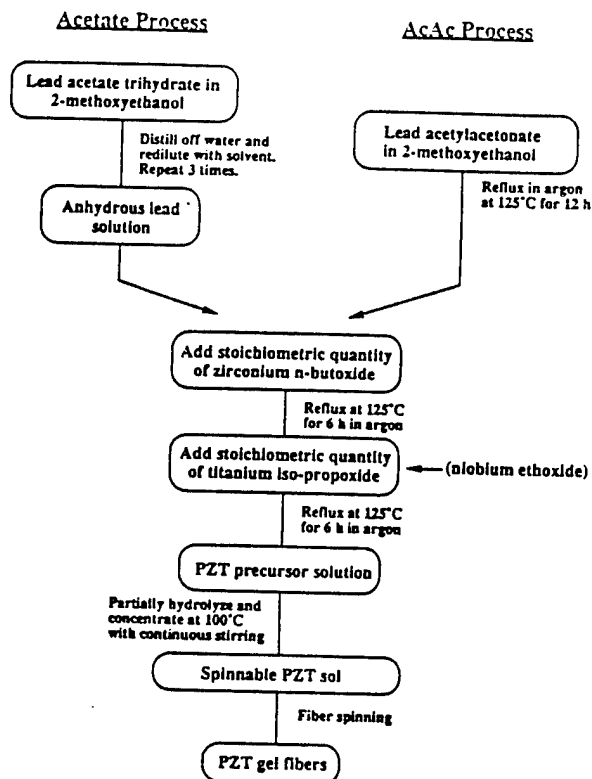


Figure 1. Scheme for the preparation of Pb(Zr,Ti)O₃ fibers using lead acetate trihydrate (Acetate process) and lead acetylacetonate (AcAc process) as a lead source.

precursor solution (Selvaraj et al., 1993). For convenience, samples produced using lead acetylacetonate are designated "AcAc processed", and those using lead acetate trihydrate "Acetate processed". Based on the work by Blum and Gurkovich (1985) and later by Budd, Day, and Payne (1985), zirconium *n*-butoxide [Zr(Obu)₄]¹ (80% solution in *n*-butanol) and titanium isopropoxide [Ti(OPr)₃]¹ were used as the zirconium and titanium sources, respectively. For niobium modified PZT, niobium ethoxide [Nb(OC₂H₅)₃]² was added during the addition of the titanium precursor stage. Stoichiometric quantities of each chemical were weighed out in accordance with the PZT formulations Pb(Zr_{0.48}Ti_{0.52})O₃ and Pb_{0.988}(Ti_{0.48}Zr_{0.52})_{0.976}Nb_{0.024}O₃, as reported in Jaffe, Cook, and Jaffe (1971).

A solution of 0.1 ml of water and 5 ml of 2-methoxyethanol was added to the various PZT precursors (0.02 M) containing 0.1 ml conc. HNO₃ to ensure condensation and hydrolysis reactions. The solution was concentrated by stirring at ~120°C and then cooled to ~40°C to form a viscous resin. The spinnability of the sol was empirically determined by dipping a glass rod into the viscous medium and pulling up to draw a fiber. A systematic rheological study is underway to determine the optimum viscosity range for fiber drawing.

The precursor solution was transferred to a vessel consisting of a spinneret and a plunger as shown schematically in Figure 2(a) (Hayes, 1989). Fibers were extruded through the

spinneret with twelve 100 μm diameter holes at ~7 kPa of pressure. The spun-drawn fibers were collected on a rotation drum with a variable speed control, as described in Figure 2(b). Factors involved in controlling the diameter of the fibers are: (1) viscosity of the sol, i.e., control of hydrolysis and condensation reaction, (2) spinneret diameter, and (3) speed of the take-up drum.

Fibers with diameters ranging from 10 to 80 μm were fabricated. The fibers were dried at room temperature for approximately 12 hours, cut into lengths of ~10 cm and fired at temperatures from 750°C to 1250°C for 10 minutes. A heating rate of ~1°C/min was used to allow the decomposition of organics being in the order of 10 to 15 wt% after solvent evaporation, which was previously determined by thermogravimetric analysis (TGA) (Selvaraj et al., 1992). For samples fired at temperatures >1200°C, a lead atmosphere was created to minimize lead loss. The sintering condition of 750°C for 10 minutes was chosen based on a previous study (Selvaraj et al., 1992) which was high enough to enable the formation of the desired perovskite structure, yet low enough to fire in open air without lead loss. This may be an important factor in the future when continuous fiber spinning and subsequent firing are desired. Firing temperatures at 1250°C were used to examine densification behavior and grain growth, being similar to that used for conventionally processed PZT ceramics.

Fiber poling experiment was performed by using extruded PZT-5H fiber (120 μm in diameter) obtained from CeraNova Corp. for the ease of handling. Figure 3 describes the apparatus for fiber poling in which PZT fiber is threaded through two small holes (0.45 mm diameter), one hole in a large metal plate (25 cm square), the other in a large metal sphere (10 cm diameter), 2 to 4 cm apart. The plate is at ground potential, the sphere is gradually raised to a sufficient voltage to significantly exceed the coercive field of the

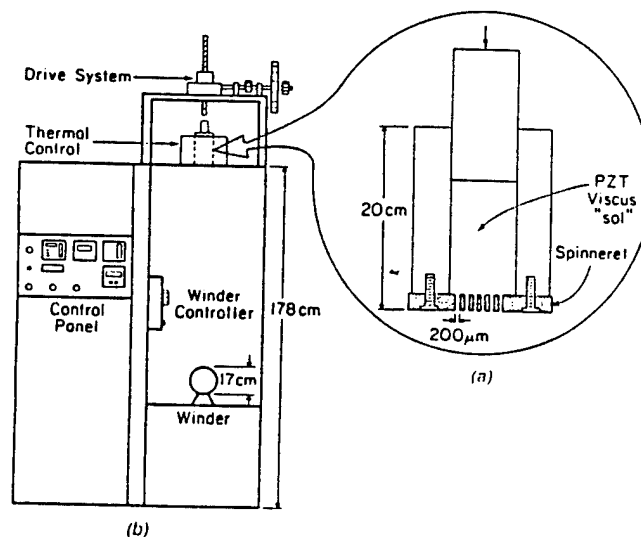


Figure 2. Fiber spinning apparatus. Schematic drawing of vessel and spinneret (a), and overview of the apparatus (b).

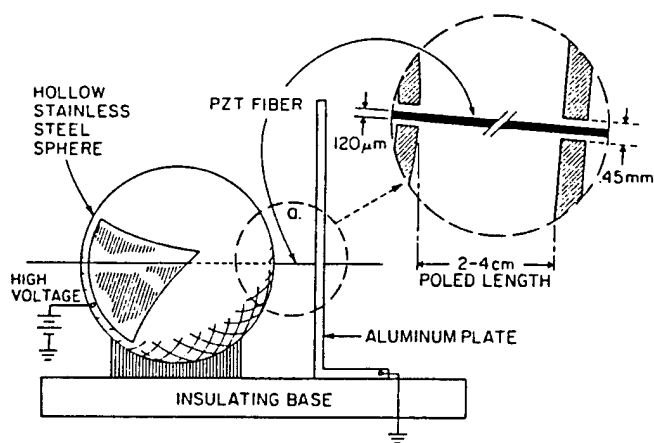


Figure 3. Fiber poling apparatus.

PZT. The high voltage side is a sphere in order to reduce the breakdown and corona effects that exist at the edge of a plate. In the static field case, the electric field in and around the fiber is nearly uniform.

We have assumed that the charge accumulated in a ring that the fiber was threaded through was dissipated by one of the following:

1. Corona formation from the surface of the sample to the circumference of the hole
2. Air breakdown in the same way a corona could be caused
3. Conduction through the fiber if the fiber is physically touching the circumference of the hole
4. Surface conduction

Characterization

Crystallinity and phase analysis of the fibers as a function of thermal treatment were determined using x-ray diffraction (XRD) analysis.³ The microstructure, i.e., grain size and degree of porosity, and diameter of the fibers were examined using scanning electron microscopy (SEM).⁴ Energy dispersive spectroscopy (EDS)⁵ was used to semi-quantitatively determine Zr:Ti and Pb:(Zr,Ti) ratios.

The room temperature dielectric properties ($K @ 10$ KHz) of sintered fibers were determined from capacitance measurements using a LCR meter and the holder presented in Figure 4. An external amplifier/divider circuit was employed to improve the sensitivity of the LCR meter⁶ by a factor of 100 by increasing the applied signal to $\sim 150 V_{rms}$. A small amount of air-dry silver was applied to both ends of the fiber to ensure electrical contact. Fibers 1 to 2 cm and 20 to 30 μm in diameter in length were used. Because of the extreme geometry of these fibers, thus the very small capacitance of often less than 0.5 fF, very special care had to be

taken to control the uniformity of the electric field within the three terminal parallel plate fixture. Because the capacitance to free space of even a short segment (under 20 μm) of fiber along its length can be greater than the end-to-end capacitance, it is critical that permittivity, as well as later described hysteresis measurements, be made in an environment with a controlled and, in this case, uniform electric field to avoid "shorting out" the measurement signal through an inadvertent T-network to ground. This is distinctly different from bulk or thin film measurements but is a crucial consideration in fiber measurements. Measurements were first made with the fiber in place, then removed, and the difference was used as the sample's capacitance. This process corrected for the contribution to the measured value from both stray capacitance and direct (air gap) capacitance. The diameter of the guard electrode (~ 5 cm) was chosen to ensure a uniform field in the neighborhood of the sample even with the fibers ~ 2 cm in length. The size of the active low electrode in the fixture (0.5 mm in diameter) was calculated so that its contribution to the total capacitance would be no greater than that of even the smallest diameter fiber.

The ferroelectric nature of the fibers was confirmed through polarization electric field (P-E) measurements with fibers only ~ 3 mm long, owing to voltage limitation of the

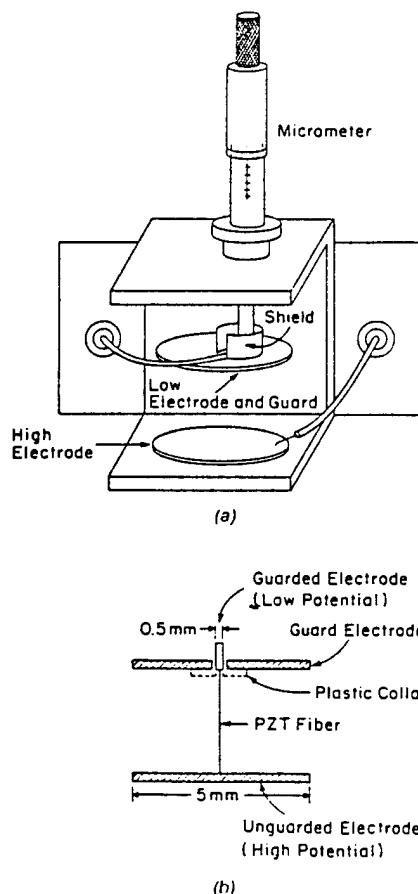


Figure 4. Fixture for fiber permittivity and polarization measurements (a), and section view of electrode configuration (b).

³Model DMC 105, Scintag diffractometer, Sunnyvale, CA.

⁴Model DS-130, International Scientific Instruments, Inc., Santa Clara, CA.

⁵EMAX 8000 Series, Horiba Instruments, Inc., Irvine, CA.

⁶Model 4274 LCR meter, Hewlett Packard, Palo Alto, CA.

power supply,⁷ i.e., 10 kV. A specially-built automated system was used which applies the excitation field and collects the charge while maintaining a virtual-ground state, similar to a classical Sawyer-Tower measurement, but the charge is collected by active circuitry rather than a passive capacitor. This holds the low side of the measurement circuit to within a few millivolts of ground, which is necessary to control the shape of the electric field for the same reason as in the permittivity measurement. To avoid electrical breakdown, the entire fixture was immersed in a fluorocarbon fluid.⁸ Fields of >3 MV/m, typically at a frequency of 10 Hz, were used.

The degree of poling after the poling experiment described in the previous section was measured by observing the shift of the first P-E hysteresis loop.

To contrast both the physical and electrical characteristics of the fibers, disks (~ 1 cm in diameter) were prepared from gel-powders derived from the same sols used to draw fibers. Upon pressing and binder⁹ burnout, the disks were densified over a temperature range from 1000°C to 1400°C and characterized above. In addition to dielectric and polarization hysteresis, fully densified samples were poled at 120°C with an electric field of 25 kV/cm. The level of poling was determined using a Berlincourt piezo d_{33} meter.¹⁰ The samples were allowed to age ~ 24 hours prior to measurement.

In addition to chemical and electrical characterization, the mechanical integrity of the PZT fibers was also investigated. The tensile strength was determined for selected fibers at the Nagasaki University of Japan, using a technique described by Iwanaga et al. (1992). Specimens 1 to 2 mm in length, diameter range between 26 to 36 μm , were glued to carbon fiber and the direct tensile strength was measured with a load range of 1 to 10 g.

RESULTS AND DISCUSSION

Microstructural Analysis

Optical photographs of as-spun and fired fibers (@ 750°C) are shown in Figures 5(a) and (b), respectively. A representative XRD spectra of AcAc processed PZT fibers fired at 750°C and 1250°C are presented in Figure 6, both revealing the presence of a well-crystallized perovskite phase. Figure 7 presents SEM micrographs of Acetate processed PZT, fired at (a) 750°C, (b) 1250°C, and (c) Nb-PZT fired at 1250°C. As presented, the diameters of the fibers were in the range of 20 to 50 μm , showing little evidence of porosity on the surface of the fiber. The Acetate and AcAc (not shown in the figures) processed fibers fired at 750°C were found to possess similar microstructures. SEM ex-

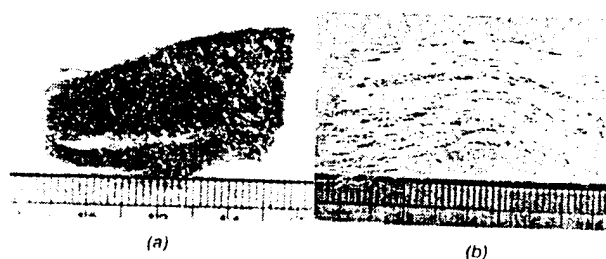


Figure 5. Photographs of (a) as spun, (b) fired PZT fiber.

amination of the cross section of the fibers revealed 10 to 20% fine porosity uniformly distributed across the fibers, except near the dense surface, with grain sizes on the order of 0.2–0.3 μm . Fibers processed at 1250°C possessed dense microstructures with grain sizes in the range of 2 to 8 μm . A small amount of closed porosity (~ 0.3 μm in diameter), both in grains and at grain boundaries, was evident in the cross-sectional view of the fiber after the pull test, as shown in Figure 8. The fracture surface was intergranular. The fibers with Nb-PZT (AcAc processed) composition fired at 1250°C showed uniform and finer grain size, 1 to 3 μm , and little porosity. The smaller grain size is due to the niobium substitution, which tends to inhibit grain growth of PZT in addition to many other characteristics governed by this "A-site vacancy additive". Acetate processed Nb-PZT fiber could not be drawn successfully, due to the rapid increase in "sol" viscosity. Differences between the two lead sources were inconclusive in this study, though use of lead acetylacetonate reduced reflux time drastically.

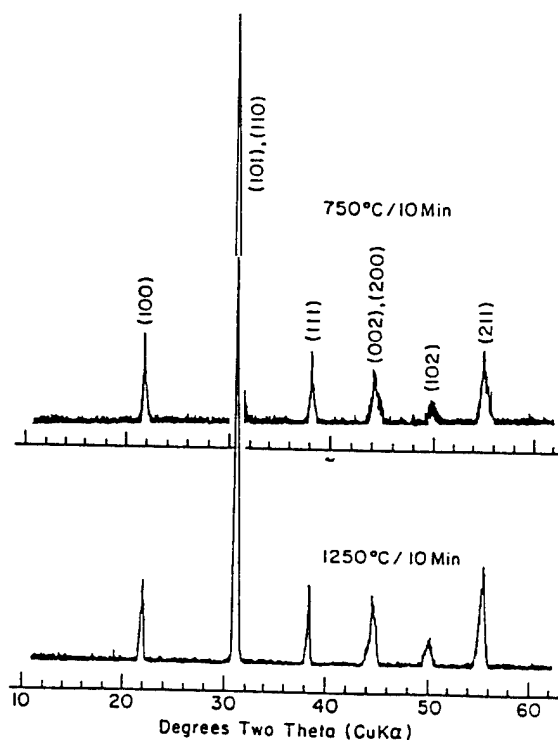


Figure 6. XRD pattern for the fibrous PZT heat-treated at 750°C for 10 min and at 1250°C for 10 min.

⁷High Voltage Power Supply, Model 610A, Trek Incorp., Medina, NY.

⁸Fluorinert FC-40, 3M Corp., St. Paul, MN.

⁹Polyvinyl Alcohol binder (PVA).

¹⁰Berlincourt Piezo d_{33} meter, Channel Products, Inc., Chagrin Falls, OH.

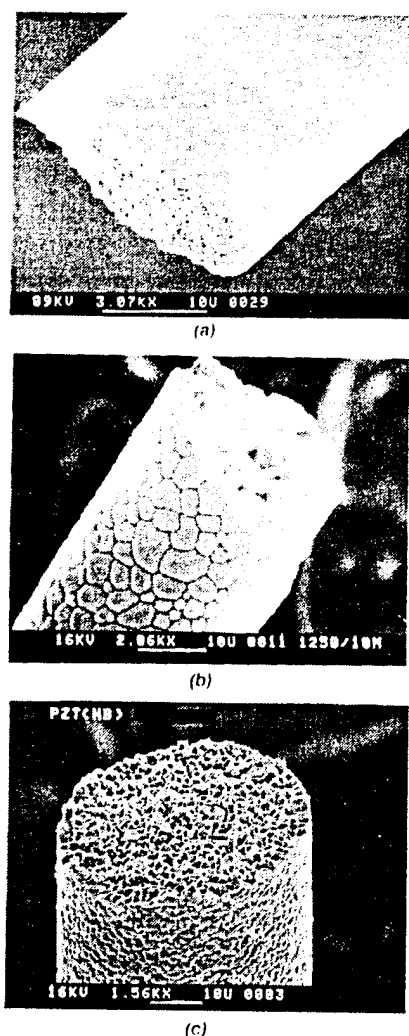


Figure 7. SEM micrograph of: (a) acetate processed PZT fired at 750°C for 10 min, (b) acetate processed PZT fired at 1250°C for 10 min, (c) AcAc processed Nb-PZT fired at 1250°C for 10 min.

Compositional Analysis

EDS analysis of PZT fibers (both Acetate and AcAc processed) indicated that the Zr:Ti ratio was rich in Zr being shifted to approximately 55:45 as confirmed by the lack of tetragonal splitting [(002) and (200)] in the XRD patterns (Figure 6). This trend was confirmed by dielectric measurements of the fired pellets prepared from the same solution. The dielectric constant (K) dramatically decreased upon poling ($\sim 48\%$) reflecting a PZT composition well on the rhombohedral side of the morphotropic phase boundary (MPB) (Jaffe et al., 1971). The reason for this compositional shift is currently being investigated.

Electrical Properties

The dielectric constant values of the various fibers processed are summarized in Table 1. Due to the small input signals, dielectric loss of the PZT fibers was not measured. Both Acetate and AcAc processed PZT fibers showed com-



Figure 8. SEM micrograph of fracture surface of PZT fiber (fired at 1250°C for 10 min) after tensile test.

parable dielectric values to that of the bulk ceramics disk samples made from the same solution. The dielectric constant of the samples fired at 750°C was lower, which was probably due to the combination of porosity and smaller grain size. Piezoelectric d_{33} coefficients of the PZT-poled ceramic disk samples were found to be ~ 150 pC/N, which is lower than reported value (~ 223 pC/N) (Jaffe et al., 1971). This was believed to be due to the MPB compositional shifting of Zr:Ti. Poled ceramic disks of Nb-PZT exhibited d_{33} of ~ 350 pC/N close to the reported value (374 pC/N) (Jaffe et al., 1971). Dielectric and piezoelectric properties of the bulk (disk) samples were necessary to determine the quality of precursors and to provide expected values for the fibers fabricated from the same "sol".

Representative room temperature hysteresis polarization E-field behavior for AcAc processed Nb-PZT fired at 1250°C is shown in Figure 9(a) along with the polarization measurements performed on bulk (disk) samples [Figure 9(b)] as a comparison. Only Nb-PZT fiber data is presented due to the high coercive fields of unmodified PZT. The ferroelectric nature of a single piezoelectric fiber has not been reported before. The P-E hysteresis provides direct evidence that these fibers can be polarized to induce the desired piezoelectric properties. Comparison with the disk sample revealed that the level of remanent polarization of the fibers

Table 1. Dielectric constant of sol-gel derived PZT and Nb-PZT fibers.*

Ceramic	Pb Precursor	Heat Treatment Temp. [°C]/ Time [min]	Dielectric Constant (% error)
PZT	Acetate	750/10	670 (15)
PZT	Acetate	1250/10	870 (10)
PZT	AcAc	750/10	500 (15)
PZT	AcAc	1250/10	700 (10)
Nb-PZT	AcAc	750/10	1250 (15)
Nb-PZT	AcAc	1250/10	1100 (15)

*Fiber: average diameter of 30 μm .

($P_r = 37 \mu\text{C}/\text{cm}^2$) was similar to the bulk sample and coercive field was somewhat higher ($E_c = 19 \text{ kV}/\text{cm}$).

When the E-field is applied to the previously poled sample parallel to the poled direction, the first P-E loop is shifted to either upward or downward depending on the direction of the field. Therefore, the very first P-E loop was measured to determine whether or not the fiber was poled after the application of E-field by the method described in Figure 3 in "Experimental Procedures". Figure 10 shows the first P-E loop of one of the examples of the segment of the poled fiber. Nearly complete shift of the hysteresis indicates that the fiber has been poled.

Mechanical Properties

Preliminary data for the tensile strength of PZT fibers fired at 750°C and 1250°C determined using the pull test

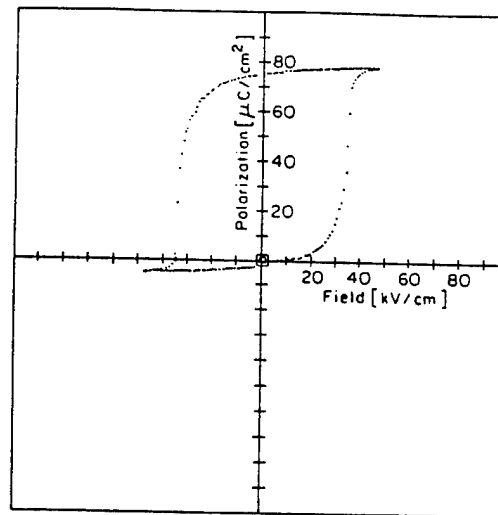
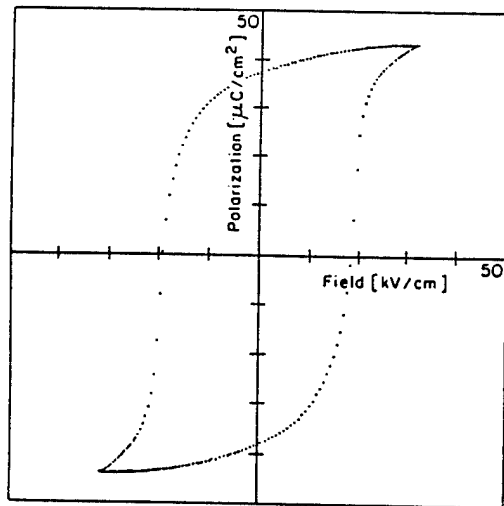
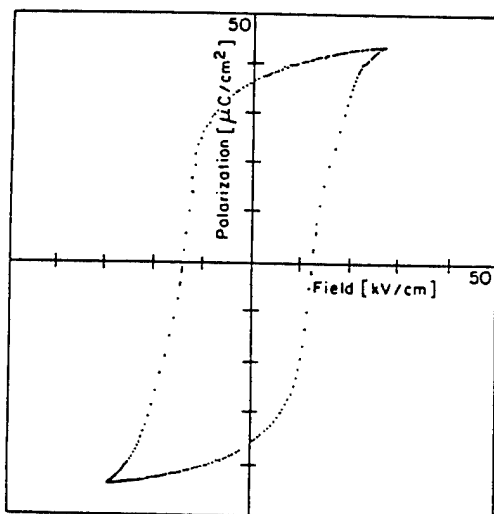


Figure 10. The first polarization hysteresis loop of Nb-PZT fiber poled using the apparatus shown in Figure 3.



(a)



(b)

Figure 9. Polarization hysteresis of (a) Nb-PZT fiber (diameter 30 μm), (b) Nb-PZT pellet prepared from the same sol as the fiber was spun.

were 36 MPa and 40 MPa, respectively. Tensile strengths of $\sim 55 \text{ MPa}$ were found for Nb-PZT fibers. This higher value may be attributed to its smaller and more uniform grain size. Finer diameter fibers tended to give larger tensile strength values, though more data with different diameter samples is required to confirm this. Tensile strength values for bulk PZT ceramics reported in the literature is on the order of $\sim 76 \text{ MPa}$ (Berlincourt, Krueger, and Near, 1987), with modulus of rupture using 3-point flexure in the range of 10 to 40 MPa (Pohanka et al., 1983). Therefore, the fiber tensile strength found for the fibers in this work is similar to that of the bulk ceramic. This range, however, is an order of magnitude less than comparable glass fibers (700 MPa) and substantially less than that for Al₂O₃ fibers (1500 MPa) reported in the literature (Cooke, 1991). Incorporation of PZT fibers into a structural matrix, therefore, cannot be a simple substitution with structural fibers, and hence careful handling and design must be considered.

CONCLUSIONS

Amorphous PZT and Nb-PZT fibers with average diameters of 30 μm have been successfully spin-drawn from sol-gel processed PZT precursor sol using a continuous batch spinning apparatus. Two different lead sources, lead acetate trihydrate and lead acetylacetonate, were examined. All of the fibers showed pure crystalline perovskite structure after heat treatment at 750°C, and further densification and grain growth were evident after 1250°C firing.

Single fiber dielectric constant and polarization hysteresis measurements were successfully performed using a specially built fixture. Dielectric constant values of the fibers fired at 750°C were lower than that of fibers fired at 1250°C due to porosity and reduced grain size. The dielectric con-

stant of fibers fired at 1250°C was comparable with that of bulk ceramic values. Polarization E-field measurements of Nb-PZT fibers indicated that the level of remanent polarization ($37 \mu\text{C}/\text{cm}^2$) was similar to that of bulk samples with the coercive field (19 kV/cm) being slightly higher. Fiber poling apparatus was built to demonstrate continuous poling using 120 μm diameter extruded fiber. The clear shifting of the first P-E hysteresis loop indicated that the fiber had been poled with this method.

Preliminary data for the tensile strength of PZT fibers revealed values similar to that of bulk PZT, though Nb-PZT fiber values were higher than that of pure PZT fibers, probably due to its denser microstructure and smaller, uniform grain size.

ACKNOWLEDGEMENTS

A special thanks to Professor Dan Edie and his group at Clemson University for letting us use their equipment and for their help. The authors would like to acknowledge the contribution of Professor Hiroshi Iwanaga of Nagasaki University for fiber mechanical measurements. Also, the authors wish to thank Drs. L. Eric Cross, Keith Brooks, and Qiyue Jiang for their help for this project. This project was supported by Office of Naval Research Grant No. N00014-92-1391, program monitor Dr. Lawrence Kabacoff.

REFERENCES

- Berlincourt, D., H. H. Krueger and C. Near. 1987. "Important Properties of Morgan Matroc Piezoelectric Ceramics (PZT-4, PZT-5A, PZT-5H, PZT-8)", Technical Paper No. 226, Morgan Matroc Inc.
- Blum, L. B. and S. R. Gorkovich. 1985. *J. Mater. Sci.*, 20:4470.
- Budd, K. D., S. K. Dey and D. A. Payne. 1985. *Brit. Ceram. Proc.*, 39:107.
- Chen, K.-C., H. Zheng and J. D. Mackenzie. 1991. "Method for Making Piezoelectric Ceramic Fibers", U.S. Patent #5,072,035, December 10, 1991.
- Cooke, T. F. 1991. "Inorganic Fibers—A Literature Review", *J. Am. Ceram. Soc.*, 74:2959-2978.
- Crawley, E. and J. deLuis. 1987. "Use of Piezoelectric Actuators as Elements of Intelligent Structures", *ACAA Journal*, 25:1373-1385.
- Gururaja, T. R., W. A. Schulze, T. R. ShROUT, A. Safari, L. Webster and L. E. Cross. 1981. "High Frequency Applications of PZT/Polymer Composite Materials", *Ferroelectrics*, 39:1245.
- Hagood, N. W. and A. von Flotow. 1991. "Damping of Structural Vibration with Piezoelectric Materials and Passive Electrical Networks", *J. Sound and Vibrations*, 146:243-268.
- Hayes, G. J. 1989. "Controlled Melt Spinning of Carbon Fiber", M. S. Thesis, Clemson University.
- Iwanaga, H., T. Iwasaki, K. Reizen, T. Matsunami, M. Ichihara and S. Takeuchi. 1992. "Method for Tensile Experiments with Ceramic Fibers Having a Diameter of a Few Microns", *J. Am. Ceram. Soc.*, 75:1297-1299.
- Jaffe, B., W. R. Cook, Jr., and H. Jaffe. 1971. *Piezoelectric Ceramics*. NY: Academic Press, pp. 135-183.
- Klicker, K. A., J. V. Biggers and R. E. Newnham. 1981. "Composite of PZT and Epoxy for Hydrostatic Transducer Applications", *J. Am. Ceram. Soc.*, 64:5-9.
- Park, H. 1991. "PZT Fibers", *ONR Review of Piezoelectric and Electrostrictive Material for Transducer Applications*, State College, PA, April 22, 1991.
- Pohanka, R. C., P. L. Smith and J. Pasternak. 1983. "Static and Dynamic Strength of Piezoelectric Materials", *Ferroelectrics*, 50:285-291.
- Ramachandran, A. R., Q. C. Xu, L. E. Cross and R. E. Newnham. 1991. "Passive Vibration Damping", *Proceedings of the First Joint U.S./Japan Conference on Adaptive Structures*, Nov. 13-15, 1990, Maui, Hawaii, B. Wada, J. L. Fanson and K. Miura, eds., Lancaster, PA: Technomic Publishing Co., Inc., pp. 523-528.
- Selvaraj, U., K. Brooks, A. V. Prasadara, S. Komarneni, R. Roy and L. E. Cross. 1993. "Sol-Gel Fabrication of $\text{Pb}(\text{Zr}_{0.52}\text{Ti}_{0.48})\text{O}_3$ Thin Films Using Lead Acetylacetonate as the Lead Source", *J. Am. Ceram. Soc.*, 76:1441-1444.
- Selvaraj, U., A. V. Prasadara, S. Komarneni, K. Brooks and S. K. Kurtz. 1992. "Sol-Gel Processing of PbTiO_3 and $\text{Pb}(\text{Zr}_{0.52}\text{Ti}_{0.48})\text{O}_3$ Fibers", *J. Mater. Res.*, 7:992-996.
- Seth, V. 1990. "Polycrystalline Ferroelectric Fiber", U.S. Patent #4,921,328, May 1, 1990.
- Takeuchi, H. and C. Nakaya. 1986. "PZT/Polymer Composite for Medical Ultrasonic Probes", *Ferroelectrics*, 68:53.
- Waller, D. J., A. Safari, R. Card and M. P. O'Toole. 1990. "Lead Zirconate Titanate Fiber/Polymer Composites Prepared by a Replication Process", *J. Am. Ceram. Soc.*, 73:3503-3506.
- Yoshikawa, S., U. Selvaraj, K. G. Brooks and S. K. Kurtz. 1992. "Piezoelectric PZT Tubes and Fibers for Passive Vibration Damping", *Proceedings of IEEE, 8th International Symposium on Application of Ferroelectrics*, Greenville, S. C., Aug. 30-Sept. 2, 1992, pp. 269-272.

APPENDIX 58

Rate Controlled Sintering of Low Temperature Cofired Ceramic Multilayers used for Electronic Packaging

W. S. Hackenberger, and T. R. Shrout, Center for Dielectric Studies, Intercollege Materials Research Laboratory, The Pennsylvania State University, University Park, PA 16802 U.S.A.
A. Nakano, TDK Corporation, 200, Tachisawa Hirasawa Nikaho-machi Yuri-gun Akita-ken 018-04 Japan

R.F. Speyer, School of Materials Science and Engineering, Georgia Institute of Technology, Atlanta, GA 30332 U.S.A.

ABSTRACT

Rate controlled sintering (RCS), the process of directly controlling sintering shrinkage with a feedback loop mechanism, was used to densify a commercial ceramic multilayer substrate (a low temperature cofireable ceramic -- LTCC). The substrate consisted of alumina loaded glass insulator layers with fritted silver conductor layers. The effect of one constant heating rate and three constant shrinkage rates on the conductor/insulator interface was studied using acoustic microscopy, scanning electron microscopy, capacitance measurements, and equivalent series resistance. An optimal shrinkage rate was found that resulted in fewer conductor/insulator delaminations and conductor film discontinuities than did the other shrinkage and heating rates studied. It is postulated that the changes in heating rate needed to maintain a constant shrinkage rate shift and/or reduce the peak densification rates of the constituent materials limiting the transient tensile stresses.

I. Introduction

When the sintering of a particulate material is constrained, as is the case in multilayer cofired ceramics and thick films, transient tensile stresses can develop that oppose the material's effective sintering stress [1 - 3]. These tensile stresses can also lead to defect formation (sintering damage) through creep processes [2, 4]. The common types of sintering damage that have been observed in metal/ceramic multilayers include warping [5], cracking in the ceramic layer [4], delamination of the metal/ceramic interface [6], and void formation in the metal layer [4]. Since sintering materials are viscous or viscoelastic, stress develops in response to strain rates rather than strain as is the case for elastic materials. In this work direct control of the strain rate for a sintering multilayer electronic substrate was achieved using rate controlled sintering. As will be shown, this allowed us to influence the transient stresses that arise during cofiring.

II. Experimental Procedure

A commercial tape-cast, glass-alumina composite insulator material (E.I. Du Pont de Nemours 851AT Green Tape) and a screen-printable, fritted silver conductor ink (E.I. Du Pont de Nemours 6142D) were chosen as the target materials for this study. Multilayers were constructed by first printing 2.54 cm square pieces of tape with 8 mm x 1.5 mm pads of silver ink. The printed layers were dried and then 20 layers were stacked and laminated at 34 MPa and 75 °C or 15 min. The printing pattern and stacking sequence were such that each laminate could be diced into sixteen samples with a multilayer capacitor configuration. After dicing binder burnout was done at 400 °C for 1 hour in a box furnace with flowing air.

The multilayers were densified using an RCS dilatometer with an infrared imaging furnace. This instrument, which has been described in the literature [7], has a very low thermal mass. As a result it provides a much greater degree of control over the shrinkage rate than has been possible with more conventional dilatometry and furnace equipment. Multilayer samples were sintered at a constant heating rate (CHR) of 25 °C/min or by RCS at constant shrinkage rates of 0.5, 1.5, or 6 %/min. For the RCS trials, the samples were heated to the sintering onset temperature at a constant heating rate of 25 °C/min. Shrinkage was monitored in the radial direction (i.e. in the casting/printing plane), and both the CHR and RCS samples were sintered to a target shrinkage of

13 %. This was determined by sintering multilayers in a conventional furnace at 850 °C for 15 min (the manufacturer's recommended profile). Once the target shrinkage was reached, the control system abruptly reduced the furnace temperature 300 °C to stop sintering and "freeze in" the final microstructure. Five samples were sintered for each of the four profiles investigated.

The multilayers were characterized using scanning acoustic microscopy, capacitance vs. frequency measurements, equivalent series resistance, and finally scanning electron microscopy (SEM) of cut and polished cross sections. The shrinkage behavior of individual components of the multilayer was also evaluated. For the substrate material this was done by sintering 20 layer monoliths (substrates without any silver films) in the dilatometer. For the silver, shrinkage was measured on free standing films using an optical microscope with a hot stage.

III. Results and Discussion

The temperature and shrinkage profiles for RCS are shown in figure 1. Note that at the onset of sintering the furnace temperature surged in order to initialize shrinkage control. The heating rate then slowed to a nearly constant value for the remainder of the sintering schedule. Acoustic microscopy of the sintered multilayers indicated that there were no defects in samples sintered at a constant shrinkage rate of 1.5 %/min while there were some defective samples for each of the three other sintering profiles. SEM of cut and polished cross sections of the multilayers revealed that the defects were either delaminations of the electrode/insulator interface or discontinuities and porosity in the electrodes (see figure 2a - e).

Before the SEM analysis, the samples' capacitance and equivalent series resistance (ESR) were measured. The capacitance of a multilayer is reduced by electrode/insulator delaminations. This results from the parasitic capacitance contributed by the air gap in series with the higher dielectric constant insulator. The ESR measurement was used to verify that sample geometry variations were not responsible for any observed fluctuations in capacitance. The average capacitance was found to be highest for the samples sintered at 1.5 %/min indicating fewer delaminations. However, since the degree of delamination will vary from sample to sample, the standard deviation of capacitance for several samples is expected to be a better basis for comparison. This is shown in figure 3. As can be seen the samples sintered at 1.5 %/min had the smallest capacitance variation and samples conventionally sintered at a constant heating rate of 25 °C/min had the largest variation in capacitance.

The sintering behavior of individual components of the multilayer provided some explanation for the above observations. Since the transient stress that drives delamination depends on strain rate, the shrinkage curves for the insulator and silver were differentiated with respect to time. These are shown in figure 4 for two heating rates (25 and 50 °C/min). At the onset of sintering in the insulator, which corresponds to the softening temperature for silver film's glass frit, the silver underwent its peak strain rate. For cofired systems the faster sintering material is in tension; therefore, at the frit softening temperature the silver film was under a high level of tensile stress. This could cause the film porosity and discontinuities observed in many of the samples. It may have also weakened the interface; however, actual interface fracture (delamination) usually occurs near the end of cofiring when the film shrinkage rate is low and the insulator densification rate is at a maximum [8].

If the heating rate was increased there tended to be more overlap between the film and insulator shrinkage rate curves (figure 4). Since the RCS schedules had a temperature surge while the film went through its peak shrinkage rate, there may have been a large initial overlap between the film and insulator shrinkage rate during RCS. This could have both reduced the incidence of film discontinuities and strengthened the interface. The choice of a moderate shrinkage rate for the rest of the cofiring schedule would then have maintained the tensile stress below a safe level to prevent delamination.

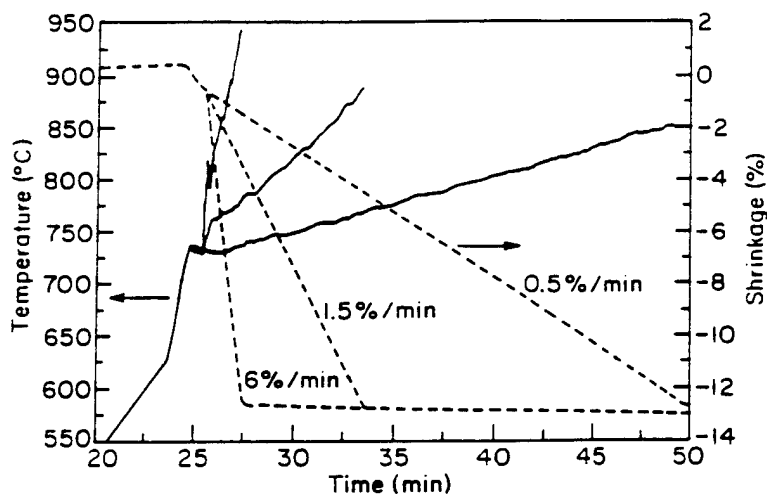


Figure 1: Examples of rate controlled sintering shrinkage and temperature profiles.

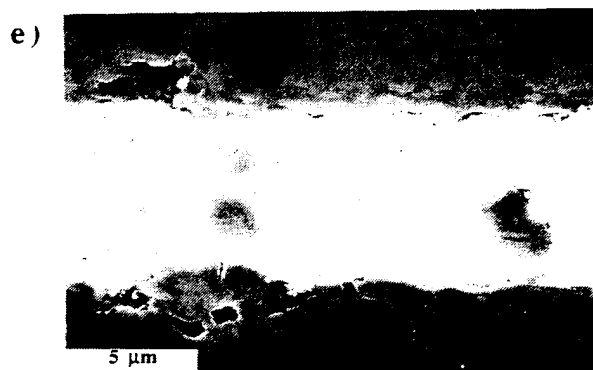
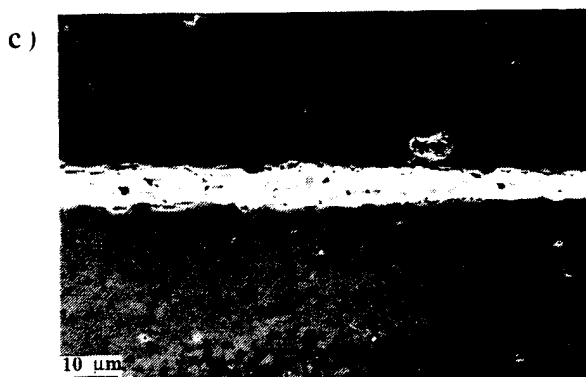
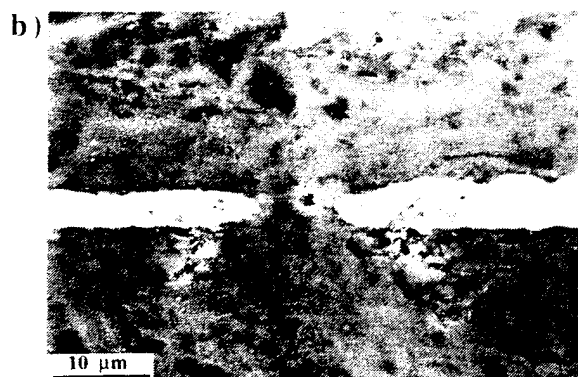
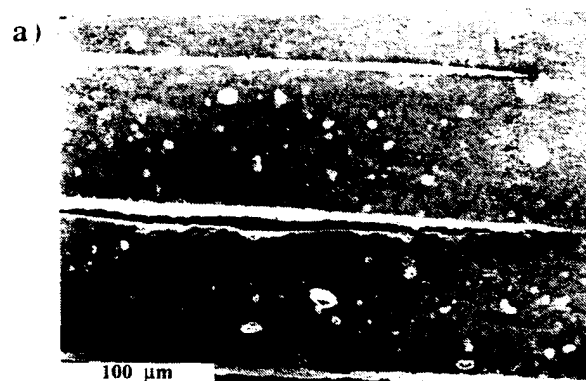


Figure 2: Conductor/insulator interfaces and defects in multilayer samples: a) delaminations for CHR sintering at 25 °C/min, b) and c) film discontinuities and porosity for RCS of 0.5 %/min, d) defect free interface for RCS of 1.5 %/min, and e) low density regions on insulator side of interface for RCS of 6 %/min.

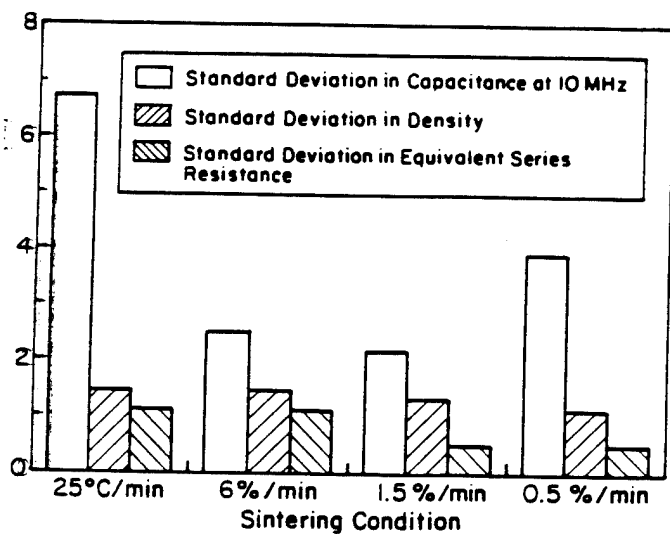


Figure 3: Standard deviation in capacitance, density, and ESR vs. sintering condition.

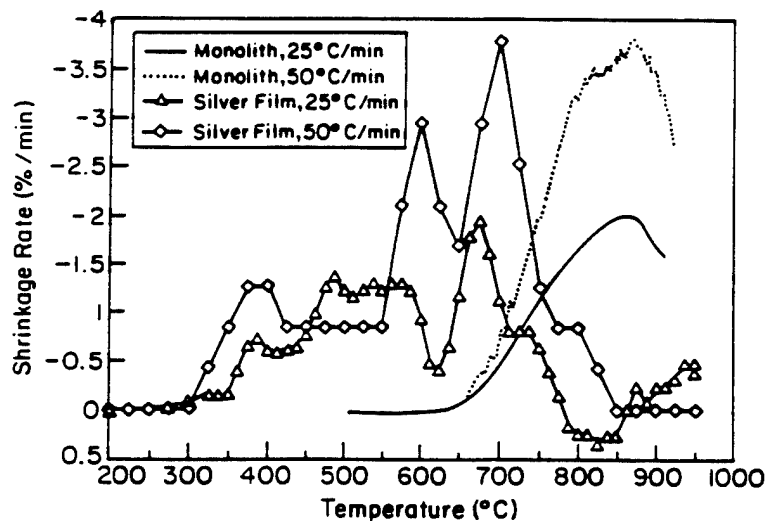


Figure 4: Shrinkage rates for free standing conductor films and insulator monoliths.

Summary

Rate controlled sintering at constant shrinkage rates was performed on LTCC multilayer substrates. An optimal shrinkage rate was found that minimized the incidence of conductor/insulator delamination and conductor film discontinuities compared to conventional constant heating rate sintering. The temperature profile needed to maintain a constant shrinkage rate tended to create more overlap between the conductor and insulator shrinkage rates during the initial stages of cofiring. This would have reduced tensile stress in the film and possibly strengthened the conductor insulator interface. A relatively moderate shrinkage rate for the remainder of cofiring may have kept the tensile stress in the insulator below a critical level for delamination. Currently investigations into the effect of RCS on the properties of multilayer inductors and capacitors (NPO and X7R) are underway.

References

- [1] G.W. Scherer and T. Garino, "Viscous Sintering on a Rigid Substrate," *J. Am. Ceram. Soc.*, **68** [4] 216-220 (1986).
- [2] A.G. Evans, "Consideration of Inhomogeneity Effects in Sintering," *J. Am. Ceram. Soc.*, **65** [10] 497-501 (1982).
- [3] R.K. Bordia and R. Raj, "Sintering Behavior of Ceramic Films Constrained by a Rigid Substrate," *J. Am. Ceram. Soc.*, **68** [6] 287-292 (1985).
- [4] T. Cheng and R. Raj, "Flaw Generation during Constrained Sintering of Metal-Ceramic and Metal-Glass Multilayer Films," *J. Am. Ceram. Soc.*, **68** [3] 120-127 (1989).
- [5] G. Lu, R.C. Sutterlin, and T.K. Gupta, "Effect of Mismatched Sintering Kinetics on Camber in a Low-Temperature Cofired Ceramic Package," *J. Am. Ceram. Soc.*, **76** [8] 1907-1914 (1993).
- [6] J.G. Pepin, W. Borland, P. O'Callaghan, and R.J.S. Young, "Electrode-Based Causes of Delamination in Multilayer Ceramic Capacitors," *J. Am. Ceram. Soc.*, **72** [12] 2287-2291 (1989).
- [7] W.S. Hackenberger and R.F. Speyer, "A Fast-Firing Shrinkage Rate Controlled Dilatometer Using an Infrared Image Furnace," *Rev. Sci. Instrum.*, **65** [3] 701-706 (1994).
- [8] W.S. Hackenberger, T.R. Shrout, J.P. Dougherty, and R.F. Speyer, "Sintering Phenomena and Microstructural Development in LTCC Multilayer Substrates"; pp. 215-220 in *Proceedings of the International Symposium on Microelectronics* (Dallas, TX, November, 1993).

APPENDIX 59

DOMAIN-GRAIN SIZE RELATION IN MORPHOTROPIC PHASE BOUNDARY, $\text{Pb}(\text{Zr}_{0.52}\text{Ti}_{0.48})\text{O}_3$

C.A. Randall, N. Kim, W. Cao, and T.R. Shrout
Materials Research Laboratory
The Pennsylvania State University
University Park, PA 16802 U.S.A.

A grain size investigation of the structure-property relations in morphotropic phase boundary composition Lead Zirconium Titanate (PZT) ceramics has been performed over the grain size (G.S) range of 0.1 to 10 μm . We report on the dielectric and piezoelectric measurements in relation to the grain size, domain size (D.S), and domain configurations in the ceramic. The elastic-domain size was compared to the traditional parabolic relation ($\text{DS} \sim \text{GS}^{1/2}$) and was found to depart at submicron grain sizes ($< 1.0 \mu\text{m}$). New insights were gained into the piezoelectric behavior with the discovery of transgranular domain coupling in the microstructures.

Introduction

With continuing miniaturization of electronic ceramics, new performance problems and challenges are anticipated for ferroelectric ceramics. Ferroelectricity, being a cooperative phenomena similar to ferromagnetism and superconductivity, is expected to show size effects on phase stability and properties. Recent work has shown that the ferroelectric phase is unstable in submicron PbTiO_3 particles, and thin film ferroelectrics have dielectric and piezoelectric properties lower than reported in bulk ceramics.^{1,2} Therefore, there is a need to investigate the effects of grain size on properties and microstructures in a bulk ferroelectric ceramic. The system selected in this study is the morphotropic phase boundary composition, PZT. Although there have been previous studies on grain size effects in PZT, results showed inconsistent trends and the grain size range were limited from 1.0 to 10 μm .³⁻⁶

Experimental

A series of undoped PZT and Nb-doped PZT, $\text{Pb}_{0.988}(\text{Zr}_{0.52}\text{Ti}_{0.48})_{0.976}\text{Nb}_{0.024}\text{O}_3$, ceramics were fabricated from powders made from reactive calcination. Reactive calcination has been shown previously to enhance the reactivity and densification of Pb-based perovskites.^{7,8} The densification and grain growth of the reactive calcined powders with both pressure and conventional sintering results in a wide variation of the mean grain size, 0.1 μm to 14 μm . The smaller grain size was limited by the agglomeration size.

The microstructure of the ceramics was investigated using both scanning and transmission electron microscopy techniques, SEM and TEM, respectively. The samples were prepared for TEM by ion-beam thinning; the polished sections were adhered to copper grids with epoxy. Poled and unpoled TEM samples were studied using a Philips 420 STEM.

Dielectric and piezoelectric measurements were performed over a wide temperature range 10K to 900K to access the intrinsic and extrinsic property contributions. The dielectric measurements were carried out with an automated HP 4274 multiple frequency impedance analyzer interfaced with an H.P. desktop computer. The piezoelectric coefficients and electromechanical coupling factors were determined as a function of composition and grain size, using a R.F. spectrum analyzer HP 4192A and a Berlincourt meter. The samples were poled in a silicone oil bath at 120°C with fields ~ 30 to 50 KV/cm based on their coercive fields (E_c) for ten to sixty minutes.

Results and Discussion

(I) Elasto-dielectric Properties

Figure 1(a) and (b) shows the dielectric constant temperature dependence for undoped and Nb-doped PZT, respectively. There is a suppression of the dielectric maximum with decreasing

grain size. The undoped PZT shows a departure from the Curie-Weiss behavior above T_c . This is most likely due to the uncompensated superoxidation of lead vacancies resulting in a p-type PZT and a space charge contribution imposed on the dielectric anomaly. The Curie-Weiss behavior is observed in Nb-doped PZT and the Curie constant is independent of grain size, which reflects a pure ferroelectric transition. The transition temperature, T_c , in the Nb-doped PZT was also concluded to be independent of grain size. The room temperature poled dielectric constant was found to continuously decrease with reducing grain size, along with a continuous increase in dielectric loss in Nb-doped PZT.

The space-charge effects present in the undoped PZT ceramics limit the interpretation of undoped PZT and, therefore, we will only consider the piezoelectric properties of Nb-doped PZT as a function of grain size. Figure 2 shows a systematic decrease of the piezoelectric coefficients d_{33} and d_{31} with decreasing grain size at room temperature.

Dielectric and piezoelectric properties in ferroelectrics are dependent on both intrinsic and extrinsic mechanisms. Intrinsic contributions are from the relative ionic motion that preserves the original crystal structure. At room temperature in soft PZTs intrinsic contributions are only 30% of the total magnitude of the given property. The remaining extrinsic contributions are the result of domain walls and defect dipoles. The extrinsic mechanisms are thermally activated processes; at lower temperatures the extrinsic properties become frozen out and hence the intrinsic properties dominant. Figure 3 shows k_p and k_{31} , the planar and transverse coupling coefficients, as a function of grain size at temperatures 300K, 100K, and 15K, respectively. The low temperature electromechanical coupling is independent of grain-size and, therefore, infers that the domain mechanisms are responsible for the property changes at room temperature.

(II) Microstructural Characterizations

Grain size and domain size distributions were determined for the PZT ceramics. Figure 4(a) and (b) shows typical histograms for the size distribution of grain sizes and domain sizes, respectively. The grain size distributions were determined from polished and etched SEM micrographs, and the domain size distributions from TEM micrographs. The grain size distributions were found to be relatively symmetrical, whereas the domain size distributions shows strong asymmetry. Therefore, the mean was used to describe the grain size, and the mode (the most frequently occurring size) was used to characterize the size of the domains. Special care was taken to ensure that TEM sample preparation did not change the domain configurations while thinning the bulk ceramic to thin foils, i.e., maintain the domain configuration as a metastable state. Experiments on poled samples and thermal cycling confirmed the validity of the domain size observed in TEM, as discussed in an earlier paper.⁹

Figure 5 shows the generalized data of grain size-domain size relation in morphotropic phase boundary PZT. A constant exponent holds for grain sizes above $1.0\text{ }\mu\text{m}$, but for domain sizes in the $0.1\text{ }\mu\text{m}$ grains there is a departure from the constant exponent. The constant exponent in this study was found to be approximately $m \approx 1/2$, consistent with previous bulk ceramic studies. However, domain size in the fine grain materials shows smaller domain sizes or higher domain densities than predicted by the parabolic scaling relation. Similar departures have been reported in thin film ferroelectrics.¹⁰

In addition to the smaller domains, there is a change in the domain configurations. The domain configurations observed in a ceramic with grain size below $1.0\text{ }\mu\text{m}$ are much simpler than in the larger grain size ceramics. In a morphotropic phase boundary composition PZT, there are 14 possible polarization (domain) states. However, the simple twin band structures observed in the $0.1\text{ }\mu\text{m}$ grains clearly demonstrates a reduction in domain states per grain.

The domain structures observed in the poled PZT ceramics are shown to be strongly influenced by the neighboring grain/domain structures, both in regard to domain size, periodicity, and orientation. TEM observations showed an elastic coupling of the non- 180° domains across grain boundaries. The alignment of domain configurations demonstrates that the switching process has to be both intra- and transgranular. The transgranular coupling is anticipated to be extremely important for piezoelectric properties. The mechanical coupling efficiency is expected to be

reduced by such elastic interactions. In finer grain ceramics, the transgranular coupling would be more dominant as the grain boundary density increases, therefore suggesting the piezoelectric coupling coefficients would be further reduced.

The microscopy results can account qualitatively for the grain size effects observed in the elasto-dielectric properties. The piezoelectric properties are suppressed owing to the reduction in domain states (i.e. switchable directions) in each grain. Piezoelectric properties are also reduced owing to the higher probability of transgranular domain coupling in finer grain materials. On the other hand, the dielectric loss increases with the decrease of grain size at room temperature owing to the higher density of domain walls. This does not necessarily increase the polarizability of the grain as there are fewer domain states in each grain, and the domain walls are pinned at the grain boundaries.

Conclusions

This study establishes a relationship between the dielectric and piezoelectric properties in Nb-doped PZT ceramics of morphotropic phase boundary composition with grain size variations from 0.1 μm to 10 μm . The size dependence of the properties was extrinsically controlled as shown by the thermal measurements, which was also confirmed by the systematic changes in domain size and configuration. Poled domain structures demonstrated the importance of transgranular switching in the poling process of a piezoelectric ceramic.

References

1. K. Ishikawa, K. Yoshikawa, and N. Okada; Phys. Rev. B **37**[10] 5852 (1988).
2. K. Uchino, E. Sadaraga, V. Yamaguchi, and H. Yamamura, Proc. 91st Am. Cer. Soc. on Dielectrics (1989).
3. K. Okazaki and K. Nagata, J. Soc. Mat. Sci. Jpn. **4**, 404 (1972).
4. A.H. Webster and T.B. Weston, J. Canadian Ceram. Soc., **37**, 41 (1968).
5. H.T. Martirena and J.C. Burfoot, J. Phys. C: Solid State Science **7** 3182 (1974).
6. T. Yamamoto, Ceram. Bull. **71**[6] 978 (1992).
7. P. Philippe, J.P. Dougherty, and T.R. Shrout, J. Mat. Res. **5**[12] 2901 (1990).
8. T.R. Shrout, Proc. 1st Intl. Meeting on Chemistry of Electronic Ceramic Mat. (1990).
9. W. Cao and C.A. Randall, Submitted J. Phys. and Chem. Solids.
10. B. Tuttle, MRS Meeting, Boston, MA (1994).

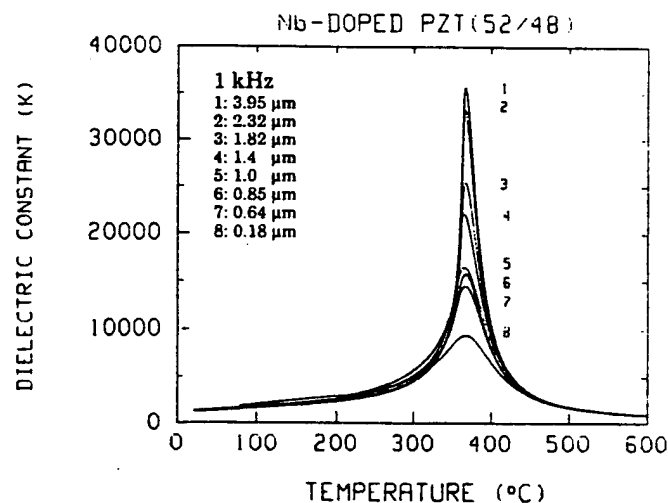
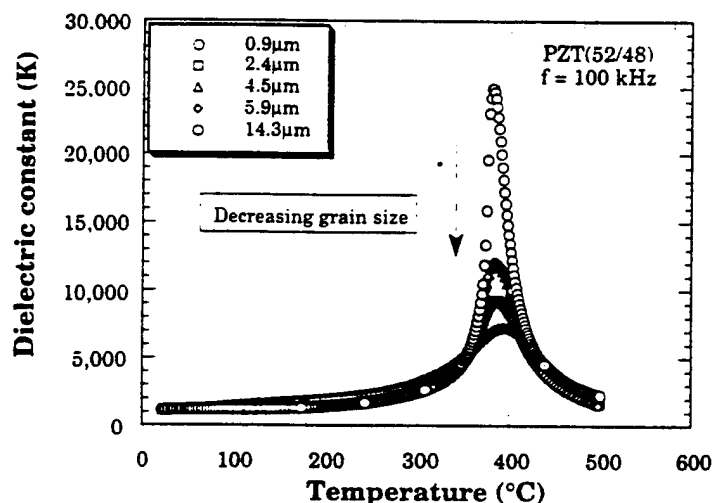


Figure 1. Dielectric constant temperature dependence in (a) undoped and (b) doped PZT ceramics with a range of grain sizes

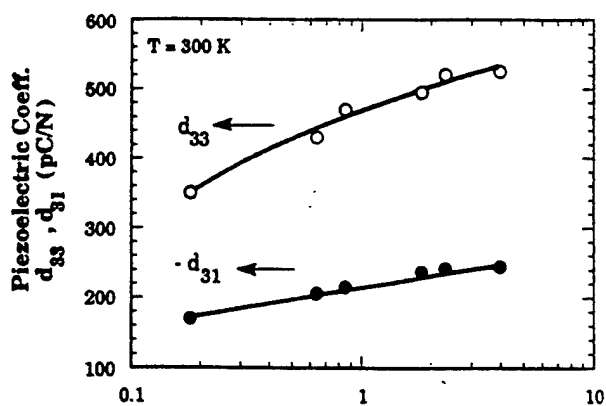


Figure 2. Piezoelectric coefficients, d_{33} and d_{31} , versus logarithmic grain size in Nb-doped PZT.

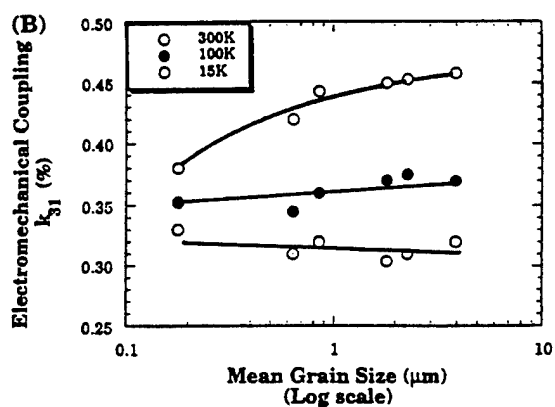
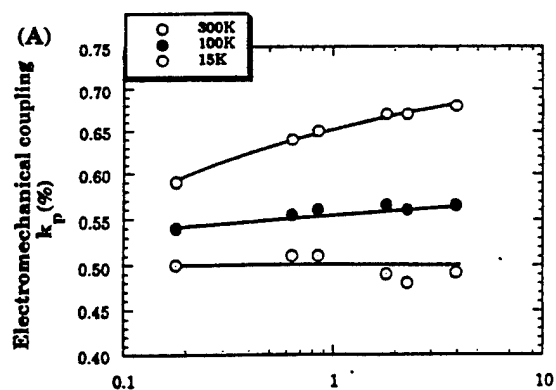


Figure 3 (a) and (b). Electromechanical coupling coefficient as a function of grain size and temperature.

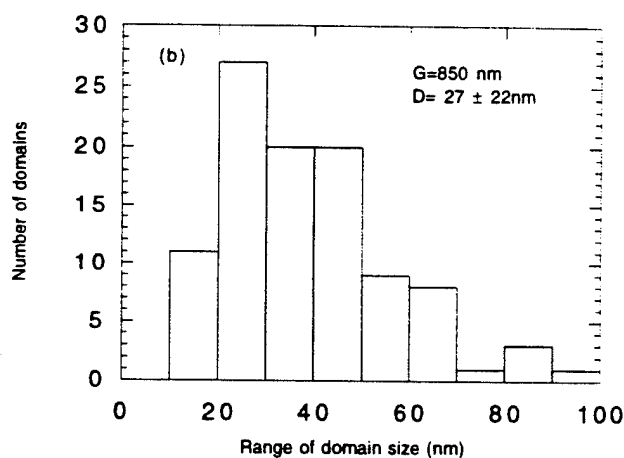
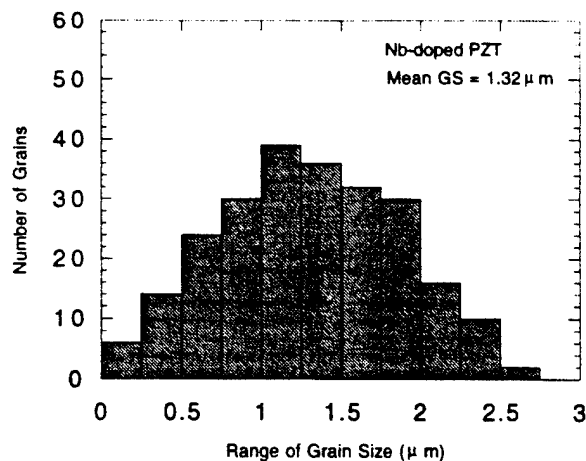


Figure 4. (a) Grain size distribution and (b) domain size distribution for Nb-doped PZT.

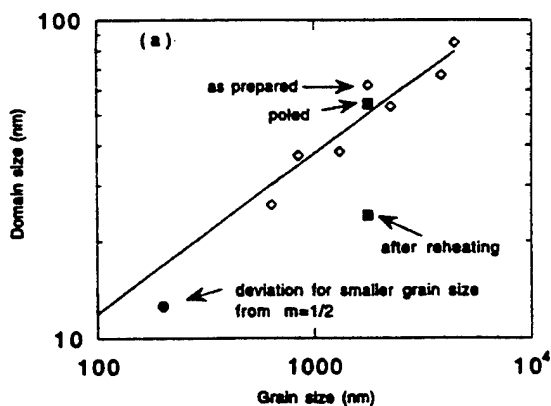


Figure 5. Log-Log plot of the grain size—domain size relation in Nb-doped PZT ceramics.

APPENDIX 60

Investigation of the Dielectric Properties of Bismuth Pyrochlores

David P. Cann, Clive A. Randall, and Thomas R. Shrout

Materials Research Laboratory,

The Pennsylvania State University, University Park, PA 16802, U.S.A.

The dielectric properties of polycrystalline bismuth-based pyrochlores of the general chemical form $\text{Bi}_2(\text{B}_{2/3}^{2+}\text{B}_{4/3}^{5+})\text{O}_7$ and $\text{Bi}_2(\text{B}^{3+}\text{B}^{5+})\text{O}_7$, where $\text{B}^{2+} = \text{Mg}$, Cu , Zn , and Ni , $\text{B}^{3+} = \text{Sc}$ and In , and $\text{B}^{5+} = \text{Nb}$ and Ta , were investigated as a function of temperature and frequency. At low temperatures ($T \sim 100$ to 150 K), a dielectric dispersion was universally observed within these systems. The dielectric dispersion was analyzed using phenomenological models often used for describing dipolar glass systems. Similar activation energies and pre-exponential damping frequencies are found to exist with dipolar glasses such as RADP ($\text{Rb}_x\text{H}_2\text{PO}_4-(\text{NH}_4)_{1-x}\text{H}_2\text{PO}_4$), $\text{K}_{1-x}\text{Li}_x\text{TaO}_3$, $\text{KBr}_{1-x}\text{CN}_x$, and $\text{KI}_{1-x}(\text{NO}_2)_x$.

Keywords: A. spin glasses
 A. ferroelectrics
 D. dielectric response
 D. phase transitions

I. INTRODUCTION

Bismuth-based pyrochlores have recently been found of interest for low-fire high frequency dielectric applications.^{3,4} In contrast to conventional microwave dielectric materials, e.g. $\text{Ba}(\text{Mg}_{1/3}\text{Ta}_{2/3})\text{O}_3$ and $\text{Zr}(\text{Sn,Ti})\text{O}_4$ that require high sintering temperatures ($T_{\text{sinter}} > 1600 \text{ K}$) the low sintering temperatures of bismuth pyrochlores ($T_{\text{sinter}} \leq 1400 \text{ K}$) and dielectric properties with low losses ($\tan \delta \sim 10^{-4}$) and dielectric constants up to 150 make them promising candidates for cofired decoupling capacitors in multichip module packaging applications, so-called LTCC packages (low temperature cofire ceramics).

The cubic pyrochlore structure has the general formula unit $\text{A}_2\text{B}_2\text{X}_6\text{Y}_1$. As shown in Figure 1, the crystal structure is a derivative of the fluorite structure AX_2 where the unit cell is doubled and the A site is differentiated into both A and B sites. The relatively large A cation is in eightfold coordination, with oxygen anions, while the smaller B cation resides in sixfold coordination forming a (BO_6) oxygen octahedra.² Of the seven oxygen anions, one is separate from the (BO_6) octahedra and its only bond is to the A cations, located in the voids between the (BO_6) octahedra. Thus, the structural polyhedra description can be referred to as a strongly bound three dimensional network of (BO_6) octahedra with (A_4O) tetrahedra in the interstices.

The cation solubilities within the pyrochlore structure are similar to that of the perovskite. However, the pyrochlore compositions have received far less attention in terms of compositional-property relations. The $\text{Bi}_2\text{O}_3\text{--ZnO--Nb}_2\text{O}_5$ systems are of interest for the dielectric properties, with dielectric permittivities ~ 100 with a low dielectric loss tangent, $\tan \delta$

≤ 0.0001 . There have been only a few studies into these bismuth compositions³⁻⁶, the most extensive work by Golovshchikova et al.⁶ Consistent with these earlier reports, a dispersive dielectric anomaly is found at low temperature ($\sim 100\text{K}$).

The objective of this work was to expand upon and verify the dielectric-compositional relations of various bismuth pyrochlores. Phenomenological analysis of the dielectric anomaly is also made and discussed in relation to dipolar glass systems. Using these models, predictions can be projected to the high frequency behavior, where real technological advantages are anticipated for the pyrochlore polycrystalline dielectrics.

II. EXPERIMENTAL

Sample preparation: The starting materials were reagent grade oxide powders of Bi_2O_3 , ZnO , Nb_2O_5 , Ta_2O_5 , In_2O_3 , Sc_2O_3 , CuO and NiO , and a carbonate powder, MgCO_3 . Powders were tested for loss on ignition and the batch composition was appropriately compensated. The columbite precursor method was used as is commonly performed in perovskite materials⁸. Stoichiometric mixtures of powders of the base composition $\text{Bi}_2(\text{B}_{2/3}^{2+}\text{B}_{4/3}^{5+})\text{O}_7$ and $\text{Bi}_2(\text{B}^{3+},\text{B}^{5+})\text{O}_7$ were milled for 24 hours in alcohol with zirconia media. These powders were then dried and calcined at $700\text{-}800^\circ\text{C}$ for 4 hours in open alumina crucibles. Powder X-ray diffraction (XRD) was performed to verify the formation of the pyrochlore structure after solid state reaction of the oxide powders. The powders were remilled and dried before pressing into 12.5 mm discs. Approximately 3 weight percent

organic binder was added to assist in the pressing. Discs were sintered in air at temperatures ranging from 950°C-1100°C. At these temperatures there was negligible weight loss during sintering and therefore no excess Bi_2O_3 was added to the batch formulation.

The geometry of the sintered discs was typically 10.5 mm in diameter and 1 mm in thickness. The density of the samples was found to be greater than 97 percent of theoretical density as determined geometrically. The surfaces of the sintered discs were ground parallel and gold electrodes were applied by sputtering.

Dielectric Measurements: Dielectric measurements were carried out using multifrequency meters (Hewlett-Packard 4274A and 4275A LCR meters) in conjunction with a computer controlled temperature chamber. The temperature of the samples was varied from 100 K to 400 K. Measurements were made while cooling at a rate of 2 K per minute. The measurement frequencies utilized to measure the dispersion varied from 100 Hz to 100 kHz in decade steps, and room temperature dielectric properties were measured up to 1 MHz. The sample capacitances were typically 100-200 pF. Dielectric constants were calculated using the geometric area and thickness of the discs.

III. RESULTS

Results of Processing: XRD measurements on sintered samples revealed that samples were single phase cubic pyrochlore. In some cases, however, a secondary phase was present in small amounts (<5%) composed of the B-

site pre-cursor elements (e.g. MgNb_2O_6 , JCPDS 33-875). The presence of this phase suggests the existence of free Bi_2O_3 in the sample. It is probable that a similar A-site and oxygen deficient stoichiometry exists for the Bi-based pyrochlores in this study. The excess Bi_2O_3 and ZnO predicted from this stoichiometry could be present in amounts not detectable by XRD. Careful density measurements and XRD data is required to determine the exact stoichiometry.

For most compositions investigated here, the x-ray powder diffraction profile shows similar features, as typified by cubic pyrochlore $\text{Bi}_2(\text{ScTa})\text{O}_7$ shown in Figure 1. The cubic lattice parameters ranged between 10.54 Å to 10.75 Å. The $\text{Bi}_2(\text{Cu}_{2/3}\text{Nb}_{4/3})\text{O}_7$, however, showed a tetragonal distortion. Figure 2 demonstrates the differences between the cubic and tetragonal powder diffraction profiles.

Dielectric results: Table I presents the room temperature (1 MHz) dielectric data for the pyrochlore ceramics synthesized in this research. The cubic bismuth pyrochlore ceramics have dielectric constants ranging from 67 to 250 with low dielectric losses $\tan \delta$ (<0.011). Lower loss values and lower dielectric constants were recorded for the tantalum containing composition, similar to Ta and Nb perovskite microwave dielectrics, $\text{Ba}(\text{Mg}_{1/3}\text{Ta}_{2/3})\text{O}_3$ and $\text{Ba}(\text{Mg}_{1/3}\text{Nb}_{2/3})\text{O}_3$, respectively. The real and imaginary parts of the dielectric properties as a function of temperature for the $\text{Bi}_2\text{ScNbO}_7$, $\text{Bi}_2\text{ScTaO}_7$, $\text{Bi}_2\text{Mg}_{2/3}\text{Nb}_{4/3}\text{O}_7$, and $\text{Bi}_2\text{Zn}_{2/3}\text{Nb}_{4/3}\text{O}_7$ pyrochlore are given in Figure 2. The Cu-containing pyrochlore showed high losses at all frequencies probably due to changes in valence state of the Cu ion. A frequency dispersive decrease in the real part of the dielectric permittivity and a correlated peak in the imaginary part was

found at low temperatures for all compositions. In some cases, only the onset of the anomaly could be seen at 100 K, as shown in Figure 2 for $\text{Bi}_2\text{Zn}_{2/3}\text{Nb}_{4/3}\text{O}_7$.

IV. DISCUSSION

For the pyrochlore compounds studied, a typical frequency dispersion is observed where the maxima in ϵ'' is shifted to higher temperatures with increased measurement frequency, as shown in Figure 3. Also, a corresponding decrease in ϵ' is observed in the same temperature regime. The corresponding dielectric dispersion is similar to that found in relaxor ferroelectrics, where the temperature at which this dispersion occurred appears to be a function of composition. In the case of $\text{Bi}_2\text{Zn}_{2/3}\text{Nb}_{4/3}\text{O}_7$, $\text{Bi}_2\text{Zn}_{2/3}\text{Ta}_{4/3}\text{O}_7$, and $\text{Bi}_2\text{Mg}_{2/3}\text{Ta}_{4/3}\text{O}_7$, the maxima in ϵ'' was well below 100 K, whereas in the Sc and In containing pyrochlores the maxima resides between 125 and 200 K. The temperature shift in the dielectric relaxation with composition showed no systematic relationship to crystal chemical descriptions such as atomic mass and ionic radii. The dielectric maximum in the complex lead perovskite relaxors also is independent of the cation mass and ionic radii. After extensive studies in the perovskite relaxor system systems, it is believed that symmetry breaking defects play a more important role in controlling the nature of the dielectric spectra⁹. Similar behavior may be operating in the cubic bismuth pyrochlores; further comparisons are made through analysis of the relaxation behavior.

Qualitatively, similar dielectric relaxations to the bismuth pyrochlores have also been observed in compounds such as RADP¹² ($\text{Rb}_x\text{H}_2\text{PO}_4\text{-(NH}_4\text{)}_{1-x}$).

$_x\text{H}_2\text{PO}_4$), $\text{K}_{1-x}\text{Li}_x\text{TaO}_3$ ¹³, $\text{KBr}_{1-x}\text{CN}_x$ ¹⁴, and $\text{KI}_{1-x}(\text{NO}_2)_x$ ¹⁵., all referred to as dipolar and quadrupolar glasses. A comprehensive understanding of the dipolar glass dielectric behavior is still developing. However, it is possible to analyze the dielectric relaxation with a number of modified Arrhenius plots.

Consider first the basic Arrhenius equation, which was originally developed to model polar liquids and gas dielectric properties¹⁶. The observed behavior is noted to be similar to that characteristic of electric dipolar and quadrupolar glasses^{10,11} such as RADP^{12} ($\text{Rb}_x\text{H}_2\text{PO}_4-(\text{NH}_4)_{1-x}\text{H}_2\text{PO}_4$), $\text{K}_{1-x}\text{Li}_x\text{TaO}_3$ ¹³, $\text{KBr}_{1-x}\text{CN}_x$ ¹⁴, and $\text{KI}_{1-x}(\text{NO}_2)_x$ ¹⁵.

For these systems, the dielectric data can be fitted to an Arrhenius-type equation of the following form:

$$\frac{1}{\tau_c} = \nu_0 \exp \left[\frac{-E_a}{k_B T} \right] \quad (1)$$

where τ_c is the characteristic relaxation time, E_a is the activation energy, and the pre exponential, ν_0 , is the attempt jump frequency. Figure 4 presents an Arrhenius plot for the pyrochlores with full dispersion above 100 K, showing the linear relationship between the measuring frequency ($f = \nu / 2\pi = 1 / 2\pi\tau$) and the reciprocal of the temperature at which ϵ'' is maximum. Table II lists the fitting parameters, ν_0 and E_a , obtained from Eq. (1). The highest anticipated jumping frequency would be directly related to the ionic vibration of the lattice and hence $\nu_0 \approx 10^{13}$ Hz. In the $\text{K}(\text{Br},\text{CN})$ system^{14,17-19}, the parameters ν_0 and E_a obtained from this kind of analysis typically have values on the order of 10^{12-16} Hz and 0.05 eV, respectively. High jump frequencies 10^{16} to 10^{19} Hz suggest a further

refinement of the model to describe the dielectric relaxation in pyrochlores despite the excellent fit in Figure 4.

Recently, similar unphysical parameters were also found from fitting the dielectric dispersion of the perovskite Pb-based relaxors such as $\text{Pb}(\text{Mg}_{1/3}, \text{Nb}_{2/3})\text{O}_3$ ¹⁹. In many dipolar glass systems^{10,11} and in PMN²⁰, the anomalous magnitudes of the parameters v_0 and E_a could be reconciled by using a modification to the Arrhenius equation, the empirical Vogel-Fulcher equation:

$$\frac{1}{\tau_c} = v_0 \exp \left[\frac{-E_a}{T - T_F} \right] \quad (2)$$

In the Vogel-Fulcher equation, a parameter T_F is introduced as the freezing temperature of the dipolar glass state. T_F is regarded as the absolute temperature where the dynamic reorientation of dipolar cluster polarization no longer can be thermally activated. For the data in this research, however, the optimum fit of Eq. (2) was obtained with $T_F \sim 0$, which is equivalent to the simple Arrhenius equation (Eq. (1)), and therefore inadequately describes these pyrochlore systems.

An alternative model to describe dipolar glass dielectric dispersion was proposed by Binder and Young^{10,11} and is essentially a further modification of the Arrhenius Law:

$$\frac{1}{\tau_c} = v_0 \exp \left[- \left(\frac{E_a}{T} \right)^{zv} \right] \quad (3)$$

where zv is an additional fitting parameter. In this case, the activation energy, E_a , is given in units of absolute temperature. This equation was originally derived to describe the dynamics of domain wall nucleation. Table III lists v_0 and E_a values derived from the plot of Eq. (3) (Figure 4)

With the aim of obtaining an operational dielectric at microwave frequencies, the Arrhenius equations and modified Arrhenius equations can be useful in estimating the temperature at which the dielectric dispersion will occur. At room temperature, the pyrochlore compositions in this study typically had dielectric constants at 1 MHz ranging from 60 to 200 and dielectric losses of approximately 10^{-3} to 10^{-4} . These low loss characteristics make them promising candidates for high frequency dielectric applications. However, the loss peak associated with the dielectric dispersion observed in these materials could possibly increase the losses at high frequencies at room temperature.

By using the Arrhenius equations for the pyrochlore compositions in this study, the temperature at which the loss peak occurs at high frequency can be estimated by extrapolation. Table IV show T_{\max} extrapolated from the Arrhenius parameters in Table II obtained from the dielectric data. For compositions in which T_{\max} was below 100 K and hence could not be measured, average values of ν_0 and E_a were assumed. As shown in Table IV, the Sc and In containing compositions would have loss peaks at 1 GHz approaching room temperature and would not be suitable for high frequency applications. However, there are a number of compositions which have 1 and 10 GHz loss peaks well below room temperature, e.g. $\text{Bi}_2\text{Zn}_{2/3}\text{Nb}_{4/3}\text{O}_7$, $\text{Bi}_2\text{Zn}_{2/3}\text{Ta}_{4/3}\text{O}_7$, and $\text{Bi}_2\text{Mg}_{2/3}\text{Ta}_{4/3}\text{O}_7$.

V. CONCLUSIONS

In bismuth pyrochlores with different compositions, a dielectric anomaly was found in all samples at temperatures ranging from <100 K to

With the aim of obtaining an operational dielectric at microwave frequencies, the Arrhenius equations and modified Arrhenius equations can be useful in estimating the temperature at which the dielectric dispersion will occur. At room temperature, the pyrochlore compositions in this study typically had dielectric constants at 1 MHz ranging from 60 to 200 and dielectric losses of approximately 10^{-3} to 10^{-4} . These low loss characteristics make them promising candidates for high frequency dielectric applications. However, the loss peak associated with the dielectric dispersion observed in these materials could possibly increase the losses at high frequencies at room temperature.

By using the Arrhenius equations for the pyrochlore compositions in this study, the temperature at which the loss peak occurs at high frequency can be estimated by extrapolation. Table IV show T_{\max} extrapolated from the Arrhenius parameters in Table II obtained from the dielectric data. For compositions in which T_{\max} was below 100 K and hence could not be measured, average values of ν_0 and E_a were assumed. As shown in Table IV, the Sc and In containing compositions would have loss peaks at 1 GHz approaching room temperature and would not be suitable for high frequency applications. However, there are a number of compositions which have 1 and 10 GHz loss peaks well below room temperature, e.g. $\text{Bi}_2\text{Zn}_{2/3}\text{Nb}_{4/3}\text{O}_7$, $\text{Bi}_2\text{Zn}_{2/3}\text{Ta}_{4/3}\text{O}_7$, and $\text{Bi}_2\text{Mg}_{2/3}\text{Ta}_{4/3}\text{O}_7$.

V. CONCLUSIONS

In bismuth pyrochlores with different compositions, a dielectric anomaly was found in all samples at temperatures ranging from <100 K to

room temperature. Using the thermally activated dielectric relaxation equations, it is possible to make approximations of the dielectric behavior at higher frequencies ~ 1 GHz at room temperature. The anomaly was characterized by a frequency dispersive decrease in the real part of the dielectric constant, and a corresponding peak in the imaginary part of the dielectric constant. The anomaly appears similar to the dispersion that occurs at the freezing temperature of dipolar glass systems. These data were analyzed using a number of Arrhenius-type plots with reasonable accuracy and shows characteristics common to dipolar glass systems. Additionally, the dielectric constant and loss coupled with the low sintering temperatures all show the potential for packaging applications, such as microwave capacitors for LTCC applications.

ACKNOWLEDGMENT

The authors would like to acknowledge the assistance of Dr. Scott L. Swartz for his helpful discussions and review of the manuscript.

TABLE I. Room temperature dielectric data for some pyrochlore compositions measured at 1 MHz.

Composition	K	$\tan \delta$
$\text{Bi}_2\text{Zn}_{2/3}\text{Nb}_{4/3}\text{O}_7$	143	.00025
$\text{Bi}_2\text{Zn}_{2/3}\text{Ta}_{4/3}\text{O}_7$	67	.0001
$\text{Bi}_2\text{Mg}_{2/3}\text{Nb}_{4/3}\text{O}_7$	210	.0003
$\text{Bi}_2\text{Mg}_{2/3}\text{Ta}_{4/3}\text{O}_7$	80	.0001
$\text{Bi}_2\text{Ni}_{2/3}\text{Nb}_{4/3}\text{O}_7$	122	.0001
$\text{Bi}_2\text{ScNbO}_7$	174	.008
$\text{Bi}_2\text{ScTaO}_7$	143	.0053
$\text{Bi}_2\text{InNbO}_7$	142	.0024
$\text{Bi}_2\text{InTaO}_7$	89	.0008
$\text{Bi}_2\text{Cu}_{2/3}\text{Nb}_{4/3}\text{O}_7$	250	.08

TABLE II. Fitting Parameters ν_0 and E_a obtained from the simple Arrhenius Equation [Eq. (1)].

Composition	ν_0 (Hz)	E_a (eV)
$\text{Bi}_2\text{ScNbO}_7$	1.23×10^{19}	0.508
$\text{Bi}_2\text{ScTaO}_7$	5.84×10^{19}	0.498
$\text{Bi}_2\text{InNbO}_7$	2.64×10^{17}	0.418
$\text{Bi}_2\text{InTaO}_7$	6.03×10^{16}	0.348
$\text{Bi}_2\text{Mg}_{2/3}\text{Nb}_{4/3}\text{O}_7$	2.31×10^{16}	0.319

TABLE III. Fitting Parameters ν_0 and E_a obtained from the modified Arrhenius Equation with the parameter $zv=2$. [Eq. (3)].

Composition	ν_0 (Hz)	E_a (eV)
$\text{Bi}_2\text{ScNbO}_7$	2.93×10^{11}	0.061
$\text{Bi}_2\text{ScTaO}_7$	6.31×10^{11}	0.058
$\text{Bi}_2\text{InNbO}_7$	2.07×10^{10}	0.045
$\text{Bi}_2\text{InTaO}_7$	4.43×10^{10}	0.053
$\text{Bi}_2\text{Mg}_{2/3}\text{Nb}_{4/3}\text{O}_7$	9.42×10^{09}	0.041

Table IV. High frequency T_{\max} values extrapolated from the simple Arrhenius equations [Eq. (1)].

Composition	1 GHz	10 GHz
	T_{\max}	T_{\max}
$\text{Bi}_2\text{ScNbO}_7$	254 K	281 K
$\text{Bi}_2\text{ScTaO}_7$	233 K	257 K
$\text{Bi}_2\text{InNbO}_7$	250 K	284 K
$\text{Bi}_2\text{InTaO}_7$	225 K	257 K
$\text{Bi}_2\text{Zn}_{2/3}\text{Nb}_{4/3}\text{O}_7$	<156 K	<183 K
$\text{Bi}_2\text{Zn}_{2/3}\text{Ta}_{4/3}\text{O}_7$	<156 K	<183 K
$\text{Bi}_2\text{Mg}_{2/3}\text{Nb}_{4/3}\text{O}_7$	<156 K	<183 K
$\text{Bi}_2\text{Mg}_{2/3}\text{Ta}_{4/3}\text{O}_7$	<156 K	<183 K
$\text{Bi}_2\text{Ni}_{2/3}\text{Nb}_{4/3}\text{O}_7$	<156 K	<183 K

REFERENCES

- ¹T. Takada, S. F. Wang, S. Yoshikawa, S. J. Jang, & R. E. Newnham, *J. Am. Ceram. Soc.* **77**, 1909 (1994).
- ²E. Aleshin & R. Roy, *J. Am. Ceram. Soc.* **45**, 18 (1965).
- ³M. F. Yan, H. C. Ling, & W. W. Rhodes, *J. Am. Ceram. Soc.* **73**, 1106 (1990).
- ⁴D. Liu, Y. Liu, S. Q. Huang, & X. Yao, *J. Am. Ceram. Soc.* **76**, 2129 (1993).
- ⁵F. Jona, G. Shirane, & R. Pepinsky, *Phys. Rev. B* **98**, 903 (1955).
- ⁶G. I. Golovshchikova, V. A. Isupov, A. G. Tutov, I. E. Myl'nikova, P. A. Nikitina, & O. I. Tulinova, *Sov. Phys. - Solid State* **14**, 2539 (1973).
- ⁷G. A. Smolenskii, V. A. Isupov, G. I. Golovshchikova, & A. G. Tutov, *Izv. Akad. Nauk SSSR, Neorg. Mat.* **12**, 255 (1974).
- ⁸S. L. Swartz & T. R. Shrout, *Mater. Res. Bull.* **17**, 1245 (1982).
- ⁹A.P. Levanyuk & A. S. Sigov, *Defects and Structural Phase Transitions*, p. 146. Gordon and Breach, New York (1988).
- ¹⁰K. Binder & A. P. Young, *Rev. Mod. Phys.* **58**, 801 (1986).
- ¹¹J. A. Mydosh, *Spin Glasses: An Experimental Introduction*, Taylor & Francis, Washington, DC (1993).
- ¹²E. Courtens, *Phys. Rev. Lett.* **52**, 69 (1984).
- ¹³U. T. Höchli, *Phys. Rev. Lett.* **48**, 1494 (1982).
- ¹⁴M. Julian & F. Luty, *Ferroelectrics* **16**, 201 (1977).
- ¹⁵I. Yamamoto, N. Ohtani, & S. Hirotsu, *Jap. J. Appl. Phys.* **24 Suppl.** 24-2, 992 (1985).
- ¹⁶P. Debye, *Polar Molecules*. Dover, New York (1945).
- ¹⁷N. O. Birge, Y. H. Jeong, S. N. Nagel, S. Bhattacharya, & S. Susman, *Phys. Rev. B* **30**, 2306 (1984).
- ¹⁸A. Loidl, R. Feile, & K. Knorr, *Phys. Rev. Lett.* **48**, 1263 (1982).
- ¹⁹S. Bhattacharya, S. R. Nagel, L. Fleishman, & S. Susman, *Phys. Rev. Lett.* **48**, 1267 (1982).
- ²⁰E. V. Colla, E. Yu. Koroleva, N. M. Okuneva, & S. B. Vakhrushev, *J. Phys. Cond. Matt.* **4**, 3671 (1992).
- ²¹D. Viehland, S. J. Jang, L. E. Cross, & M. Wuttig, *J. Appl. Phys.* **68**, 2916 (1990).
- ²²N. N. Kolpakova, M. Polomska, & J. Wolak, *Ferroelectrics* **126**, 151 (1992).
- ²³G. I. Skanavi, Ia. M. Ksendzov, V. A. Trigubenko, & V. G. Prokhvatilov, *Sov. Phys. JETP* **6(33)**, 250 (1958).
- ²⁴L. E. Cross, *Proc. I.E.E.* **109**, 407 (1962).
- ²⁵F. Jona & G. Shirane, *Ferroelectric Crystals*, p. 14. Pergammon Press, New York (1962).

Figure 1. Comparison of the fluorite structure and the pyrochlore structure. Note that the A site of the fluorite structure is differentiated into both A and B sites. Of the eight X sites in the fluorite structure, in the pyrochlore structure one is removed and the seventh (Y) anion is bound only to the A atoms.

Figure 2. Comparison of the powder XRD data for cubic pyrochlore $\text{Bi}_2\text{ScTaO}_7$ and the tetragonal pyrochlore $\text{Bi}_2\text{Cu}_{2/3}\text{Nb}_{4/3}\text{O}_7$.

Figure 3. Real and imaginary parts of the dielectric permittivities measured from 100 Hz to 100 kHz.

Figure 4. Arrhenius plots for the bismuth pyrochlores using Eq. (1) on the left and Eq. (3) on the right.

